A Multi-wavelength Study of Novae in M31

A Thesis
Submitted for the Degree of

Doctor of Philosophy

to

The Department of Physics
Pondicherry University
Puducherry 605 014, India

by

Judhajeet Basu
Indian Institute of Astrophysics
Bengaluru 560 034, India

August 2025

A Multi-wavelength Study of Novae in M31

by

Judhajeet Basu

Indian Institute of Astrophysics

Indian Institute of Astrophysics
Bengaluru - 560 034, India

Thesis title	:	**A Multi-wavelength Study of Novae in M31**
Author	:	**Judhajeet Basu**
Address	:	Indian Institute of Astrophysics, II Block, Koramangala, Bangalore - 560 034, India
Email (Primary)	:	judhajeet.basu@iiap.res.in
Email (Secondary)	:	judhajeet20@gmail.com
Supervisor	:	**Dr. Sudhanshu Barway**
Address	:	Indian Institute of Astrophysics, II Block, Koramangala, Bangalore - 560 034, India
Email	:	sudhanshu.barway@iiap.res.in

Declaration of Authorship

I hereby declare that the research contained in this thesis is the result of the investigations carried out by me at the Indian Institute of Astrophysics, Bengaluru, under the supervision of **Dr. Sudhanshu Barway**. This work has not been submitted for awarding a degree or any other qualification either in this university or any other institution.

Judhajeet Basu
PhD Student
Indian Institute of Astrophhysics,
Bengaluru 560 034,
India

Sign: Judhajeet Basu

Date: 08 August 2025

Certificate

This is to certify that the thesis titled **"A Multi-wavelength Study of Novae in M31"** submitted to Pondicherry University by Mr. Judhajeet Basu for the award of the degree of Doctor of Philosophy, is based on the results of the investigations carried out by him under my supervision and guidance, at Indian Institute of Astrophysics, Bangalore. This thesis has not been submitted to any other university or institute for the award of any degree, diploma, fellowship, etc.

Dr. Sudhanshu Barway
Thesis Supervisor
Indian Institute of Astrophysics,
Bengaluru 560 034
India

Sign: 

Date: 08/08/2025

List of Publications

A. Publications included in this thesis

1. *Survival of the accretion disk: UV–X-ray case study of the 2024 eruption of the LMC Recurrent Nova 1968-12a.* **Basu, J.** , G. C. Anupama, J. U. Ness et al. 2025, ApJ, 994, 229.

2. *Discovery and Detailed Study of the M31 Classical Nova AT 2023tkw: Evidence for Internal Shocks.* **Basu, J.**, Kumar, R., Anupama, G. C., et al. 2025, ApJ, 980, 129.

3. *Exploring the Archives: A Search for Novae in UVIT Snapshots of M31.* **Basu, J.** , Krishnendu, S., Barway, S., et al. 2024, ApJ, 971, 8.

4. *Multiwavelength Observations of Multiple Eruptions of the Recurrent Nova M31N 2008-12a.* **Basu, J.** , M. Pavana, G. C. Anupama et al. 2024, ApJ, 966, 44.

B. Conference Proceedings

1. *M31 nova survey using GIT and UVIT with a focus on the multiple eruptions of the remarkable recurrent nova M31N 2008-12a.* **Basu, J.** , Pavana, M., Anupama, G. C., et al. 2024, 42nd meeting of the Astronomical Society of India (ASI), 42, P102.

2. *"Shock"-ing results from M31: Detailed analysis of the slow classical nova AT 2023tkw (GIT20230919aa).* **Basu, J.** , Kumar, R., Anupama, G. C., et al. 2025, 43rd meeting of the Astronomical Society of India (ASI), 50.

C. Other contributed publications [Not part of this thesis]

1. *Challenging Classical Paradigms: Recurrent Nova M31N 2017-01e, a BeWD system in M31?* Chamoli, S., **Basu, J.** , et al. *(accepted for publication in ApJ).* arXiv 2508.02227.

2. *Searching for Gravitational Wave Optical Counterparts with the Zwicky Transient Facility: Summary of O4a.* Ahumada, T., Anand, S., Coughlin, M. W., ... **Basu, J.** , et al. 2024, PASP, 136, 114201.

3. *Science with the Daksha high energy transients mission.* Bhalerao, V., Sawant, D., Pai, A., ... **Basu, J.** , et al. 2024, Experimental Astronomy, 57, 23.

4. *Far-ultraviolet to Near-infrared Observations of SN 2023ixf: A High-energy Explosion Engulfed in Complex Circumstellar Material.* Teja, R. S., Singh, A., **Basu, J.** , et al. 2023, *Astrophys. J. Lett.*, 954, L12.

5. *India's First Robotic Eye for Time-domain Astrophysics: The GROWTH-India Telescope.* Kumar, H., Bhalerao, V., Anupama, G. C.,... **Basu, J.** et al. 2022, *Astron. J.*, 164, 90.

D. Non-refereed publications

1. *GIT observations of AT 2025nsa in M31.* Chamoli, S., **Basu, J.** , Barway, S., et al. 2025, The Astronomer's Telegram, 17241, 1.

2. *Spectroscopic observation of the transient AT 2024afyi in M33.* Chamoli, S., **Basu, J.** , Anupama, G. C., et al. 2025, The Astronomer's Telegram, 16965.

3. *Spectroscopic confirmation of the 2024 outburst of M31N 2008-12a.* **Basu, J.** , Chamoli, S., Barway, S., et al. 2024, The Astronomer's Telegram, 16945.

4. *Spectroscopic confirmation of AT 2024aayx as a nova in M31.* **Basu, J.** , Chamoli, S., Barway, S., et al. 2024, The Astronomer's Telegram, 16908.

5. *GIT observations of the M31 nova AT 2024zaq.* **Basu, J.** , Chamoli, S., Barway, S., et al. 2024, The Astronomer's Telegram, 16884.

6. *Spectroscopic confirmation of AT 2024aayx as a nova in M31.* **Basu, J.** ., Chamoli, S., Barway, S., et al. 2024, The Astronomer's Telegram, 16908.

7. *GIT observations of the 2024 outburst of the recurrent nova M31N 2017-01e.* **Basu, J.** , Kumar, R., Anupama, G. C., et al. 2024, The Astronomer's Telegram, 16759.

8. *LIGO/Virgo/KAGRA S240422ed: Himalayan Chandra Telescope follow-up of the Swift/XRT source S240422ed_X101 2024.* Swain, V., Waratkar, G., ..., **Basu, J.** , ..., et al., GCN, 36287.

9. *AstroSat/UVIT detection of the RN M31N 2013-10c.* **Basu, J.** , Chamoli, S., Barway, S., Anupama, G. C., 2024, The Astronomer's Telegram, 16526.

10. *GIT observations of AT 2023yqt in M31.* Chamoli, S., **Basu, J.** , Barway, S., et al., 2023, The Astronomer's Telegram, 16368.

11. *Spectroscopic confirmation of the 2023 outburst of M31N 2008-12a.* **Basu, J.** , Barway, S., Anupama, G. C., Chamoli, S., Kumar, S. P., 2023, The Astronomer's Telegram, 16367.

12. *HCT detection of the 2023 eruption of M31N 2008-12a.* **Basu, J.** , Barway, S., Anupama, G. C., et al. 2023, The Astronomer's Telegram, 16364.

13. *Spectroscopic classification of AT 2023tkw (GIT230919aa) as a nova in Fe II phase.* **Basu, J.** , Kumar, R., Anupama, G. C., et al. 2023, The Astronomer's Telegram, 16311.

14. *Pre-discovery GIT detection of AT 2023uri in M31.* Chamoli, S., **Basu, J.** , Swain, V., et al. 2023, The Astronomer's Telegram, 16293.

15. *GIT detection of AT 2023uiq in M31.* Chamoli, S., **Basu, J.** , Swain, V., et al. 2023, The Astronomer's Telegram, 16292.

16. *GIT discovery of an optical transient in M31.* Kumar, R., Swain, V., **Basu, J.** , et al. 2023, Transient Name Server AstroNote, 255.

17. *GIT and HCT observations of the nova AT 2023prq / ZTF23aaxzvrr near M31.* **Basu, J.** , Swain, V., Teja, R. S., et al. 2023, The Astronomer's Telegram, 16198.

18. *Search for the progenitor of SN 2023ixf in archival AstroSat UVIT images.* **Basu, J.** , Barway, S., Anupama, G. C., et al. 2023, The Astronomer's Telegram, 16064

19. *GROWTH-India Telescope pre-discovery detection and follow-up of the M31 Nova AT 2022acwk.* **Basu, J.** , Swain, V., Kumar, H., et al. 2023, The Astronomer's Telegram, 15864

20. *AstroSat UVIT observations of the 2022 outburst of Recurrent Nova M31N2008-12a.* **Basu, J.** , Barway, S., Anupama, G. C., et al. 2022, The Astronomer's Telegram, 15810

21. *HCT optical spectroscopy of the 2022 outburst of recurrent nova M31N 2008-12a.* **Basu, J.** , Barway, S., Anupama, G. C., et al. 2022, The Astronomer's Telegram, 15790

22. *GROWTH-India Telescope observations of the 2022 outburst of Recurrent Nova M31N2008-12a.* **Basu, J.** , Swain, V., Kumar, H., et al. 2022, The Astronomer's Telegram, 15789

23. *GROWTH-India Telescope observations of the nova AT 2022yax in M31.* **Basu, J.** , Barway, S., Anupama, G. C., et al. 2022, The Astronomer's Telegram, 15706

24. *GROWTH-India Telescope follow-up observations of the nova AT 2022cpe in M31.* **Basu, J.** , Kumar, H., Anupama, G. C., et al. 2022, The Astronomer's Telegram, 15249

25. *Optical spectroscopy of the 2021 outburst of recurrent nova M31N 2008-12a.* Sonith, L. S., **Basu, J.** , Anupama, G. C., et al. 2021, The Astronomer's Telegram, 15045

26. *GROWTH-India telescope follow-up of 2021 eruption of recurrent nova M31N 2008-12a.* **Basu, J.** , Kumar, H., Anupama, G. C., et al. 2021, The Astronomer's Telegram, 15038

List of Conferences

Conference Presentations

1. European Astronomical Society Annual Meeting. SS43a: Novae: From Accretion to Post-Eruption Phenomena. 23–27 June 2025. University College Cork, Ireland (online).
   Talk: *Chasing Nova Explosions: From Surveys to Recurrence to Shockwaves*

2. IIA in-house symposium. 1–3 Apr 2025. IIA Bangalore.
   Talk: *Observing Nova Outbursts from Space: UV and X-Ray Study of Novae in M31 and LMC with AstroSat and Swift*

3. Transients from Space. 11–13 Mar 2025. STScI Baltimore (USA).
   Poster: *Observing Nova Outbursts from Space: A Detailed UV and X-Ray Study of Novae in M31 and LMC with AstroSat and Swift*

4. Astronomical Society of India 43rd Meeting. 15–19 Feb 2025. NIT Rourkela.
   Talk: *"Shock"-ing results from M31: Detailed analysis of the slow classical nova AT2023tkw*

5. NUVA e-meeting "The impact of UV surveys in Astronomy". 15–17 October 2024 (online).
   Talk: *Exploring the Archives: A Search for Novae in UVIT Snapshots of M31*

6. IIA in-house symposium. 26–28 Mar 2024. IIA, Bangalore.
   Poster and Flash Talk: *Multi-wavelength observations of multiple eruptions of the recurrent nova M31N 2008-12a*

7. Astronomical Society of India 42nd Meeting. 31 Jan – 4 Feb 2024. IISc Bangalore.
   Poster: *M31 nova survey using GIT and UVIT with a focus on the multiple eruptions of the remarkable recurrent nova M31N 2008-12a*

8. REcent Trends in the study of Compact Objects (RETCO-V). 03–05 Apr 2023. KSO, Kodaikanal.

Talk: *Multiwavelength observations and optical spectra modelling of the extragalactic nova M31N 2008-12a*

9. IIA in-house symposium. 30–31 Mar 2023. IIA, Bangalore.
   Poster: *Multi-wavelength Studies of RN M31N 2008-12a*

10. Young Astronomer's Meet (YAM). 09–13 Nov 2022. ARIES, Nainital (online).
    e-poster: *Multi-wavelength Study of an extra-galactic recurrent Nova in M31*

11. Celebrating Seven Years of AstroSat. 28–29 Sep 2022. ISRO HQ, Bangalore.
    Poster: *AstroSat UVIT and SXT Observations of Novae in M31*

Schools and Workshops

1. AI/ML Applications in Astronomy: Generative AI & Agentic Coding. 29-30 May 2025. IIA Bangalore.
   Attended in-person and was a volunteer.

2. ZTF Summer School. 24-28 July 2023. U Minnesota, USA.
   Attended online.
   Theme: Transients.

3. First UVEX Community Workshop. 13-15 Mar 2023. Pasadena, USA.
   Attended Online.

4. Indo-French CEFIPRA Astronomy Meeting (IFCAM)-III SKA/MSE and Multi-wavelength Synergies Workshop. 09-13 Jan 2023. IIA Bangalore.
   Attended in-person.

5. ZTF Summer School 2022. 25-29 July 2022. U Minnesota, USA.
   Attended online.
   Theme: Multi-messenger Astrophysics.

6. Astronomical Data Analysis using Python. 08 Nov - 18 Dec 2021. IUCAA, Pune.
   Attended online.

Acknowledgement

I thank my supervisor, Dr. Sudhanshu Barway, for his unwavering support throughout my PhD journey. His valuable guidance and steadfast backing helped me overcome various challenges I faced over the years. By encouraging collaborations, he motivated me to grow as an independent researcher. Whether academic or administrative matters, his calm way of dealing with situations has been an inspiring lesson. I also fondly recall the many occasions he treated us to lunch and dinner, which helped strengthen our bond during these five years through good food and conversations.

I would also like to thank my close collaborator, Prof. G. C. Anupama, for her invaluable insights that helped shape and improve the scientific content of my thesis. I have learned a great deal from her vast experience in transient astronomy, especially in novae. Her approach to research inspired me to be more meticulous and thoughtful in my own work.

I would like to acknowledge my collaborator, Prof. K. P. Singh, from whom I learnt X-ray astronomy. I am grateful to my senior, Dr. Pavana M., for her immense help and assurance with data, modelling, and writing during my initial years. I am thankful for having 'super seniors' working on supernovae like Dr. Anirban Dutta, Dr. Rishabh Singh Teja, and Dr. Avinash Singh, who helped me with the basics of astronomy and motivated me to be in the field of astronomical transients. I would like to thank my junior colleague Shatakshi Chamoli for her help and the inquisitive conversations I had with her. I extend my gratitude to my collaborator, Dr. Varun Bhalerao, and his group at IIT Bombay, which includes Dr. Harsh Kumar, Vishwajeet, Utkarsh, Gaurav, and Ravi, for their assistance with the GROWTH-India Telescope (GIT) operations and data processing, and for the discussions during the weekly calls. I cherished my time spent with them at IIT Bombay while working on GIT. I would also like to thank my collaborators Krishnendu S., Prof. Peter Hauschildt, Dr. Jan-Uwe Ness, Viraj Karambelkar,

Kaustav K. Das, Dr. Mansi Kasliwal, Dr. Shubham Srivastav, Sonith L. S., Dr. Anirban Dutta, and Dr. Arvind Balasubramanian.

I am grateful to my teachers in school, tuition, and in my college at IIT Kharagpur, who helped me establish a good base in Physics and in Science in general, without which I would not have been able to start my PhD journey. I am also thankful to the faculty at IIA and IISc Bangalore for their course on the fundamentals of Astronomy. I thank my project supervisors during my undergraduate studies, Prof. Sayan Kar, Prof. Amitesh Omar, Prof. Boudewijn Roukema, and Prof. Dipankar Banerjee, for encouraging me to work in Astrophysics.

I would like to thank my doctoral committee members, Prof. D. K. Sahu and Prof. S. Sivaprakasam, and my comprehensive examiner, Prof. Vikram Rana, for providing valuable suggestions to improve my work. I thank the director of IIA, Prof. Annapurni Subramaniam, the deans of IIA, Prof. G. C. Anupama, Prof. B. E. Reddy, and Prof. Sivarani Thirupathi, and the Board of Graduate Studies (BGS) chairs at IIA, Prof. Umanath S. Kamath, Prof. Maheswar Gopinathan, and Dr. Piyali Chatterjee, for providing a research-friendly environment at IIA. I thank the BGS office and BGS members, computer support, auditorium staff, library staff, the dean's office, the director's office, and the members of the administrative section at IIA for their help with various official work. I would also like to thank the HoD of Physics, the CoE, the library personnel, and the administrative team at Pondicherry University for their assistance with the official matters. I thank the IIA outreach team for increasing the visibility of my work. I am thankful to the staff at CREST, notably Pramod, Srikanth, Surya, Aditya, Nayana, Yogita, Sujith, and Mulchand, for their help during observations. I extend my thanks to Dorje Angchuk, Tsewang Stanzin, Sonam, and other members of IAO, Hanle, as well as Venkatesh and other members of VBO, Kavalur, for their warm welcome and assistance during my visit to the observatories. I also thank the staff at Bhaskara hostel, IIA canteen, and at CREST who took care of meals

and accommodation during these five years.

This PhD journey has been a lot less tumultuous because of my friends. I am thankful to my reliable batchmates Soumyaranjan, Sipra, Neeraj, and Amrutha for their company through thick and thin. I was lucky to have seniors like, in no particular order, Satabdwa, Deepak, Partha, Swastik, Athira, Debjit, Prajwel, Vikrant, Jyoti, Sioree, Indrani, Bibhuti, Raghu, Bharat, Anohita, Manjunath, Shubham, Dhanush, Aratrika, and others for their wisdom and support in various aspects of my PhD. Also, thanks to my juniors, likewise in no particular order, Saili, Chandan, Abishek, Lupamudra, Rupesh, Shashank, Pravash, Arav, Kanan, Khushbu, Anisha, Sriram, Hrishav, Annu, Swagata, Ajay, Sankalp, and others for making my life vibrant during these years. I am grateful to my unfailingly supportive friends Sunayana, Shubhangi, and Sushant for their company in exchange for the innumerable times I treated them. I would also like to thank everyone who shared the field and court with me. Being part of sports activities kept me mentally and physically grounded throughout my research journey, and I am truly grateful for the companionship.

I would also like to thank my college friends Subhadip, Abhikbrata, Anirudh, Chirantan, Baibhab, Sai Sumanth, Kushal, and Omprakash, whose continued journey in academia has been a constant source of motivation and has helped maintain our enthusiasm for research. If any names have slipped my mind, please accept my heartfelt thanks, your contribution is valued and appreciated.

Last, but not least, I would like to thank my family, especially my parents, for encouraging me to start, continue, and finally finish this journey. Special shoutout to my amazing sister, brother, brother-in-law, and my adorable nephew who always made me feel at home (in Bangalore), away from home (in Kolkata).

★✻

Data and Software usage

Data accumulation: We are grateful to the support staff and the observers at Vainu Bappu Observatory (VBO) Kavalur, Centre for Research and Education in Science and Technology (CREST) Hosakote, and Indian Astronomical Observatory (IAO) Hanle for observation assistance. The facilities at IAO, CREST, and VBO are operated by the Indian Institute of Astrophysics (IIA), Bangalore. We also thank the TAC for accepting our Target of Opportunity (ToO) proposals. We thank the numerous PIs who accommodated our ToO requests to observe transient phenomena with the HCT.

We acknowledge the use of the GROWTH-India telescope (GIT) data. GIT is a 70 cm telescope with a 0.7° field of view set up by IIA and the Indian Institute of Technology Bombay (IITB) with funding from the Indo-US Science and Technology Forum and the Science and Engineering Research Board, Department of Science and Technology, Government of India. It is located at the IAO, Hanle. We acknowledge funding by the IITB alumni batch of 1994, which partially supports the operation of the telescope. Telescope technical details are available online*.

This work uses the Soft X-ray Telescope (SXT) and the Ultraviolet Imaging Telescope (UVIT) data from the *AstroSat* mission of the Indian Space Research Organisation (ISRO). We thank the *AstroSat* TAC for allowing us ToO time for observations. We thank the SXT and UVIT payload operation centers for verifying and releasing the data via the ISSDC data archive and providing the necessary software tools. We thank the PIs of the archival observations used in this study.

We acknowledge the use of public data from the *Swift* and Zwicky Transient Facility (ZTF) data archives.

We acknowledge the observers at Keck Observatory and the developers of

*https://sites.google.com/view/growthindia/

the Keck data reduction tools.

Light Curve & Spectra Modeling: Light curve modeling and statistics were performed with Gaussian Process Regression techniques using `scikit-learn` (Pedregosa et al. 2011). Different modelling codes were used to model novae spectra at different bands in different phases. `CLOUDY` (Ferland et al. 2017a; Chatzikos et al. 2023) was used to model the photoionized phase of novae while `PHOENIX` (Hauschildt & Baron 1995; Hauschildt et al. 1997; Hauschildt 2008) was used to model the optically thick expanding atmosphere phase of novae. `XSPEC v12.12.0` (Arnaud 1996) was used to model the X-ray spectra during the supersoft phase of novae.

Data Reduction and Analysis: Softwares used for data reduction and analysis include:

UVIT data reduction was performed using `CCDLAB` (Postma & Leahy 2017, 2021a).

Optical imaging and spectroscopic data reduction were performed with `IRAF v2.16.1` (Tody 1993).

This work has also used software and web tools obtained from NASA's High Energy Astrophysics Science Archive Research Center (HEASARC), a service of the Goddard Space Flight Center and the Smithsonian Astrophysical Observatory. It includes `HEASOFT v6.25, XIMAGE v4.5.1`, and `XSELECT v2.4e` (Nasa High Energy Astrophysics Science Archive Research Center (Heasarc) 2014).

`Python v3.6.6` (Van Rossum & Drake 2009) and its packages `NumPy` (Harris et al. 2020), `SciPy` (Virtanen et al. 2020), `Pandas` (Wes McKinney 2010), `Matplotlib` (Hunter 2007), `astroquery` (Ginsburg et al. 2019), `photutils` (Bradley et al. 2023), `Spalipy` (Lyman 2021), `extinction` (Barbary 2021) were extensively used in the thesis for data analysis and plotting.

Astromatic software `SExtractor` (Bertin & Arnouts 1996a), `SWarp` (Bertin

et al. 2002), `SCAMP` (Bertin 2006) and `PSFEx` (Bertin 2011) were used to prepare optical and UV images for photometry.

`SAOImageDS9` (Joye & Mandel 2003) was particularly useful in visually analysing astronomical FITS files.

Others: Various resources available online, such as NASA ADS and `arXiv`, were used during this thesis to survey literature. GitHub was used for file sharing and keeping a record of code and data. Grammarly was used to ensure proper English in the thesis. Overleaf was used to compile this thesis and the papers written during this PhD work.

To my

parents

&

my family

⁕

"Photons are the messengers of the universe. They are all we have, and from them, we have learned nearly all we know about the cosmos."

— Anonymous

Abstract

We present a comprehensive multi-wavelength study of extragalactic novae, with particular emphasis on rapidly recurring systems and their ultraviolet (UV) properties. Novae are thermonuclear runaway reactions that occur on the semi-degenerate surfaces of accreting white dwarf stars in close binary systems. These are important astrophysical laboratories for understanding binary evolution, accretion physics, shock formation, and galactic chemical enrichment. Through systematic observations using space-based UV and X-ray telescopes, along with ground-based optical observations, this work contributes to our understanding of nova physics across different evolutionary phases and recurrence timescales.

We present the first systematic UV survey of novae in M31 using archival UVIT data. Through analysis of 19 different fields covering significant portions of M31, we developed background subtraction techniques to detect faint novae, particularly in the bright galactic bulge region. The resulting catalogue includes 42 novae detected in both outburst and quiescent phases. Quiescent novae showed signs of an accretion disc, whereas erupting novae showed signs of a shrinking photosphere. This work addressed the observational gap in systematic quiescent UV studies of extragalactic novae.

The focus then shifts to M31N 2008-12a, a remarkable rapidly recurring nova with annual eruptions from 2008 to 2024. Through multi-wavelength observations covering eight consecutive eruptions (2017-2024), we investigated the unparalleled consistency in light curve morphology, spectroscopic properties, and supersoft X-ray evolution. The analysis reveals that M31N 2008-12a hosts a white dwarf near the Chandrasekhar limit, making it a potential Type Ia supernova progenitor. We found strong evidence for jet-like bipolar structures that provide insights into nova explosion geometry. Anti-correlated UV and X-ray fluxes during the supersoft phase hinted towards disc activity resuming soon after each eruption.

This leads to a study on rapidly recurring systems, focusing on LMCN 1968-12a, the first discovered extragalactic recurrent nova. Using simultaneous UV and X-ray observations of its 2024 eruption, we investigated the survival of the accretion disk following nova outbursts. The multi-wavelength light curves reveal distinct emission components: supersoft X-rays from the white dwarf surface at temperatures of $\sim 10^6$ K, and UV emission from an irradiated accretion disk at $\sim 2 \times 10^4$ K. The persistence of UV emission during the plateau phase provides strong evidence for disk survival and rapid reformation within days of the eruption.

We end the study of individual events with a detailed study of the slow classical nova AT 2023tkw, discovered by the GROWTH-India Telescope in M31. The nova exhibited a complex light curve with multiple peaks and dips. Optical-infrared observations reveal internal shock mechanisms responsible for the observed light curve variability, challenging traditional nova models and demonstrating the importance of shock-induced heating in nova explosions.

The thesis ends with a summary of the key outputs from the thesis. We also briefly describe how synergies between upcoming and modern space-based UV and X-ray observatories and ground-based optical, infrared and radio observatories will lead to a comprehensive multi-wavelength understanding of novae populations, and will also be a key to unlocking the mysteries of outlier events.

These results contribute to our understanding of nova physics, particularly the role of accretion discs in rapid recurrence, the nature of massive white dwarf systems, shock mechanisms in classical novae, and the potential connections between rapidly recurring novae and Type Ia supernova progenitors. Through this comprehensive approach, the work successfully covers a diverse class of novae ranging from slow classical systems to the fastest-recurring extragalactic novae known, providing insights into the opposite ends of the spectrum of nova behaviour and evolution.

Contents

List of Figures

List of Tables

Chapter 1

Introduction

"Wonder is the beginning of wisdom."

— Socrates

Novae are one of the spectacular transient phenomena in the universe. These cataclysmic events, triggered by thermonuclear runaway (TNR) reactions in a thin layer just above the surface of accreting white dwarf (WD) stars, represent one of the important classes of stellar explosions, along with supernovae. The study of novae provides crucial insights into binary star system evolution, accretion processes, nucleosynthesis, shock and jet mechanisms, and the chemical enrichment of galaxies.

1.1 The Binary System

Novae originate within interacting binary star systems, fundamentally comprising a mass accretor (the WD primary), a mass donor (the secondary), and the mass

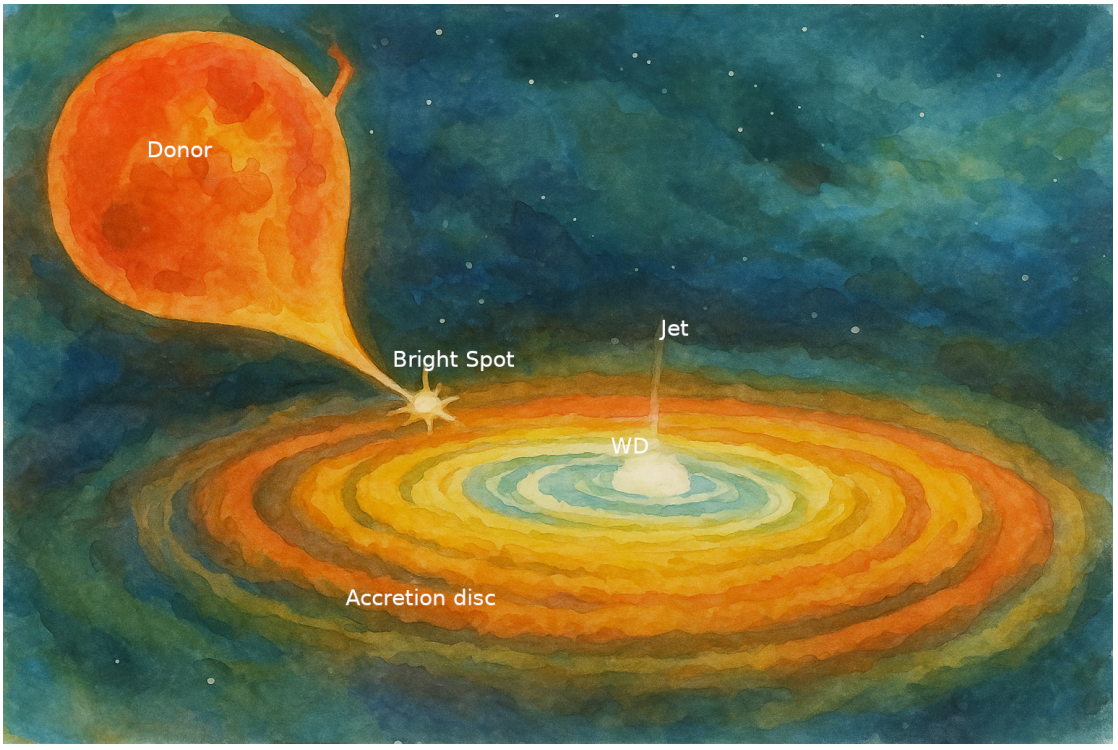

FIGURE 1.1: Artificial Intelligence rendition of a nova binary system with a non-magnetic WD. Image created by OpenAI's ChatGPT (`v GPT-4o`; OpenAI 2025).

transporter (the accretion disc).

1.1.1 White Dwarf

The WD, which acts as the primary, is the stellar remnant serving as the site of the thermonuclear reaction. This compact, evolved object is sustained by electron degenerate pressure. This state is reached after exhausting the nuclear fuel in a Sun-like star. The mass of the WD (M_{WD}), its core temperature and composition, and the rate at which matter is accreted are all critical factors that determine the outcome of the H-rich mass transfer (Starrfield et al. 2000; Townsley & Bildsten 2004; Yaron et al. 2005; Nomoto et al. 2007). WDs found in nova systems can be either carbon-oxygen (CO) or oxygen-neon (ONe) types, with CO WDs originating from stars with zero age main sequence masses (M_{ZAMS}) typically up to

7–8 $M_\odot$, and ONe WDs from stars with M_{ZAMS} between 8 to 10 $M_\odot$ (Doherty et al. 2015). Overabundances of elements like C, O, and Ne in the ejecta are often observed in novae spectra. This metallicity enhancement indicates dredge-up from the WD's surface into the atmosphere, as temperatures during the TNR are not high enough to synthesise such heavy elements (Ferland & Shields 1978; Williams et al. 1985; Gehrz et al. 1998a). Certain nova systems, including GK Per, DQ Her, and V1500 Cyg, have been recognised as containing magnetic WDs.

During an eruption, the WD luminosity can reach, or even exceed, the Eddington limit (L_{Edd}) in the case of WDs with mass nearing the Chandrasekhar limit ($M_{WD} \rightarrow M_{Ch} \approx 1.44\ M_\odot$). A key method for estimating the WD's mass directly involves measuring the temperature of the supersoft X-ray source emitted during the nova event. The WD's luminosity during this sustained burning period can be around 10^{37}–10^{38} erg s^{-1}.

$$T_{\rm eff} \approx \left(\frac{L}{4\pi\sigma R_{\rm WD}^2}\right)^{1/4} \approx 6 \times 10^5\ {\rm K} \left(\frac{L}{10^{38}\ {\rm erg\ s^{-1}}}\right)^{1/4} \left(\frac{R_{\rm WD}}{10^9\ {\rm cm}}\right)^{-1/2} \tag{1.1}$$

The temperature can be used to determine the WD radius using Equation 1.1. The WD mass can then be obtained from the radius using the relation given in Equation 1.2 from Nauenberg (1972).

$$R_{\rm WD} \approx 8.9 \times 10^8\ {\rm cm} \left(\frac{M_{\rm WD}}{M_\odot}\right)^{-1/3} \left[1 - \left(\frac{M_{\rm WD}}{M_{\rm Ch}}\right)^{4/3}\right]^{1/2} \tag{1.2}$$

Higher M_{WD} values imply higher densities and temperatures for a given accreted mass (M_{acc}), leading to a smaller ignition mass (M_{ig}) for the TNR (Wolf et al. 2013).

1.1.2 Secondary Star

The secondary star is the companion that continuously supplies the H-rich material to the WD. The donor star is typically a main-sequence star that fills its Roche lobe, leading to the formation of cataclysmic variables (CVs). These systems are generally characterised by short orbital periods, typically ranging between 1.4 and 10 hours (Warner 1995). Some nova systems also have a sub-giant companion with an orbital period ranging in the order of days (Darnley et al. 2012). In contrast, some novae feature an evolved giant star as their secondary, often associated with longer orbital periods exceeding 100 days (Mikolajewska 2010). Among all the observed novae, 20–40% have red-giant secondaries (Williams et al. 2016). A very rare class, known as helium novae, of which V445 Pup is a prototype (Kato & Hachisu 2003a), involves a helium star as the companion. It transfers mass to the WD via unstable helium burning, which results in hydrogen-deficient spectra (Ashok & Banerjee 2003).

A nova eruption can also significantly impact the companion star, potentially leading to ablation and irradiation, which may temporarily increase its mass-transfer rate (Figueira et al. 2025).

1.1.3 Accretion Disc

The accretion disc forms around the WD as the H-rich material is transferred from the secondary star. The inflowing gas carries significant angular momentum, which prevents it from directly striking the WD surface and instead causes it to spread out into a disc. Its luminosity is directly linked to the mass accretion rate ($\dot{M}$) onto the WD. The mass transfer from the secondary typically occurs via Roche-Lobe Overflow (RLOF) through the inner Lagrangian point (L1).

During quiescence, the strong blue continuum and emission lines observed are understood to arise from the accretion disc surrounding the WD primary. Modelling of the accretion disc spectrum can yield estimates of mass transfer rates. Nova CV systems typically have mass-transfer rates $\dot{M} \approx 10^{-11}$–10^{-7} $M_{\odot}$ year^{-1} (Patterson 1984). The accretion disc spectrum generally exhibits a sharp cutoff at shorter wavelengths due to a finite inner radius and at longer wavelengths due to a finite outer radius. Magnetic fields of the WD can disrupt the accretion disc, affecting the flow of gas near its inner edge.

The three different components of a nova binary system emit predominantly at different wavelengths. The hot WD peaks in soft X-rays to extreme ultraviolet (EUV), the accretion disc peaks around near ultraviolet (NUV) to optical, whereas the cooler secondary peaks in optical to infrared (IR). Spectral Energy Distribution (SED) evolution tracing the temporal evolution of fluxes of all three components, along with that of the ejecta, has been shown in Skopal (2015).

1.2 The Physical Nature of Novae

Nova eruptions occur in CVs where a WD primary accretes material from a companion star, typically a main sequence, subgiant, or red giant star (Starrfield et al. 2016; Kato et al. 2022). The fundamental process begins when H-rich material from the secondary star accumulates above the surface of the WD through either direct pile-up of the secondary star's winds or via an accretion disc. As this material builds up, it forms a degenerate layer at the base of the accretion disc that becomes increasingly hot and dense due to compression by the WD's intense gravitational field.

As more matter is accumulated in a shell, the density increases and so does the

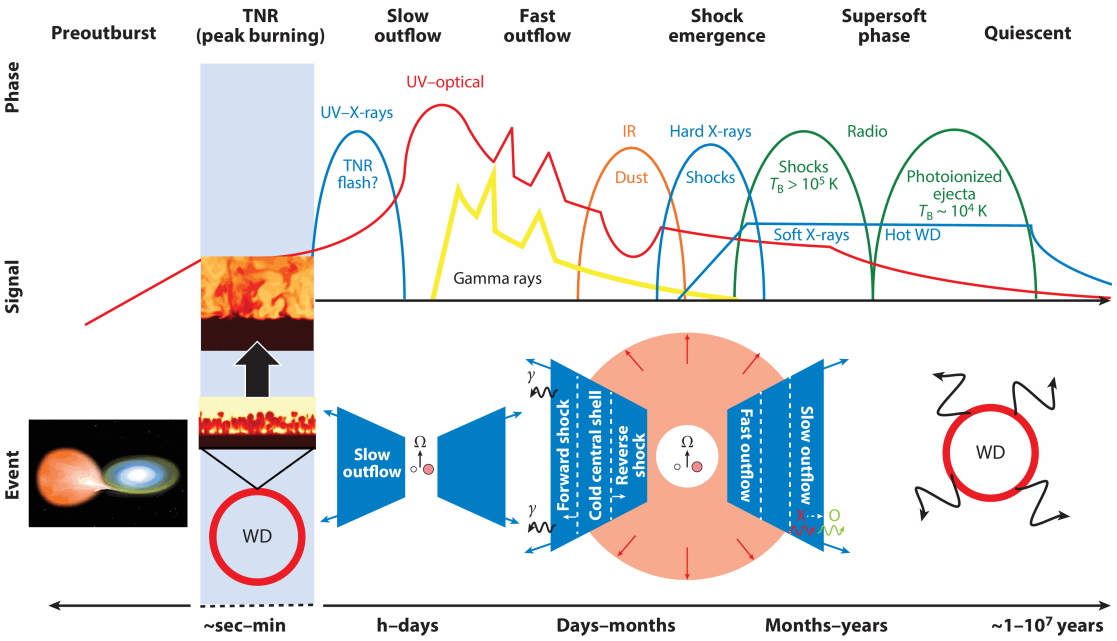

FIGURE 1.2: The trigger and aftermath of a nova eruption depicted through a light curve. Figure adapted from Chomiuk et al. (2021a).

pressure, reaching a critical value of around 10^{20} dyn cm^{-2}, making the conditions favourable for nuclear burning of hydrogen (Munari 2025). As a result of the thermonuclear burning, the temperature rapidly increases since the degenerate matter can not expand. This further fuels the nuclear chain reactions and results in a runaway. The runaway reaction releases enormous amounts of energy, typically around 10^{45} ergs, and increases the temperature to the Fermi value ($\sim 10^8$ K). As a result, the degeneracy is lifted, and material is expelled at velocities exceeding 500 km s^{-1} (Starrfield et al. 2016). The ejected mass (M_{ej}) during a single eruption typically ranges from 10^{-7} to 10^{-4} $M_\odot$, which is usually of the order of M_{acc}. M_{acc} is limited by M_{ig}, the minimum mass required to trigger a TNR. The properties of the WD and the accretion rate determine M_{ig} and hence M_{acc} and M_{ej} (Gehrz et al. 1998b; Hernanz & Jose 1998; Starrfield 1999).

The TNR process triggers nucleosynthesis reactions that produce heavy elements, which are dispersed into the interstellar medium (ISM) along with dredged-up material with the ejecta. This makes novae important contributors to galactic

chemical evolution, particularly for elements like lithium, carbon, nitrogen, oxygen, and various isotopes (Starrfield et al. 2020).

Subsequent to the eruption, the decline in nova light curves may exhibit a variety of features arising from multiple physical processes (Figure 1.2), as outlined in the subsequent sections.

1.3 Nova eruption in a Hertzsprung-Russell Diagram

When a nova erupts, it follows a distinct path on the Hertzsprung-Russell Diagram (HRD). Initially, the system is in a quiet state (Stage A; refer to Figure 1.3), where the WD slowly accretes material from the companion star, and its luminosity is relatively low. As the outburst is triggered, TNR at the base of the accreted layer ensues, causing the system's luminosity to rapidly increase while its photospheric radius stays nearly constant. This period includes the moment when the nuclear energy production rate reaches its maximum (Stage B, defined as t=0) and when the photospheric temperature achieves its peak during the brightening phase (Stage C). A brief burst of X-rays (Stage D) is predicted during this early brightening (Kato et al. 2022). This elusive event has also been detected once (König et al. 2022). As the star's outer layers continue to rapidly expand, the surface temperature drops, and strong outflows, known as optically thick winds, begin to emerge from the photosphere (Stage E). The expansion continues until the star's photosphere is at its maximum radius (Stage G). At this point, the wind mass loss rate also peaks, and the photospheric temperature reaches its lowest value.

Following the maximum expansion, the nova enters the decay phase. During this time, the amount of material in the outer envelope diminishes, and so does the

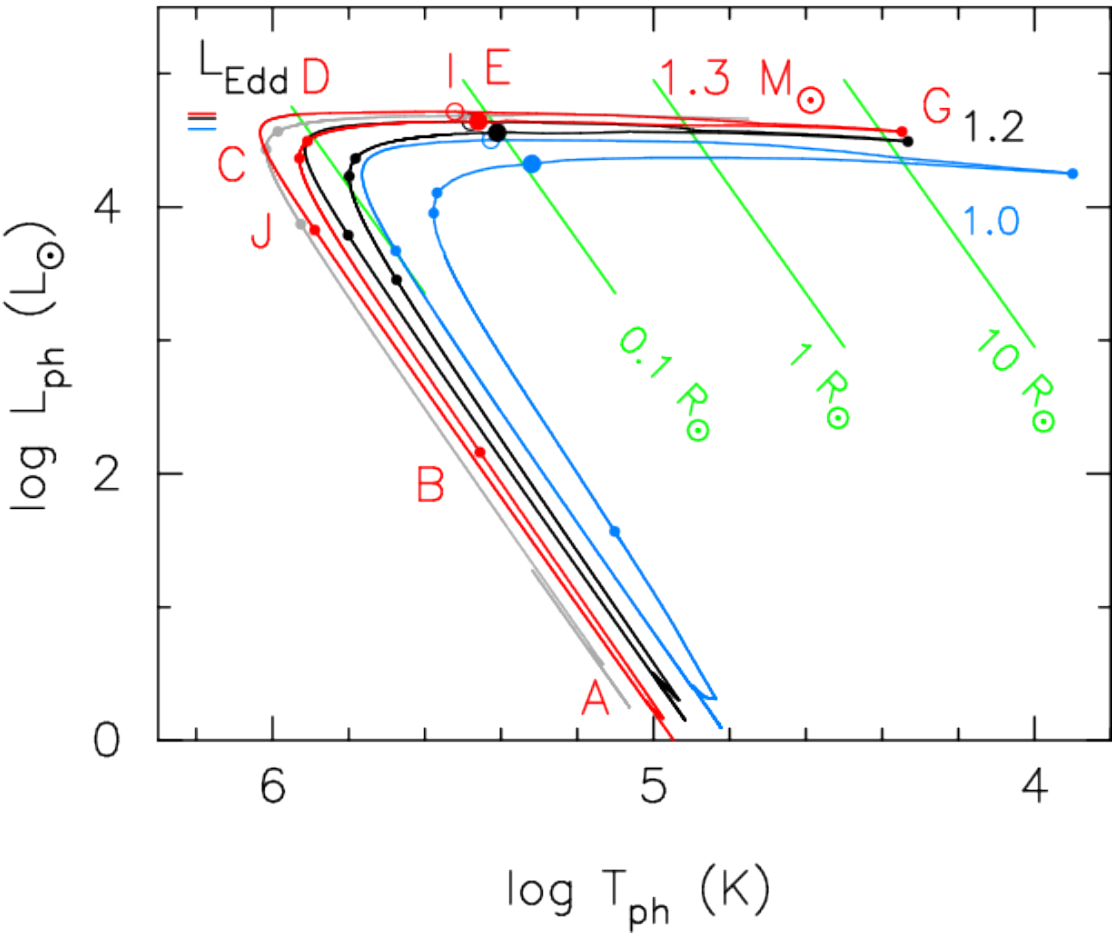

FIGURE 1.3: Evolution of nova systems during their eruption along the Hertzsprung-Russell Diagram. The evolutionary tracks for 1.0 $M_\odot$ (blue), 1.2 $M_\odot$ (black), 1.3 $M_\odot$ (red), and 1.35 $M_\odot$ (grey) WDs are shown. See text for description of phases labelled alphabetically. The short horizontal coloured lines indicate L_{Edd} for each mass. The green straight lines represent constant photospheric radii. Figure adapted from Kato et al. (2024).

opacity, primarily due to the continuous wind mass loss and the ongoing hydrogen burning. This reduction in mass causes the photospheric radius to shrink back, and the surface temperature to gradually increase as the inner hotter layers are exposed. Eventually, the optically thick winds cease completely (Stage I). This marks the beginning of the supersoft X-ray source (SSS) phase, where the system is bright in soft X-rays originating from the residual nuclear burning on the WD's envelope. The SSS phase continues until the supersoft X-ray luminosity drops to roughly one-tenth of its peak value (Stage J). It is important to note that the photospheric luminosity, or brightness observed from the star's surface, generally does

not exceed the Eddington luminosity (L_{Edd}) as shown in Figure 1.3. When novae appear brighter than this limit, it is often explained by additional radiation, such as free-free emission, originating from the ejecta located outside the photosphere, rather than from the photosphere itself (Kato et al. 2022, 2024).

Figure 1.3 shows the evolution of a 1.0 $M_\odot$ (blue), 1.2 $M_\odot$ (black), 1.3 $M_\odot$ (red), and 1.35 $M_\odot$ (grey) WDs during a nova outburst. The more massive the WD, the higher the luminosity and temperature during its evolution. Such systems also evolve on faster timescales.

1.4 Classification of Novae

Novae exhibit significant diversity in their observational characteristics, leading to multiple classification schemes based on different criteria.

One of the key observational distinctions seen in novae is between classical novae (CNe) and recurrent novae (RNe). CNe are systems where only a single eruption has been observed. These systems generally harbour less massive WDs ($0.8\ M_\odot \lesssim M_{WD} \lesssim 1.2\ M_\odot$) and experience relatively low mass accretion rates ($\dot{M} \lesssim 10^{-8}\ M_\odot\ yr^{-1}$), requiring substantial time to accumulate M_{ig} (Yaron et al. 2005; Shara et al. 2018). RNe, in contrast, are systems that have been observed to erupt multiple times within human timescales. These systems typically contain more massive WDs ($M_{WD} \gtrsim 1.2\ M_\odot$) and have higher mass accretion rates ($10^{-8} \lesssim \dot{M} \lesssim 10^{-6}\ M_\odot\ yr^{-1}$), allowing them to reach the ignition threshold more rapidly (Yaron et al. 2005; Shara et al. 2018). The recurrence period can vary dramatically, from as short as one year for M31N 2008-12a (Darnley et al. 2014) to nearly a century for systems like V2487 Ophiuchi (Schaefer 2010). Novae with a recurrence period of less than 10 years have recently been classified as rapidly

recurrent novae (RRNe; Darnley & Henze 2020). These systems consist of extremely massive WDs close to M_{Ch} and are believed to be progenitors of Type Ia supernovae through the single-degenerate scenario. All novae are believed to be recurrent, with the CNe having long recurrence periods of hundreds to thousands of years. Novae occurring on symbiotic binaries, i.e., with red giant companions, are also termed as symbiotic novae (Munari 2025).

Historically, novae have been classified by their rate of decline. The nova speed class is defined by t_3 or t_2 (days of 3 or 2 mag decline from optical maximum, respectively) as defined by Payne-Gaposchkin & Kiess (1958). This includes

- very fast novae ($t_2 \leq 10$ day)
- fast novae ($11 \leq t_2 \leq 25$ day)
- moderately fast nova ($26 \leq t_2 \leq 80$ day)
- slow novae ($81 \leq t_2 \leq 150$ day)
- very slow novae ($151 \leq t_2 \leq 250$ day)

Novae have also been classified based on their spectroscopic properties into three main categories: Fe II novae, which show prominent iron lines in their spectra; He/N novae, characterised by strong helium and nitrogen lines; and hybrid novae, which exhibit characteristics of both types (Williams 1992, 2012). However, more recently, Aydi et al. (2024) has shown that these spectral classes arise due to an observational bias for novae of different speed classes. The spectral classes are not distinct classes but phases that novae go through due to the changes in the opacity, ionisation, and density of the nova ejecta as it evolves. Novae typically evolve through three spectroscopic phases: an early He/N phase during the rise, an Fe II phase near optical peak, and a late He/N phase during the decline, before

transitioning to the nebular phase. This spectral sequence appears universally across all novae, though the duration of each phase depends on the speed class.

The light curve morphology provides another classification criterion, with novae exhibiting smooth (S), cuspy (C), plateau (P), flat-topped (F), jittery (J), dusty (D), or oscillatory (O) behaviour (Strope et al. 2010a). These different characteristics reflect the complex interplay between the WD mass and magnetic field, accretion rate, binary orbital parameters, and the composition of the accreted material.

1.5 The Multi-wavelength Nature of Nova Eruptions

Modern observational astronomy has revealed that nova eruptions are a truly multi-wavelength phenomena (see Figure 1.4). The initial explosion produces a hot, dense pseudo-photosphere that emits primarily in the optical and UV wavelengths. As the ejecta expand and cool, the emission peaks shift to longer wavelengths. However, not all novae peak in the optical. The ones with massive WDs and hence low M_{ej}, evolve *fast*, and the peak may not go redward of UV.

In the UV, novae show distinctive evolution patterns. During the early phases, the hot pseudo-photosphere dominates the UV emission. As the system evolves, the UV emission can reveal signatures of the underlying accretion disc, particularly during the later phases when the ejecta become optically thin (Selvelli & Gilmozzi 2013, 2019). UV studies of galactic novae have been conducted since the launch of IUE (Starrfield 1986), but systematic UV surveys of extragalactic novae have been limited.

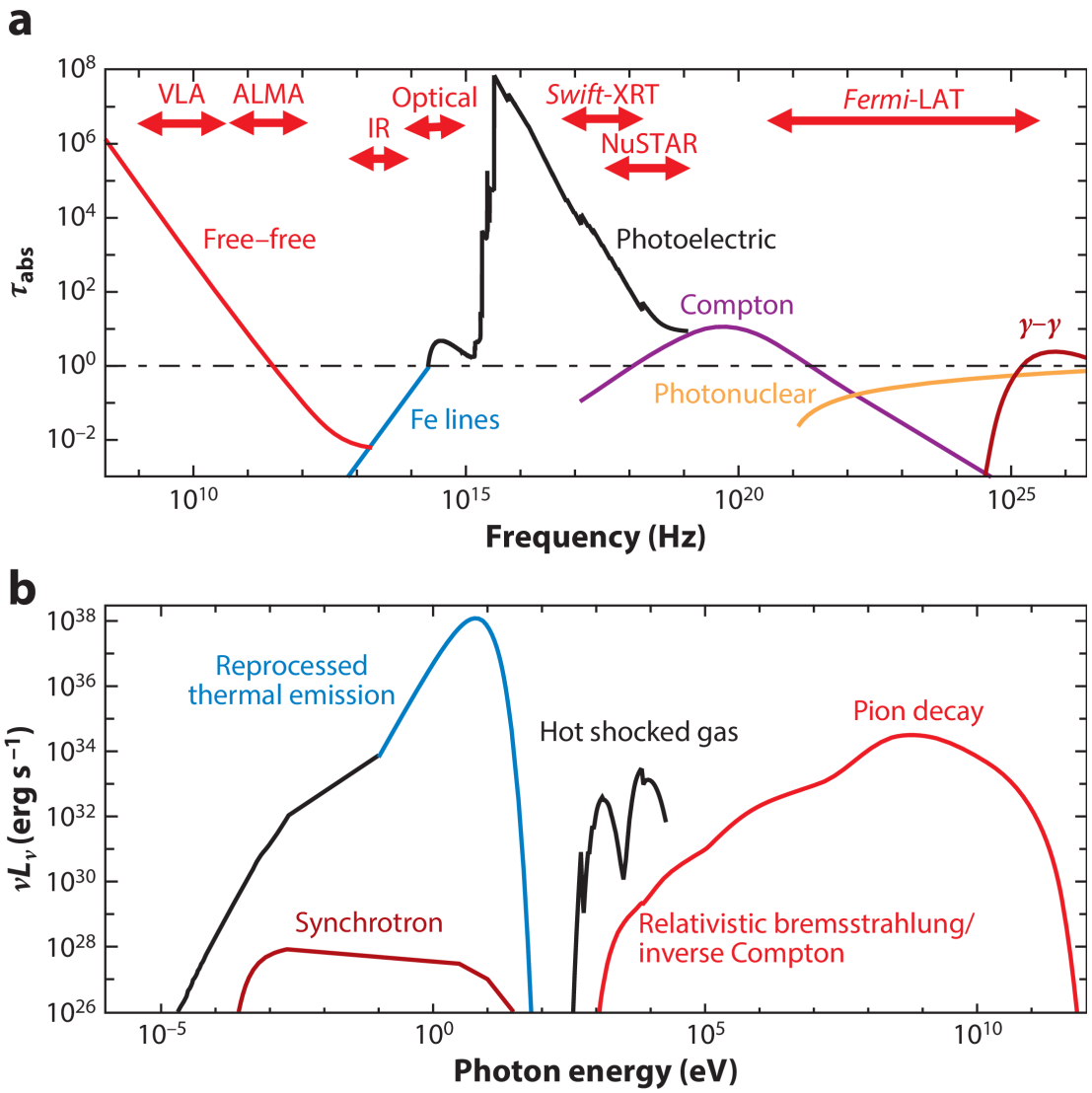

FIGURE 1.4: Simulation revealing the absorptive optical depth *(top)* and SED *(bottom)* during a nova eruption. The figure has been adapted from Chomiuk et al. (2021a).

The X-ray emission from novae is particularly important for understanding the post-eruption evolution. The SSS phase typically begins days to weeks after the optical maximum, when the expanded photosphere contracts and the hot WD envelope becomes visible. This phase is characterised by thermal emission with temperatures of $\sim 10^6$ K and provides crucial information about the WD mass and the nuclear burning in the residual layer around the WD (Krautter 2008; Pietsch 2010).

Hard X-rays have been detected in novae for several decades and are attributed to shocked ejecta (Bode & Kahn 1985a; Lloyd et al. 1992; Orio et al. 2001; Mukai et al. 2008). Recent advances in high-energy astronomy have also revealed γ-ray emissions from novae, further strengthening the presence of internal shocks and particle acceleration processes (Li et al. 2017; Aydi et al. 2020a; Chomiuk et al. 2021a). Shocks in novae have become more evident and are also backed up by models (Metzger et al. 2014; Martin et al. 2018a). However, these high-energy radiations, constrained by sensitivity, can be tested only on galactic novae. These observations have fundamentally changed our understanding of nova physics, revealing that these systems are not simply expanding fireballs but complex, multi-component phenomena involving shock interactions and structured ejecta.

1.6 Novae as Laboratories for Stellar Physics

Nova systems serve as excellent laboratories for studying various fundamental astrophysical processes. The extreme conditions during the thermonuclear runaway provide insights into nuclear mechanisms under degenerate conditions, while the subsequent evolution allows us to study shock physics, mass-loss mechanisms, and the interaction between stellar winds and the interstellar medium.

The WD masses in nova systems can be constrained through various observational techniques, including the turn-on time of the supersoft X-ray source, the recurrence period, and spectroscopic modelling of the ejecta. These measurements are crucial for understanding the evolution of CVs with massive WDs and their potential role as Type Ia supernova progenitors (Hillman et al. 2016b; Wang 2018b).

The morphology and kinematics of nova ejecta provide information about the explosion mechanism and the binary system geometry. High-resolution spectroscopy

reveals complex velocity structures that suggest non-spherical mass ejection, often interpreted as evidence for bipolar outflows or jets (Aydi et al. 2020b; Chomiuk et al. 2021a).

1.7 Extragalactic Nova Studies

While the majority of detailed nova studies have focused on systems in our own galaxy, extragalactic novae are useful for population studies and understanding nova physics in different galactic environments. The Andromeda Galaxy (M31) has been a particularly important target for extragalactic nova research.

M31, with its favourable viewing angle, proximity, and high nova rate, has been a treasure trove for nova hunters. Over 1100 novae have been discovered in M31 over the past century (Pietsch 2010; Darnley & Henze 2020), making it an ideal laboratory for studying nova populations (see Figure 1.5). The galaxy hosts numerous recurrent novae, including systems with remarkably short recurrence periods such as M31N 2008-12a, which erupts annually (Darnley et al. 2014; Henze et al. 2018e).

The LMC, being less distant, provides access to novae in a different galactic environment with lower metallicity. Systems like LMCN 1968-12a, with its 4.3-year recurrence period, offer insights into RRNe in metal-poor environments (Kuin et al. 2020).

Extragalactic novae also provide opportunities to study these systems without the complications of interstellar extinction that often affect galactic observations. The uniform distance to novae within a single galaxy allows for direct comparison of their intrinsic properties and enables population studies that are difficult to conduct with galactic samples. These studies have revealed that nova rates follow

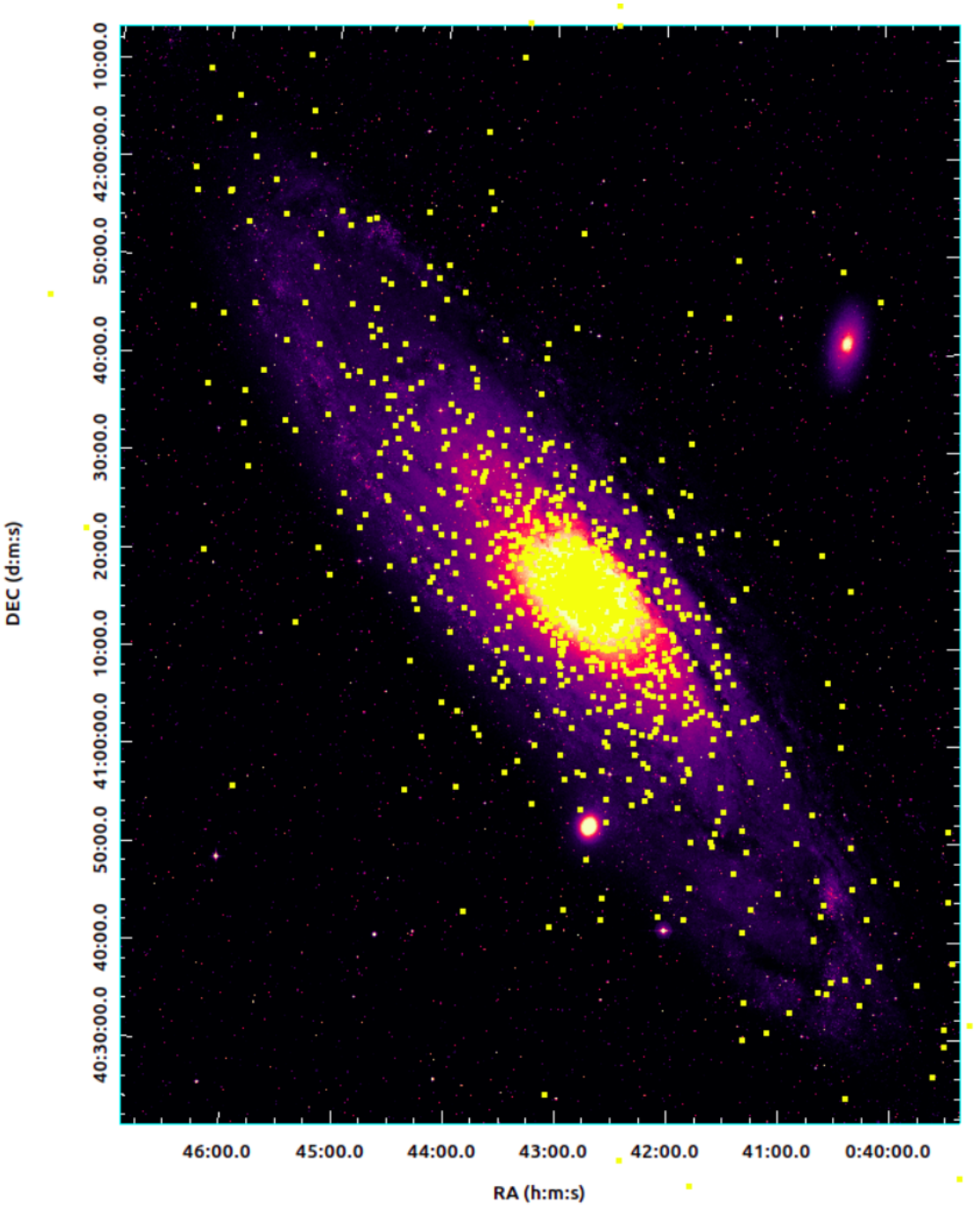

FIGURE 1.5: All detected novae in M31 overplotted on UVIT F148W mosaic of M31.

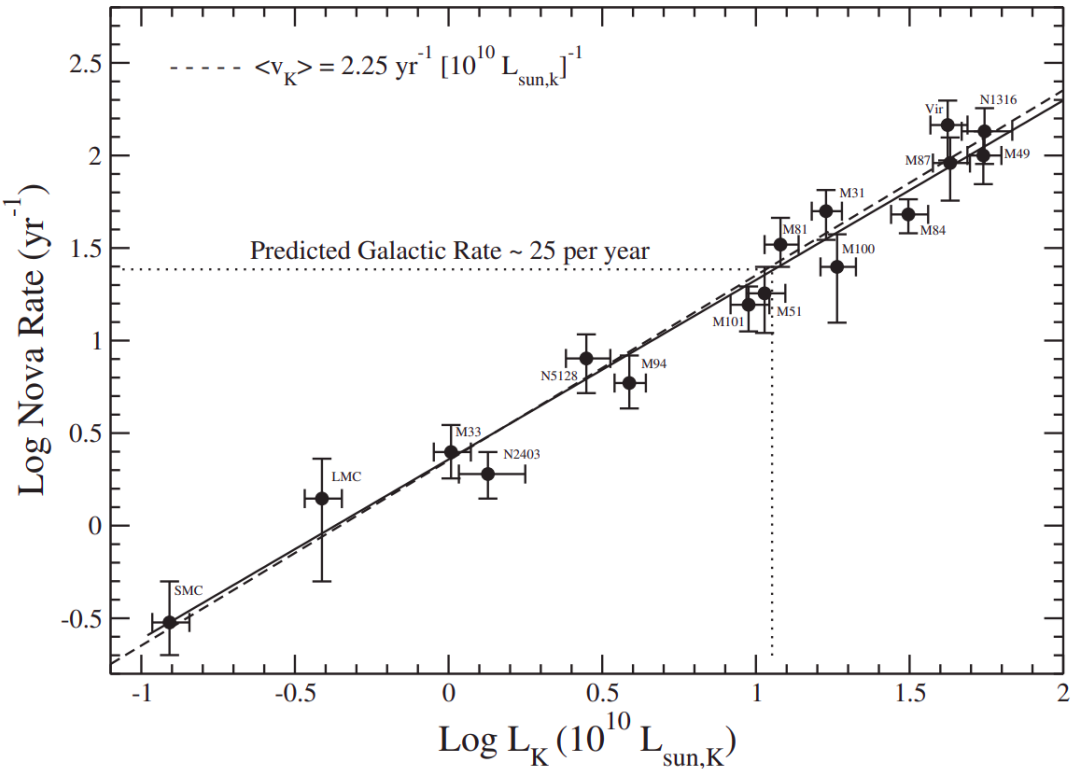

FIGURE 1.6: Nova rates as a function of K-band luminosity in nearby galaxies. Figure adapted from Shafter et al. (2014)

the K-band luminosity of galaxies (Shafter et al. 2014 and references within), and within a galaxy, they trace the older stellar populations (see Figure 1.6).

1.8 The Role of Accretion Discs in Nova Systems

As the site where thermonuclear reactions occur, the accretion disc is fundamental to a nova eruption. However, the fate of the accretion disc during and after the eruption has been a subject of considerable debate. Traditional models suggested that the disc would be completely destroyed by the explosion, but recent observations of RRNe have challenged this view. Systems like U Sco (Ness et al. 2012; Anupama et al. 2013a; Muraoka et al. 2025) and M31N 2008-12a (Darnley et al.

2017b) show evidence that at least part of the accretion disc survives the eruption and accretion resumes within days or weeks after the nova outburst.

The survival of the accretion disc has important implications for the recurrence timescale and the long-term evolution of nova systems. Even if the disc is completely destroyed, accretion can resume immediately after an outburst. However, in the case of full disruption of the disc, the time taken for the accreted mass to reach M_{ig} is longer. But if the disc is partially destroyed and accretion resumes immediately, the time taken to reach M_{ig} is lower for the same accretion rate. The short recurrence period observed in some systems is, thus, a combination of WD mass, mass accretion rate, and the extent of disc disruption.

UV observations are particularly sensitive to emission from accretion discs, as the hot disc material produces strong UV emission. The detection of UV emission during the later phases of nova eruptions, when the ejecta has become optically thin, can provide direct evidence for disc survival and renewed accretion activity.

1.9 Observational Challenges and Techniques

The study of novae presents numerous observational challenges. The rapid evolution of these systems requires prompt follow-up observations, often within hours or days of discovery. The unpredictable nature of nova eruptions means that dedicated monitoring programmes are essential for catching these events in their early phases.

Modern time-domain astronomy, with surveys like the ZTF (Bellm et al. 2019), Asteroid Terrestrial-impact Last Alert System (ATLAS; Tonry et al. 2018), All Sky Automated Survey for SuperNovae (ASAS-SN; Shappee et al. 2014), and

various robotic telescope networks, has revolutionised discovery and follow-up of transients, including novae. These facilities provide the high cadence observations necessary to discover novae and follow up on their subsequent evolution.

Spectroscopic follow-up is crucial for understanding the physical processes in nova eruptions. The rapidly changing spectral characteristics reflect the evolving physical conditions in the ejecta, from the initial hot, dense pseudo-photosphere to the later nebular phases (Aydi et al. 2024). Multi-epoch spectroscopy allows us to track the expansion of the ejecta and interaction between layers (if any), measure the ejected mass, and determine the composition of the material.

Image subtraction techniques such as ZOGY (Zackay et al. 2016) have become essential for transient discovery, particularly in crowded fields like the central region of M31. These methods can reveal faint novae that would otherwise be hidden in the bright galactic background, enhancing the completeness of nova surveys.

1.10 Theoretical Models and Simulations

The interpretation of nova observations relies on theoretical models that describe the physics of the TNRs and the subsequent evolution of the system. These models must account for the complex interplay between nuclear physics, hydrodynamics, and radiative transfer in the extreme conditions found in nova explosions.

One-dimensional models such as `MESA` (Paxton et al. 2011) and `SHIVA` (José & Hernanz 1998) have provided fundamental insights into the TNR process and the relationship between WD mass, accretion rate, and nova characteristics (Hillman et al. 2016a; Starrfield 2017; Wang 2018a). Nonetheless, novae are intrinsically

three-dimensional in nature. This complexity has led to the advancement of comprehensive multi-dimensional simulations, demonstrated by `FLASH` (Fryxell et al. 2000), which have been integrated into other simulations (José et al. 2020) to account for the asymmetries observed in nova ejecta.

Spectral synthesis models, such as those based on the `PHOENIX` code (Hauschildt et al. 1997; Hauschildt 2008; Husser et al. 2013), allow detailed comparison between observed spectra and theoretical predictions during the optically thick phase of nova outburst. As the ejecta becomes optically thin, photoionisation dominates, and its effects can be clearly seen in the observed spectra. `CLOUDY` (Ferland et al. 2017a; Chatzikos et al. 2023) has been monumental in modelling these spectra and determining the abundances and ejecta properties. These models can constrain physical parameters such as the expansion velocity and elemental abundances, providing crucial tests of our understanding of nova physics.

1.11 Thesis Overview

This thesis aims to study novae in M31 across different wavelength regimes from X-rays to IR. We have observed and analysed CNe and RNe and modelled their light curves and spectra wherever it was feasible. We aimed at understanding physical processes such as photoionisation, accretion resumption, and ejecta properties during a nova outburst. The thesis is divided into the following chapters

- *Chapter 2* describes the observational facilities used during this doctoral work. It also describes the software and modelling tools used in the thesis.
- *Chapter 3* discusses the study of novae in M31 based on AstroSat archival data in the UV. It presents a UV catalogue of M31 novae, with detections during both quiescence and outburst.

- *Chapter 4* focuses on the detailed multi-wavelength study of the remarkable, recurrent nova M31N 2008-12a. It includes both observations and modelling of the object.

- *Chapter 5* deals with rapidly recurring novae. It includes a comparative study of M31N 2008-12a, LMCN 1968-12a, and U Sco.

- *Chapter 6* describes the slow classical nova AT 2023tkw in M31 that showed signatures of shock interaction. In terms of its properties, it shows a stark contrast to the RRNe, highlighting the diversity of novae.

- *Chapter 7* discusses future prospects of studying novae and their connection to Type Ia supernovae. It briefly describes the current and upcoming interesting prospects in novae, such as shocks and nova-super-remnant structures.

Chapter 2

Methodology

> "Science progresses best when observations force us to alter our preconceptions."
>
> — Vera Florence Cooper Rubin

2.1 Observational Facilities

2.1.1 Ground-based Optical Telescopes

Ground-based optical and IR telescopes used in this thesis work are discussed in the following sections.

FIGURE 2.1: The Himalayan Chandra Telescope dome (left) and the telescope as seen from inside (right).

2.1.1.1 Himalayan Chandra Telescope

The 2-meter Himalayan Chandra Telescope (HCT) is located at IAO, Hanle, India (see Figure 2.1). HCT houses the Himalayan Faint Object Spectrograph Camera (HFOSC), the TIFR Near Infrared Spectrometer and Imager (TIRSPEC), and the Hanle echelle spectrograph (HESP)[*].

The HFOSC provides both imaging and spectroscopic capabilities[†] and played a crucial role in our optical observations of novae. It features a 2K × 4K CCD detector with an image scale of 0.296″ pixel^{-1}, yielding a field of view (FoV) of 10′ × 10′ in the central 2K × 2K region.

For spectroscopy, we primarily utilised grism 7, which delivers a low resolution (R ≈ 1200) spectrum covering the wavelength range of 3500–7500 Å. This configuration proved ideal for monitoring the spectral evolution of novae, capturing

[*] https://www.iiap.res.in/centers/iao/facilities/hct/
[†] https://www.iiap.res.in/documents/614/hfosc_man.pdf

essential emission features such as the Balmer series, Fe II multiplets, and Helium lines.

For photometric monitoring, HFOSC was used with standard Bessell $BVRI$ and SDSS $g'r'i'$ filters. Typical exposure times ranged from 60 to 300 seconds per filter, adjusted according to the brightness of the target and the sky conditions. The instrument's sensitivity made it particularly valuable for late-time monitoring of novae during the decline phases.

2.1.1.2 GROWTH-India Telescope

FIGURE 2.2: GIT dome (left) and as seen from inside (right).

GIT (Kumar et al. 2022)[‡] is a 0.7-meter fully robotic telescope also located at IAO, Hanle (see Figure 2.2). It is equipped with a 4096 × 4108 Andor iKon-XL CCD camera providing an image scale of 0.67″ pixel^{-1} and a wide FoV of 0.7°. This wide-field capability makes GIT particularly effective for survey-type observations of nearby galaxies.

GIT was instrumental in our nova survey programs, conducting daily observations of M31 in g' and r' bands during the visible months (July to February). The automated pipeline processes images nightly, enabling rapid detection of transients

[‡] https://sites.google.com/view/growthindia/about

through image subtraction techniques. For M31 observations, Pan-STARRS reference images were used for image subtraction.

The robotic telescope allowed for rapid ToO observations and consistent monitoring of detected transients. For detailed follow-up observations, we typically obtained multiple exposures in each filter per night, which were either analysed individually or stacked using `SWarp` (Bertin 2010) to improve signal-to-noise ratio (SNR) for fainter objects.

2.1.1.3 J.C. Bhattacharyya Telescope

The 1.3-meter Jagadish Chandra Bhattacharyya Telescope (JCBT)[§] at VBO, Kavalur, India, provided complementary optical observations. This telescope is equipped with a 2K × 4K UK Astronomy Technology Centre (UKATC) CCD detector with a 15-micron pixel size, corresponding to an image scale of $0.3''$ pixel^{-1} and an FoV of $10' \times 20'$.

JCBT was primarily used for photometric observations in the B and V bands, with typical exposure times ranging from 600 to 1800 seconds, depending on target brightness. These observations complemented the HCT and GIT data.

2.1.1.4 Palomar 200-inch Hale Telescope

The Palomar 200-inch (P200) Hale telescope equipped with the Double Beam Spectrograph (DBSP) provided low-resolution (R $\sim$ 1000) spectroscopy covering the wavelength range of 3400-10500 Å (Oke & Gunn 1982). The instrument

[§] https://www.iiap.res.in/?q=centers/vbo#Telescopes_VBO

features separate blue (3400-5600 Å) and red (5650-10500 Å) cameras, allowing simultaneous coverage across the entire optical spectrum.

2.1.1.5 Keck Telescopes

The 10-meter Keck telescopes at the W. M. Keck Observatory provided both optical and near-infrared (NIR) observations of top quality:

- Keck I with the Low-Resolution Imaging Spectrometer (LRIS) delivered optical spectroscopy spanning 3000-10250 Å (Oke et al. 1995). The blue and red dispersion regions covered 3000-5650 Å and 5650-10250 Å, respectively.
- Keck II with the Near-Infrared Echellette Spectrometer (NIRES) provided NIR spectroscopy corresponding to the JHK bands (Wilson et al. 2004).

The high sensitivity of these large telescopes enabled us to obtain high-quality spectra even for fainter extragalactic novae.

2.1.2 Space-based Observatories

The space-based observatories used for obtaining data are discussed in the following sub-sections.

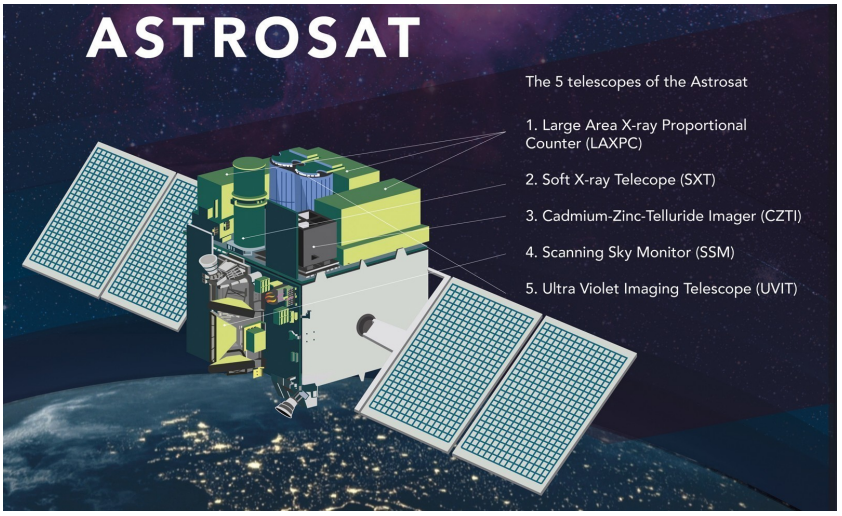

FIGURE 2.3: Artist's impression of the *AstroSat* satellite ¶.

2.1.2.1 AstroSat

AstroSat, India's first dedicated multi-wavelength space observatory, (Singh et al. 2014; Figure 2.3) played a crucial role in our studies of novae in ultraviolet (UV) and X-ray wavebands. The primary instruments used were:

Ultraviolet Imaging Telescope (UVIT; Tandon et al. 2017a): UVIT consists of twin telescopes with 38 cm diameter mirrors, providing a circular field of view of 28′. One telescope is dedicated to the far-ultraviolet (FUV) channel, and the other serves both near-ultraviolet (NUV) and visible channels. UVIT offers a spatial resolution of approximately 1.5", making it ideal for studying extragalactic UV sources.

Extensive ground-based and in-orbit calibrations have been carried out for UVIT to ensure the scientific accuracy and reliability of its data products. The instrument's performance metrics and calibration measurements are described in Subramaniam et al. (2016), with further refinements and early science observations were reported by Tandon et al. (2017b,c).

Our observations primarily utilised the FUV channel with the F148W and F172M filters (see Figure 2.4). UVIT's unique capability to detect wavelengths down to 1000 Å provided critical information about the hot components in nova systems. The high spatial resolution of UVIT also allowed us to resolve novae in the crowded central regions of M31.

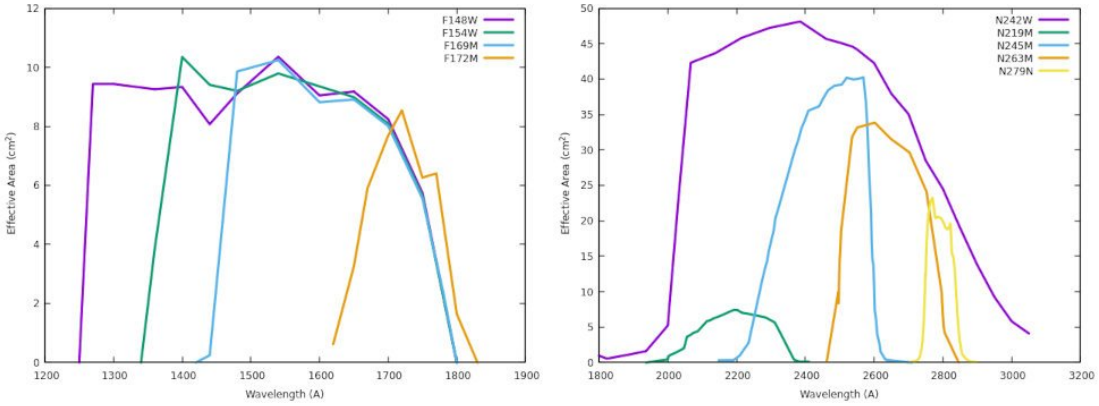

FIGURE 2.4: Effective area as a function of wavelength of FUV (*left*) and NUV (*right*) filters of UVIT.

Soft X-ray Telescope (SXT; Singh et al. 2017): SXT operates in the 0.3–8.0 keV range and observes in parallel with UVIT, making it particularly suitable for studying the SSS phase of novae. SXT has an effective area of 90 cm^2 at 1.5 keV. Its FoV is 40′ with a pixel scale of 4.12″ $pixel^{-1}$. The telescope Point Spread Function (PSF) is around 5′. It has an energy resolution of 80-150 eV (Singh & Bhattacharya 2017; Bhattacharyya et al. 2021). SXT provided simultaneous X-ray observations along with UV by UVIT, aiding the study of these hot sources over a wide range of wavelengths.

2.1.2.2 Swift

NASA's *Swift* observatory (Gehrels et al. 2004) has been essential for our multi-wavelength studies of novae, particularly for monitoring eruptions with its two main instruments:

Ultraviolet/Optical Telescope (UVOT; Roming et al. 2005): UVOT has a diameter of 30 cm and provides a FoV of $17' \times 17'$. It provides a resolution of $2.5''$ but provides high-cadence UV and optical imaging data in multiple filters: V, B, U, $UVW1$, $UVM2$, and $UVW2$ (Poole et al. 2008). These observations allowed us to track the UV evolution of novae from the earliest stages through the decline phase and into quiescence when possible.

X-Ray Telescope (XRT; Burrows et al. 2005): XRT has an effective area of 110 cm^2 and provides a PSF of $18''$. It has a FoV of $23.6' \times 23.6'$. XRT monitored the emergence and evolution of the SSS phase in the 0.3–10 keV range. Like SXT, we focused primarily on the 0.3–2.0 keV range where most SSS emission is concentrated.

2.2 Data Reduction and Analysis Methods

2.2.1 Optical Data Processing

2.2.1.1 Photometric Reduction

For ground-based optical imaging data, the procedures followed were

Pre-processing: Initial data reduction included bias subtraction, flat-fielding, and cosmic ray correction. For the GIT data, these steps were performed using the telescope's automated pipeline (Kumar et al. 2022a), while for the HCT and JCBT data, standard routines in IRAF (Tody 1993) were employed. When multiple exposures of the same field were obtained in a single night, they were stacked

using `SWarp` (Bertin 2010) to improve the SNR, particularly for fainter sources. Image subtraction techniques (Zackay et al. 2016) were used for novae in the central bulge of M31. We used Pan-STARRS reference images for the GIT data to perform host-subtracted photometry.

Photometric Techniques: PSF photometry was our preferred method for crowded fields, performed using standard IRAF routines. The PSF radius was typically set at three times the full width at half maxima (FWHM) of stellar profiles, which was determined using `SExtractor` (Bertin & Arnouts 1996b). Counts (C) from a star were obtained by fitting a PSF and then converted to the apparent magnitude scale given below

$$m = -2.5 \log_{10}(C) + ZP \tag{2.1}$$

where ZP is the Zero Point, which is fixed for each image by calibrating with respect to field stars.

Calibration: Photometric calibration was achieved through :

- Differential photometry with respect to local standard stars was used to account for zero points. Pan-STARRS data was used for calibrating $g'r'i'z'$ filters, and SDSS data was used for u' filter.
- For studies requiring filter transformations, conversions from $BVRI$ to $g'r'i'$ were performed using established transformations from the literature, such as those in Jester et al. (2005).
- For M31N 2008-12a, the magnitudes of local standard stars from previous studies (Darnley et al. 2016) were used as references for calibration.

2.2.1.2 Spectroscopic Reduction

Optical spectra were processed following these standard procedures:

Basic Processing: All spectra were bias-subtracted and cosmic-ray corrected before extraction. For HFOSC data, this was performed using standard IRAF routines.

Wavelength and Flux Calibration: For HFOSC spectra, these were performed using arc lamp spectra (FeAr for Gr7 in HFOSC). Spectro-photometric standard stars were used to correct for instrumental response and establish flux scaling. Absolute flux calibration was achieved using zero points obtained from contemporaneous broadband photometry, typically performed within a few hours of the spectroscopic observations when possible.

DBSP spectra were processed using the `dbsp_drp` Python package implemented within the `pypeit` framework (Mandigo-Stoba et al. 2022). Keck LRIS spectra were processed with the `idl` package (Perley 2019) and flux-calibrated using standard star observations. Keck NIRES spectra were reduced, extracted, and wavelength-calibrated using sky emission lines with the `spextool` IDL tool (Cushing et al. 2004) and telluric-corrected using `xtellcor` (Vacca et al. 2003).

Extinction Correction For extragalactic objects, extinction correction was an essential step in our analysis. For M31 novae, extinction values were calculated from a $1'$ region around each nova in the M160 resolution dust map of M31 (Draine et al. 2014). For the LMC nova, we used $E(B-V) = 0.07 \pm 0.01$ based on previous studies from Kuin et al. (2020). We applied the CCM89 extinction law from Cardelli et al. (1989) using the `extinction` package to correct the spectra.

2.2.2 Ultraviolet Data Processing

2.2.2.1 AstroSat UVIT Data Reduction

UVIT data processing involved these key steps:

Pipeline Processing: Level 1 data was downloaded from the Indian Space Science Data Center (ISSDC) and processed using `CCDLAB` software (Postma & Leahy 2017, 2021b) following these steps:

- Flat-fielding
- Drift correction to account for spacecraft motion
- Cosmic ray rejection to clean the images
- Registration and merging of orbit-wise images to increase SNR
- Astrometric calibration of merged images

Photometric Extraction:

- PSF photometry was performed with an aperture correction term derived from "good stars" (bright with high SNR) to account for the broad PSF wings in UVIT images
- Zero points for photometric calibrations in the AB system were adopted from Tandon et al. (2020)
- For crowded fields like M31, we developed specialized image subtraction techniques:

- Template subtraction: Multiple epoch UVIT images of the same field were median-combined after normalising by exposure time. This template was then subtracted from individual epoch images.
- Isophote modelling: We modelled the bulge of M31 using the `isophote` module to create a smooth representation of the galaxy light. Subtracting this model revealed point sources above the nuclear brightness level.

These techniques were essential for detecting novae that would otherwise be hidden in the bright M31 bulge, increasing our detection efficiency for central novae.

2.2.2.2 Swift UVOT Data Analysis

UVOT L2 data were downloaded, and photometry was performed using these steps:

- The `uvot` task in `HEASOFT` was used to extract magnitudes
- Source regions of 5″ radius was used
- Background subtraction was chosen from a source-free region. For crowded fields, background regions were carefully selected to ensure no contamination from nearby sources
- Calibration followed the UVOT photometric (AB) system (Poole et al. 2008; Breeveld et al. 2011)

2.2.3 X-ray Data Processing

2.2.3.1 AstroSat SXT Data Reduction

SXT data processing followed these procedures:

Initial Processing

- Level 2 data was downloaded from ISSDC
- Cleaned event files from different orbits were merged using `SXTTools` in `Julia`
- For novae in crowded fields (like M31), a source region smaller than the usual SXT source area ($7'$ vs $12'$) was chosen to avoid contamination

Light Curve and Spectral Extraction

- Bin sizes were adjusted (typically 3000-8000s) to optimise SNR
- `XSELECT` was used to extract light curves in the 0.3-2.0 keV energy range
- Spectra were extracted using `XSPEC` from merged SXT cleaned event files
- New ARF files were generated corresponding to the chosen source extraction region
- In `XSPEC`, spectral analysis was conducted under the assumption of Poisson statistics (`cstat`), owing to the low count rates observed in extragalactic nova studies.

- The ISM absorption was addressed utilising the Tübingen-Boulder model (`tbabs`), with the relevant abundance values taken from Wilms et al. (2000).

2.2.3.2 Swift XRT Data Analysis

XRT high-level data was downloaded and analysed using multiple approaches:

Count Rate Determination

- `XIMAGE sosta/optimise` analysis was primarily used as it corrects for vignetting, dead time loss, background subtraction, and PSF of the instrument.
- For SSS light curves, data were typically restricted to the 0.3-2.0 keV range.

Spectral Analysis

- ARF files were generated from the exposure maps.
- RMF files were taken from the calibration database.
- Spectral analysis was performed in `XSPEC` assuming Poisson statistics (`cstat`) due to low counts in many extragalactic nova observations.
- ISM absorption was accounted for using the Tübingen–Boulder (`tbabs`) model with appropriate abundances from Wilms et al. (2000).

2.3 Data modelling Tools

2.3.1 PHOENIX Model Atmospheres

PHOENIX is a general-purpose stellar and planetary atmosphere code that we used for modelling nova spectra, particularly during the optically thick phases. It can be used to model expanding atmospheres such as those seen in novae and supernovae (Hauschildt & Baron 1995). The code solves the radiative transfer equation in spherical geometry, accounting for millions of atomic and molecular transitions (Hauschildt et al. 1997). It provides a non-local thermodynamic equilibrium (NLTE) treatment for many species. PHOENIX allows the determination of important nova parameters: effective temperature of the pseudo-photosphere, expansion velocity of the ejecta, and chemical abundances in the nova atmosphere.

Our implementation of PHOENIX for nova modelling involved:

- Key parameters included model temperature (T), luminosity (L), density parameter N in $\rho \propto r^{-N}$, expansion velocity (v_0), and metallicity (z) (Schwarz et al. 1997).
- For typical novae, we assumed a luminosity of approximately 50,000 $L_\odot$ (Kato et al. 2024) and a density parameter $N = 3$, which previous studies by Schwarz et al. (1997, 1998, 2001) have shown fit nova spectra well.
- A grid search approach was used, varying temperature (6000-30000 K), expansion velocity (1000-1500 km s^{-1}), and metallicity (0-0.4) to find optimal fits.

2.3.2 CLOUDY Photoionization modelling

CLOUDY (`v22.0`; Ferland et al. 2017a; Chatzikos et al. 2023) is a spectral synthesis code that we employed to model the emission spectra of novae, particularly during their nebular phases when the ejecta becomes optically thin. With CLOUDY, we simulated spectra for comparison with observations. Using the synthetic spectra, the density, temperature, and chemical abundances of the ejecta and its mass could be constrained.

Our Cloudy implementation for novae typically included the following model parameters:

- Ionising source: Usually modelled as a blackbody with temperature determined from X-ray observations or theoretical constraints.
- Hydrogen density: Varied according to the nova phase, typically 10^7-10^9 cm^{-3} for the nebular phase.
- Elemental abundances: Often enhanced above solar values, particularly for CNO elements due to nuclear processing.
- Geometry: Spherical expansion with inner and outer radii calculated from emission line velocities and time since eruption.
- Filling factor: Typically 0.1-0.3 to account for clumping in the nova ejecta.

2.3.3 X-ray Spectral Analysis

XSPEC was our primary tool for modelling the X-ray emission from novae, particularly during the SSS phase. Our analyses included simple absorbed blackbody

models (`tbabs` × `bbody`) for characterisation of SSS emission. Using blackbody modelling, we could extract parameters like WD surface effective temperature and column density (N_H).

Chapter 3

A catalogue of novae in M31 from the UVIT archives

"Somewhere, something incredible is waiting to be known."

— Carl Sagan

The work presented in this chapter is based on the publication: Basu et al. (2024c), 'Exploring the Archives: A Search for Novae in UVIT Snapshots of M31', 2024, ApJ, 971, 8.

3.1 Introduction

One of the most extensively studied galaxies for novae is M31, due to its favourable observational properties, namely, prolonged visibility for over half the year, relatively close distance, an inclination (77.5°) that allows for a clear view of both the bulge and disk populations, and a high nova occurrence rate. The frequent

detection of recurrent novae in M31, especially those with short recurrence intervals (less than 10 years), such as M31N 2008-12a (Darnley et al. 2016; Basu et al. 2024d), M31N 2017-01e (Shafter et al. 2022a; Chamoli et al. 2025), M31N 2013-10c (Shafter et al. 2024a), M31N 1990-10a, and M31N 1963-09c, has drawn significant interest from astronomers investigating the nova population in this galaxy. M31 has been the focus of optical nova surveys for several decades (Arp 1956; Rosino 1964, 1973; Ciardullo et al. 1987; Rosino et al. 1989; Sharov & Alksnis 1991; Tomaney & Shafter 1992; Rector et al. 1999; Shafter & Irby 2001; Darnley et al. 2004, 2006; Kasliwal et al. 2011; Shafter et al. 2011b; Lee et al. 2012; Williams et al. 2014, 2016; Rector et al. 2022), while X-ray observations have been more recent, with a few major studies conducted over the past two decades (Pietsch et al. 2007; Pietsch 2010; Henze et al. 2010, 2011, 2014b). In contrast, surveys in the IR (Shafter et al. 2011a) and UV (Cao et al. 2012) remain relatively sparse. The quiescent phases of M31 novae have been explored using high-resolution HST optical imaging, with studies by Williams et al. (2014, 2016) aiming to identify nova progenitors.

In the Milky Way, UV studies of novae date back to the launch of the International Ultraviolet Explorer (IUE), with foundational work summarised by Starrfield (1986) and others. Selvelli & Gilmozzi (2013) analysed the UV SEDs of 18 Galactic novae in quiescence, a work which was later expanded to include eruption-phase data by Selvelli & Gilmozzi (2019) to provide a more comprehensive picture of old nova systems. More recently, Page et al. (2020a, 2022a) compiled UV and X-ray light curves of Galactic novae observed with Swift.

UV studies of extragalactic novae remain rare. Notable exceptions include Cao et al. (2012) for M31, and Lessing et al. (2023) and Shara et al. (2023) for M87, which primarily focused on outburst characteristics, spatial distribution, nova rates, and population properties. In the Magellanic Clouds, low nova rates (Mróz

et al. 2016) and large field sizes have contributed to limited observational coverage across wavebands. Nevertheless, targeted studies of individual novae, such as SMCN 2016-10a (Aydi et al. 2018), Nova LMC 1971b (Bode et al. 2016), and Nova LMC 1968 (Kuin et al. 2020), have revealed insights into their UV behaviour during quiescence. Despite these efforts, no systematic study has yet been published that specifically investigates the quiescent phase of extragalactic novae in the UV. Although nova systems in M31 and other galaxies are expected to exhibit properties similar to those in the Milky Way, this observational gap must be addressed to achieve a comprehensive understanding

This chapter presents the search for novae in M31 in the UV bands using archival AstroSat/UVIT data. We discuss the detection methods used and provide a catalogue of the novae detected during outburst and quiescence. Non-detection upper limits in the UV bands are also provided for all other novae.

3.2 The data set

UVIT onboard AstroSat has conducted multiple observations of the M31 across various UV filters and over several epochs. The datasets and observational summaries compiled by Leahy et al. (2020, 2021) serve as a foundational basis for this work. In addition to the fields discussed in those studies, we have also incorporated more recent observations conducted by the same Principal Investigator (PI), as well as archival data from other UVIT programs targeting different regions of M31. A comprehensive summary of all UVIT fields and datasets utilised in this study is provided in Table 3.1 and the full table is available in GitHub*.

*https://github.com/judha-basu/Thesis-files/blob/df321b879170a46d8778eb349b7a06de5f3044d9/UVIT_M31_obs_log

TABLE 3.1: UVIT observation log of all images, including co-added frames, in which at least one nova was detected. The full table, which includes details of all individual and co-added frames analysed in this work, is given in GitHub.

Observation ID	RA (deg)	DEC (deg)	Filter	Field	Obs Epoch (BJD)	Exp time (s)	Limiting Mag (AB)	Novae detected
A02_028T01_9000000724	10.71683	41.12430	F148W	M31 01	2457671.85662	7736.347	22.94	18
A02_028T01_9000000724	10.71683	41.12430	F172M	M31 01	2457672.19496	3611.883	21.39	14
A02_028T01_9000000724	10.71683	41.12430	N219M	M31 01	2457671.85657	7780.686	22.08	12
A02_028T01_9000000724	10.71683	41.12430	N279N	M31 01	2457672.19491	3627.438	21.53	11
A07_007T04_9000003310	10.70412	41.27929	F148W	M31 01	2458805.25645	17045.731	23.37	17
A07_007T04_9000003310	10.70412	41.27929	F169M	M31 01	2458804.85075	10426.754	22.63	15
A07_007T04_9000003310	10.70412	41.27929	F172M	M31 01	2458806.27133	16606.192	22.34	15
A10_002T04_9000004022	10.59843	41.21609	F148W	M31 01	2459174.71396	11759.864	23.10	18
A02_028T03_9000000788	11.01776	41.54606	F148W	M31 02	2457704.13548	7942.829	22.69	3
A02_028T03_9000000788	11.01776	41.54606	F172M	M31 02	2457704.48574	5350.934	21.48	2
A02_028T03_9000000788	11.01776	41.54606	N219M	M31 02	2457704.13543	7986.231	22.01	2
A02_028T03_9000000788	11.01776	41.54606	N279N	M31 02	2457704.48567	5544.727	21.33	3
A10_002T05_9000004000	11.13728	41.48918	F148W	M31 02	2459167.97966	12610.195	22.77	1
A04_022T02_9000002184	11.33933	41.88125	F148W	M31 08	2458292.30948	3371.811	22.85	1
A04_022T02_9000002184	11.33933	41.88125	F172M	M31 08	2458292.98608	9017.513	22.29	1
A05_004T03_9000002508	9.87699	40.36606	F148W	M31 15	2458435.07551	4610.422	23.04	1
A05_004T03_9000002508	9.87699	40.36606	F169M	M31 15	2458435.27774	9286.96	22.69	1
A05_004T03_9000002538	9.86651	40.37805	F148W	M31 15	2458449.21674	2104.392	22.72	1
A05_004T03_9000002538	9.86651	40.37805	F169M	M31 15	2458449.42980	9224.752	22.76	1
Co-added frames *	10.70959 †	41.27957 †	F148W	M31 01	2458550.60901 ‡	36541.942	23.54	3 #
Co-added frames *	10.70959 †	41.27957 †	F172M	M31 01	2458239.23315 ‡	20218.075	22.50	1 #

Notes

* Co-added frames include all the images of the same field in the same filter combined together. For example, the co-added frame of the M31 01 field in the F148W filter includes the sum of F148W images with Obs ID A02_028T01_9000000724, A07_007T04_9000003310 and A10_002T04_9000004022.

† RA DEC of the co-added frames are the centres of the co-added images.

‡ Observation epochs for co-added frames are the mid-point of the first and last observation.

The number of novae detected in the co-added frames but not in the individual images.

3.2.1 Creating a mosaic

To construct a complete FUV view of M31, we combined the F148W filter images from all 19 observed fields into a single composite mosaic. Prior to mosaicking, individual images were normalised by their respective exposure times to ensure uniformity in pixel intensity scales. These normalised images were then assembled using the `SWarp` software (Bertin et al. 2002), which resamples and co-adds overlapping frames based on World Coordinate System (WCS) information. Exposure weight maps generated by `CCDLAB` were employed as input weights during tiling to account for edge effects and overlapping regions. The final FUV mosaic of M31 is presented in Figure 3.1.

3.2.2 Background removal from the M31 bulge

The central bulge of M31 is dominated by intense galactic background light, which poses a significant challenge for detecting faint point sources. The removal of this background contribution is therefore essential for a reliable search within this high-surface-brightness region. To address these limitations, we employed two independent approaches to construct background-subtracted templates for nova detection in the bulge.

The first method involves the construction of a median-combined background template using multiple epochs of imaging of the same field in a given UVIT filter. As demonstrated by Tandon et al. (2020), UVIT detectors exhibit consistent sensitivity across multi-year observations. Consequently, image normalisation required only scaling by exposure time. Given the stability of the PSF in space-based data, no PSF matching was performed prior to stacking. The exposure-normalised images were registered with sub-pixel accuracy and then median-combined to create

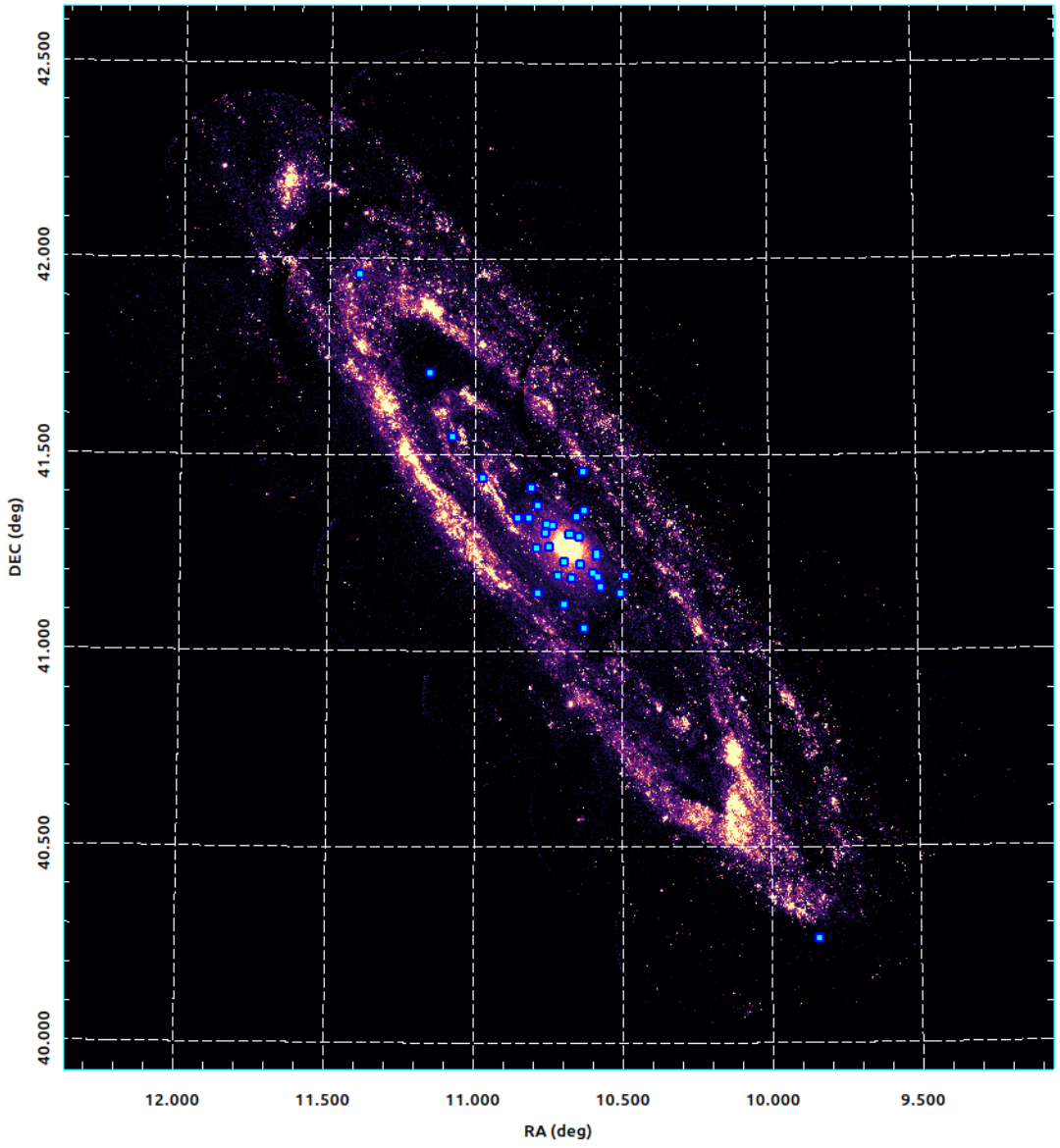

FIGURE 3.1: UVIT F148W mosaic image of M31 generated using SWarp. The locations of all the novae detected in the archival images are marked in the figure.

a master background frame. While this approach effectively removes transients with timescales shorter than the longest baseline constructed from half the observation epochs ($\sim$ 2 years), it imposes an inherent upper limit on timescale sensitivity. However, this baseline is significantly longer than the typical evolutionary timescales for most novae. This median template was then subtracted from each individual epoch image to highlight transient point sources, including potential nova candidates.

In the second approach, we modelled the bulge's smooth light distribution using elliptical isophotal fitting. This was accomplished via the `isophote` module within the `photutils` Python package (Bradley et al. 2023). For each epoch, isophotes were fitted over a semi-major axis range extending up to approximately 400 pixels (corresponding to $\sim$2.78'), covering the nuclear region of M31. The resulting model image, representing the underlying galactic light distribution, was then subtracted from the original image to isolate point sources with flux exceeding the modelled brightness profile.

Both techniques proved effective in mitigating the dominant bulge background and enabled the identification of four novae that would otherwise remain obscured by the bright galactic core. The results of both methods, along with example difference images illustrating detected novae, are presented in Figure 3.2.

3.2.3 Detection of sources

A comprehensive list of M31 novae, updated as of 19 May 2022, is maintained on a website hosted by the Max Planck Institute for Extraterrestrial Physics[†] (Pietsch 2010). Forced photometry was performed at the coordinates of all listed novae to search for UV counterparts in the available UVIT datasets. Additionally,

[†] https://www.mpe.mpg.de/~m31novae/opt/m31/M31_table.html

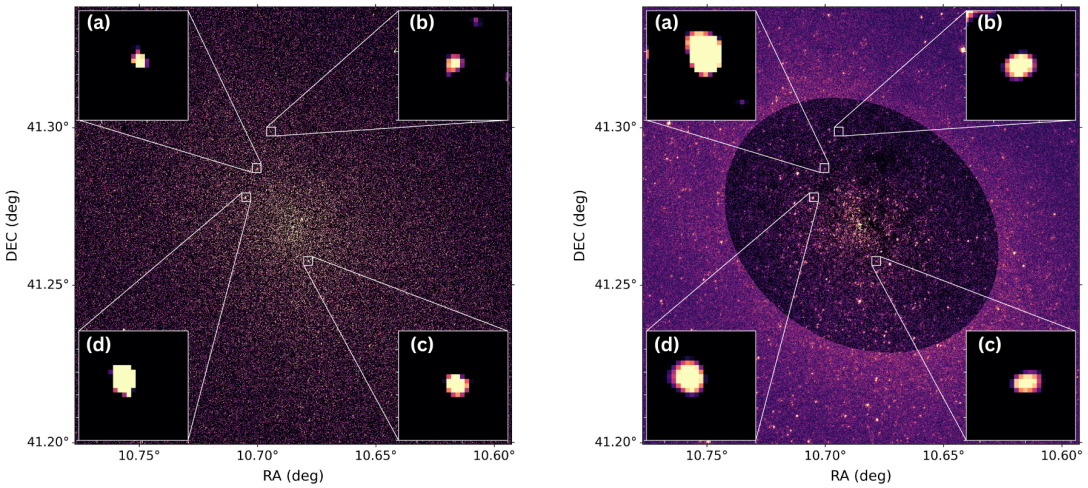

FIGURE 3.2: Difference images illustrating the detection of novae in the bulge of M31: (a) M31N 2016-03e, (b) M31N 2015-05a, (c) M31N 2016-05b, and (d) M31N 2016-03c. Each panel shows an inset zoomed on the nova location. *Left:* Results from the median-combined template subtraction method. *Right:* Results from the isophotal model subtraction method.

we examined the positions of novae that erupted after the most recent UVIT observations (post-November 2020, for which data are publicly available) to search for pre-eruption UV magnitudes or to establish upper limits on their quiescent brightness.

All candidate detections were subjected to rigorous visual inspection to eliminate false positives. In crowded regions where source confusion could arise within a 5" radius of the nova position, the detections were excluded. A detection threshold of 3σ above the local background was used to reject spurious faint sources. The limiting magnitude in the F148W filter for deep exposures (>10 ks) near the central bulge of M31 was determined to be approximately 23 AB magnitudes for a 3σ detection. In less crowded outer regions, the limiting magnitude was approximately 0.5 mag deeper. The average limiting magnitude for each field is listed in Table 3.1, though it is important to note that sensitivity varies spatially across the image. The spatial distribution of detected novae is shown in Figure 3.3, and their photometric and positional details are summarised in Table 3.2.

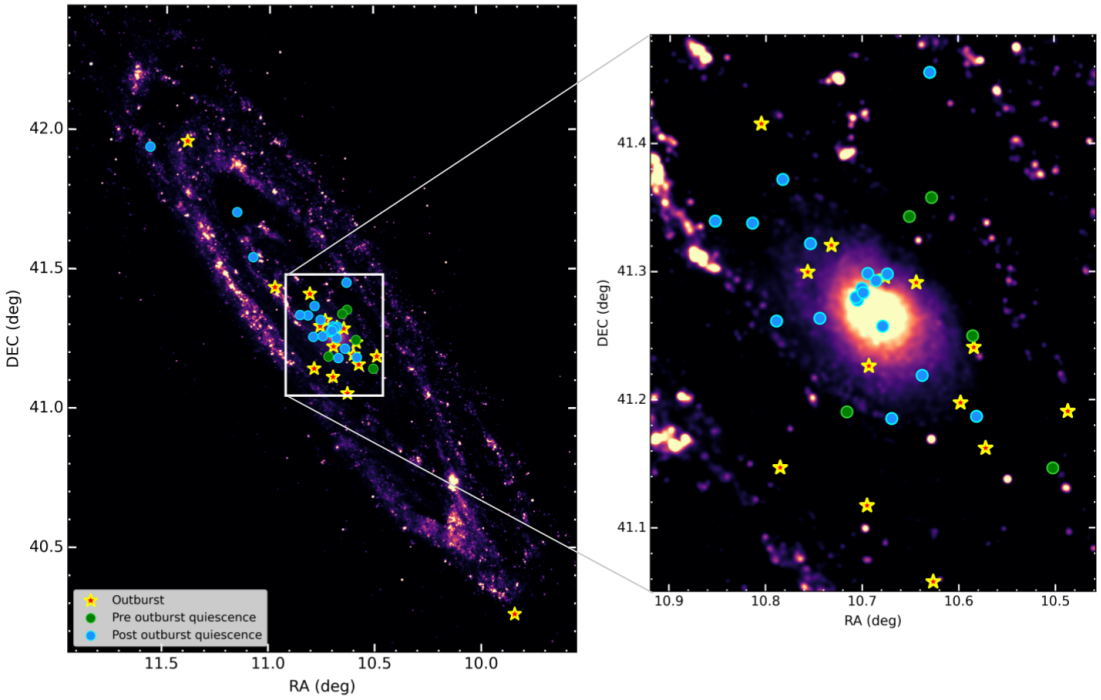

FIGURE 3.3: UVIT F148W mosaic image of M31 with detected novae. The inset shows a zoomed-in version of the M31 central region.

TABLE 3.2: List of M31 novae detected in UVIT images and their F148W mags. Additional photometric data of these novae at different epochs, and in other filters are available in the electronic version.

Name M31N	RA (HH:MM:SS)	DEC (DD:MM:SS)	Discovery Date (JD)	Observation Date (JD)	Mag (F148W) AB	Class (Phase)	t_2 (days)	Ref.
Detected at post outburst quiescence								
2015-02a †	00:42:33.06	+41:13:08.90	2457047.810	2457671.8566	23.27 ± 0.24	Fe II	–	1-3
2015-10b †	00:43:15.34	+41:20:16.60	2457321.460	2457671.8566	22.54 ± 0.13	Fe II	100.3 ± 75.8 (R)	4,5,75
2016-02b	00:44:37.03	+41:42:26.40	2457430.370	2457430.3700	22.01 ± 0.12	Fe II	–	6
2016-03b	00:42:19.51	+41:11:13.70	2457446.280	2457671.8567	22.16 ± 0.14	Nova	41.5 ± 7.1 (R)	67,68,75
1994-09b	00:42:58.52	+41:15:49.80	2449622.800	2457671.8566	21.88 ± 0.13	–	–	32
2010-12b	00:42:31.08	+41:27:20.30	2455540.620	2457671.8566	21.64 ± 0.09	–	$3(R)^*$	33,34
2013-10c	00:43:09.32	+41:15:41.60	2456574.800	2457671.8566	24.32 ± 0.30	Nova	5.5 ± 1.7 (R)	35,36,75
2015-12d	00:43:07.79	+41:22:19.30	2457387.220	2457671.8566	21.72 ± 0.10	–	–	–
2018-12a	00:42:40.65	+41:11:08.00	2458455.320	2458788.0143	23.31 ± 0.14	Fe II	–	39-42
2018-12d	00:43:24.62	+41:20:22.30	2458474.090	2458788.0143	23.33 ± 0.12	Nova	–	42,43
2019-06b	00:42:41.73	+41:17:53.70	2458661.560	2458788.0143	22.75 ± 0.14	–	–	44
2019-07c †	00:43:00.90	+41:19:19.40	2458672.510	2458788.0143	21.53 ± 0.06	–	–	45
2019-08b	00:44:18.25	+41:32:47.20	2458725.440	2459167.9797	22.00 ± 0.08	Fe II	$>57(r')$, $>53(g')^*$	46,47
2015-05a	00:42:46.60	+41:17:55.3	2457153.56	2457671.8566	23.66 ± 0.31	Nova	–	69,70
2016-03c	00:42:49.14	+41:16:40.1	2457430.24	2457671.8566	21.85 ± 0.13	Nova	–	71,68
2016-03e	00:42:48.05	+41:17:13.4	2457464.27	2457671.8566	22.78 ± 0.18	–	–	72
2016-05b	00:42:42.88	+41:15:27.4	2457536.55	2457671.8566	22.89 ± 0.29	Fe II	–	68,73,74
2017-06g	00:46:17.94	+41:56:26.1	2457922.69	2458061.9118	20.87 ± 0.12	–	–	76
Detected at post outburst quiescence in coadded frames ‡								
1985-09c	00:42:44.50	+41:17:35.0	2446320.74	2458550.6090	23.24 ± 0.10	–	–	77

Table 3.2 continued from previous page

1998-09e	00:42:49.53	+41:16:47.9	2451083.28	2458550.6090	23.02 ± 0.09	–	–	78
2010-03a	00:42:47.74	+41:17:01.4	2455257.25	2458550.6090	23.18 ± 0.10	Nova	–	79,80
				Detected at pre outburst quiescence				
2019-12b	00:42:20.47	+41:15:00.00	2458833.090	2457671.8566	23.42 ± 0.25	Fe II	50(r'), 27(g') *	60-62
2021-07d	00:42:00.58	+41:08:48.30	2459420.380	2458788.0143	22.99 ± 0.13	–	–	–
2019-11f [o]	00:42:51.76	+41:11:26.60	2458814.160	2457671.8566	22.95 ± 0.21	–	–	59
2020-10b [o]	00:42:30.67	+41:21:28.50	2459127.230	2457671.8566	22.15 ± 0.13	–	–	63,64
2020-10d [o]	00:42:36.20	+41:20:35.50	2459101.180	2457671.8566	23.12 ± 0.20	–	–	65
				Detected during outburst				
2016-08b †	00:41:56.82	+41:11:27.60	2457611.050	2457671.8566	20.71 ± 0.12	–	42.6 ± 4.3 (R)	7,8,75
2016-08e	00:43:53.29	+41:26:21.60	2457630.420	2457704.1355	20.83 ± 0.06	Fe II	60.6 ± 16.7 (R)	9,10,75
2016-09a	00:42:55.66	+41:19:14.50	2457654.300	2457671.8566	23.56 ± 0.22	Fe II	57.0 ± 35.1 (R)	11,12,75
2016-09b	00:42:17.29	+41:09:44.40	2457657.660	2457671.8566	21.18 ± 0.09	Fe II	43.9 ± 17.3 (R)	13-15,75
2018-05a	00:45:34.90	+41:57:40.40	2458246.700	2458292.3095	20.84 ± 0.12	–	–	16
2019-11a	00:42:30.37	+41:03:29.50	2458789.760	2458805.2565	22.92 ± 0.15	Nova	49(r') *	17,18
2020-09b	00:42:46.30	+41:13:35.50	2459117.200	2459174.7140	23.36 ± 0.18	Fe IIb	–	19,20
2020-09c	00:43:08.38	+41:08:50.00	2459121.790	2459174.7140	21.64 ± 0.08	Fe II	17(r'), 15(g') *	21,22
2020-10f	00:42:20.17	+41:14:28.00	2459154.530	2459174.7140	20.74 ± 0.05	Nova	–	23-25
2020-11a	00:42:46.79	+41:07:03.10	2459155.080	2459174.7140	21.82 ± 0.09	Nova	–	26,27
2020-11c	00:43:13.15	+41:24:56.00	2459159.240	2459174.7140	19.05 ± 0.03	Fe IIb	20(r') *	28-31
2019-09b	00:42:42.32	+41:17:45.80	2458740.280	2458788.0143	21.72 ± 0.07	He/N	–	48-50
2019-10c †	00:43:01.56	+41:17:59.60	2458776.280	2458788.0143	21.09 ± 0.05	Fe II	18(r'), >22(g') *	54-58
2021-03a	00:42:34.49	+41:17:29.80	2459188.680	2459174.7140	22.89 ± 0.15	–	–	66
2018-08b	00:39:21.90	+40:15:48.80	2458344.080	2458435.0755	20.92 ± 0.10	Fe II	–	37,38
2019-10a [q]	00:42:23.53	+41:11:52.20	2458759.300	2458788.0143	21.78 ± 0.08	Nova	>18(r'), >29(g') *	51-53

Notes

† Also reported by Leahy et al. (2021)

^{o} Also detected around outburst (within $\sim$ 100 days after outburst and $\sim$ 10 days before outburst)

^{q} Also detected at quiescence (more than 100 days after outburst or 30 days before outburst)

* t_2 determined from linear interpolation of the optical data around ($m_{max} - 2$)

‡ Observation date for co-added images is the midpoint of the first and last observation

References - (1) Ovcharov et al. (2015a), (2) Fabrika et al. (2015), (3) Delvaux et al. (2015), (4) Williams & Darnley (2015a), (5) Williams & Darnley (2015b), (6) Darnley & Williams (2016a), (7) Kasliwal & Cao (2018a), (8) Hornoch & Kucakova (2016a), (9) Hornoch & Kucakova (2016b), (10) Fabrika et al. (2016c), (11) Hornoch et al. (2016c), (12) Fabrika et al. (2016a), (13) Hornoch & Kucakova (2016c), (14) Valcheva et al. (2016), (15) Fabrika et al. (2016b), (16) Conseil (2018), (17) Campaner (2019), (18) Soraisam et al. (2019b), (19) Zhang & Gao (2020a), (20) Williams et al. (2020a), (21) Hornoch & Kucakova (2020a), (22) Williams et al. (2020c), (23) Zhang & Gao (2020b), (24) Valcheva et al. (2020), (25) Soraisam et al. (2020), (26) Zhang & Gao (2020c), (27) Srivastav et al. (2020), (28) Belligoli (2020), (29) Fabrika et al. (2020), (30) Balcon (2020), (31) Hornoch & Kucakova (2020b), (32) Tomaney & Crotts (1996), (33) Pietsch et al. (2010a), (34) Cao et al. (2012), (35) Ovcharov et al. (2013), (36) Hornoch et al. (2013), (37) Kasliwal & Cao (2018b), (38) Darnley et al. (2018a), (39) Zhang & Gao (2018a), (40) Valcheva et al. (2018), (41) Hornoch & Kucakova (2018), (42) Williams et al. (2019a), (43) Zhang & Gao (2018b), (44) Hornoch & Kusnirak (2019), (45) Hornoch & Kucakova (2019a), (46) Conseil (2019), (47) Williams et al. (2019b), (48) Hornoch & Kucakova (2019b), (49) Zhang & Gao (2019a), (50) Lee et al. (2019), (51) Carey (2019), (52) Dahiwale & Fremling (2020), (53) Soraisam et al. (2019a), (54) Nordin et al. (2019), (55) Hornoch & Kucakova (2019c), (56) Madrigal-Aguado et al. (2019), (57) Williams et al. (2019c), (58) Fabrika et al. (2019), (59) Zhang & Gao (2019b), (60) Jiang et al. (2019), (61) Hornoch et al. (2019), (62) Williams et al. (2020b), (63) Zhang & Gao (2020d), (64) Hornoch & Kucakova (2020c), (65) Zhang & Gao (2020e), (66) Fremling (2020), (67) Hornoch & Kucakova (2016d), (68) Martin et al. (2018b), (69) Hornoch & Honkova (2015), (70) Ovcharov et al. (2015b), (71) Hornoch et al. (2016a). (72) Hornoch et al. (2016b), (73) Hornoch & Kucakova (2016e), (74) Darnley & Williams (2016b), (75) Clark et al. (2024), (76) Shumkov et al. (2017), (77) Ciardullo et al. (1987), (78) Sharov et al. (2000), (79) Pietsch et al. (2010b), (80) Hornoch et al. (2010)
For more references check https://www.mpe.mpg.de/ m31novae/opt/m31/M31_table.html

To enhance sensitivity and search for fainter nova remnants, we co-added multiple observations of the same field taken with the same filter. This image stacking improved the limiting magnitudes by 0.2–0.4 mag (see Table 3.1). Using the co-added frames of the central M31 region, we detected three old novae — M31N 1985-09c, M31N 1998-09e, and M31N 2010-03a — all with observed FUV magnitudes fainter than 23 AB mag (see Table 3.2). FUV and NUV magnitudes for all detected novae, along with upper limits for non-detections (based on the deepest available exposures in each filter) can be accessed at this GitHub link[‡].

[‡] https://github.com/judha-basu/Thesis-files/blob/d3f6fc5e79eab2ef748b29eea38d30b8415cb12b/UVIT_M31_novae_catalog.csv

3.2.4 Photometry

Photometry was performed using the standard procedures described in §2.2.2.1. For novae located in the central bulge, we tested both aperture and PSF photometry on the background-subtracted difference images. However, aperture photometry yielded inconsistent results due to unreliable background subtraction, and PSF fitting frequently diverged due to structural residuals. To mitigate potential systematic biases introduced by these residuals in high-surface-brightness regions, we reverted to performing PSF photometry with aperture correction on the original science frames, following the same procedure as for novae in less crowded regions. This ensured methodological consistency across the entire sample.

Photometric measurements for all detected sources across filters and epochs are provided in Table 3.2, with additional filter-specific detections and upper limits compiled in a CSV file available in this GitHub link[§].

3.3 Science Results from the archives

All novae identified in the archival UVIT images are marked in Figure 3.3 and catalogued in Table 3.2. Nova outbursts exhibit a wide range of durations and decline rates—quantified by t_2 or t_3, which represent the time taken for the light curve to decline by 2 or 3 magnitudes from peak brightness, respectively (Warner 2008). These characteristics are governed by the intrinsic properties of the system, particularly the mass and composition of the WD and the nature of the binary companion. Theoretical models by Hachisu & Kato (2006) suggest that the duration of the outburst phase is sensitive to the WD mass and its chemical

[§]https://github.com/judha-basu/Thesis-files/blob/d3f6fc5e79eab2ef748b29eea38d30b8415cb12b/UVIT_M31_novae_catalog.csv

composition. Observational studies, such as that of Strope et al. (2010a), have analysed optical light curves of over a hundred novae, highlighting the diverse post-outburst processes that can shape the light curve. In the UV bands, the morphology and timescales of the light curves are also variable and often related to the SSS phase (Page et al. 2022a), which itself is dependent on the WD mass (Hachisu & Kato 2006; Henze et al. 2011).

Given the broad distribution in nova speed classes, we adopt a conservative duration of 100 days to define the outburst phase. This 100-day window covers the primary eruption phase for the majority of the speed classes in our sample. Based on the models of (Hachisu & Kato 2006), this interval corresponds to a decline of approximately 7 magnitudes for a typical 0.9 $M_{\odot}$ CO WD, ensuring that even moderately slow novae have significantly faded before being classified as quiescent novae. To account for early UV flashes and possible pre-eruption dips, we also consider any UVIT detection occurring within 20 days prior to the reported eruption date as part of the outburst phase. All other detections, which are either >100 days after outburst or >20 days before outburst, are classified as occurring during quiescence.

In total, we detect 42 novae in the various UVIT fields of M31. Notably, nearly 90% of these are located within a 90' × 90' region centered on M31, consistent with results from optical and IR surveys, where nova occurrence correlates with the underlying galactic stellar light that traces the older stellar populations (Rector et al. 2022). The following sections provide a detailed discussion of novae detected in different evolutionary phases, along with an analysis of their SEDs.

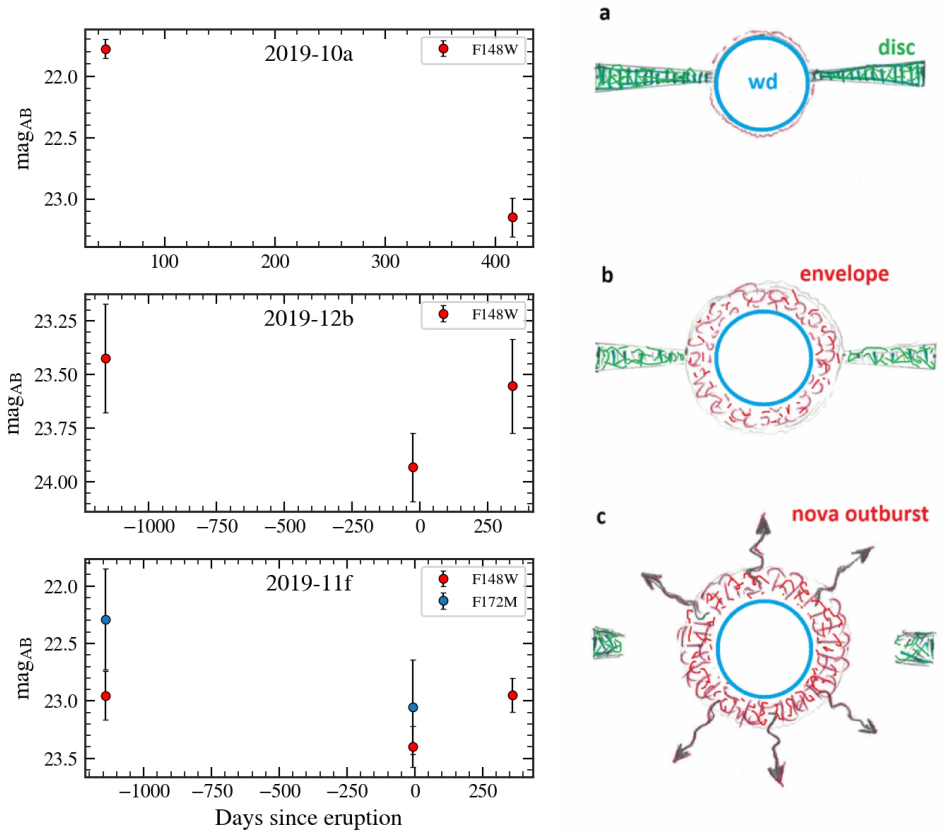

FIGURE 3.4: *Left:* UVIT light curves of some interesting novae. *Right:* Accumulation of H-rich material around the WD, resulting in an optically thick medium before eruption. Figure adapted from Zamanov et al. (2023).

3.3.1 Lightcurves

3.3.1.1 Novae at Quiescence

A total of 23 novae were detected during their quiescent phases, with 21 identified post-eruption. One nova, M31N 2021-07d, was detected prior to its eruption, and M31N 2019-12b was observed both before and after its outburst. The F148W AB magnitudes of these quiescent novae range from 21.5 to 24. Depending on the mass of the WD and the mass accretion rate, the FUV emission in this filter may originate from both the WD and the accretion disk. Additionally, the observed magnitude is sensitive to the system's orbital inclination (Warner 2008).

3.3.1.2 Pre-eruption dips

The F148W light curve of nova M31N 2019-12b (middle panel, Figure 3.4) exhibits a marginal ∼0.5 mag dip approximately 28 days prior to eruption. Zamanov et al. (2023) suggested that such dips may result from the formation of a dense, optically thick shell around the WD preceding the eruption 3.4. Similar pre-eruption dips, with magnitudes of ∼1 mag, have been reported in systems like T CrB in the optical band (Schaefer 2023; Maslennikova et al. 2024). Since extinction effects are more pronounced in the UV, dips caused by such shells would be more significant in bluer bands. Although the available data do not allow for precise quantification of the maximum drop in brightness, the observed decrease in the FUV supports the presence of a potential pre-eruption dip.

Most other novae observed multiple times during quiescence showed minimal variation between epochs, reinforcing the findings of Selvelli & Gilmozzi (2013), who reported near-constant fluxes at quiescence. This consistency is indicative of stable accretion disks radiating at steady luminosities.

Among the older novae, M31N 2010-12b and M31N 1994-09b were detected at all observed epochs and in multiple filters. Additionally, three old novae, M31N 2010-03a, M31N 1998-09e, and M31N 1985-09c, were identified in the co-added frames. Their detection in multiple bands suggests the presence of bright accretion disks. High mass accretion rates during quiescence can sustain elevated disk luminosities. System inclination and the intrinsic brightness of the WD, which illuminates the disk, may also contribute. Furthermore, residual FUV flux may arise from extended SSS phases in some systems.

3.3.1.3 Novae Detected During Outburst

Fifteen novae were detected within 100 days following their eruptions, and five of these were observed within 20 days post-eruption. Nova M31N 2021-03a was the only system observed shortly before outburst, with a detection 14 days prior. Most novae identified exclusively during the outburst phase are both fast and bright, with F148W magnitudes around 19–20. Six of these novae were observed only once in the F148W filter, while four were detected in multiple bands. Their SEDs are discussed in Section 3.3.2.

In the early stages of the outburst, the dominant source of UV photons is the expanding and receding photosphere. As the photosphere recedes, the FUV flux ($\sim$ 1000-2000 Å) becomes increasingly dominated by reprocessed emission from the hot nuclear burning on the WD surface. In some cases, contributions from the inner accretion disk, which may survive partial disruption during eruption, could also enhance the FUV luminosity.

3.3.1.4 Novae Detected Both at Quiescence and During Outburst

Four novae were detected during both quiescent and outburst phases. M31N 2019-10a was observed in the F148W filter at 46 and 415 days after eruption, showing a decline in brightness consistent with a fading light curve (top-left panel, Figure 3.4).

M31N 2019-11f displays a marginal pre-eruption dip similar to M31N 2019-12b (see Section 3.3.1.2). It was observed in F148W at 1140 and 8 days before, and at 360 days after, the eruption. The pre-eruption dip is further supported by F172M observations taken at the same pre-eruption epochs. As shown in the bottom

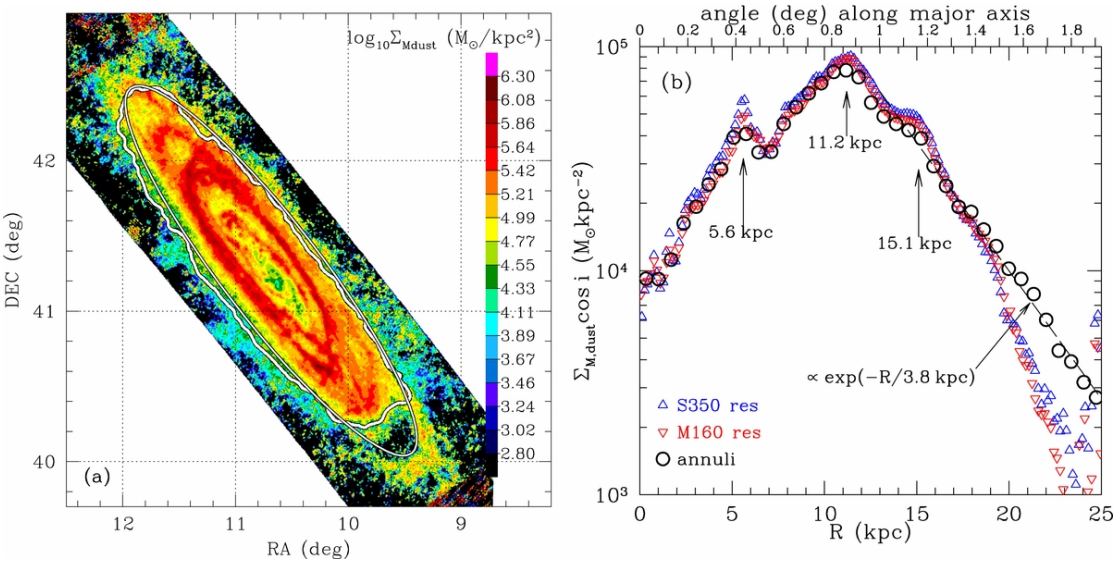

FIGURE 3.5: Dust mass distribution in M31 obtained from the M160 dust maps. Adopted from Draine et al. (2014).

panel of Figure 3.4, a decline in brightness is evident around 8 days prior to the eruption.

The remaining two novae, M31N 2020-10b and M31N 2020-10d, exhibit variations of 0.4 and 0.7 magnitudes, respectively, between epochs. However, given that these variations are comparable to the photometric uncertainties, their significance remains unclear.

3.3.2 Spectral Energy Distributions

Out of the 35 detected novae, 13 have near-simultaneous (within two days) observations in multiple NUV and FUV filters, allowing construction of their SEDs.

To correct for extinction toward M31, we utilized the M160 resolution dust mass maps from Draine et al. (2014). While these maps provide necessary full spatial

coverage of M31 (Figure 3.5), the model-derived A_V values consistently overestimate extinction when compared to measurements from the PHAT survey (Dalcanton et al. 2015). This discrepancy arises because the Draine et al. (2014) models, optimized for infrared emission, overpredicted the dust mass density (B. T. Draine, private communication, 2024). Although the PHAT survey provides more accurate local extinction values based on individual stellar photometry, its coverage is limited to approximately one-fourth of the M31 disk. Therefore, to maintain a homogeneous extinction correction across our entire sample, we adopted the Draine et al. (2014) maps but applied a corrective scaling factor of 0.5 to align them with the PHAT-based calibration. Accordingly, the A_V values were corrected and used for extinction correction. UVIT AB magnitudes were converted to fluxes using the calibration from Tandon et al. (2017c), and extinction correction was performed using the extinction laws of Cardelli et al. (1989), implemented through the `extinction` package in `Python` (Barbary 2021). The resulting extinction-corrected SEDs, expressed as F_λ vs λ, are shown in Figure 3.6. The observed SEDs, in terms of mag vs λ, are also shown in the top-left panel of Figure 3.6.

The top-right panel of Figure 3.6 highlights novae detected during post-outburst quiescence. Their SEDs were fitted with a power-law of the form $F_\lambda \propto \lambda^{-\alpha}$, and the resulting slopes (α) are summarized in Table 3.3. A slope of $\alpha = 7/3$ is characteristic of standard accretion disks (Frank et al. 1992), and the measured slopes fall within uncertainties of this value, hinting towards the presence of accretion disks in these systems (Selvelli & Gilmozzi 2013). Notably, the F148W flux is often lower than that in F172M, suggesting that disk emission begins to decline shortward of 1600 Å, potentially revealing a contribution from the WD's blackbody tail.

Four novae were observed during their outburst phases in multiple filters, and their SEDs are shown in the lower-left panel of Figure 3.6. Two of them, M31N 2016-09a and M31N 2016-09b, were detected within 18 days of eruption. Based on their

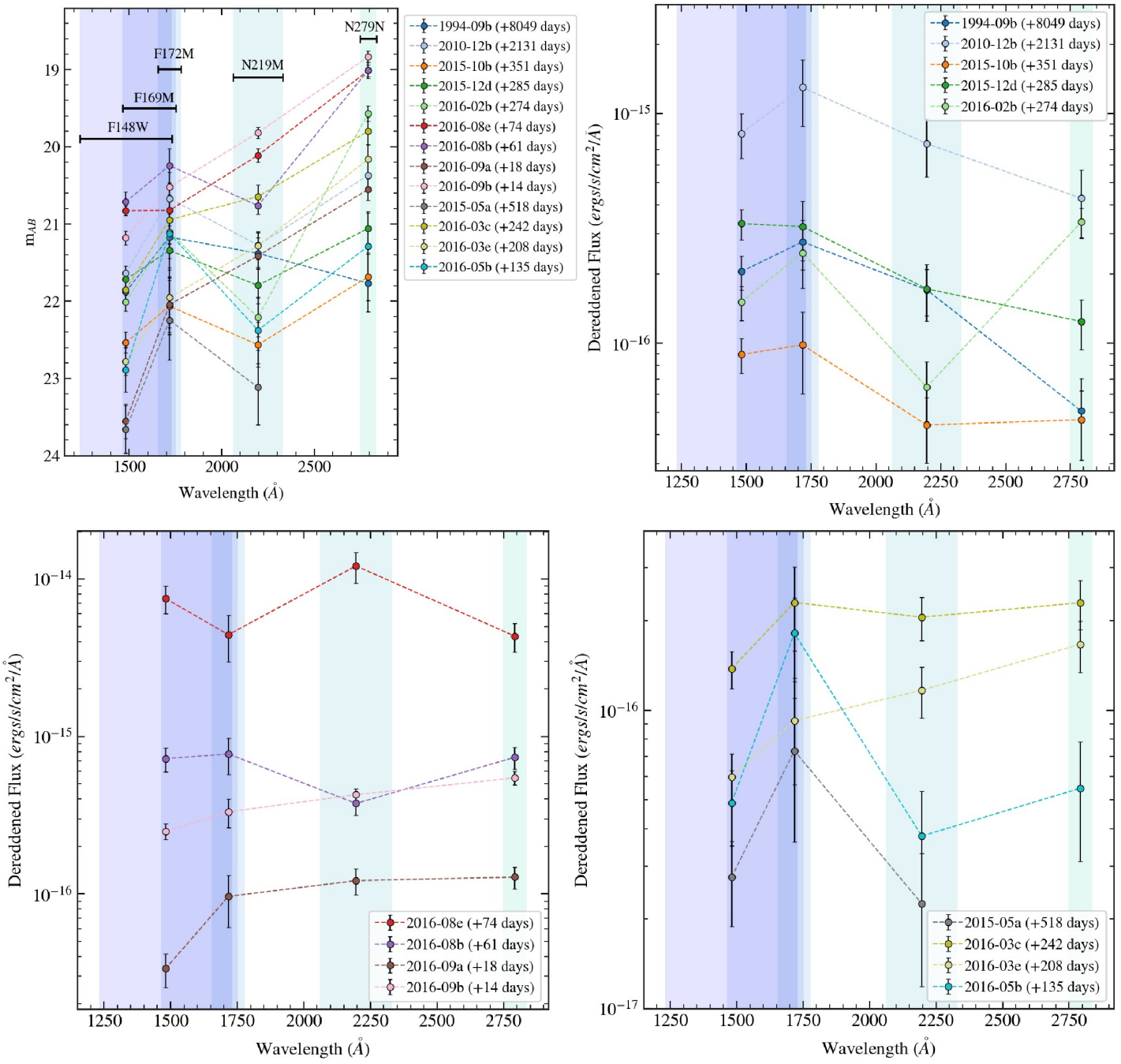

FIGURE 3.6: SEDs of novae observed with UVIT. The *top-left* panel shows the observed SEDs (in AB magnitude) of novae detected after outburst, plotted as a function of wavelength. UVIT filter bandpasses are also indicated. The extinction-corrected SEDs, converted to flux units (F_λ), are shown in the remaining panels: novae detected during post-outburst quiescence (*top-right*), novae observed close to outburst (*bottom-left*), and novae located in the central region of M31 (*bottom-right*).

TABLE 3.3: α values of novae with accretion disk signatures. α corresponds to the power-law between F_λ vs λ when errors in A_V are not taken into account, whereas α_2 corresponds for the same power-law when errors in A_V are taken into account.

Nova	α	α_2
M31N 1994-09b	2.71 ± 0.81	3.28 ± 0.79
M31N 2010-12b	2.29 ± 0.01	2.29 ± 0.94
M31N 2015-10b	2.01 ± 0.96	1.34 ± 1.32
M31N 2015-12d	2.15 ± 0.33	1.92 ± 0.82

speed classes, both are classified as moderately fast and were confirmed to be in their Fe II spectral phase (see Table 3.2). Their SEDs show increasing flux from FUV to NUV, indicating that the peak emission likely lies in the NUV/optical. During the peak of the outburst, the nova's pseudo-photosphere reaches its largest radius, shifting the SED peak toward longer wavelengths. While very fast novae may peak in the UV, slower novae can peak in the optical or even the IR. As the eruption progresses and the photosphere contracts, hotter regions near the WD are exposed, causing the SED peak to shift blueward. The observed SEDs likely capture these novae during the receding phase of their pseudo-photospheres.

The SEDs of novae M31N 2016-02b, M31N 2016-08e, and M31N 2016-08b deviate from the expected accretion disk power-law and/or photospheric blackbody profiles. This deviation could arise from the presence of UV spectral features. Selvelli & Gilmozzi (2013) noted prominent UV emission lines in quiescent novae, including C IV 1550 Å, as well as weaker features such as N V 1240 Å, Si IV 1400 Å, He II 1640 Å, O III] 1666 Å, and N III] 1750 Å. Absorption features due to metals like Si II 1190 Å, O I+Si II 1303 Å, C II 1335 Å, and N V 1240 Å can also affect the SED shape. During outbursts, UV spectra are typically dominated by emission lines until the "Fe curtain" phase begins. The evolution of these features is discussed in detail by Shore (2008).

Another possible cause of deviation is uncertainty in extinction correction. Since the extinction bump at 2175 Å affects the N219M band, even minor errors in A_V can result in significant deviation of flux estimations in both FUV and NUV. The SED of the quiescent nova M31N 2016-02b, for instance, may be under-corrected. Likewise, M31N 2016-08e and M31N 2016-08b, both observed during outburst, may have been over- and under-corrected, respectively. Over-correction could imply that the nova lies in the foreground of M31's dust disk, experiencing less extinction than predicted, while under-correction may suggest that the nova resides on the far side of M31, behind denser dust columns.

However, we emphasize that higher SNR observations for the source, and extinction are required to definitively model these systems at quiescence.

The situation is further complicated for novae detected in the central region of M31 (lower-right panel of Figure 3.6). The bulge region exhibits a complex UV structure. While Leahy et al. (2023) demonstrated that a single-component model can approximate the bulge's FUV profile, an eight-component model provides a significantly better fit. Such complexity introduces contamination effects that vary across UV bands and depend on the precise positions of the novae. Additionally, the uncertain 3D locations of these novae within the bulge hinder accurate estimates of column densities and extinction, making the analysis of their SEDs challenging.

3.4 Summary

Astronomers have long investigated novae in M31, primarily through optical observations spanning over a century, and more recently in X-rays over the past few

decades, to better understand their spatial distribution, eruption rates, and evolutionary characteristics across different phases. In contrast, UV studies remain relatively sparse. This work leverages multi-band data from the UVIT onboard AstroSat to explore novae across both their eruptive and quiescent states. The key findings from this study are summarised below:

- We analysed 91 sets of UVIT images of M31 obtained since 2016, detecting at least one nova in 19 of them. Over 80% of the identified novae were located in or near the galaxy's central bulge, consistent with the findings of other surveys that show a correlation between nova occurrence and the underlying galactic light tracing the older stellar population.
- Two distinct image subtraction techniques were employed to suppress the background light from M31's central bulge, enabling the detection of four novae that were otherwise obscured by its brightness.
- A total of 42 novae were identified, with 15 observed in multiple UVIT filters spanning the FUV and NUV bands. Several novae were also detected across multiple epochs. Additionally, upper limits were determined for over 1000 known novae that remained undetected in individual and co-added frames.
- SEDs of novae during quiescence exhibit clear signatures of accretion disk emission, supporting its dominant contribution to UV luminosity in this phase. SEDs of two novae observed during outburst indicate they were captured during the photospheric recession phase.
- FUV light curves of two novae display possible pre-eruption dips, potentially caused by the accumulation of accreted material in a shell around the WD. Moreover, multi-epoch photometry of quiescent novae reveals near-constant brightness, suggesting stable accretion rates in these systems.

Chapter 4

From Many to One: M31N 2008-12a, a Special Recurrent Nova

"You must have chaos within you to give birth to a dancing star."

— Friedrich Nietzsche

The work presented in this chapter is based on the publication: Basu et al. (2024e), 'Multiwavelength Observations of Multiple Eruptions of the Recurrent Nova M31N 2008-12a', 2024, ApJ, 966, 44.

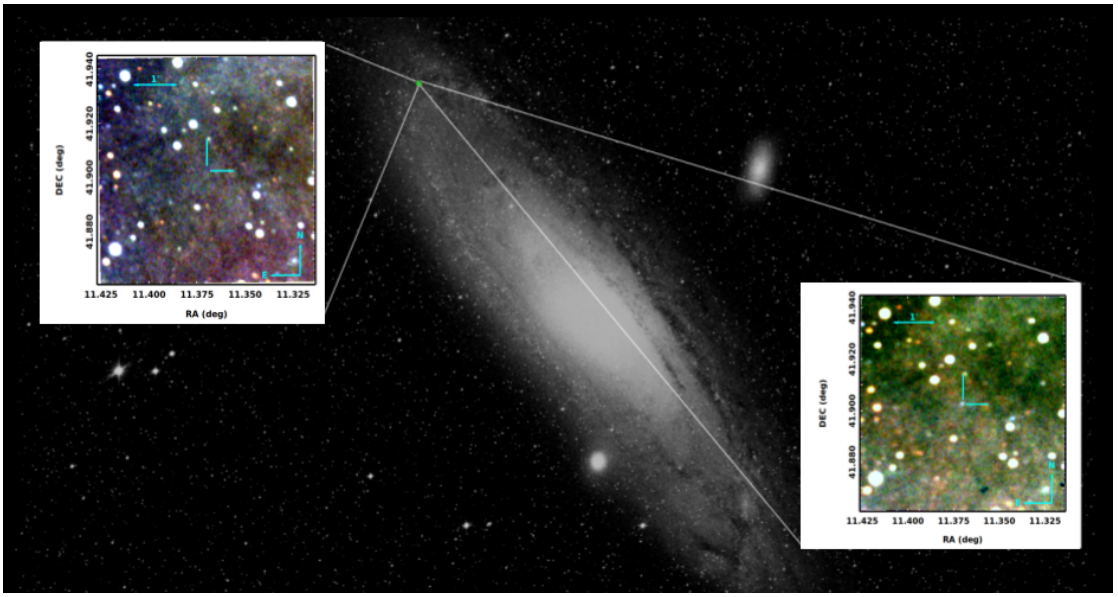

FIGURE 4.1: Location of M31N 2008-12a in the Andromeda galaxy. Shown in the insets are the nova field at quiescent (*left*) and during outburst (*right*).

4.1 Introduction

M31N 2008-12a stands out as an exceptional recurrent nova (RN) in M31 (see Figure 4.1), with eruptions recorded every year from 2008 to 2024 (Table 4.1). It was first discovered during its 2008 eruption by Nishiyama & Kabashima (2008), though archival searches have since uncovered earlier outbursts in 1992, 1993, and 2001. Since the 2013 eruption, the nova has been monitored extensively across multiple wavelengths to investigate the nature of its unusually short recurrence time (2013: Darnley et al. 2014; Henze et al. 2014a; Tang et al. 2014); (2014: Darnley et al. 2015c; Henze et al. 2015b); (2015: Darnley et al. 2016, 2017c,b); (2016: Henze et al. 2018f).

The optical light curves and spectra of M31N 2008-12a display excellent consistency across eruptions. The spectra are dominated by Balmer, He, and N lines, while the light curves show a rapid rise to peak within ~ 1 day, followed by a fast linear decline over the next 4 days. This is succeeded by a plateau phase lasting until about day 8, characterised by a slower decline and occasional variability.

TABLE 4.1: Record of eruption history of M31N 2008-12a till 2024

Eruption date[(a)] (UT)	Discovery mag (Filter)	Time since last eruption (days)	SSS t_{on} date[(b)] (UT)	Detection waveband (Observatory)	Ref.
(1992 Jan 28)	···	···	1992 Feb 03	X-ray (ROSAT)	1, 2
(1993 Jan 03)	···	341	1993 Jan 09	X-ray (ROSAT)	1, 2
(2001 Aug 27)	···	···	2001 Sep 02	X-ray (Chandra)	2, 3
2008 Dec 25	···	···	···	Visible (Miyaki-Argenteus)	4
2009 Dec 02	···	342	···	Visible (PTF)	5
2010 Nov 19	···	352	···	Visible (Miyaki-Argenteus)	2
2011 Oct 22.5	···	337.5	···	Visible (ISON-NM)	5–8
2012 Oct 18.7	···	362.2	<2012 Nov 06.45	Visible (Miyaki-Argenteus)	8–11
2013 Nov 26.95 ± 0.25	18.9 (R)	403.5	≤2013 Dec 03.03	UV/X-ray (Swift); Visible (iPTF)	5, 8, 11–14
2014 Oct 02.69 ± 0.21	18.86 (r')	309.8 ± 0.7	2014 Oct 08.6 ± 0.5	UV/X-ray (Swift); Visible (LT)	8, 15
2015 Aug 28.28 ± 0.12	19.09 (r')	329.6 ± 0.3	2015 Sep 02.9 ± 0.7	UV/X-ray (Swift); Visible (LCO)	14, 16–18
2016 Dec 12.32 ± 0.17	17.62 (V)	471.7 ± 0.2	2016 Dec 17.2 ± 1.1	UV/X-ray (Swift); Visible (Itagaki)	19–23
2017 Dec 31.58 ± 0.20†	18.41 (clear)	384.3 ± 0.4	2018 Jan 05.6 ± 0.5	UV/X-ray (Swift); Visible (WCO)	24–27
2018 Nov 06.67 ± 0.13†	19.15	310.1 ± 0.3	2018 Nov 13.2 ± 0.5	UV/X-ray (Swift); Visible (LT)	28–31
2019 Nov 06.60 ± 0.11†	19.40	364.9 ± 0.2	2019 Nov 12.4 ± 0.5	UV/X-ray (Swift); Visible (HO)	32–34
2020 Oct 30.49 ± 0.34†	18.74 (g')	358.9 ± 0.4	2020 Nov 05.5 ± 0.9	UV/X-ray (Swift); Visible (LT)	35–38
2021 Nov 14.17 ± 0.21†	18.7 (clear)	379.7 ± 0.5	2021 Nov 19.2 ± 0.6	UV/X-ray (Swift); Visible (Itagaki)	39–42
2022 Dec 02.50 ± 0.34†	19.18 (r')	383.3 ± 0.5	2022 Dec 07.5 ± 0.5	UV/X-ray (Swift); Visible (LCOGT)	43–45
2023 Dec 05.28 ± 0.07†	18.63 (CV)	367.8 ± 0.4	2023 Dec 11.1 ± 0.3	Visible (HMT, XO)	46–50
2024 Dec 12.99 (discovery)	18.56 (CV)	373.71	2024 Dec 18.29	UV/X-ray (Swift); Visible (BGO SMU)	51–52

Notes: Eruption history updated from Tang et al. 2014; Darnley et al. 2015c; Henze et al. 2015a; Darnley et al. 2016; Henze et al. 2018f; Basu et al. 2024e.

† Determined in this work (Basu et al. 2024e).

(a) Enclosed in brackets are the archival detections in X-ray data taken from Henze et al. 2015a.

(b) ROSAT data was used to estimate the SSS t_{on} for 1992 and 1993. The Chandra detection on 2001 Sep 08 UT was taken to be the middle of a typical SSS phase of 12 days to constrain the date of eruption.

··· indicates unavailability of information.

References - (1) White et al. (1995), (2) Henze et al. (2015a), (3) Williams et al. (2004), (4) Nishiyama & Kabashima (2008), (5) Tang et al. (2014), (6) Korotkiy & Elenin (2011), (7) Barsukova et al. (2011), (8) Darnley et al. (2015c), (9) Nishiyama & Kabashima (2012), (10) Shafter et al. (2012), (11) Henze et al. (2014a), (12) Tang et al. (2013), (13) Darnley et al. (2014), (14) Darnley et al. (2016), (15) Henze et al. (2015b), (16) Darnley et al. (2015a), (17) Darnley et al. (2015b), (18) Henze et al. (2015c), (19) Henze et al. (2018f), (20) K. (2016), (21) Itagaki et al. (2016), (22) Henze et al. (2016a), (23) Henze et al. (2016b), (24) Boyd et al. (2017), (25) Henze et al. (2018b), (26) Henze et al. (2018c), (27) Naito et al. (2018), (28) Henze et al. (2018a), (29) Darnley et al. (2018b), (30) Tan & Gao (2018), (31) Henze et al. (2018d), (32) Darnley et al. (2019a), (33) Oksanen et al. (2019), (34) Darnley et al. (2019b), (35) Galloway et al. (2020), (36) Darnley et al. (2020b), (37) Darnley & Page (2020), (38) Darnley et al. (2020a), (39) Itagaki et al. (2021), (40) Tan et al. (2021), (41) Darnley & Pag (2021a), (42) Darnley & Pag (2021b), (43) Perez-Fournon et al. (2022), (44) Shafter et al. (2022b), (45) Darnley et al. (2022), (46) Sun et al. (2023), (47) Shafter et al. (2023b), (48) Perez-Fournon et al. (2023), (49) Basu et al. (2023a), (50) Balcon (2023), (51) Zhao & Ren (2024), (52) Page & Darnley (2024).

The UV light curves show a comparable pattern: a steep initial drop followed by a plateau-like decline. This plateau phase coincides with the start of the SSS phase, which, like the UV and optical light curves, is also remarkably similar across eruptions.

The 2016 eruption (Henze et al. 2018f) notably deviated from this trend. It followed a longer-than-usual inter-eruption interval and featured a short-lived, cuspy structure in the optical light curve. The UV and X-ray fluxes also declined earlier than in previous eruptions. This atypical behaviour was attributed to a potentially lower accretion rate in the lead-up to the eruption.

Theoretical modelling aimed at explaining the short recurrence interval and rapid onset of the SSS phase suggests that the WD in M31N 2008-12a is close to the Chandrasekhar limit (Tang et al. 2014; Kato et al. 2014a). Deep Hα and HST imaging have revealed a large elliptical nebula (134 pc $\times$ 90 pc) surrounding the system (Darnley et al. 2015c), indicating that the system may have been erupting for over a million years (Darnley et al. 2019d), and could continue doing so for another $\sim 20,000$ years before the WD reaches M_{Ch} (Darnley et al. 2017b).

This chapter presents optical photometric and spectroscopic data from the 2017–2024 eruptions, as well as UV and soft X-ray observations from both archival *Swift* data and new *AstroSat* observations. We employ spectroscopic modelling to investigate the physical conditions during the eruptions and derive system parameters. We compare the 2017–2024 activity with prior eruptions, discussing implications for the WD mass, accretion rate, and recurrence timescale.

4.1.1 Eruption History

For a rapidly evolving recurrent nova like M31N 2008-12a, tightly constraining the eruption epoch is essential for accurate light curve modelling and for investigating its recurrence behaviour. We estimated the eruption times for all events (2017-2024) using available discovery and pre-discovery magnitudes, as well as upper limits from non-detection. Although the exact eruption moments remain uncertain, we approximate them as the mid-point between the last non-detection and the first detection for each year. The growing interest of amateur astronomers and the expansion of wide-field surveys over the past decade have enabled eruption epochs to be constrained to within about a day. The uncertainty associated with each eruption date is taken as the time span between the last non-detection and the first detection. The eruption dates are summarised in Table 4.1.

The 2017 eruption was detected just in time to qualify as the "2017 eruption," being discovered on Dec 31.77 UT by Boyd et al. (2017) and confirmed spectroscopically on the same day by Darnley et al. (2017a). The most recent prior non-detection was on Dec 31.38 UT, with an upper limit of $m_{clear} = 19$ mag (Naito et al. 2018).

In 2018, the eruption was discovered on Nov 06.80 UT at 19.15 ± 0.05 mag by Darnley et al. (2018b) and spectroscopically confirmed later that day by Darnley et al. (2018c). The last non-detection was reported by Tan & Gao (2018) at >21.20mag on Nov 06.54 UT in a clear filter.

The 2019 eruption was detected on Nov 06.71 UT by Oksanen et al. (2019) at 19.40 mag, with spectroscopic confirmation by Darnley et al. (2019e) on Nov 06.83 UT. Since no last non-detection data were publicly available, we adopted the eruption date reported in Darnley et al. (2019b).

The 2020 eruption was discovered on Oct 30.89 UT by Darnley et al. (2020b), though pre-discovery images detected the nova roughly 90 minutes earlier at $m_g = 18.74$ (Galloway et al. 2020). The last non-detection prior to this had a limit of $m_g > 19.4$. Spectroscopic confirmation was obtained on the following day (Darnley 2020).

In 2021, the eruption was first reported by Itagaki et al. (2021) on Nov 14.38 UT and confirmed by Wagner et al. (2021). The latest pre-eruption upper limit was provided by Tan et al. (2021), who reported $m_{clear} > 19.00$ mag on Nov 13.96 UT.

The 2022 eruption was discovered by Perez-Fournon et al. (2022) on Dec 02.83 UT, with no detection as late as Dec 02.61 UT at $m_L > 19.60$mag (Shafter et al. 2022b). Spectroscopic confirmation followed on Dec 03.84 UT (Darnley & Healy 2022), marking the 15th recorded consecutive eruption of M31N 2008-12a.

The 2023 eruption was initially discovered by Sun et al. (2023) on Dec 05.54. However, earlier pre-discovery detections were recorded on Dec 05.35 by Perez-Fournon et al. (2023) at a magnitude of 19.137 ± 0.180. The eruption timing was further constrained by the earliest non-detection on Dec 05.208, with a limit of $>$ 21.3 mag (Shafter et al. 2023b). Spectroscopic confirmation was reported on Dec 06.582 by Basu et al. (2023a).

The 2024 eruption was discovered by Zhao et al. (2024) on Dec 13.0074 UTC at a magnitude of 18.6 ± 0.2 (CV). Earlier detections from the same telescope on Dec 12.98 helped constrain the eruption date (Zhao & Ren 2024). Spectroscopic confirmation followed on Dec 13.75 UTC (Basu et al. 2024b).

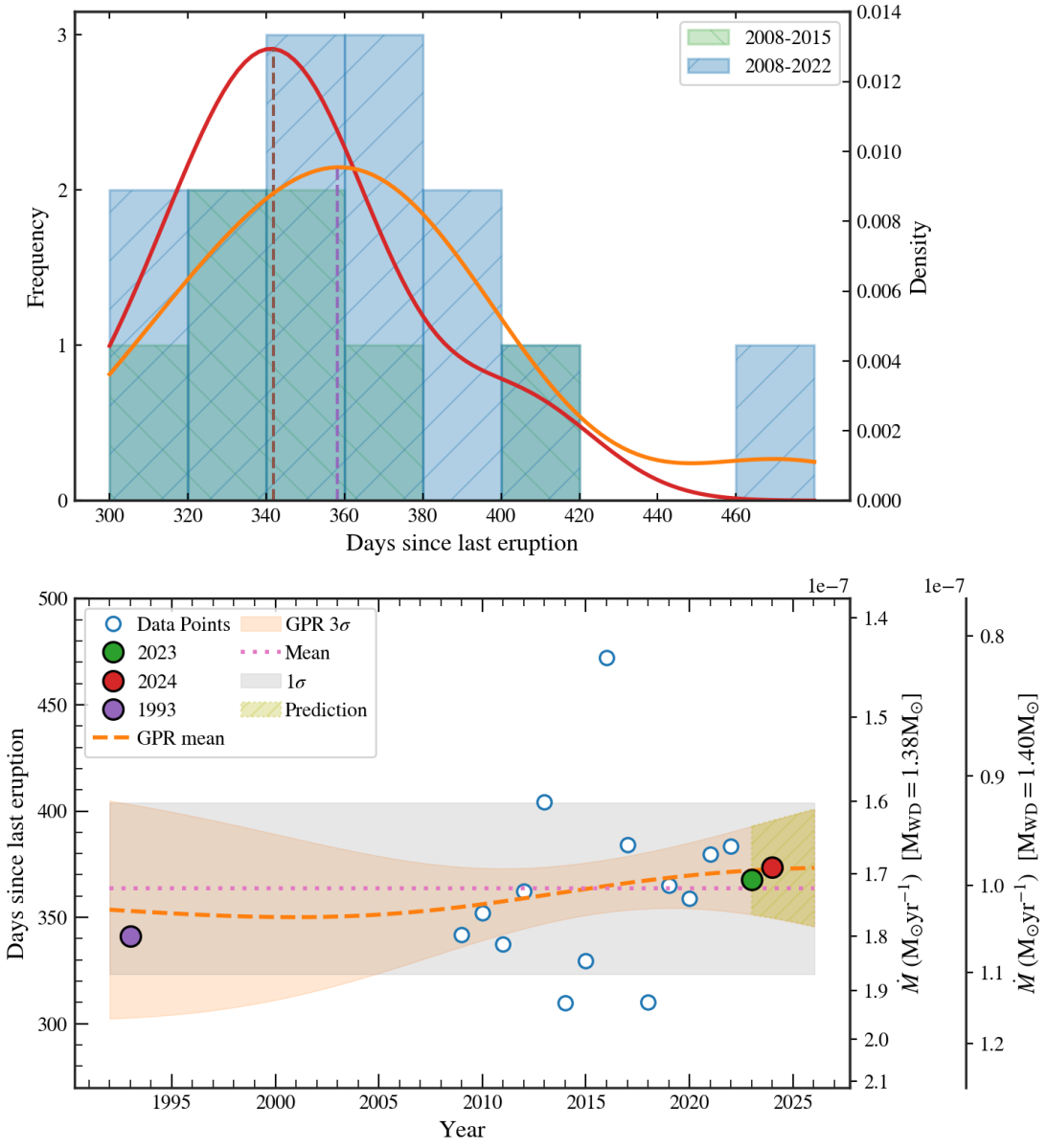

FIGURE 4.2: Recurrence period distribution and eruption history of M31N 2008-12a. Actual eruption dates of the 2023 and 2024 eruptions are overplotted on their predicted dates from GP regression.

4.2 Recurrence Period and Nature of WD

4.2.1 Trends in the recurrence period

Following the 2015 eruption, the mean recurrence period of M31N 2008-12a was estimated to be $P_{rec} = 351 \pm 13$ days by Darnley et al. (2016), later revised to 363 ± 52 days by Henze et al. (2018f) after the anomalously late 2016 eruption. It should be noted that Darnley et al. (2016) provides the standard error on the mean while Henze et al. (2018f) provides the standard deviation of the recurrence period. Since then, the nova has erupted eight more times, with most inter-eruption intervals exceeding the mean recurrence period, except for 2018 (310.1 days) and 2020 (355.9 days). By the time of the 2022 eruption, the updated mean recurrence period stood at $P_{rec} = 363.6$ days, with a standard deviation of 40.3 days (Figure 4.2, top panel). Notably, the median recurrence period also increased from 347 days in 2016 (Henze et al. 2018f) to 360.5 days in 2022.

Figure 4.2 (top panel) illustrates two histograms representing recurrence periods for two different intervals: 2008–2015 and 2008–2022. For the former (green histogram), the recurrence period has a mode of 340 days, and its kernel density estimate (KDE) peaks at 341.28 days, with a FWHM of 67.27 days. When including eruptions through 2022 (blue histogram), the mode shifts to 360 days, and the KDE peaks at 358.18 days with a broader FWHM of 96.36 days. These recent eruption intervals show a suggestive trend toward longer periods, with 5 out of the last 7 events falling above the mean. A binomial test indicates that such a distribution has a 22.6% probability of occurring by chance. While this does not meet the standard threshold for statistical significance ($p < 0.05$), the increase in the latest intervals motivates further monitoring.

To explore this trend further, we plotted the recurrence period as a function of

eruption year (bottom panel of Figure 4.2) and employed Gaussian Process (GP) regression to model the temporal evolution. A Matern kernel was used with a typical length scale of 15 years and an amplitude set to the median of the recurrence period. We tested the model on data from 2008–2021, which successfully predicted the 2022 eruption within 3σ uncertainty. Including the 2022 data in the training set, we projected future eruptions. Although we excluded the 1993 eruption from the GP fit due to the large time gap, a backward extrapolation shows the 1993 event lies within the model's error bounds. For comparison, a constant-period model (mean $\pm$ 1σ) is also shown in the figure. Both models are consistent with the 2023 and 2024 eruption timing within 1σ, though the GP model more accurately captures evolving trends, potentially reflecting changes in the accretion rate.

We note, however, that this model applies only to the regular eruption pattern. Outlier events, such as the 2016 eruption, remain unpredictable with the current approach.

4.2.2 Estimating the WD mass

In a theoretical investigation into the potential mass growth of WDs accreting material from non-degenerate companions, Hillman et al. (2016a) explored a broad range of accretion rates and identified the conditions—specifically, limits on the accretion rate and initial WD mass—under which a WD can grow to the Chandrasekhar mass. Using their relation for hydrogen accretion, $\log \dot{M} = -A \log D - B$, where D is the recurrence period and the coefficients A and B depend on the WD mass, we estimate accretion rates for M31N 2008-12a eruptions over the past 15 years. For each value of assumed WD mass, the constants A and B were derived from a linear fit to the $\log D$–$\log \dot{M}$ parameter space. The resulting accretion rates for WD masses between 1.20 $M_\odot$ and 1.40 $M_\odot$ are shown in the top panel of Figure 4.3.

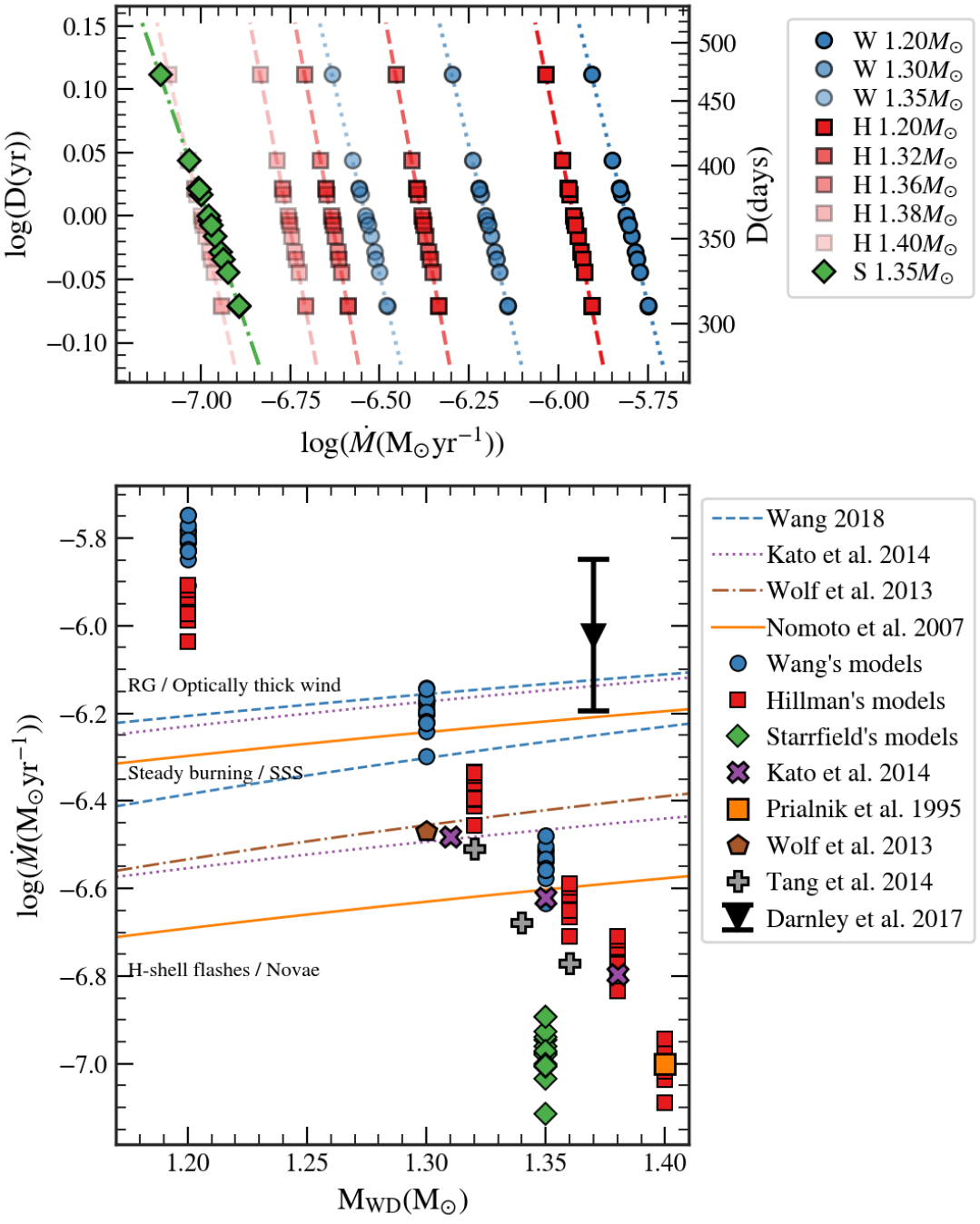

FIGURE 4.3: Top: Observed recurrence periods versus accretion rates for different WD masses. The legend labels "W," "H," and "S" refer to accretion rates calculated using the models of Wang (2018a), Hillman et al. (2016a), and Starrfield (2017), respectively, from the inter-eruption times. Bottom: Accretion rate parameter space for M31N 2008-12a. Accretion rates from the top panel are shown in blue (Wang), red (Hillman), and green (Starrfield). Other markers indicate the position in the parameter space for 1-year recurrence period values from the literature. Stable and critical accretion rate boundaries from four studies are plotted as horizontal lines. The accretion rate range derived by Darnley et al. (2017b) during quiescence is shown in black.

Complementing this, Wang (2018a) used the `MESA` stellar evolution code to simulate the binary evolution of WDs accreting H-rich material for various masses and accretion rates. Adopting a composition of H:He:Metals = 70:28:2, we fitted a power-law relation to their results for massive WDs (1.20–1.35 $M_\odot$) and used it to estimate accretion rates for each eruption cycle of M31N 2008-12a. These values are also presented in the top panel of Figure 4.3.

We plot these derived accretion rates versus WD mass in the bottom panel of Figure 4.3, alongside theoretical predictions from Kato et al. (2014a), Prialnik & Kovetz (1995), Wolf et al. (2013), and Tang et al. (2014) for systems with ∼1-year recurrence periods. In the $M_{WD} - \dot{M}$ space, if $\dot{M}$ exceeds a critical threshold ($\dot{M} > \dot{M}_{cr}$), the WD undergoes surface hydrogen burning at a steady rate, resembling a red giant, while excess mass is lost via optically thick winds (Kato & Hachisu 1994; Hachisu et al. 1996). If the accretion rate falls below this threshold but remains above the stable-burning limit ($\dot{M}_{cr} > \dot{M} > \dot{M}_{st}$), the WD can sustain stable surface burning, appearing as a supersoft X-ray source (Kato et al. 2014a). For lower accretion rates ($\dot{M} < \dot{M}_{st}$), hydrogen burning becomes unstable, resulting in thermonuclear runaways or nova eruptions—characteristic of recurrent novae like M31N 2008-12a.

The critical and stability thresholds adopted from Wang (2018a), Kato et al. (2014a), Wolf et al. (2013), and Nomoto et al. (2007) are plotted in the bottom panel of Figure 4.3. Variations in these thresholds stem from differences in the physical assumptions and computational treatments in each model.

Our analysis suggests that WDs with masses below 1.30 $M_\odot$ require unfeasibly high accretion rates to match the observed ∼1-year recurrence, making such low masses unlikely for M31N 2008-12a. WDs in the 1.32–1.36 $M_\odot$ range fall into the unstable "H-shell flash" regime in some models, while masses above 1.36 $M_\odot$ consistently lie within the nova eruption region ($\dot{M} < \dot{M}_{st}$) across all models. This

supports the interpretation that the WD in M31N 2008-12a likely exceeds 1.36 $M_{\odot}$, enabling it to undergo annual nova outbursts.

Interestingly, Starrfield (2017) produced `MESA`-based models showing that stability lines may disappear entirely for WDs near 1.35 $M_{\odot}$. In these systems, initial hydrogen flashes give way to helium flashes, allowing mass growth toward the Chandrasekhar limit. This challenges traditional models that impose strict upper limits on stable accretion.

Notably, none of these theoretical models align with the accretion rates inferred from accretion disc modelling by Darnley et al. (2017b), which show significant phase-dependent variation between eruption, SSS, and quiescence. In Figure 4.3, we illustrate the quiescent accretion range, which lies above predictions from most standard models. This discrepancy suggests that models like those by Starrfield, which allow high accretion without imposing an upper stability threshold, may be more appropriate for such extreme systems. Yet, even these may fall short of matching the observationally derived accretion rates of this extraordinary recurrent nova.

4.3 Optical Photometric and Spectroscopic Evolution

4.3.1 Lightcurve

Figure 4.4 presents the optical light curves of the 2017–2024 eruptions, combining our observations with publicly available data. Photometry of observed data is

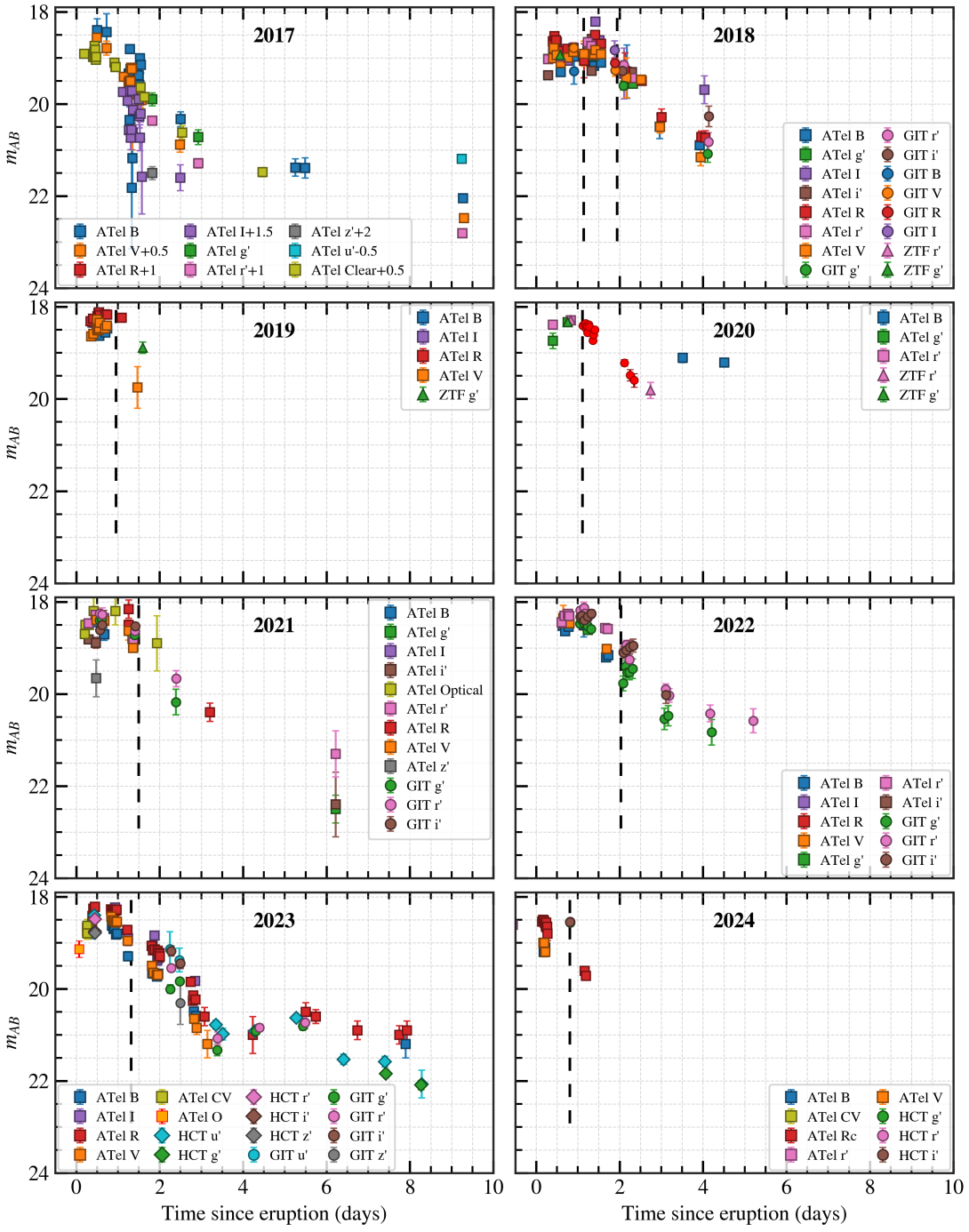

FIGURE 4.4: M31N 2008-12a optical lightcurves from 2017 to 2024 eruptions. Publicly available data from ATels are included with observations from GIT, HCT, and JCBT. Spectral epochs are marked in vertical dashed lines.

available in the GitHub link *. These light curves consistently exhibit a rapid rise to peak brightness within less than a day of discovery, followed by a fast decline with $t_2 \approx$ 2–4 days in the $g'r'i'$ bands. A concise description of each eruption's optical light curve over this period is provided below.

In 2017, the nova declined rapidly for the first four days across all bands, followed by a slower fading phase. The decline rates were smilar in r' band (0.84 ± 0.12 mag day^{-1}) and g' (0.74 ± 0.19 mag day^{-1}) bands well within 1σ. However, the limited number of data points questions its statistical significance.

The 2018 eruption exhibited a broader peak phase. After the initial rise, the magnitude dropped by $\sim$0.4 mag in the $BVRI$ filters, then plateaued briefly for about 0.3 days. This was followed by a modest rebrightening of 0.2–0.3 mag over $\sim$0.7 days. Notably, the R-band peak in 2018 ($\sim$18.50 mag) was fainter than in other years. The early decline in 2018 was slower in r' (0.68 ± 0.03 mag day^{-1}) and i' (0.53 ± 0.04 mag day^{-1}) compared to g' (0.84 ± 0.02 mag day^{-1}).

The 2019 light curve is sparsely sampled, capturing only the rise and maximum. The nova brightened by about 0.4 mag in all filters within 0.5 days. The R-band peak magnitude of 18.12 was among the brightest recorded.

In 2020, the g' band captured a rise at $\sim$1.2 mag day^{-1}, while r' followed the decline from peak at 0.89 ± 0.05 mag day^{-1} over two days. Sparse sampling restricted the analysis primarily to the r' band.

The 2021 eruption was detected nearly a day before peak. The i' band exhibited a sharper rise than g' and r'. The nova faded rapidly in g' (1.25 ± 0.20 mag day^{-1}), more moderately in r' (0.88 ± 0.13 mag day^{-1}), and showed a noticeable flux enhancement in r' around day 6 post-eruption.

*https://github.com/judha-basu/Thesis-files/blob/f914aae4730894b73c2b084f7565590975d68199/optical_phot_table.csv

The 2022 eruption showed a light curve consistent with earlier years. The rise was captured in r' at a rate of $\sim$2 mag day^{-1}—the fastest observed in this six-year span. It subsequently declined steeply in g' (1.01 ± 0.05 mag day^{-1}), more gradually in r' (0.79 ± 0.03 mag day^{-1}), and slowest in i' (0.69 ± 0.06 mag day^{-1}).

In 2023, the light curve shows an initial rise at a rate of $\sim$1 mag day^{-1}, followed by a linear decline similar to previous eruptions. This eruption was monitored for a longer duration—up to day 8 post-eruption. By combining our observations with those from Shafter et al. (2023a), we obtain an extended light curve that reveals a plateau phase in the optical bands, marked by a rebrightening of approximately 0.5 mag. This plateau phase coincides with both the onset of the SSS phase and the UV plateau, suggesting a common physical origin.

In contrast, the 2024 eruption is poorly sampled, with too few data points to allow a meaningful analysis of its light curve evolution.

In general, the nova exhibits its fastest decline in the bluer bands with progressively slower fading in redder filters. The late-time evolution, captured through deep exposures, reveals a plateau phase characterised by a temporary increase in optical flux before the nova fades beyond detection.

4.3.2 Spectroscopy

The optical spectra with good SNR are presented in Figure 4.5, with key emission features marked. Spectra obtained on 2021 Nov 14.8 UT and 2022 Dec 3.73 UT were too noisy for analysis and are therefore excluded. All spectra have been dereddened using $E(B-V) = 0.10$ (Darnley et al. 2017c). Acquired within the first three days post-eruption, the spectra exhibit a blue continuum and prominent

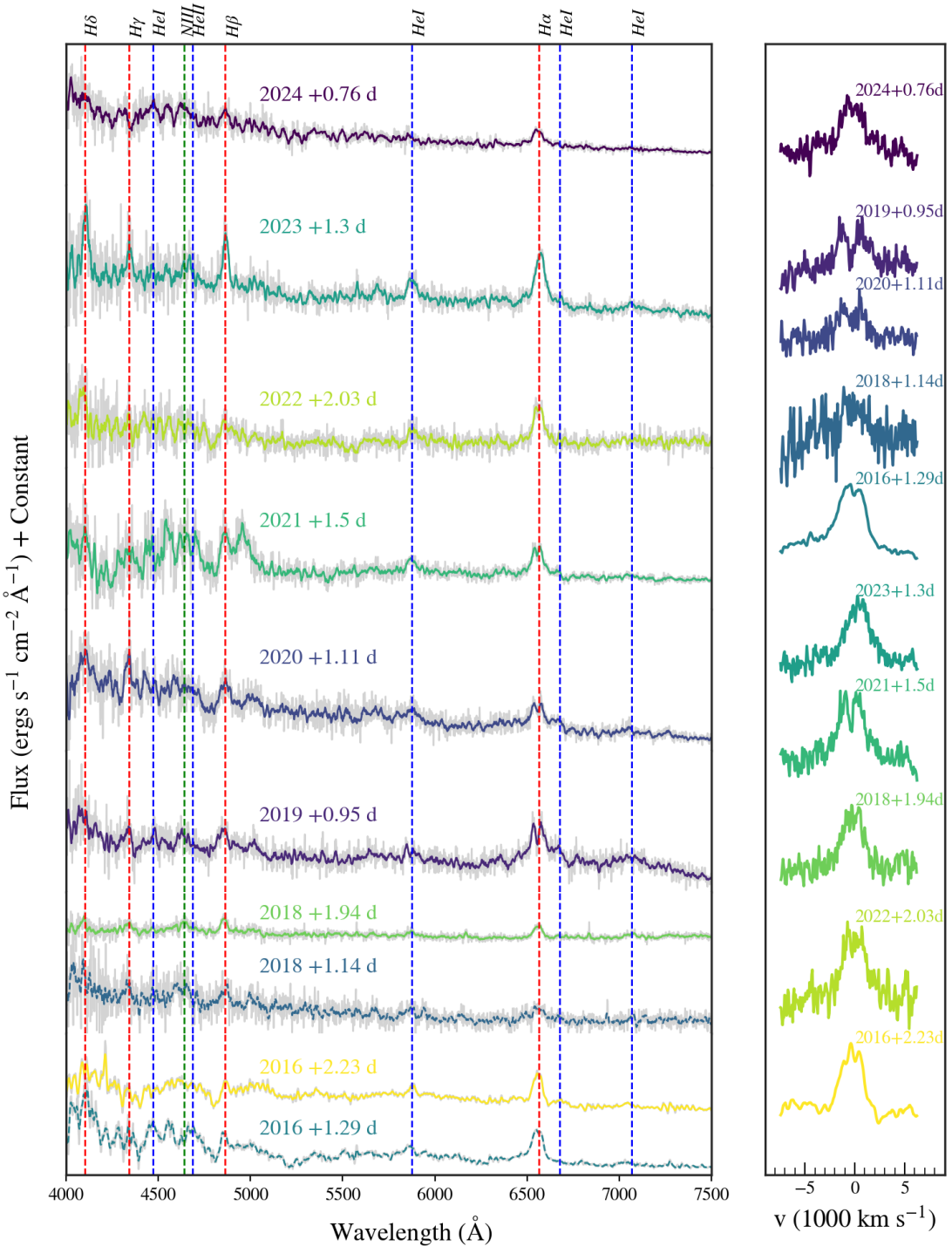

FIGURE 4.5: Optical spectral evolution across multiple eruptions of M31N 2008-12a.

TABLE 4.2: Optical spectroscopic observations of 2018–2024 eruptions of M31N 2008-12a.

Date (UT)	Telescope	Instrument	Grating	Exp (s)
2018 Nov 07.8	HCT	HFOSC	Gr7	2700
2018 Nov 08.6	HCT	HFOSC	Gr7	3600
2019 Nov 07.5	HCT	HFOSC	Gr7	3000
2020 Oct 31.6	HCT	HFOSC	Gr7	3600
2021 Nov 14.8	HCT	HFOSC	Gr7	2100
2021 Nov 15.6	HCT	HFOSC	Gr7	3600
2022 Dec 03.7	HCT	HFOSC	Gr7	3600
2022 Dec 04.5	HCT	HFOSC	Gr7	3600
2023 Dec 06.6	HCT	HFOSC	Gr7	2700
2024 Dec 13.8	HCT	HFOSC	Gr7	3600

emission lines from the Hydrogen Balmer series and HeI (4471, 5876, and 6678Å). In some epochs, emission from HeII (4686 Å) and NIII (∼4640 Å) is also detected.

Darnley et al. (2016), using a combined spectrum from multiple eruptions, reported several additional features. While most are not clearly visible in the individual spectra presented here, a few faint lines are identifiable in merged spectra obtained at similar post-eruption phases. For example, HeI 4922 Å and NII 5679 Å are visible in combined early-phase spectra from 2018 (1.14d) and 2020 (1.11d), while later-phase merged spectra from 2018 (1.94d), 2022 (2.03d), and 2016 (2.23d) reveal HeII 4686 Å, HeI 5016 Å, NII 5679 and 6346 Å, and Raman-scattered OIV 6830 Å as shown in Figure 4.6.

Table 4.3 lists the line fluxes of prominent emission features detected in individual spectra, along with the FWHM velocities derived from Gaussian fits using `IRAF`. These velocities have been corrected for instrumental broadening by deconvolving the spectral resolution determined from night sky lines. Within the first day of

TABLE 4.3: Flux and FWHM velocities of identified lines in the spectra of 2016-2024 eruptions.

Identification		**2016** (+2.23 d)			**2018** (+1.94 d)			**2019** (+0.95 d)		
		λ (Å)	Flux $\times 10^{-15}$ (erg cm^{-2} s^{-1})	Velocity (km s^{-1})	λ (Å)	Flux $\times 10^{-15}$ (erg cm^{-2} s^{-1})	Velocity (km s^{-1})	λ (Å)	Flux $\times 10^{-15}$ (erg cm^{-2} s^{-1})	Velocity (km s^{-1})
4101	H I	···	···	···	4094.52	2.37 ± 0.60	1954 ± 226	···	···	···
4340	H I	4333.90	2.54 ± 0.70	1952 ± 271	4340.02	2.61 ± 0.41	3546 ± 416	4335.70	4.08 ± 0.39	2274 ± 272
4471	He I	4489.07	0.96 ± 0.30	1637 ± 258	4468.84	1.95 ± 0.47	2618 ± 409	···	···	···
4640	N III	···	···	···	4642.11	2.01 ± 0.42	2386 ± 279	4632.18	6.42 ± 0.51	4113 ± 233
4861	H I	4862.06	3.32 ± 0.91	2233 ± 472	4856.94	3.35 ± 0.44	2278 ± 162	4850.50	6.80 ± 0.50	3121 ± 158
5876	He I	5877.73	1.77 ± 0.37	1974 ± 217	5871.05	1.22 ± 0.45	2023 ± 336	5861.49	1.76 ± 0.25	3092 ± 292
6563	H I	6556.99	8.15 ± 0.39	2407 ± 73	6558.89	4.42 ± 0.83	2581 ± 206	6559.45	23.20 ± 1.99	5099 ± 180
6678	He I	6678.70	1.79 ± 0.50	3024 ± 477	6667.21	0.57 ± 0.12	1235 ± 195	6671.71	3.63 ± 0.61	1921 ± 172
7065	He I	7042.55	1.34 ± 0.08	2655 ± 191	7064.87	1.79 ± 0.21	3144 ± 210	···	···	···
Identification		**2020** (+1.11 d)			**2021** (+1.50 d)			**2022** (+2.03 d)		
		λ (Å)	Flux $\times 10^{-15}$ (erg cm^{-2} s^{-1})	Velocity (km s^{-1})	λ (Å)	Flux $\times 10^{-15}$ (erg cm^{-2} s^{-1})	Velocity (km s^{-1})	λ (Å)	Flux $\times 10^{-15}$ (erg cm^{-2} s^{-1})	Velocity (km s^{-1})
4101	H I	···	···	···	···	···	···	···	···	···
4340	H I	4336.68	6.65 ± 0.27	2000 ± 52	···	···	···	···	···	···
4471	He I	···	···	···	···	···	···	···	···	···
4640	N III	···	···	···	···	···	···	···	···	···
4861	H I	4861.88	8.65 ± 0.55	3549 ± 143	4863.05	14.8 ± 2.57	3055 ± 398	4870.23	6.25 ± 1.38	4015 ± 472
5876	He I	5878.37	4.19 ± 1.13	3598 ± 576	5871.49	5.20 ± 0.60	2370 ± 139	5880.52	4.69 ± 0.32	2839 ± 122
6563	H I	6557.92	10.24 ± 1.47	4011 ± 336	6556.97	18.80 ± 0.16	3564 ± 56	6562.23	15.40 ± 0.37	2924 ± 53
6678	He I	6661.61	2.92 ± 0.10	2330 ± 52	6663.74	1.73 ± 0.12	1343 ± 52	···	···	···
7065	He I	7044.02	1.53 ± 0.35	2386 ± 447	7051.42	1.29 ± 0.10	1940 ± 112	···	···	···
Identification		**2023** (+1.3 d)			**2024** (+0.76 d)					
		λ (Å)	Flux $\times 10^{-15}$ (erg cm^{-2} s^{-1})	Velocity (km s^{-1})	λ (Å)	Flux $\times 10^{-15}$ (erg cm^{-2} s^{-1})	Velocity (km s^{-1})			
4340	H I	4345.06	1.95 ± 0.11	1884 ± 73	···	···	···			
4861	H I	4865.93	3.81 ± 0.15	1913 ± 53	4862.43	3.94 ± 0.28	2145 ± 91			
5876	He I	5875.36	2.27 ± 0.07	2667 ± 50	6557.24	6.70 ± 0.37	2866 ± 137			
6563	H I	6570.76	6.30 ± 0.23	2724 ± 71	···	···	···			

eruption, expansion velocities reach up to ∼5000 km s^{-1}, typical of very fast novae. At these early phases, line profiles are not fully developed, and only the strongest features are observed. These trends are consistent with previous observations of M31N 2008-12a (Henze et al. 2018f; Darnley et al. 2016, 2015c).

By $\gtrsim$1.5 days after the eruption, the emission lines narrow to ∼3000 kms^{-1}. This deceleration may result from the expansion and fading of the fastest ejecta

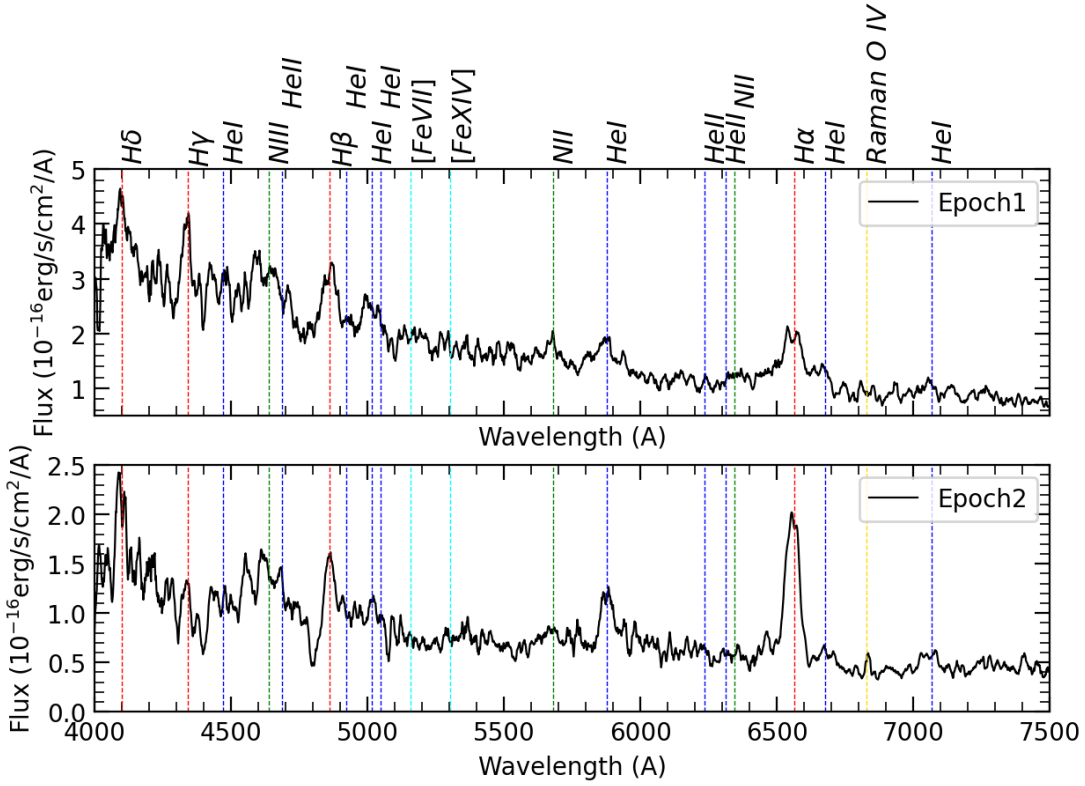

FIGURE 4.6: Merged spectra from early phase (Epoch 1) and late-phase (Epoch 2), revealing faint features.

components (Shore et al. 1996) or from interaction with the surrounding circumbinary medium. We find the velocity evolution follows a power-law decay: $v_{exp} \propto t^{-0.27\pm0.07}$. This is very close to the estimate by Darnley et al. (2016) ($v_{exp} \propto t^{-0.28\pm0.05}$), who attribute the deceleration to shock interaction with the circumbinary environment, characteristic of phase II in the development of a shocked nova remnant (Bode & Kahn 1985b). The consistency of these two independent measurements of velocity deceleration strengthens the speculations of the nova ejecta penetrating through a dense medium such as red giant wind. This signifies the secondary being an evolved star rather than a main-sequence star, which lacks substantial material in the surroundings to decelerate the ejecta.

The Hα line profiles in Figure 4.5 further indicate a structured and time-dependent

ejecta geometry. Temporal evolution of the Hα profile reveals a clear double-peaked structure in the 2016, 2019, 2020, and 2021 spectra, typically observed between ∼0.9–1.5 days after eruption. Around two days post-eruption, this morphology evolves into a narrower, boxy profile, suggesting changes in the ejecta velocities and geometry over time.

4.4 UV Light Curve Evolution and Plateau Phase

4.4.1 Lightcurve

The UV light curves (Figure 4.7), obtained from space-based telescopes, provide extended temporal coverage of up to ∼20 days. The data files are available in the GitHub link [†]. From day 0 to ∼3 days post-eruption, the $uvw2$ magnitudes for the 2017–2024 eruptions exhibit a steady, linear decline. Lightcurve morphology is further discussed in §4.6.1. Around day 4, the onset of a plateau phase is marked by a mild re-brightening, coinciding with the SSS t_{on} phase (highlighted in Figure 4.7). During the plateau, the UV brightness declines gradually at a rate of ∼0.15 mag day^{-1}, though this decline is modulated by low-amplitude variations and is not perfectly smooth.

Similar photometric fluctuations during the plateau phase have been observed in several P-type Galactic recurrent novae, such as T Pyx, RS Oph, and U Sco, particularly in the V band (Strope et al. 2010b). However, due to limited optical photometry coverage during this phase for M31N 2008-12a, we cannot confirm the presence of similar variability in the optical bands. We therefore look forward to

[†] https://github.com/judha-basu/Thesis-files/blob/f914aae4730894b73c2b084f7565590975d68199/UV_xray_table.csv

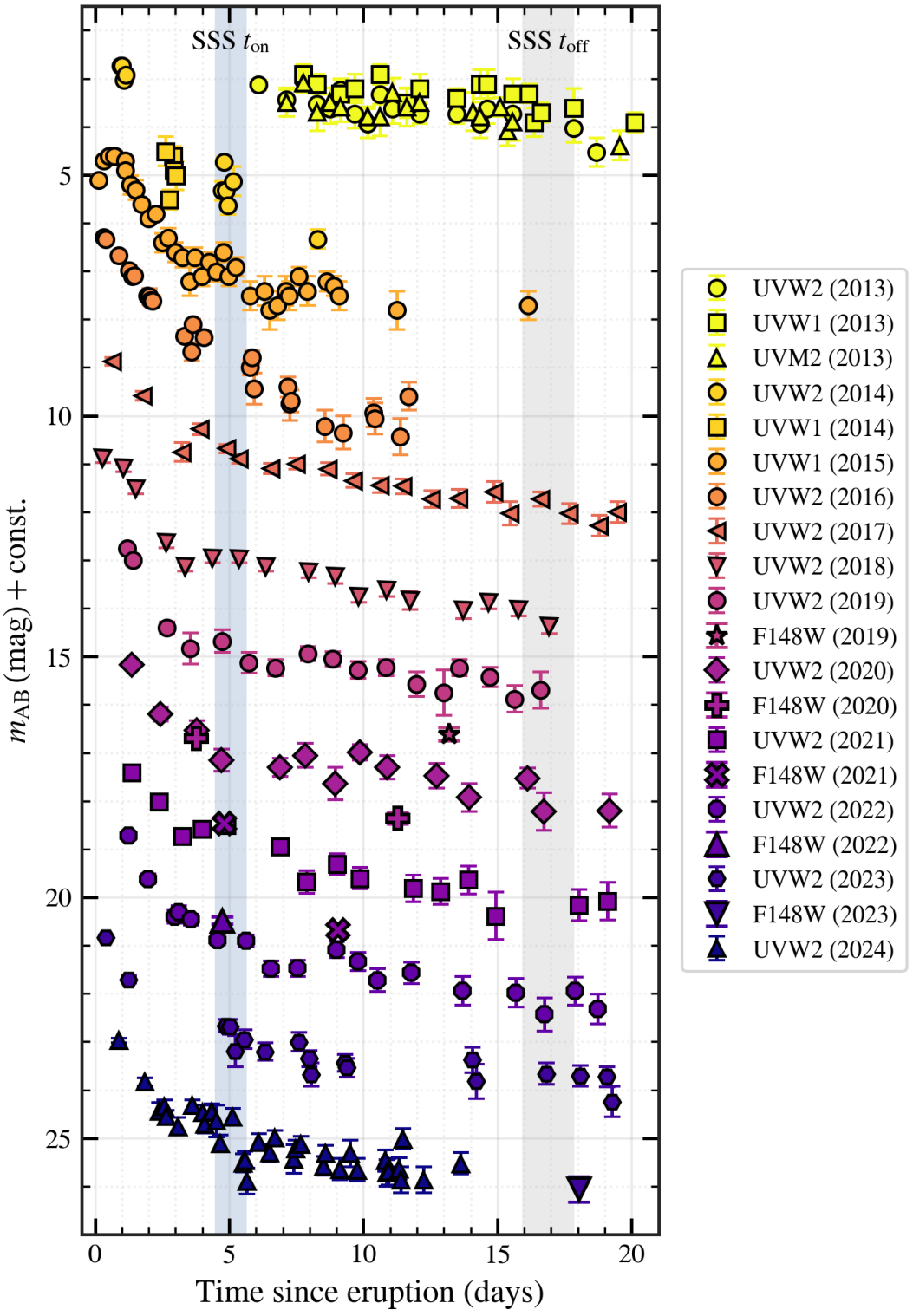

FIGURE 4.7: Swift/UVOT and AstroSat/UVIT lightcurves of M31N 2008-12a eruptions spanning from 2013 to 2024.

deep and high-cadence optical monitoring throughout the plateau phase in future eruptions.

The F148W light curve mirrors the $uvw2$ behaviour during the initial decline, but becomes noticeably fainter, by over 1 mag, relative to $uvw2$ during the SSS phase.

Overall, the UV–optical light curves from the 2017–2024 eruptions exhibit consistent evolution across all bands, in line with trends reported for previous outbursts (2013: Darnley et al. 2014; 2014: Darnley et al. 2015c; 2015: Darnley et al. 2016; 2016: Henze et al. 2018f). Notable deviations in the 2016 light curve are discussed separately in Section 4.6.

4.5 Supersoft X-ray Phase and Spectral Evolution

4.5.1 Lightcurve

Figure 4.8 presents the supersoft X-ray light curves of M31N 2008-12a during the 2017–2024 eruptions observed by XRT, overlaid with data from earlier eruptions for comparison. The 2020-21 eruptions caught by SXT are shown in Figure 4.9. The data files are available in the GitHub link [‡]. The onset of the SSS phase is usually marked by an initial detection at $\sim 10^{-2}$ counts s^{-1}, rising to $> 4 \times 10^{-2}$ counts s^{-1}, where it remains approximately steady between days 8 and 15 post-eruption. This SSS peak coincides with the UV plateau phase. From the detections and non-detections across eruptions between 2014 and 2024, we estimate the mean turn-on and turn-off times of the SSS phase to be 5.06 ± 0.60 and 16.89 ± 0.96

[‡] https://github.com/judha-basu/Thesis-files/blob/f914aae4730894b73c2b084f7565590975d68199/UV_xray_table.csv

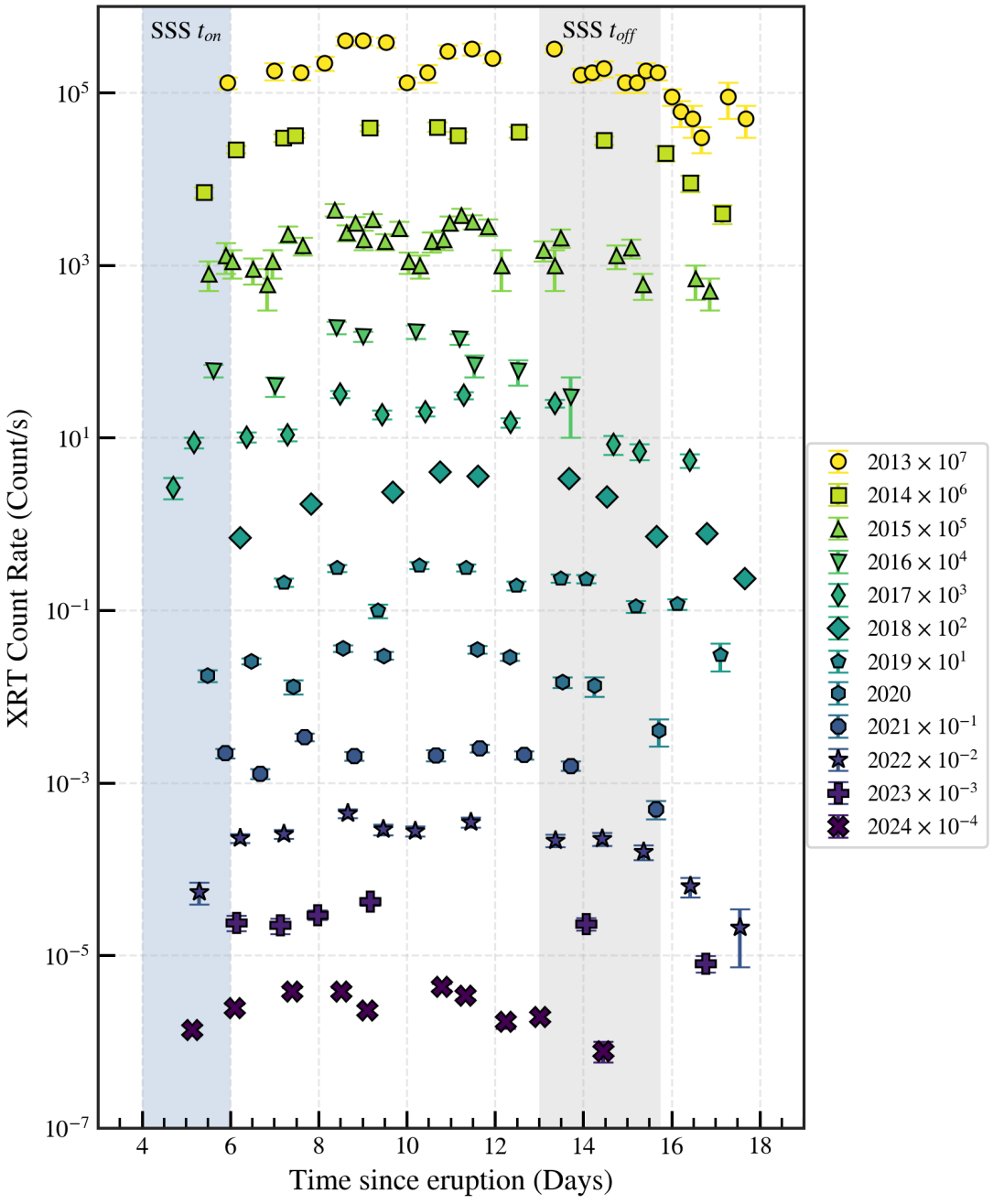

FIGURE 4.8: Swift/XRT lightcurves of M31N 2008-12a eruptions spanning from 2013 to 2024. The blue and grey shaded regions denote the mean and standard deviation of the SSS $t_{\rm on}$ and SSS $t_{\rm off}$ times respectively.

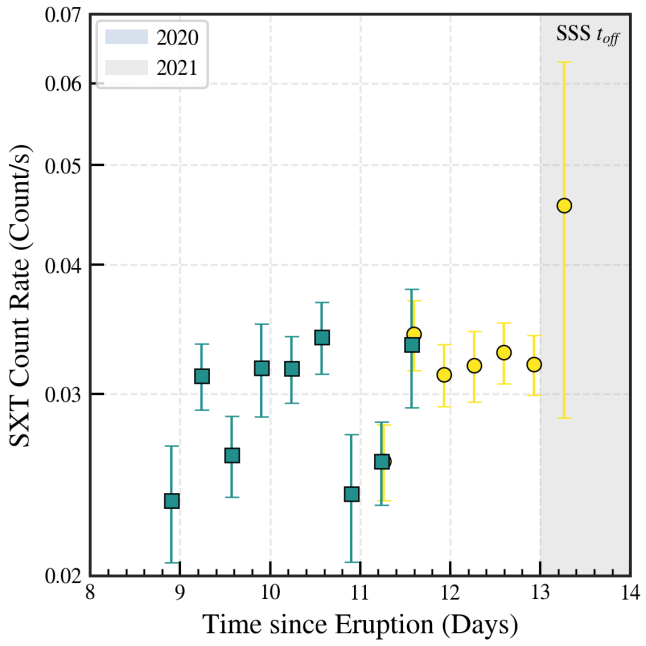

FIGURE 4.9: AstroSat/SXT lightcurves of 2020 and 2021 eruptions of M31N 2008-12a.

days after eruption, respectively, yielding an average SSS duration of 11.83 ± 1.56 days.

The soft X-ray flux is variable during the SSS rise and peak phases. Notably, multiple dips in the count rate are evident in the XRT light curves of 2017 to 2024 eruptions, one around days 6–8 and a more significant one around days 10–11. These dips are clearly visible in the SXT light curves of the 2020 and 2021 eruptions (Figure 4.9). Similar variability during the SSS phase was previously reported by Darnley et al. (2016) and Henze et al. (2018f), though the origin of these fluctuations remains unclear. High-cadence monitoring will be essential to investigate their nature. We also highlight the unusually faint and short-lived SSS phase during the 2016 eruption, which is readily distinguishable in Figure 4.8.

Previous X-ray studies of M31 novae (Henze et al. 2010, 2011, 2014b) have shown a correlation between the ejecta expansion velocity and the SSS turn-on time. Using

the relation from Henze et al. (2014b), we estimate the ejected mass from the turn-on time (∼5 days) and the expansion velocity (∼2000 ± 200 km s^{-1}) during this phase, yielding an ejecta mass range of $4.2 \times 10^{-8} < M_{\rm ej,H}/M_{\odot} < 1.02 \times 10^{-7}$. This is slightly higher than the mass inferred from optical spectral modelling (see §4.6.2), but remains below the estimated mass accreted annually. These results are comparable with the H ejecta mass of $(2.6 \pm 0.4) \times 10^{-8} M_{\odot}$ reported for the 2014 eruption (Henze et al. 2015b) as well for subsequent outbursts till 2016 (Henze et al. 2018f).

4.5.2 Spectroscopy

To enhance the SNR, we extracted XRT spectra by combining data from two consecutive days for 2017-2022 eruptions. The hydrogen column density was fixed at 1.4×10^{21} cm^{-2} (Darnley et al. 2016), while the blackbody temperature and normalization were left as free parameters to obtain the best-fit values. The temporal evolution of the SSS temperature across the 2017–2022 eruptions is shown in Figure 4.11. Both the flux and temperature peak between 10–14 days post-eruption, indicating a strong correlation between the two. During the 2020 eruption, we observe a fluctuation in temperature near the maximum, consistent with similar behaviour reported by Darnley et al. (2016). This fluctuation is not clearly seen in other eruptions, likely due to the merged nature of the data from adjacent days, which may smooth out short-timescale variations.

As discussed in the previous section, the SSS rise is characterised by significant variability, whereas the decline is more gradual and uniform. The temperature evolution (Figure 4.11) also reflects this asymmetry, suggesting distinct physical processes driving the rise and fall. The increasing flux and temperature during the rise phase are likely due to the thinning of the ejecta, allowing deeper, hotter regions near the WD surface to become visible. In contrast, the decline corresponds

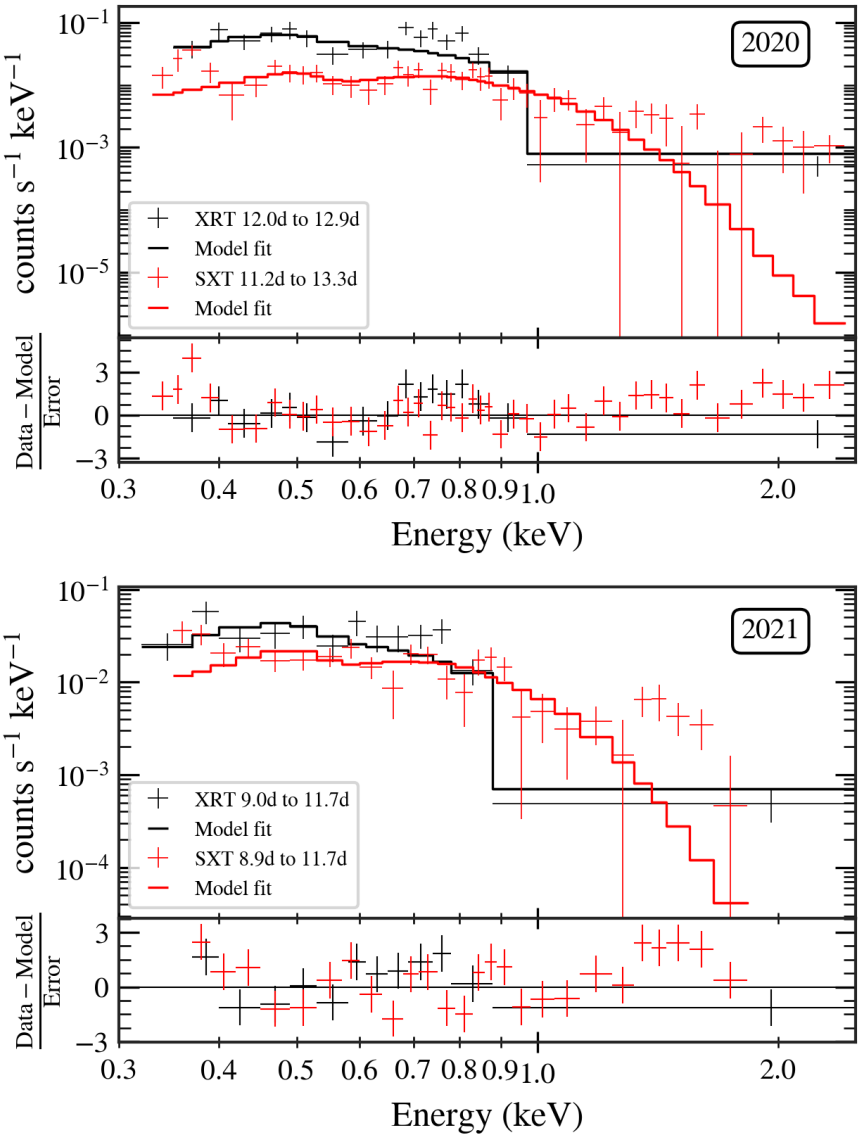

FIGURE 4.10: SXT and XRT spectra of the SSS phase during the 2020 and 2021 eruptions of M31N 2008-12a.

to the termination of residual nuclear burning after the circumstellar material has dissipated.

Figure 4.10 shows the X-ray spectra extracted from the merged SXT data, along with contemporaneous XRT spectra obtained by combining two-day snapshots. To reduce background contamination in the SXT data, owing to its broader PSF, we restrict the energy range to below 2.5 keV. Due to the supersoft nature of the

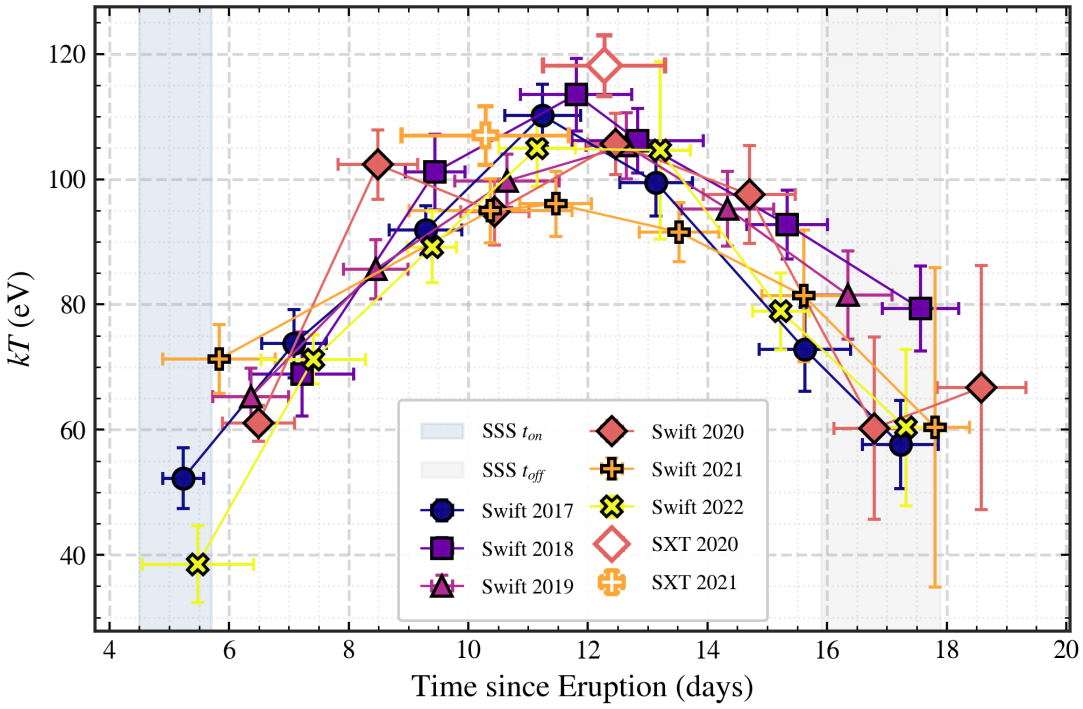

FIGURE 4.11: Evolution of temperature during the SSS phase from X-ray data.

source, the flux drops significantly above 1 keV. A faint hard X-ray tail (above 1.5 keV) is present in the SXT spectra, though its origin remains uncertain because of low SNR.

The best-fit blackbody temperatures derived from the SXT data are slightly higher than those obtained from XRT at comparable epochs (Figure 4.11). For the 2020 eruption, the modelled flux in the 0.3–2.0 keV range agrees well between the two instruments. However, for the 2021 eruption, the SXT flux is higher than that of the XRT (Figure 4.10). This discrepancy likely arises from the rapid flux and temperature variability inherent to the SSS phase in recurrent novae, combined with the non-overlapping observation times of XRT and SXT.

4.6 Discussion

4.6.1 Light curve modelling

4.6.1.1 Optical and UV

To investigate the temporal evolution of the light curves, we segmented them into three distinct phases, each corresponding to a characteristic decline rate. This analysis was carried out using the $uvw2$, g', r', and i' filters. The eruption epochs listed in Table 4.1 serve as reference points, and all subsequent timings are measured in days relative to each eruption's reference date. The three phases are defined as follows:

1. **Rise to peak:** from eruption to approximately day 1.5.
2. **Initial steep decline:** from the time of peak brightness ($t_{\max}$) to day 3.5.
3. **Slow decline:** from day 3.5 onwards.

Thanks to the dense coverage in the $uvw2$ band, we observed a further flattening in the decline rate beyond day 8. Hence, for $uvw2$, the final phase was further subdivided. A similar four-phase framework was previously adopted by Darnley et al. (2016) for earlier eruptions.

We first constructed composite light curve models using the data from the 2017–2022 eruptions and derived the parameters for each phase, as presented in Table 4.4. We then incorporated archival data from the 2013–2015 eruptions to build a unified model spanning 2013–2022. Data from the g' band remained limited due to its infrequent use prior to 2016. The 2016 eruption, which showed notable deviations,

particularly in the UV, was excluded from the model and is marked separately in Figure 4.12.

TABLE 4.4: Multi-eruption light curve model parameters of M31N 2008-12a

Filter	t^{a}_{max} (days)	m_{max} (AB)	t_2 (days)	t_3 (days)	Decline Rates (mag day^{-1}) t_{max} to 3.5	3.5 to ~ 8	> 8
			2017 – 2022				
uvw2	0.66 ± 0.26	18.82 ± 0.30	4.41 ± 0.51	14.15 ± 0.41	0.93 ± 0.03	0.17 ± 0.02	0.09 ± 0.01
g'	0.86 ± 0.04	18.27 ± 0.16	2.13 ± 0.04	···	0.90 ± 0.02	···	···
r'	0.86 ± 0.09	18.21 ± 0.27	2.37 ± 0.05	5.87 ± 5.61	0.88 ± 0.02	0.19 ± 0.18	···
i'	0.88 ± 0.12	18.30 ± 0.62	3.26 ± 0.20	···	0.56 ± 0.04	···	···
			2013 – 2022 (Excluding 2016)				
uvw2	0.66 ± 0.26	18.82 ± 0.30	4.41 ± 0.51	14.15 ± 0.41	0.93 ± 0.03	0.17 ± 0.02	0.09 ± 0.01
g'	0.86 ± 0.04	18.27 ± 0.16	2.13 ± 0.04	···	0.90 ± 0.02	···	···
r'	0.97 ± 0.02	18.44 ± 0.03	2.29 ± 0.01	6.44 ± 0.08	0.97 ± 0.01	0.21 ± 0.02	···
i'	1.14 ± 0.06	18.63 ± 0.10	2.42 ± 0.02	10.83 ± 0.32	0.88 ± 0.01	0.10 ± 0.01	···

[a]Days since eruption

The final composite light curves are shown in Figure 4.12, with corresponding parameters summarized in Table 4.4. We also applied GP regression to each band's full light curve to capture variability. The resulting fits, along with their 3σ confidence intervals, are plotted in blue.

The rise to peak

The rise to peak brightness was modelled using a quadratic function to account for both the ascent and the immediate decline post-maximum. In the *uvw2* band, data during this phase were limited, allowing only partial modelling, whereas the optical bands had better coverage. The *uvw2* and g' bands exhibit a smooth rise and decline, while the r' and i' bands display a distinct "cusp" just before reaching the peak.

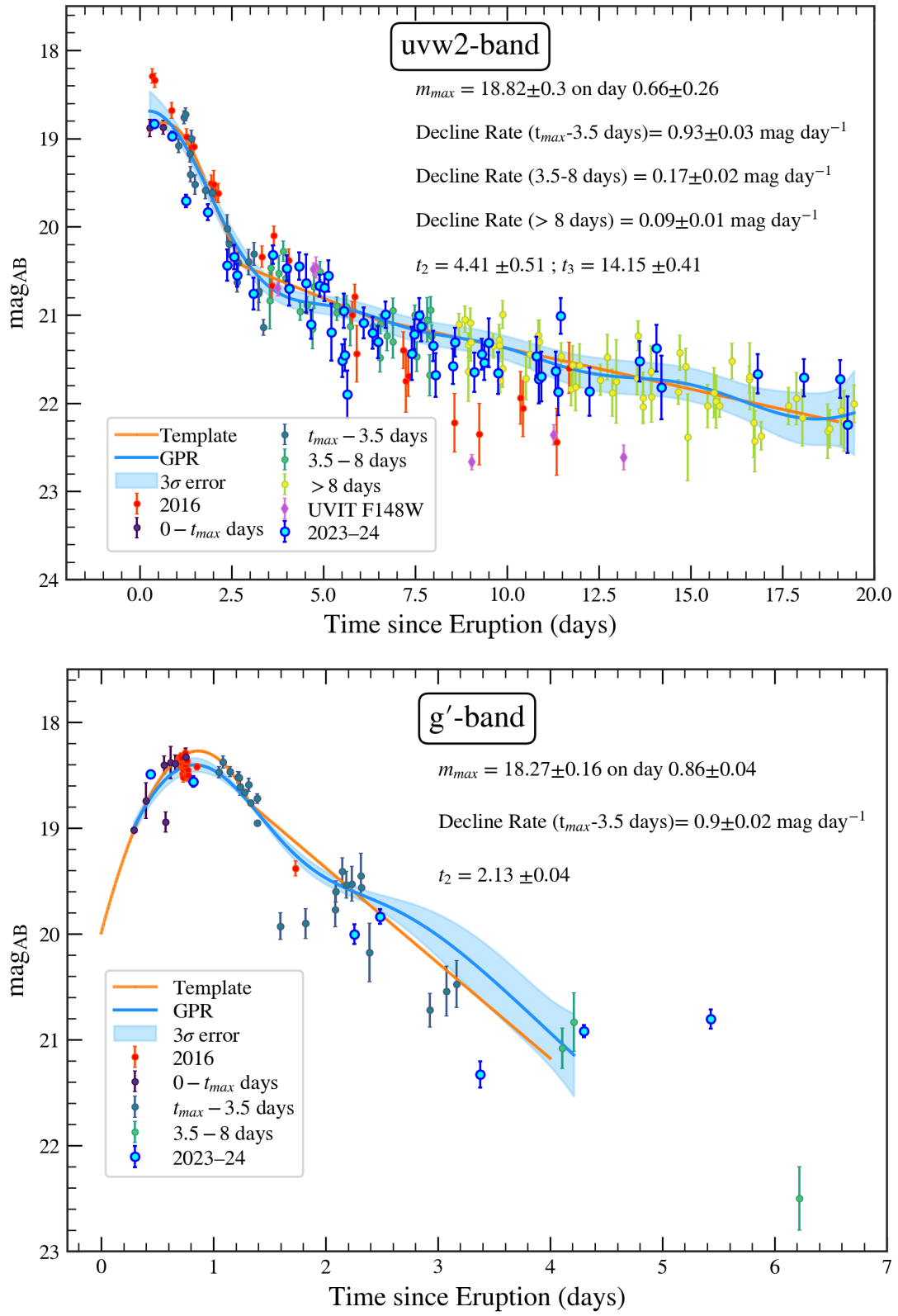

FIGURE 4.12: Light curve characteristics of the eruptions from 2013 to 2022 (excluding 2016) in the *uvw2* and g' bands. The 2016 data, identified as outliers, are highlighted in red. The light curve template, shown in orange, was constructed by combining the fitted segments across different phases for each filter. The GP mean model, along with the associated 3σ uncertainty, is plotted in blue. Overlaid on these templates are the light curves from the recent 2023 and 2024 eruptions for comparison.

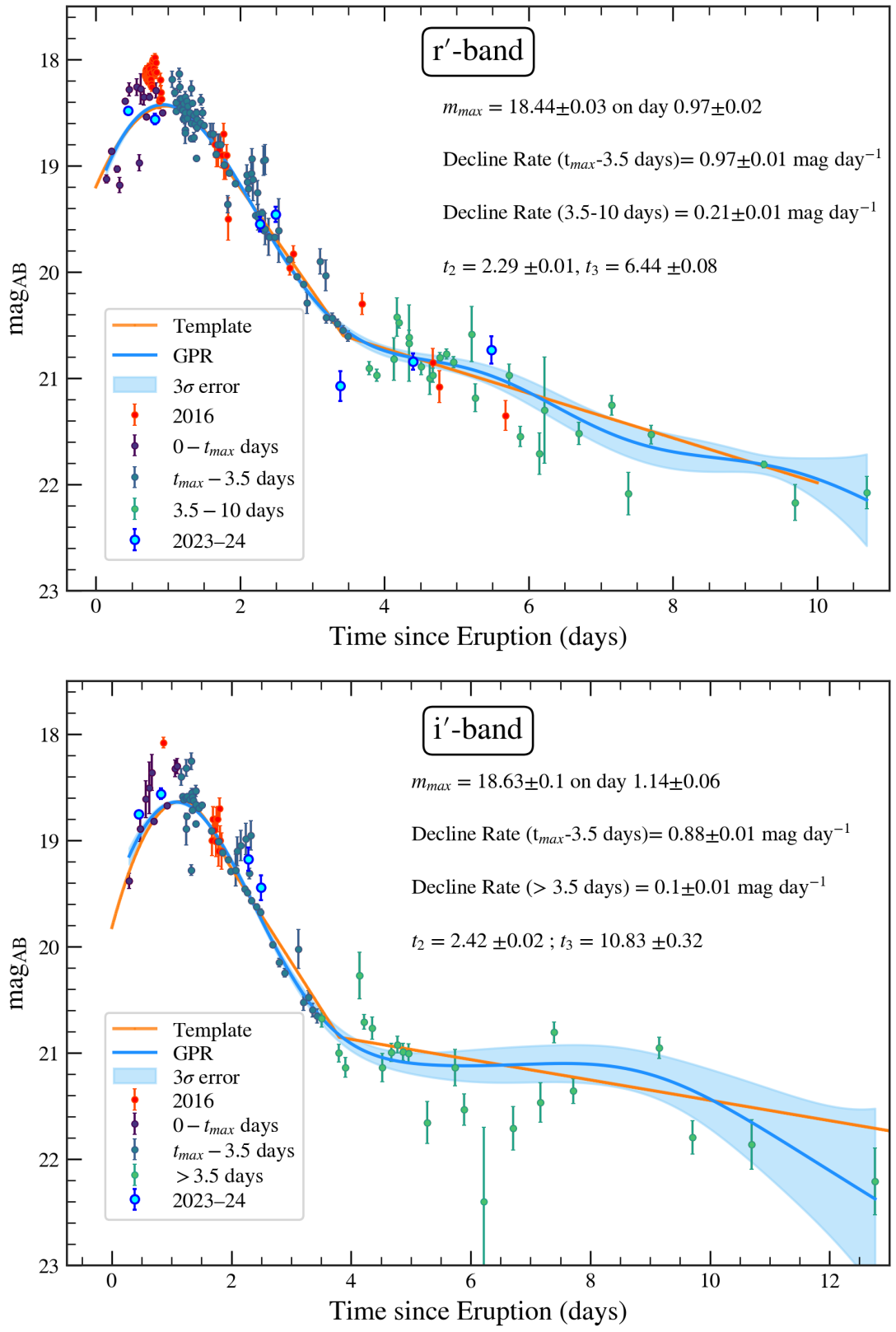

FIGURE 4.12: (continued) Same as previous but for r', and i' bands.

When combining data from 2013–2015 with that of 2017–2022, this cusp feature becomes more apparent, especially in the r' and i' bands. It is clearly visible in the 2021 and 2022 data, and tentatively present in 2018 and earlier eruptions such as 2017 (V) and 2019 (R). These findings suggest that the cusp is a recurrent feature rather than an anomaly unique to 2016, as previously speculated by Henze et al. (2018f). Sparse sampling during the rise in earlier eruptions likely caused this feature to be missed. We therefore propose that the cusp is intrinsic to the eruption and recommend early-time, high-cadence, multi-band observations in future eruptions for confirmation.

Peak times and magnitudes were derived from quadratic fits around the maxima and are listed in Table 4.4.

The initial steep decline

Following the peak, the light curves enter a phase of rapid decline, modelled as a linear decay from $t_{\rm max}$ to day 3.5. The decline rate in the $uvw2$ band is 0.93 mag day^{-1}, steeper than the $uvw1$ decline of 0.78 mag day^{-1} reported by Henze et al. (2018f). For the 2017–2022 eruptions, we found that g' declined slightly faster than r' (0.90 vs 0.88 mag day^{-1}), but when including the 2013–2015 data, r' showed a steeper drop (0.97 vs 0.90 mag day^{-1}).

These results are broadly consistent with prior findings by Darnley et al. (2016), who noted the fastest decline in the V band (1.21 mag day^{-1}), followed by B (0.99) and r' (0.97). The t_2 values derived from these decline rates are provided in Table 4.4.

Recent data of 2023 and 2024 eruptions follow the usual trend in all the filters during this phase.

Slow Decline

From day 3.5 onward, the light curves enter a slower decay phase, modelled using a linear fit. This phase overlaps with the SSS phase and includes a plateau, particularly evident in the UV. The combined data from all eruptions since 2013 provided sufficient coverage in all bands except g' to characterise this stage.

The decline rates during this phase are significantly lower (Table 4.4). While the r' band shows minor fluctuations, the $uvw2$ band displays variability. The t_3 times were measured to be 6.17 days in r', 10.83 days in i', and 14.15 days in $uvw2$.

This flattening of the light curve during SSS phase has been seen in other RNe as well. In the $uvw2$ band, we observed an additional drop in the decline rate beyond day 8, for which we modelled a separate slope. Optical data beyond day 8 is sparse, though some i' band points are available. Notably, an excess of 0.2–0.4 mag is seen in i' around day 8. This bump is captured by the GP regression and shown in blue in Figure 4.12. Recent deep observations (2023 data) in the g' and r' bands also suggest a brightening pattern during day 6 (Figure 4.12), which also marks he onset of SSS. The u' and R lightcurves in figure 4.4 are also consistent with this trend.

The light curves during this phase exhibit a long-term downward trend superimposed with short-term fluctuations, especially in $uvw2$, discussed further in §4.6.4. As the SSS phase ends (post day 18), we detect a brief UV re-brightening, followed by a decline to quiescence.

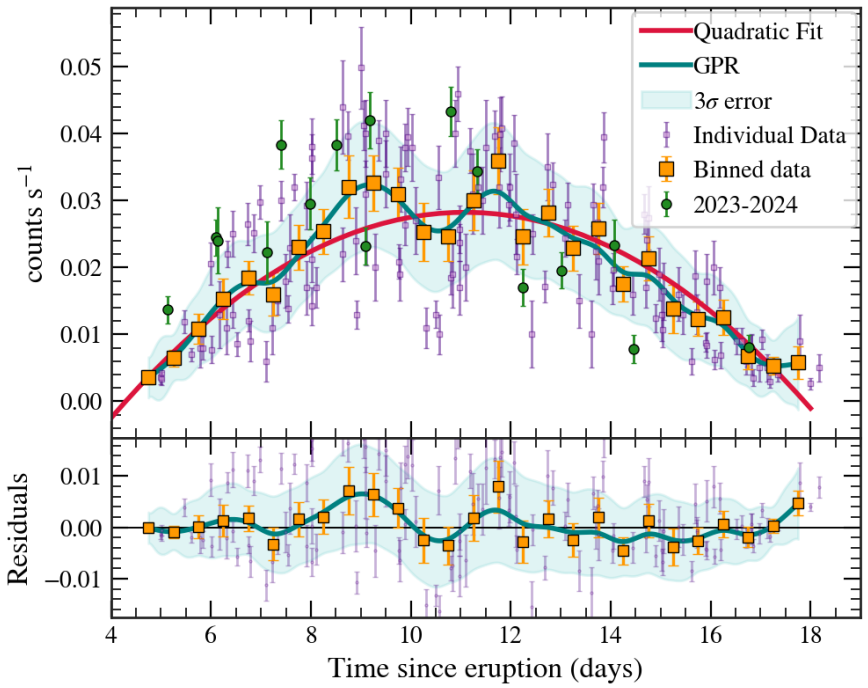

FIGURE 4.13: Combined XRT data of the SSS phase from the 2013–2022 eruptions (excluding 2016). Data points binned at 0.5-day intervals are overplotted, along with a quadratic fit shown in black. The GP regression model and its associated 3σ confidence region are displayed in blue. The residuals highlighting deviations from the simple quadratic fit are shown below. Data from the 2023 and 2024 eruptions are overlaid for comparison.

4.6.1.2 X-ray

To characterise the overall SSS evolution, we fit a simple quadratic function to the combined soft X-ray light curves from 2013–2022, excluding the atypical 2016 event due to its anomalous SSS behaviour. Figure 4.13 shows both individual and binned data sets along with the fitted model. Clear deviations from the quadratic trend are seen, particularly a peak near days 9–10, another between 11–12 days, and dips around days 7–8 and 10–11. These features appear in both binned and unbinned data, suggesting that the underlying variability lasts longer than half a day. The flux dip and rebound around days 10–11 may be a recurrent feature of the SSS phase in this nova. Beyond day 13, the decline in X-ray flux becomes smoother.

4.6.2 Spectral Modelling

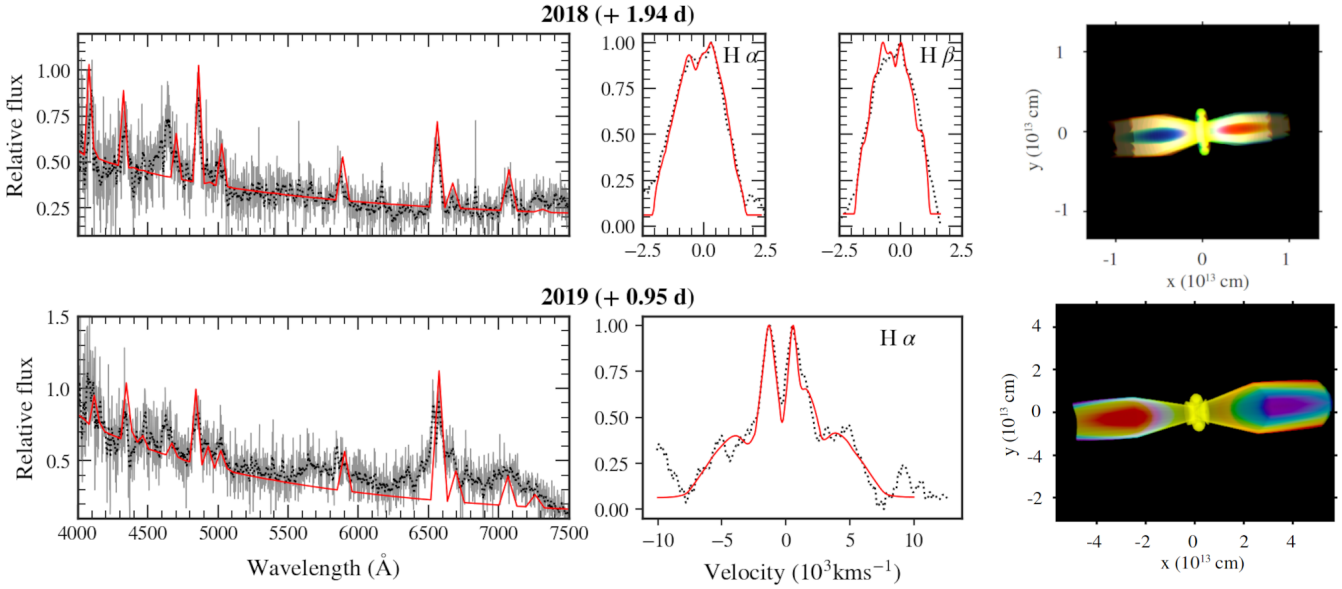

FIGURE 4.14: **Top (from left):** Best-fit `Cloudy` synthetic spectrum (red) overlaid on the observed (grey) and smoothed (black dotted) spectra from the 2018 eruption. Best-fit Hα and Hβ velocity profiles (red) are shown against the observed profiles (dotted lines). The rightmost panel shows the ejecta morphology derived using `Shape`, based on the Hα and Hβ line profiles. The X-axis corresponds to the line-of-sight direction, while the Y-axis is perpendicular to both the line of sight and the plane of the sky. Color coding represents radial velocities from 2500 km s^{-1} (red, receding) to -2500 km s^{-1} (violet, approaching). **Bottom (from left):** Same as the top row, but for the 2019 eruption. Velocity ranges in the morphological panel span from 6000 km s^{-1} (red) to -6000 km s^{-1} (violet). Note the difference in scale between the ejecta morphologies for 2018 and 2019.

To investigate the physical conditions within the nova ejecta, we employed the spectral synthesis code `Cloudy` (v17.02; Ferland et al. 2017b) to construct one-dimensional (1D) models, following the methodology described in Pavana (2020). Spectra from 2018 Nov 8.6 UT (+1.94 days) and 2019 Nov 7.6 UT (+0.95 days), which had better SNR than others, were selected for modelling. The synthetic spectra, generated using a two-component (diffuse + clump) model, are shown in the top-left and bottom-left panels of Figure 4.14 for 2018 and 2019, respectively.

For the 2018 spectrum, the central ionising source was characterised by an effective temperature of 1.06×10^5 K and a luminosity of 10^{37} erg s^{-1}. A clumpy component with a density of 10^{11} cm^{-3} and a diffuse component with a density of 10^{10} cm^{-3} were used to reproduce the observed emission lines. From the best-fit model, the ejected mass and helium abundance were estimated to be 7.21×10^{-8} M$_\odot$ and 2.47 ± 0.11 He$_\odot$, respectively, using the prescriptions from Pavana et al. (2019) and references therein.

The 2019 spectrum required a clump density of 2.24×10^{10} cm^{-3} and a diffuse density of 1.26×10^8 cm^{-3} to match the observations. The corresponding effective temperature and luminosity of the ionising source were 7.20×10^4 K and 10^{37} erg s^{-1}. The best-fit ejected mass and helium abundance were 1.3×10^{-8} M$_\odot$ and 3.09 ± 0.18 He$_\odot$, respectively. These estimates are consistent with those derived from X-ray observations (see §4.5) and with the values reported for the 2015 eruption by Darnley et al. (2016). Notably, enhanced helium abundances have also been reported in other recurrent novae, including RS Oph, V3890 Sgr, T Pyx (Anupama & Pavana 2020 and references therein), and V745 Sco (Mondal et al. 2020).

Initial attempts with the two-component model yielded high χ^2 values, indicating a poor fit. The observed spectrum contains prominent N II emission lines, which became adequately reproduced only after introducing a third, low-density diffuse component. This suggests that the He and N II lines originate in physically distinct regions within the ejecta. However, due to the limited SNR of these extragalactic spectra, extending the model to three components was deemed beyond the scope of this study. We look forward to future high-SNR spectroscopic observations to better constrain such models.

To understand the kinematics of the ejecta, we modelled the Hα line profiles observed in the 2018 and 2019 eruptions using the morpho-kinematic modelling

software `Shape` (Steffen et al. 2011), also incorporating the Hβ line for 2018. The modelling followed the approach of Pavana (2020).

For the 2018 eruption, the best-fit model consists of an asymmetric bipolar structure with extended bipolar lobes and an equatorial ring, as shown in Figure 4.14. The inferred inclination angle was $80.75° \pm 1.21°$. The outer bipolar lobes extended to 4.52×10^{12} cm from the centre, while the central bipolar cones (with an opening angle of $\sim 91°$) extended up to 3.62×10^{11} cm. The inner radius of the equatorial ring and the radius of the bipolar cones were 1.27×10^{11} cm and 5.42×10^{11} cm, respectively.

A similar structure was found for the 2019 eruption, with a best-fit inclination angle of $79.60° \pm 1.45°$. The extended bipolar lobes reached 5.58×10^{13} cm, and the central cones (with a narrower opening angle of $\sim 40°$) extended to 6.16×10^{12} cm. The inner radius of the equatorial ring and the cone radii were 4.12×10^{12} cm and 5.27×10^{12} cm, respectively. It is worth noting that the He I (6678 Å) emission line, blended with Hα, appears to originate from the inner bipolar cone region.

The structural components—extended bipolar lobes, equatorial ring, and central cones—are clearly discernible in the rendered models (Figure 4.14). The extended bipolar geometry suggests the presence of fast polar outflows, which likely contribute to the broad, high-velocity components of the hydrogen Balmer lines.

The best-fit morpho-kinematic model using `Shape` yields a high inclination of $\sim 80°$, suggesting a near edge-on orientation for the ejecta shell. This result appears to be at odds with previous literature suggesting a lower inclination (pole-on) orientation. However, such discrepancies can arise in `Shape` analyses due to the degeneracy between inclination and the intrinsic expansion velocity of the bipolar lobes.

4.6.3 Signature of jets

The origin of the cusp near maximum in the light curves has been attributed to multiple mechanisms. These include shocks resulting from a secondary ejection (Kato et al. 2009), polar outflows aligned along the line of sight, or interactions between the ejecta and the donor star (Darnley et al. 2018b). Observational signatures such as broad-winged emission features support the existence of a high-velocity component within the ejecta. Our `Shape` modelling of the Hα line profiles (and Hβ for the 2018 eruption) also reproduces fast-moving polar ejecta. Although Darnley et al. (2017c) suggested the presence of such jets based on *HST* data, they refrained from fully confirming them. The combined photometric, spectroscopic, and Hα profile modelling presented here provides stronger evidence for polar jets at high inclinations. However, the inclination angle in this system has been debated. Darnley et al. (2016) provided arguments for both high and low inclination while Darnley et al. (2017c) found evidences for low inclinations. Our `Shape` analysis favours a high inclination for this system. This discrepancy can be resolved with future high-resolution spectroscopy.

Bipolar ejecta structures, possibly linked to jets, have also been observed in RS Oph through optical imaging and spectroscopic modelling (Bode et al. 2007; Ribeiro et al. 2009), with subsequent radio confirmations of jets (O'Brien et al. 2006; Rupen et al. 2008; Sokoloski et al. 2008; Munari et al. 2022). High-velocity components in emission lines, indicative of jet activity, have also been identified in systems such as V1494 Aql (Iijima & Esenoglu 2003), U Sco (Kato & Hachisu 2003b), V6568 Sgr, and YZ Ret (McLoughlin et al. 2021a). As noted by McLoughlin et al. (2021b), jets tend to be associated with fast novae, which in turn are typically linked to massive WD characteristics that M31N 2008-12a exhibits prominently. One plausible jet formation mechanism involves bipolar winds launched during the nova eruption, funnelled through an asymmetric medium shaped by prior outbursts. Additionally, magnetic fields near the WD and accretion disc can

aid in collimating winds perpendicular to the disc plane (Ogilvie & Livio 2001). M31N 2008-12a is known to consist of a luminous accretion disc (Darnley et al. 2017b), and such discs are capable of driving supersonic outflows that may evolve into jets (Fukue 2002).

4.6.4 UV – X-ray anti-correlation

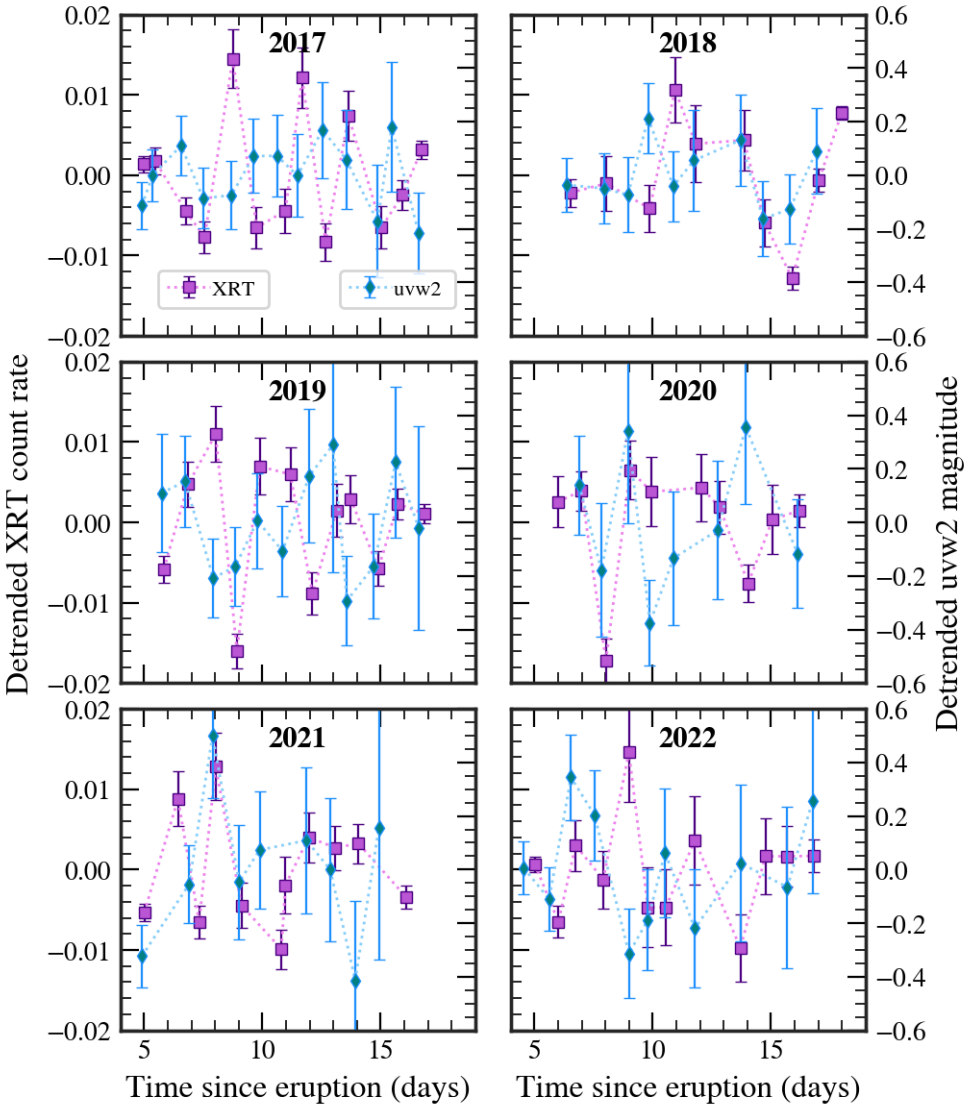

FIGURE 4.15: Detrended *Swift uvw2* and XRT light curves during the SSS phase for the 2017–2022 eruptions.

The $uvw2$ light curve for the 2016 eruption appeared significantly fainter and shorter in duration compared to those from the 2017–2022 eruptions during the SSS phase. A similar behaviour was reported for the soft X-rays by Henze et al. (2018f), who attributed it to a lower accretion rate preceding the 2016 eruption. At the time, they could not comment on the UV behaviour due to the absence of a $uvw2$ template. This motivated our investigation into the correlation between UV and soft X-ray emission during the SSS phase.

Since the UV and X-ray light curves exhibit different temporal behaviours during the SSS phase, we applied a detrending procedure before comparison. The $uvw2$ light curves were linearly detrended to account for their steady decline, while the XRT light curves were fit with a quadratic function to model their rise and fall. The detrended light curves for eruptions from 2017 to 2022 are presented in Figure 4.15.

In 2017, we observed a pronounced anti-correlation between UV and X-ray fluxes from day 7.5 to 13, with a Pearson correlation coefficient (r) of -0.76. The 2018 eruption showed an even stronger anti-correlation ($r = -0.86$) over a shorter period between day 8.5 and 11.5. In contrast, no significant correlation was observed in 2019. The 2020 and 2022 eruptions exhibited strong anti-correlations from day 9.5 to 14.5 with $r = -0.79$ and -0.68, respectively. In 2021, a mild anti-correlation ($r = -0.38$) was observed between day 9 and 14, stronger than in 2019, but weaker than the other years.

Overall, this recurring anti-correlation is most prominent during days 8 to 14 post-eruption, corresponding to the peak of the SSS phase. Although most novae show no UV–X-ray correlation (Page et al. 2022b), anti-correlations have been noted before. For example, Ness et al. (2009) reported a similar trend in V458 Vul between UV and hard X-rays (0.6–10 keV) just before the SSS onset, suggesting a common origin for both emissions. In HV Cet, Beardmore et al. (2012a) found UV

and X-ray variations to be in phase, interpreted as orbital modulation. V603 Aql also displayed correlated UV–X-ray behaviour, attributed to X-ray illumination of UV-emitting regions (Borczyk et al. 2003).

In our case, since the SSS-phase soft X-rays originate from nuclear burning on the WD's surface, the observed anti-correlation suggests that the UV emission likely originates from a region close to the WD as well. This is consistent with a scenario in which the accretion disc, or a portion of it, survives each eruption (Darnley et al. 2017c,b), continuing to emit in the UV. The variability observed in the detrended UV and X-ray light curves could arise from the gradual reformation of this partial disc. A transient, unstable, or precessing ("wobbly") nascent accretion disc may also explain the observed fluctuations.

4.6.5 Decreasing accretion rate

In § 4.2, we reported an increasing trend in the recurrence period over time. A gradual lengthening of the recurrence interval typically suggests a decrease in either the accretion rate or the WD mass (Hillman et al. 2016a; Wang 2018a). According to light curve modelling by Kato et al. (2015), the WD in M31N 2008-12a is highly massive ($\sim 1.38\ M_{\odot}$), with an accretion rate of $\sim 1.3 \times 10^{-7}\ M_{\odot}\ \mathrm{yr}^{-1}$. In contrast, Darnley et al. (2017b) modelled the accretion disc in quiescence using *HST* observations and inferred a higher accretion rate of $(0.6\text{–}1.4) \times 10^{-6}\ M_{\odot}\ \mathrm{yr}^{-1}$, assuming 50% accretion efficiency.

Meanwhile, the ejecta masses estimated per eruption (see § 4.5 and § 4.6.2) are of the order $\sim 10^{-8}\ M_{\odot}$, significantly lower than the accreted mass between eruptions. This implies that the WD experiences a net mass gain over time. The absence of Ne lines in the optical spectra is consistent with a CO WD, though it does not rule out an ONe composition. While a single spectrum might miss a line due to ionization

effects, the persistent absence suggests a CO classification. CO WDs can only reach masses $\gtrsim 1.36\ M_{\odot}$ through sustained accretion. These results collectively argue against the possibility that the increasing recurrence period arises from a decreasing WD mass.

Instead, we propose that the recurrence time is lengthening due to a gradual decline in the accretion rate (see Figure 4.2), leading to a longer timescale for reaching the critical conditions necessary for thermonuclear runaway. Several mechanisms could contribute to this decline:

1. Magnetic activity or starspots on the donor star may inhibit mass transfer (Henze et al. 2018f).

2. The donor may be slowly depleting its mass reservoir after sustaining prolonged mass transfer to power repeated hydrogen flashes over Myr timescales (Darnley et al. 2019d).

3. Orbital evolution or dynamical changes in the system may modulate accretion rates, especially in an extreme system like M31N 2008-12a.

4. The extent of accretion disc destruction during eruptions affects the recovery time of accretion. A more severely disrupted disc would require longer to reform, delaying the resumption of steady accretion.

5. The presence of a tertiary component could perturb the binary orbit, influencing the accretion process. Triple systems are known to drive unusual binary evolution pathways, as in the case of T Pyx (Knigge et al. 2022).

4.7 Summary

M31N 2008-12a is an extraordinary recurrent nova in M31, notable for its annual eruptions and remarkable consistency across optical, UV, and X-ray observations. Analysis of eruptions from 2017 to 2024 reveals a gradual increase in the recurrence period, now averaging about 364 days, possibly reflecting changes in the accretion rate onto a highly massive WD ($M_{\rm WD} \gtrsim 1.36\ M_{\odot}$). The optical and UV light curves show a rapid rise, fast decline, and a plateau phase that coincides with the SSS phase, while spectroscopic data indicate high-velocity ejecta and a structured, possibly bipolar, outflow. The SSS phase typically begins around five days after eruption and lasts about twelve days, with notable variability and flux dips observed in the X-ray light curves.

Theoretical modelling and observational constraints suggest that the white dwarf in M31N 2008-12a is growing in mass and may eventually reach the Chandrasekhar limit, making it a strong candidate for a future Type Ia supernova. The system's extreme properties: ultra-short recurrence time, high accretion rate, and consistent multi-wavelength behaviour, provide valuable insights into nova physics and WD evolution. Continued monitoring and high-cadence multi-wavelength observations will be crucial for understanding the long-term evolution of this unique system and its significance as a potential supernova progenitor.

Chapter 5

Rapidly Recurring Novae

> "Coming back to where you started is not the same as never leaving."
>
> — Terry Pratchett

The work presented in this chapter is based on the publication: Basu et al. (2025a), 'Survival of the accretion disk: UV–X-ray case study of the 2024 eruption of the LMC Recurrent Nova 1968-12a', 2025, ApJ, 994, 229.

5.1 Introduction

Rapidly recurring novae (RRNe) are a distinct subclass within the broader category of recurrent novae (RN), which are systems known to undergo multiple nova outbursts. RRNe are specifically characterized by extremely short recurrence intervals, typically less than a decade, placing them among the fastest-recurring nova systems known (Darnley & Henze 2020). As with all novae, their eruptions are

powered by a TNR on the surface of an accreting WD within a close binary system. However, to sustain such rapid recurrence, RRNe require a finely tuned combination of parameters: a very massive WD, often close to the Chandrasekhar limit ($M_{WD} > 1.3\ M_{\odot}$), and a relatively high mass accretion rate ($\dot{M} > 10^{-8}\ M_{\odot} yr^{-1}$) from the companion star (Darnley et al. 2012).

This extreme combination not only drives frequent eruptions but also links RRNe to the so-called 'faint–fast' subgroup of novae, which occupy the lower-left quadrant of the Maximum Magnitude–Rate of Decline (MMRD) relation (Yaron et al. 2005; Kasliwal et al. 2011). These systems are not intrinsically 'faint'. They appear faint in the optical because, unlike classical novae that peak in the optical, much of their radiative energy is emitted in the FUV or even EUV (Darnley et al. 2016). This characteristic SED implies that many Galactic RRNe may have been missed in the past or misclassified as other classes of transients, such as dwarf novae or flare stars, especially before the detailed monitoring of the prototype M31N 2008-12a (Darnley et al. 2017b,c; Basu et al. 2024d).

The M31N 2008-12a system is the best example of this class of novae. Its progenitor comprises a luminous accretion disk and a low-luminosity red giant donor star (Darnley et al. 2014, 2017b). Its frequent eruptions have altered its local interstellar environment, leading to the formation of a vast, expanding "super-remnant" (Darnley et al. 2019d). This remnant is composed of a persistently shock-heated medium where ejecta from successive eruptions collide, maintaining elevated temperatures and ionisation states.

M31N 2008-12a also exhibits variability in its SSS phase durations, suggesting possible eruption-to-eruption changes in the accretion disk's structure and time of reformation. The extent of damage to the accretion disk post-eruption in RNe remains debated. While it may be completely disrupted in some events, partial survival is also plausible. The extent of damage to the disk remains hidden within

the optically thick ejecta. As the ejecta expand and become optically thin, the inner disk may gradually become visible. The time to the next eruption is then dictated by a combination of the WD mass, accretion rate, and donor star characteristics (Shara et al. 2018; Hillman et al. 2020).

The essential role of massive WDs and high accretion rates in facilitating rapid recurrence has long been anticipated. Early theoretical models by Starrfield et al. (1975, 2016) and Kato et al. (2014b) predicted that short recurrence periods necessitate high WD masses. These predictions have since been validated by observations, most notably by Shara et al. (2018), who demonstrated that systems exhibiting rapid recurrence invariably involve massive WDs. A strong empirical correlation now exists: the shorter the recurrence time, the more massive the WD.

RRNe systems with carbon-oxygen (CO) WDs lack a significant amount of α-elements and are considered promising candidates for Type Ia supernova progenitors, especially under the single-degenerate scenario (Hillman et al. 2016b; Wang 2018b).

5.2 LMCN 1968-12a

5.2.1 Introduction

The recurrent nova LMCN 1968-12a, located in the Large Magellanic Cloud (LMC), was the first extragalactic RN to be discovered, with its first eruption recorded in 1968 (see Figure 5.1). Since then, it has undergone multiple eruptions (see Table 5.1). Recent observations indicate a recurrence period of approximately 4.3 years, shorter than that of any known Galactic RN and exceeded only by two extragalactic systems: M31N 2008-12a (Darnley et al. 2016; Henze et al. 2018e; Basu

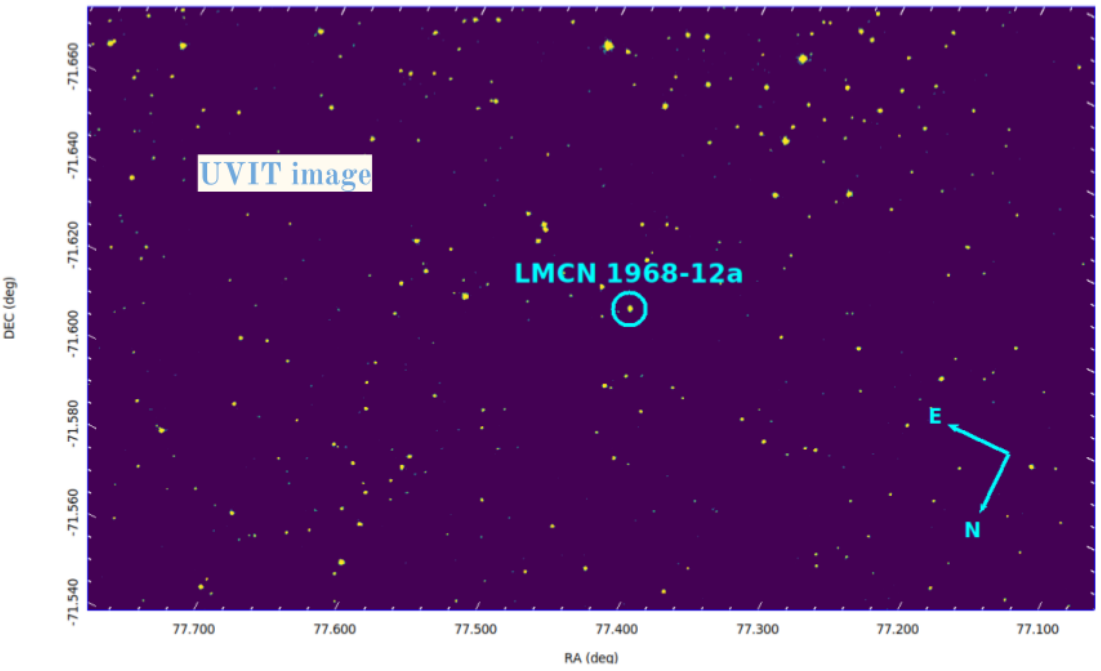

FIGURE 5.1: Location of the LMCN 1968-12a in LMC, captured by UVIT during its 2024 eruption.

et al. 2024d) and M31N 2017-01e (Shafter et al. 2022a, 2024b; Chamoli et al. 2025). LMCN 1968-12a therefore belongs to the class of RRNe associated with high-mass WDs (Darnley 2021). The previous study of this object has inferred a WD mass exceeding 1.3 $M_{\odot}$, an orbital period of 1.26 days, and an ejected mass comparable to the mass accreted between eruptions (Kuin et al. 2020). The most recent eruption of LMCN 1968-12a was detected on 2024 August 1.8 UT by the *Swift* observatory. The last pre-outburst detection was made on 2024 August 1.19 UT in the $UVW1$ filter, with a measured magnitude of 18.19 ± 0.09 mag (Darnley et al. 2024). The eruption time, estimated as the midpoint between these two epochs, is adopted as the reference time throughout this study (see Table 5.1).

5.2.2 Observations

The 2024 eruption of the recurrent nova LMCN 1968-12a was reported by Darnley et al. (2024), following a sudden optical brightening of more than 8 magnitudes

TABLE 5.1: List of all previous known eruptions of LMCN 1968-12a

Discovery (UT)	mag	filter	Eruption date (MJD)	Time since last eruption (days)	SSS t_{off} date (days)	References
1968 Dec 16.5	10.9	m_{pg}	40206.0 ± 1.5	···	···	(1)
⋮						
1990 Feb 14.1	11.2	m_{pv}	47936.1 ± ?	···	···	(2)
⋮						
2002 Oct 10	11.15 ± 0.02	V	52557.3 ± 1.0	···	···	(3)-(4)
⋮						
2010 Nov 21.2	11.7 ± 0.3	I	55521.2 ± 1.0	···	···	(5)
2016 Jan 21.2	11.5 ± 0.2	I	57407.4 ± 0.8	1886.2 ± 1.8	56.1	(4)
2020 May 06.7	13.99 ± 0.08	g	58971.9 ± 0.4	1564.5 ± 1.2	60	(6)-(7) *
2024 Aug 01.8	9.9 ± 0.1	uvm2	60523.5 ± 0.3	1551.6 ± 0.7	> 50	(8), this work

Notes: References - (1) Sievers (1970), (2) Liller (1990), (3) Pojmanski (2002), (4)Kuin et al. (2020), (5) Mróz et al. (2014), (6) Page et al. (2020b), (7) Schwarz et al. (2020), (8) Darnley et al. (2024)

over a timescale of approximately 15 hours. This dramatic rise was captured as part of *Swift*'s monthly monitoring program of the nova field. Prompt follow-up observations were triggered in both UV and X-ray bands using *AstroSat* and *Swift*, as detailed below.

5.2.2.1 Observations with *AstroSat*

Following the detection of the outburst, a ToO proposal was submitted for UV and X-ray observations with *AstroSat*. The first set of observations took place on 2024 August 15, approximately 14 days post-eruption. These consisted of two UVIT orbits: one using the F148W filter (∼180 s exposure) and one with F172M (∼760 s exposure). Concurrently, SXT observed the nova with an effective exposure time of 6600 s. A second ToO was submitted for deeper follow-up during the supersoft phase, leading to further observations on August 20–21. This included 16 UVIT orbits (totaling 12.6 ks of F148W exposure) and 23.2 ks of effective SXT exposure. The UVIT data was reduced as described in chapter 2. UV magnitudes were de-reddened using $E(B-V) = 0.07 \pm 0.01$, as estimated by Kuin et al. (2020).

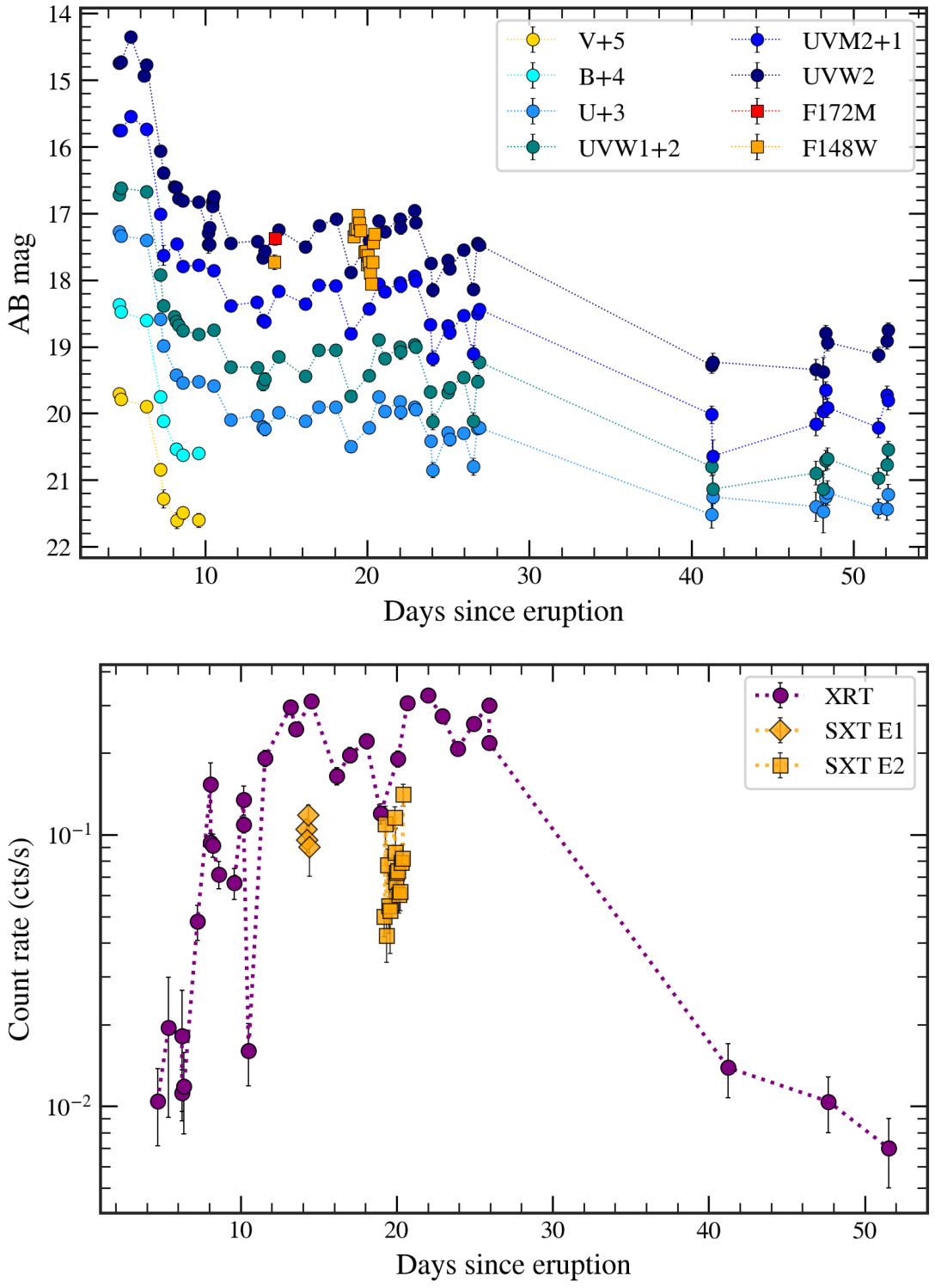

FIGURE 5.2: UV and X-ray light curves of LMCN 1968-12a during its 2024 eruption.

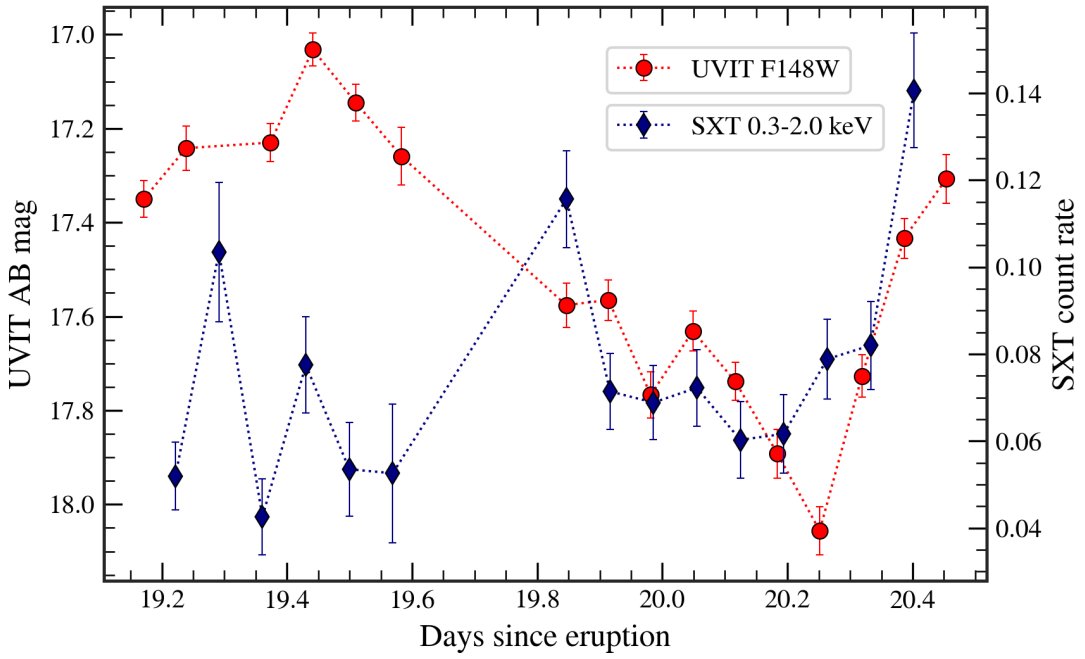

FIGURE 5.3: UVIT and SXT lightcurves obtained during the second epoch of *AstroSat* observations.

The X-ray imaging and spectroscopy methods described in Chapter 2 were used. A fixed hydrogen column density of $N_H = 1.8 \times 10^{21}$ cm^{-2} was assumed, which was estimated by Kuin et al. (2020) to be the extinction toward the source. The UV and X-ray light curves are presented in Figure 5.2. A zoomed-in view of the second epoch of *AstroSat* observations is shown in Figure 5.3.

5.2.2.2 Observations with *Swift*

Swift (Gehrels et al. 2004) has conducted monthly monitoring of the LMCN 1968-12a field, which led to the discovery of the 2024 outburst. Daily monitoring commenced on 2024 August 1 and continued through August 28, using both the UVOT (Roming et al. 2005) and the XRT (Burrows et al. 2005). Additional follow-up epochs were obtained on September 11, 18, and 22, after a brief observational gap. All Level 2 data were downloaded from the public *Swift* archive. UVOT observations were taken in the V, B, U, $UVW1$, $UVM2$, and $UVW2$ filters. The

V and B band coverage was limited to the first 10 days post-eruption, while full light curves in the other filters are shown in Figures 5.2.

XRT also simultaneously observed the source. Independent fits to the XRT spectra yielded temperature and column density values consistent with those derived from the SXT data, particularly for epochs later than 12 days post-eruption. Confidence intervals (68% and 90%) were computed using the `error` command in `xspec` and are shown in Figure 5.4.

All *AstroSat* and *Swift* data products used in this analysis are publicly available in GitHub[†].

5.3 Discussion

5.3.1 Lightcurves

Day 0 to 8: LMCN 1968-12a reached a peak brightness of 9.9 ± 0.1 mag in the $UVM2$ filter on 2024 August 1.83 UT (Darnley et al. 2024). The UV and optical light curves exhibit a steep decline over the first eight days following the eruption peak, as shown in Figure 5.2. The rate of decline is approximately 0.8 mag day^{-1} across all UVOT bands. Soft X-ray emission, indicative of the SSS phase, became detectable around day 5 and rose from the detection threshold ($\sim$0.014 counts s^{-1}) to over 0.05 counts s^{-1} in the XRT bands during this period (see Figure 5.2).

Day 8 to 24: During this phase, periodic modulations with a timescale of $\sim$1.3 days appear in all UV bands, consistent with the system's orbital period (Kuin et al. 2020). High-cadence UVIT observations around day 20 support this periodicity,

[†] https://github.com/judha-basu/LMCN_1968-12a

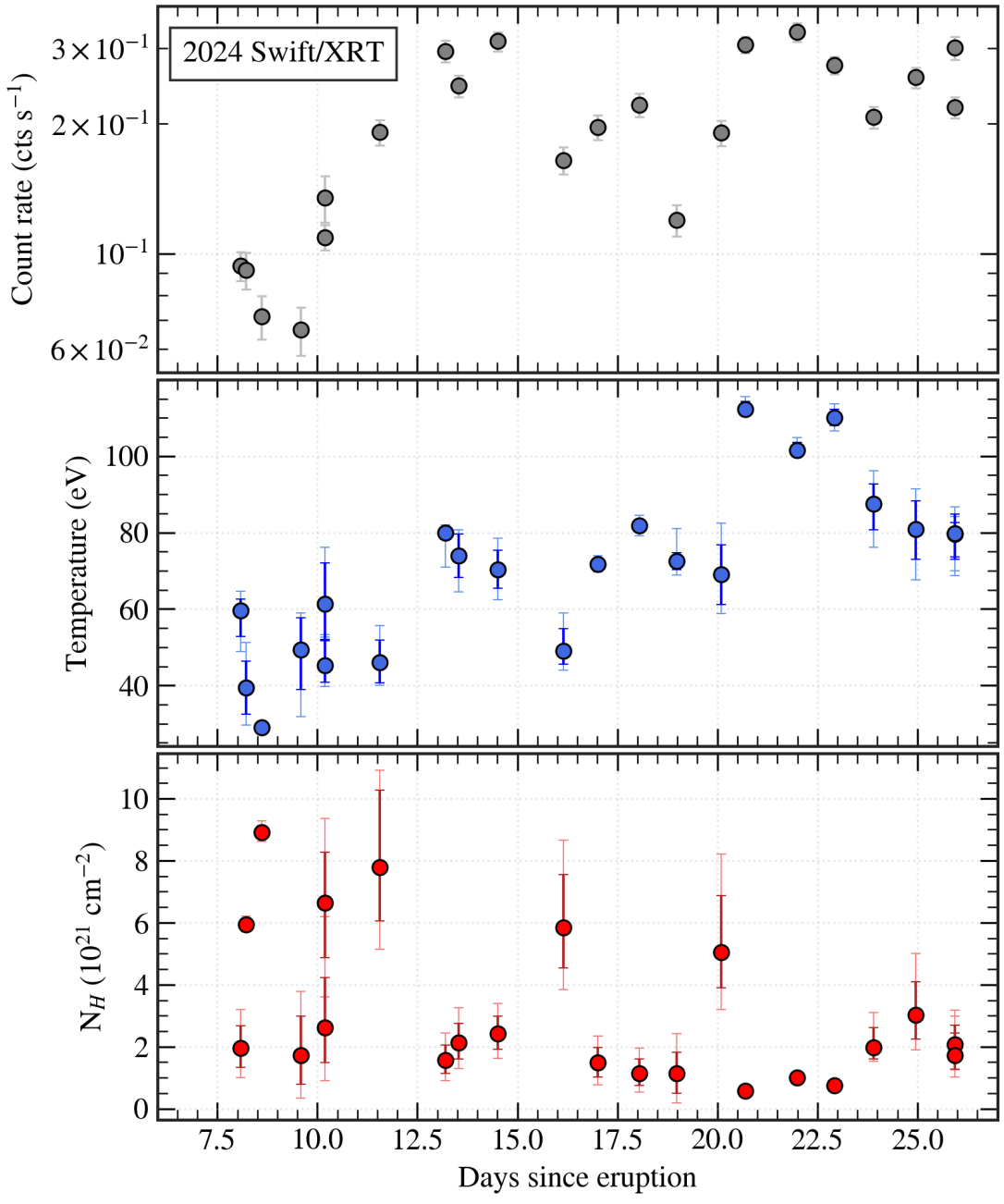

FIGURE 5.4: Evolution of column density and effective temperature of the WD during the SSS phase of the 2024 eruption of LMCN 1968-12a.

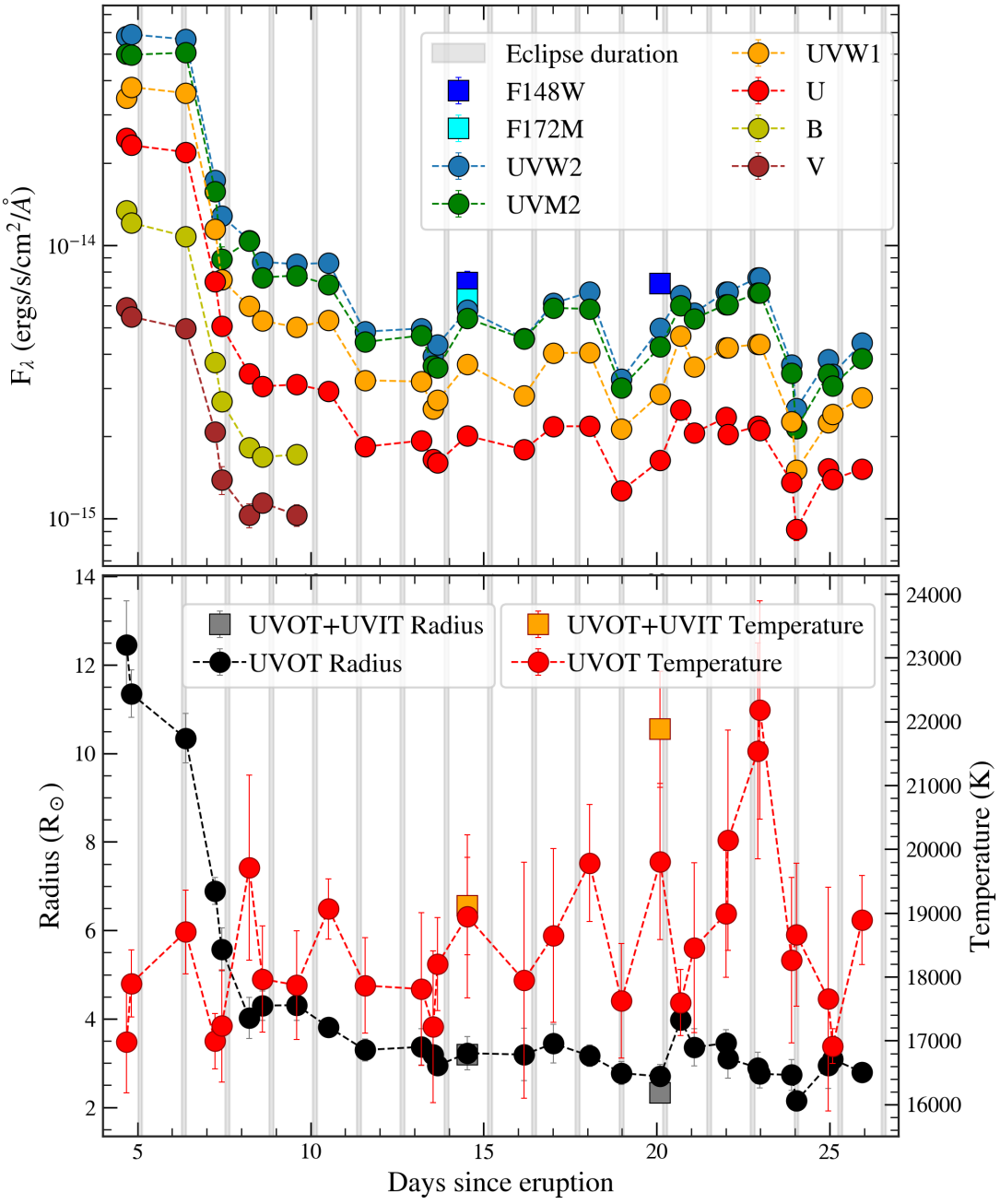

FIGURE 5.5: Temporal evolution of UVOT fluxes, along with effective temperature and blackbody radius derived from blackbody fits.

though only one cycle could be observed (Figure 5.3). Kuin et al. (2020) previously reported the eclipse duration to be ∼5% of the orbital phase. Some UVOT light curves show sharp dips (e.g., on days 19 and 24), which align with the expected eclipse windows, as overplotted on Figure 5.5, confirming that these dips are due to occultation of the WD by the secondary.

The UV light curve enters a plateau phase during this interval, with peak fluxes of the orbital modulations declining by ∼1 mag over 16 days (Figure 5.2). This plateau is a known feature in RNe and closely resembles the UV evolution observed in U Sco, another RN with a similar orbital period but somewhat longer recurrence time (Pagnotta & Schaefer 2014; Evans et al. 2023; Muraoka et al. 2024).

Concurrently, the SSS flux continued to rise, peaking at ∼0.3 counts s^{-1} in the XRT light curve. The SXT flux, at roughly one-third the amplitude due to lower sensitivity, follows the same temporal evolution. Notably, the SSS light curve shows a double-peaked structure. A similar morphology was evident in previous outbursts of LMCN 1968-12a (Figure 5.6). The X-ray and UV light curves from *AstroSat*'s second epoch (see Figure 5.3) indicate that the flux dip just after day 20 is orbital in origin, corresponding to the eclipse of the WD by the secondary star. However, this dip differs in character and timescale from the broader decline seen between days 16–20. The broader dip does not align with the expected orbital phase and is therefore not caused by the orbital motion alone.

Such double-humped or dip-like features in the SSS light curve, accompanied by increased variability, have been observed in several RNe. For example, the RN V3890 Sgr exhibited erratic X-ray variability, including both short (hour-scale) and extended (day-scale) dips (Singh et al. 2021; Ness et al. 2022). While the short-term dips were likely due to clumps of ejecta transiting the line of sight, longer dips such as the extended faint interval between days 16.8–17.8 were attributed to episodic, partially opaque outflows. These outflows had low filling factors and did

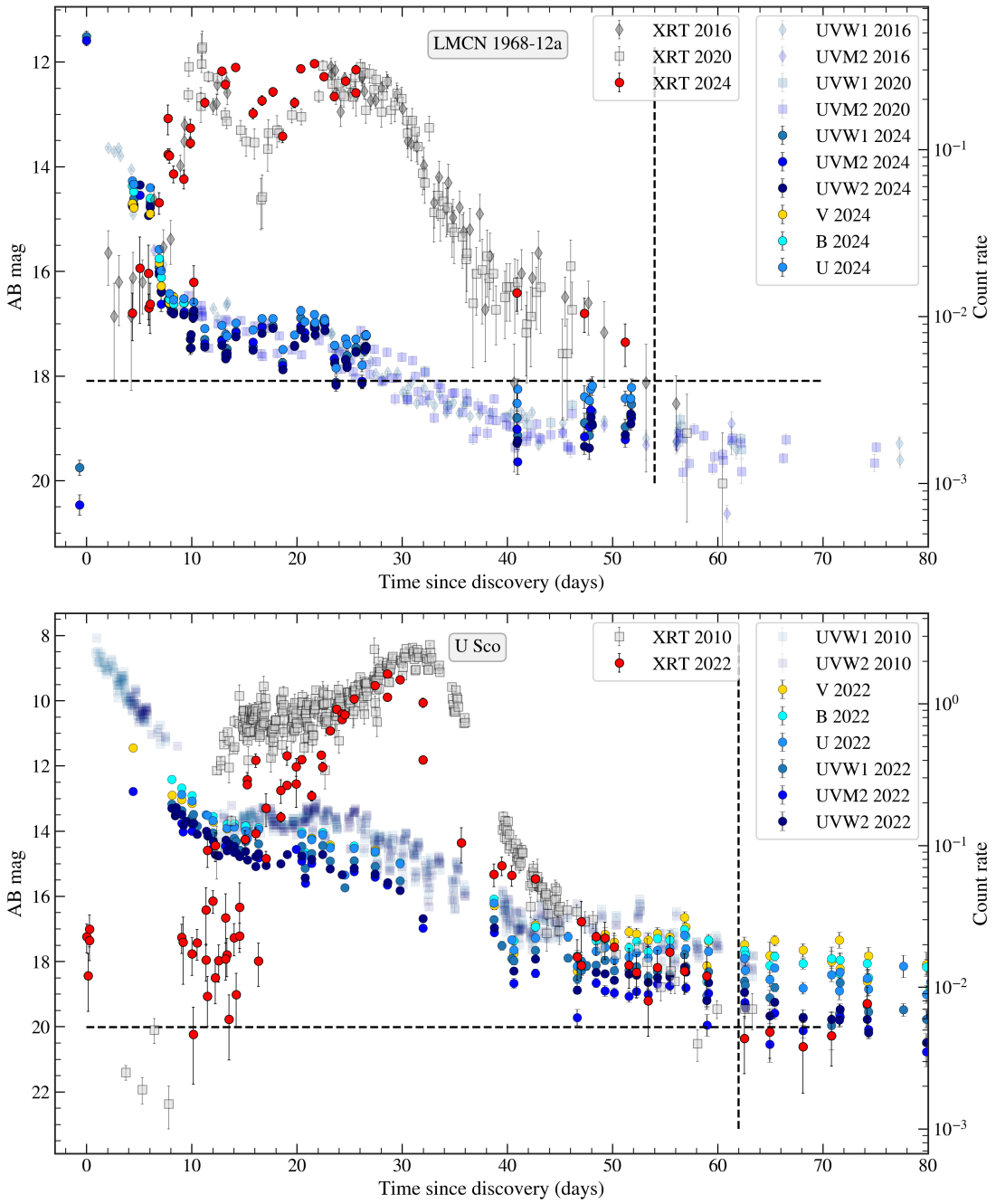

FIGURE 5.6: *Top:* UVOT and XRT lightcurves of 2024 eruption of LMCN 1968-12a overplotted on the 2016 and 2020 eruption lightcurves. The soft X-ray detection limit is shown as a horizontal dashed line, and the SSS t_{off} is marked as a vertical dashed line. *Bottom*: Same as above, but for the U Sco 2022 eruption overplotted on the 2010 eruption.

not significantly alter the spectral shape or measured column density ($N_{\rm H}$).

RN RS Oph also showed marked SSS variability during its 2006 and 2021 eruptions. Osborne et al. (2011) linked the high-amplitude, hour-scale dips during the 2006 eruption to absorption by clumpy ejecta. In contrast, the 2021 outburst showed a fainter and more complex multi-peaked SSS structure. A broad X-ray dip from day 47 to 57 was reported by Ness et al. (2023), potentially due to inhomogeneous ejecta or changes in the surrounding medium.

The 2010 eruption of RN U Sco featured a smooth rise in the X-ray beginning around day 2, followed by a plateau during days ∼12-20, and a rise to the peak that was reached around day 30, as shown in Figure 5.6 (Pagnotta et al. 2015). During the plateau, several sharp, irregular dips, over a timescale of hours, were observed. These were attributed to occultations by a re-forming accretion stream (Ness et al. 2012). The 2022 eruption showed a lower early X-ray flux, likely due to reduced accreted mass. Unlike the 2010 eruption, it did not go through a plateau phase. The rise was highly variable during days ∼10-25 to reach the peak at day 30 (Muraoka et al. 2024) as shown in Figure 5.6.

Similarly, M31N 2008-12a (see Chapter 4) displays high X-ray variability and a recurring mid-SSS phase dip during nearly every eruption (Darnley et al. 2016; Henze et al. 2018e; Basu et al. 2024e). Like in LMCN 1968-12a, these dips are persistent across multiple outbursts and suggest a non-stochastic origin.

Short-timescale dips (minutes to hours) in RNe are generally linked to clumpy ejecta or transient accretion structures obscuring the WD. However, the consistent appearance of broader dips in LMCN 1968-12a and M31N 2008-12a, particularly at similar phases across multiple eruptions, argues against such transient phenomena. Spectral fitting of the 2024 XRT data of LMCN 1968-12a during the SSS phase with a simple absorbed blackbody model (`tbabs` × `bb`) revealed a concurrent drop

in blackbody temperature (kT) and rise in $N_{\rm H}$ between days 16–20 (Figure 5.4). The broad nature and repeatability of the dip suggest it is more likely caused by obscuration from external, large-scale inhomogeneous structures rather than internal clumps.

Recent studies have reported faint, extended nebulosities, known as "nova super-remnants" around several RNe, including M31N 2008-12a (Darnley et al. 2019c), KT Eri (Shara et al. 2024a; Healy-Kalesh et al. 2024b), RS Oph (Healy-Kalesh et al. 2024a; Shara et al. 2025), T CrB (Shara et al. 2024b), and LMCN 1971-08a (Healy-Kalesh et al. 2025). These remnants, much larger than typical nova shells, are likely formed by ISM material swept up over multiple nova cycles (Healy-Kalesh et al. 2023). For RRNe like LMCN 1968-12a, repeated eruptions may contribute significantly to shaping such large-scale, inhomogeneous structures. Obscuration by these remnants could plausibly explain the prolonged SSS dips observed in LMCN 1968-12a and possibly M31N 2008-12a.

5.3.2 X-ray Spectroscopy

SXT spectra were obtained at two distinct epochs, approximately 15 and 20 days after the eruption. Orbit-wise spectra from both epochs are presented in Figure 5.7. Typical X-ray features observed during the SSS phase in novae are marked in the Figure. However, the spectral resolution of SXT being poor (see §2.1.2.1), no attempt is made towards specific line identification and analysis. As is evident from the light curve in Figure 5.2, both epochs correspond to the peak of the SSS phase. During the first epoch, the spectra are dominated by soft X-rays, with most of the emission confined below 1 keV, consistent with the supersoft nature of the source. However, toward the end of this epoch, a noticeable enhancement in flux appears near 0.6 keV and 1.5 keV.

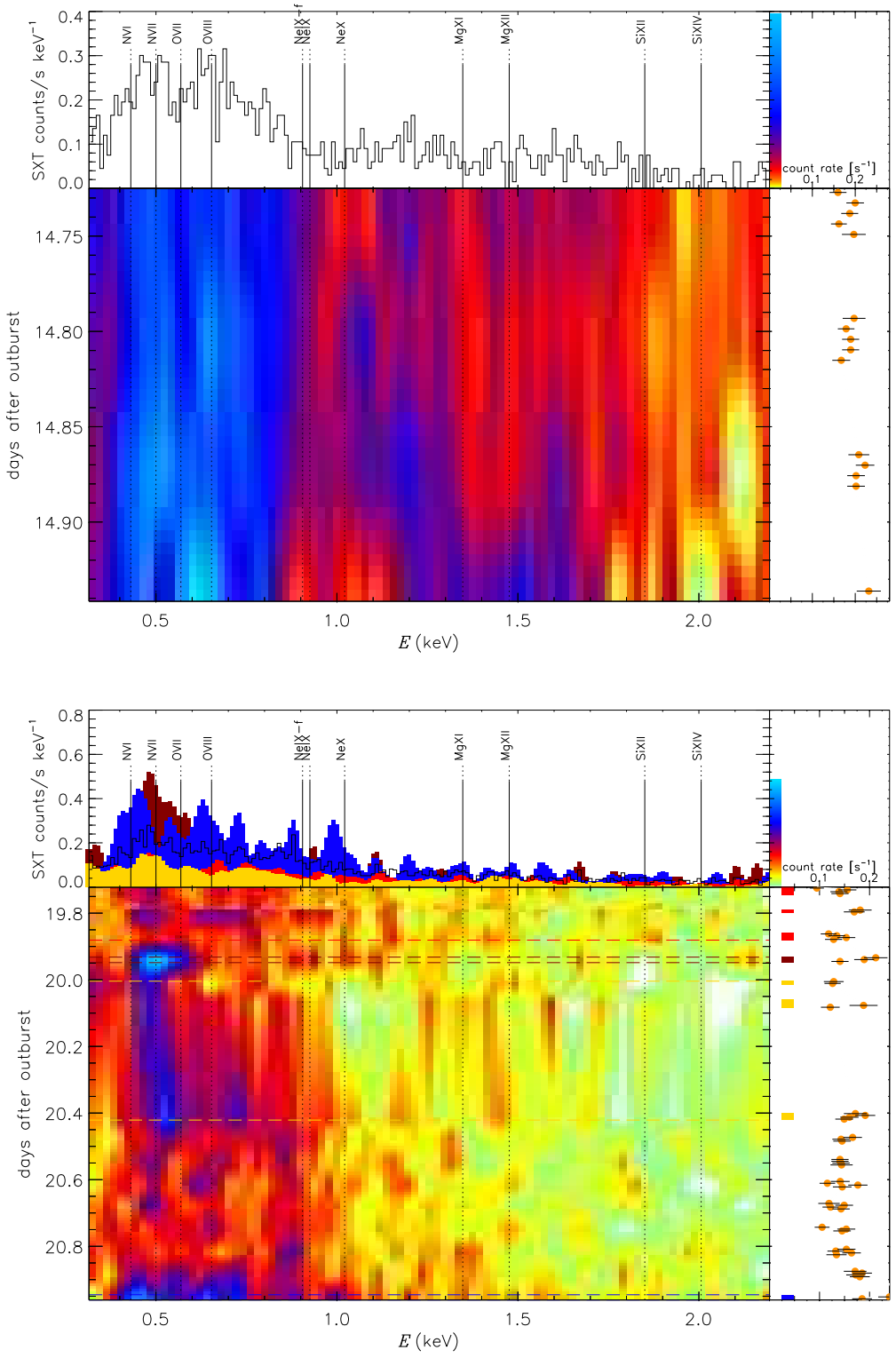

FIGURE 5.7: SXT spectral evolution during the two epochs of *AstroSat* observations of the 2024 outburst of LMCN 1968-12a. Lines typically seen in novae X-ray spectra are also marked.

In the second epoch, the emission remains largely concentrated below 1 keV, with negligible flux above 1.5 keV. The densely sampled temporal coverage during this epoch reveals significant spectral variability over short timescales. The flux increases by nearly a factor of five and subsequently declines to its original level within 4–5 hours, capturing the occultation of the WD by the secondary. By the end of the second epoch, the 0.3–1.0 keV flux begins to rise again, indicating the re-emergence of the WD from eclipse. Such hour-scale variability in the SSS emission, especially below 1 keV, is attributed to absorption by co-rotating clumpy ejecta structures, as discussed in Section 5.3.1.

5.3.3 Spectral Energy Distribution

Simultaneous observations in the NUV, FUV, and soft X-ray bands using *AstroSat* and *Swift* enabled us to construct and examine the evolving SED of the system. The SEDs corresponding to the two *AstroSat* epochs are presented in Figure 5.8. Attempts to fit the combined UV and X-ray data with a single blackbody model were unsuccessful, as the extrapolated X-ray blackbody underpredicted the UV flux. It is evident that the UV and soft X-ray emissions originate from distinct physical regions. Therefore, we modelled the UV and X-ray components separately.

The soft X-ray emission was fitted with a blackbody spectrum modified by an absorption column, while the extinction-corrected UV emission was fitted with a standalone blackbody model. It is to be noted here that blackbody fits are simplistic approximations as compared to the WD atmosphere models. However, in the case of data with poor SNR and low resolution, blackbody approximations give reasonable and easily reproducible estimates of parameters (Ness 2020). It was also shown in the previous study of LMCN 1968-12a (Kuin et al. 2020). The results from both *AstroSat* epochs, along with simultaneous *Swift* data, are shown

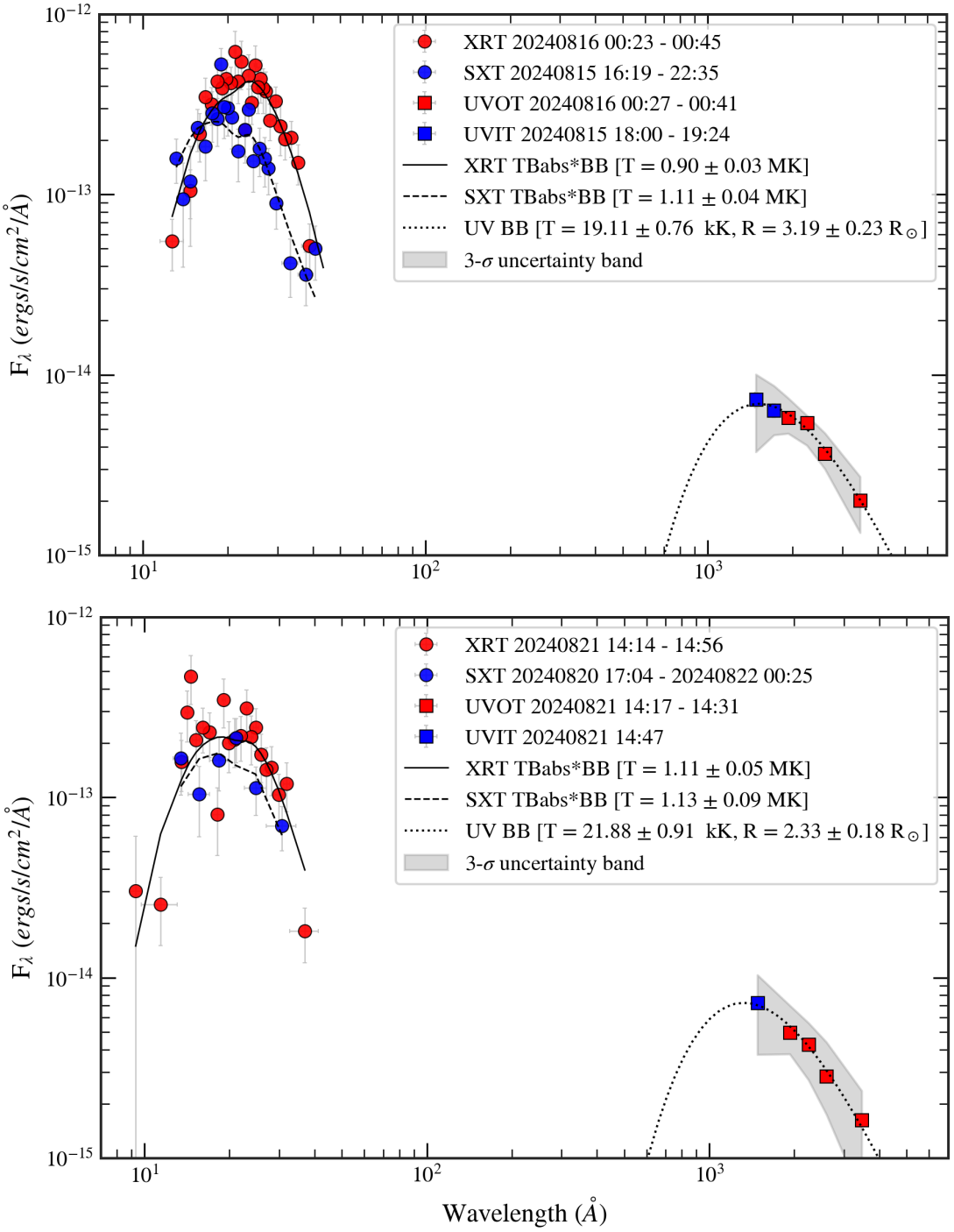

FIGURE 5.8: SEDs of the combined X-ray and UV data from both *AstroSat* and *Swift*.

in Figure 5.8. The X-ray component, associated with the SSS phase, peaks at a temperature of $\sim 10^6$ K, consistent with earlier findings by Kuin et al. (2020). It is believed to originate from the surface of the WD. In contrast, the UV component

peaks at $\sim 2 \times 10^4$ K and has an inferred source radius of about 2–3 $R_\odot$.

Additionally, individual blackbody fits were performed on the UVOT data to track the temporal evolution of the UV-emitting region's radius and temperature, as shown in Figure 5.5. The radius steadily declines from ∼12 $R_\odot$ to ∼4 $R_\odot$ until day 8, coinciding with the onset of the SSS phase. This shrinking radius indicates a receding photosphere as the ejecta thins out and the hot WD becomes visible, marking the transition to the SSS phase and the UV/optical plateau. During the SSS phase, the UV-emitting region maintains a nearly constant radius of ∼3 $R_\odot$, with a temperature range of 1.7–2.3 $\times 10^4$ K, consistent with values reported by Evans et al. (2025).

The observed UV blackbody emission, beyond day 10, cannot be attributed solely to either the evolved secondary or the accretion disk. However, if one or both are irradiated by the hot WD (with $T_{\rm eff} > 10^6$ K), they can reprocess this high-energy flux and emit in the UV/optical bands. Kuin et al. (2020) and Evans et al. (2025) ruled out irradiation of the secondary as the dominant source, as such models tend to overpredict the observed UV-optical fluxes.

The survival of the accretion disk post-eruption remains an open question. However, recent studies of RRNe like M31N 2008-12a (Basu et al. 2024d) and U Sco (Ness et al. 2012; Muraoka et al. 2025) indicate that the disk can persist into the SSS phase, plausibly in a fragmented state due to the impact of the eruption. Observational evidence for disk-related accretion streams was found in U Sco as early as 8 days post-eruption (Anupama et al. 2013b). Furthermore, hydrodynamic simulations by Figueira et al. (2025) support disk survival under specific conditions in systems like U Sco. Disk irradiation has also been proposed as the cause of the optical plateau in U Sco (see Figure 5.6) (Muraoka et al. 2024), a system with similar orbital and recurrence timescales to LMCN 1968-12a. Theoretical models

developed by Hachisu et al. (2000) for an irradiated disk and companion successfully reproduce the UV-optical light curve of U Sco. Given the strong similarities of the UV-optical lightcurve morphologies between U Sco and LMCN 1968-12a as shown in Figure 5.6, it is highly plausible that disk irradiation is also responsible for the UV-optical component observed in LMCN 1968-12a.

5.4 Conclusion

In this chapter, we presented a comparative study of the RRNe LMCN 1968-12a with another extragalactic RRNe, M31N 2008-12a, and the Galactic RRNe U Sco. For LMCN 1968-12a, we analysed the UV and X-ray light curves, X-ray spectra, and UV–X-ray SEDs from its 2024 eruption. The UV light curves display an initial rapid decline, followed by a plateau phase modulated by the system's orbital period. Concurrently, the SSS emission exhibits significant variability, including a broad, recurring dip observed across multiple eruptions. This dip is likely caused by an extended absorbing structure along the line-of-sight, potentially a nova super-remnant.

Modelling of the X-ray spectra and UV SEDs indicates that the UV and soft X-ray emissions originate from distinct physical regions. As the eruption progresses and the light curve declines, the photosphere contracts, revealing soft X-ray emission from residual nuclear burning on the WD surface at temperatures of $\sim 10^6$ K. In contrast, the UV-optical emission is dominated by an irradiated accretion disk with a characteristic temperature of $\sim 2 \times 10^4$ K.

These results, in conjunction with previous studies of similar systems, strongly suggest that the accretion disk is not completely destroyed by the nova eruption. Instead, accretion resumes within a few days, approximately coinciding with the

onset of the SSS phase ($t_{\rm on}$), highlighting the tendency to "accrete, accrete, accrete... bang! (and repeat)"[‡] in such RRNe.

[‡]The phrase was shamelessly copied from the title of Darnley (2021)

Chapter 6

AT 2023tkw in M31: Light Curves, Spectra, and Internal Shock Signatures

"When you have eliminated the impossible, whatever remains, however improbable, must be the truth."

— Arthur Conan Doyle

The work presented in this chapter is based on the publication: Basu et al. (2025b), 'Discovery and Detailed Study of the M31 Classical Nova AT 2023tkw: Evidence for Internal Shocks', 2025, ApJ, 980, 129.

6.1 Introduction

M31 has been monitored daily by GIT in the SDSS g' and r' bands during the observing months from July to February each year, starting in 2022. This is part of an ongoing program to identify nova-like transients via image subtraction, using Pan-STARRS archival images as references, following the methodology described in Kumar et al. (2022b). Transient candidates were filtered through our dedicated vetting interface. On 2023 September 19, we detected a previously unreported transient source with a magnitude slightly fainter than 20 in both g' and r' bands, located at $(\mathrm{RA, Dec})_{\mathrm{J2000}} = (00{:}41{:}24.169, +41{:}08{:}05.26)$ as shown in Figure 6.1. A check using `mpchecker`* revealed no known minor planets at this position.

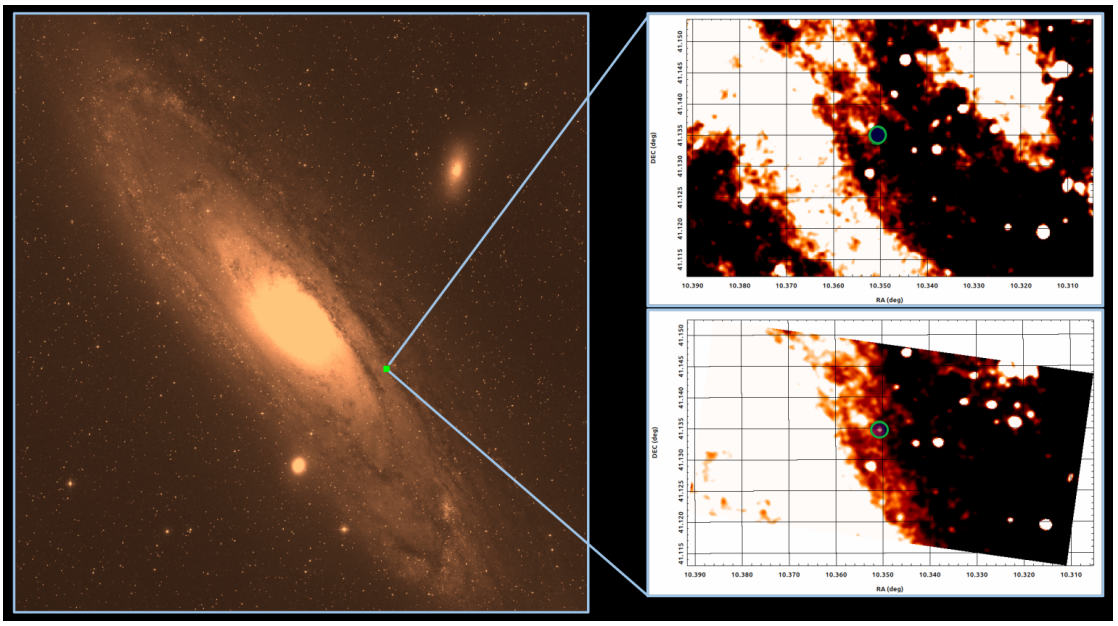

FIGURE 6.1: Location of AT 2023tkw in M31. In the insets, the nova field is shown before the eruption (*top*) and during outburst (*bottom*).

The source had not been reported to the Transient Name Server (TNS) prior to our discovery, and no match was found in the M31 nova catalogue†, the AAVSO VSX database‡, or in `SIMBAD`§. The new transient was designated GIT20230919aa

*https://minorplanetcenter.net/cgi-bin/checkmp.cgi
†https://www.mpe.mpg.de/~m31novae/opt/m31/M31_table.html
‡https://www.aavso.org/vsx/index.php
§https://simbad.cds.unistra.fr/simbad/

and subsequently reported to TNS where it received the official name AT 2023tkw (Kumar et al. 2023). The object was independently detected by ZTF (Bellm et al. 2019; Graham et al. 2019; Dekany et al. 2020) as ZTF23aayatam.

The transient was observed to be brightening at the time of discovery, indicating that it was caught during its pre-maximum phase. Follow-up spectroscopy, triggered once the source became sufficiently luminous, confirmed its classification as a nova in the Fe II spectral phase (Basu et al. 2023b).

The extinction towards AT 2023tkw was estimated using the M160-resolution dust map of M31 from Draine et al. (2014), considering a $1'$ region centered on the nova and applying the correction factor described in §3.3.2. The resulting values, $A_V = 0.621$ and $R_V = 3.1$, were adopted for dereddening all optical and IR spectra. The extinction correction was performed using the CCM89 extinction law (Cardelli et al. 1989) as implemented in the `extinction` package (Barbary 2021) in `Python`.

This chapter presents a detailed study of the slow nova AT 2023tkw, discovered by the fully robotic 0.7 m GIT (Kumar et al. 2022a) as part of its dedicated M31 monitoring campaign. Imaging and spectroscopic analyses are discussed, followed by the likely binary components of the system. We conclude with a discussion of the nova's physical characteristics.

6.2 The Secondary Star

6.2.1 Archival Non-Detections

We searched for the nova system in quiescence using archival GIT images of the nova field. Ten high-quality images in both g' and r' bands, each with an exposure time of 240 s and acquired under good seeing conditions (FWHM $\approx$ 2–3″) between July and September 2022, were selected. Two sets of co-added images were created using median and summed combinations via `SWarp` (Bertin 2010). No source was detected in up to 3σ limiting AB magnitudes of 21.3 (g') and 21.2 (r').

We also queried the ZTF forced photometry service to obtain archival upper limits spanning from 30 May 2018 to 16 July 2023, yielding approximately 850 and 1150 epochs in the g and r bands, respectively. The median 3σ limiting magnitudes were 20.9 ± 0.6 (g) and 20.7 ± 0.6 (r), with the deepest limits reaching 21.97 (g) and 21.72 (r).

Archival *AstroSat* UVIT images from 8 November 2017 also showed no detection of the source, with limiting AB magnitudes of 22.83 (F148W), 22.07 (F172M), 22.36 (N219M), and 21.87 (N279N).

The Swift XRT 2SXPS upper limit service[¶] (Evans et al. 2020) reported a non-detection with an upper limit of $< 3.1 \times 10^{-4}$ counts s^{-1} in the 0.3–10.0 keV energy range, based on data between 1 September 2006 and 26 July 2018.

The field was re-observed with GIT on 10 August 2024, when M31 became visible again. No detection of the source was made in the r' band down to a limiting AB magnitude of 18.9.

[¶] https://www.swift.ac.uk/2SXPS/ulserv.php

6.2.2 HST Photometry

The Hubble Space Telescope (HST) observed the nova field on 27 December 2022 during Cycle 29 (Program GO-16796, PI: Benjamin Williams). Observations were made with the Advanced Camera for Surveys (ACS; Ryon & Stark 2023; Hathi 2024) Wide Field Channel (WFC) using the F475W and F814W filters, with total exposure times of approximately 1000 s in each.

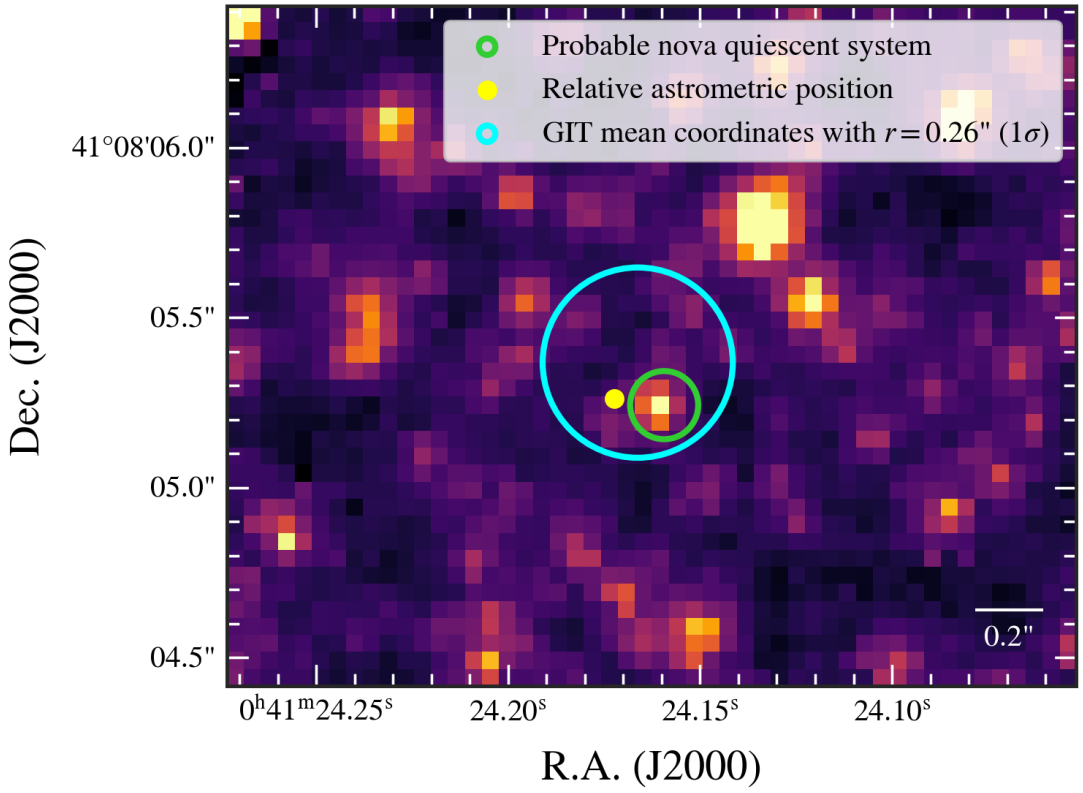

FIGURE 6.2: HST ACS/WFC image in the F814W filter, with the likely companion marked in green. The position of AT 2023tkw, aligned to the HST frame, is marked with a yellow dot. The GIT positional uncertainty is shown as a cyan circle.

To identify the quiescent system in this densely populated region (Figure 6.2), GIT images were resampled to match the ACS/WFC resolution of 0.05 arcsec pixel^{-1} using `SWarp` (Bertin 2010) and registered to the HST frame via `Spalipy` (Lyman

2021). A candidate source was identified within the GIT 1σ localization radius ($r = 0.26''$), with coordinates (α, δ) = (00:41:24.1638, +41:08:05.243). Given the local stellar density of $\rho = 0.56$ sources arcsec^{-2}, the coincidence probability of a chance alignment within the error circle is

$$P(\geq 1) = 1 - P(0) \tag{6.1}$$

$$\text{or, } P(\geq 1) = 1 - e^{-\lambda} = 1 - e^{-\rho \times \pi r^2} \tag{6.2}$$

$$\text{or, } P(\geq 1) = 11.2\% \tag{6.3}$$

While a candidate source has been identified, the selection effects of observing the M31 in red filters (F814W) must be considered. At this distance and detection threshold, the HST data samples the evolved giant population. Given that the initial mass function suggests the presence of a significantly higher number density of dwarf stars compared to giants, there is a substantial probability that the quiescent donor is a main-sequence star. In this scenario, the coincident giant would be a chance alignment. However, the identified source remains a possible candidate for a nova system.

Photometry was performed using `DOLPHOT` (Dolphin 2016), employing ACS-specific pixel area maps and PSFs for accurate calibration, following the procedures in Dolphin (2000). Sources with `crowding` > 0.2 were excluded to eliminate poorly measured stars. The remaining sources were cross-matched with the HST reference catalogue[‖] to derive median magnitude uncertainties as a function of brightness (see Figure 6.3).

We measure the AB magnitudes of the quiescent candidate as 25.75±0.13 (F475W) and 23.89 ± 0.08 (F814W). Correcting for extinction from §6.1 and assuming a distance of 778 kpc (Stanek & Garnavich 1998), we derive absolute magnitudes of 0.66 ± 0.13 and -1.35 ± 0.08 in the F475W and F814W filters, respectively.

[‖] http://dx.doi.org/10.17909/b4vg-pa17

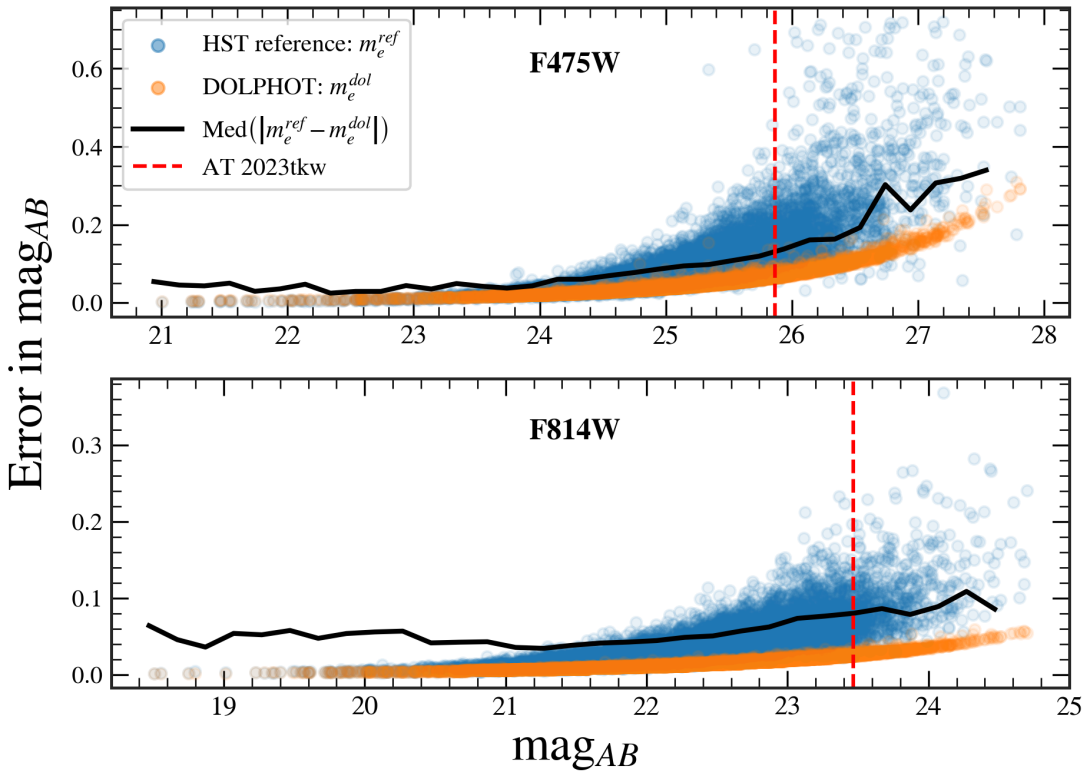

FIGURE 6.3: Photometric errors as a function of magnitude derived from HST reference catalogue ($m_e^{\rm ref}$) and `DOLPHOT` catalogue errors ($m_e^{\rm dol}$).

6.3 Photometric Evolution

6.3.1 Imaging Data

The GIT was used to observe the nova in the SDSS g', r', i', and z' filters. Following its discovery on 19 September 2023, we initiated a dedicated monitoring campaign from 20 September to 25 December 2023 with a near-daily cadence. Observations were carried out using either single or co-added 300 s exposures, depending on the object's brightness, sky conditions, and filter choice. The acquired images were reduced nightly using the pipeline outlined in Kumar et al. (2022a). Host-subtracted photometry was extracted by performing image subtraction using Pan-STARRS DR1 reference frames (Chambers et al. 2016), following the methodology described in Kumar et al. (2022b).

To complement the GIT dataset, photometry in the ZTF-g and ZTF-r filters was obtained using the ZTF forced-photometry service (Masci et al. 2019), which provides coverage at approximately three-day intervals. The ZTF light curve revealed a prolonged pre-discovery plateau beginning on 19 July 2023, which persisted for nearly two months before the nova began its rise. The photometric data from ZTF were carefully filtered following the procedures outlined in Masci et al. (2023).

All the photometric data are available at GitHub [**].

[**] https://github.com/judha-basu/Thesis-files/blob/d472c24df9aa0de10c49c737ec50969fdf1d781a/AT2023tkw_lc_data.csv

6.3.2 Multiband Light and colour curves

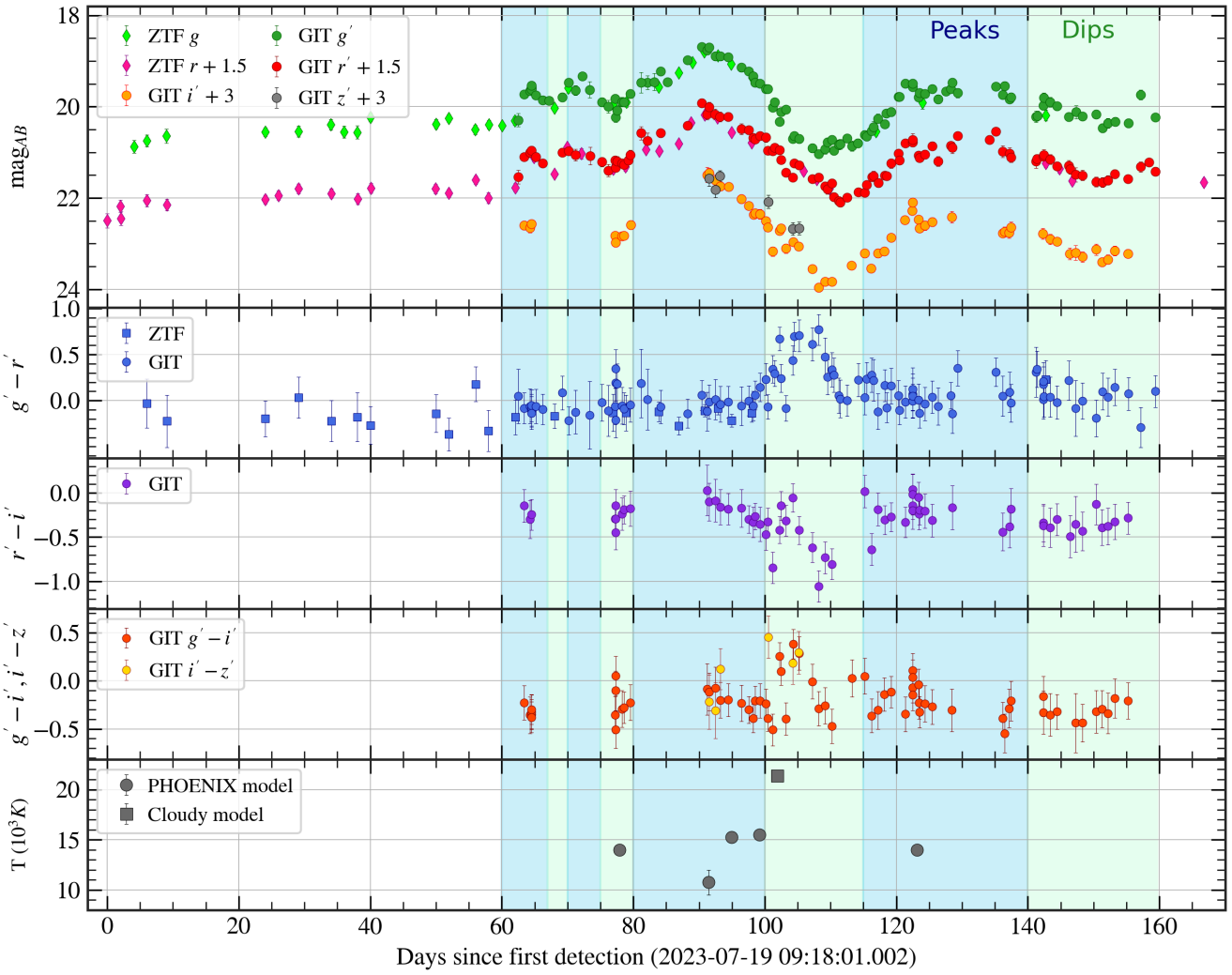

FIGURE 6.4: Optical light curve and extinction-corrected colour evolution curves are shown. The final panel displays the temperature evolution derived from spectral modelling. The data corresponding to this figure is available in GitHub [††].

The ZTF light curve (Figure 6.4) provides insight into the pre-discovery evolution of AT 2023tkw, starting from 19 July 2023. Initially, the object exhibited gradual modulations, brightening slowly by ∼1 mag over a span of 60 days. This was followed by a rapid rise of ∼1 mag in 5 days, then a decline of over 0.5 mag within the next 5 days. A second *peak-and-dip* sequence was observed over the following

10 days. The nova then brightened again from ∼20.25 mag, reaching a primary peak at $m_{\rm peak} = 18.5$ mag in 12 days, approximately 90 days after the initial detection. The extinction-corrected peak absolute magnitudes were −6.52 (g'), −6.58 (r'), and −6.40 (i'), values that are typical for M31 novae, although slightly towards the fainter end of the distribution (Shafter et al. 2009).

We note that M31 was in solar conjunction prior to mid-July, which introduces uncertainty in determining the exact eruption onset. Nonetheless, the slow rise of the nova is evident from the available light curve. M31 novae that exhibit jittery light curves often show a more gradual rise compared to those with smooth light curves (Cao et al. 2012). Following the primary peak, the nova declined by ∼2.5 mag over the next 20 days, then rose again by nearly 2 mag and maintained a jittery plateau for about 15 days. Another dip followed, this time at a slower rate, eventually fading to 20.5 mag. Our monitoring concludes with a final rise around days 155–160 before the nova fades completely. The light curve closely resembles a J-class nova as defined by Strope et al. (2010a).

The light curve of AT 2023tkw bears similarities to the historical nova RR Pic (Lunt 1926), which displayed a similarly ragged and slow rise, followed by dips and multiple peaks. A more recent analogue is Gaia22alz (Nova Velorum 2022; Aydi et al. 2023), another slow nova with a rare, gradual rise and multiple peaks. However, it should be noted that in the case of AT 2023tkw, the observed slow rise is limited to the final 2–3 magnitudes before peak brightness, and the early evolution from quiescence remains unconstrained.

A linear fit to the post-maximum decline in the g', r', and i' bands until they reach $m_{\rm peak} + 2$ yields t_2 times of 16.0, 20.2, and 15.9 days, respectively. Such short t_2 times would typically classify the nova as *fast* (Warner 2003). However, for novae with J-class light curves, which can cross the $m_{\rm peak}+2$ threshold multiple times, Strope et al. (2010a) recommends using the final crossing to determine t_2.

AT 2023tkw approaches but does not clearly cross the $m_{\rm peak}+2$ level for a second time in the g' and r' bands around day 60, whereas the i' band does cross it at day 61, albeit not definitively. Due to limited coverage beyond day 160 since the first detection (see Figure 6.4), we can only constrain $t_2 > 75$ days, confirming that AT 2023tkw is indeed a *slow* nova.

The $g'-r'$ colour increases (becomes cooler) during the major dip observed between days 100–115, as shown in Figure 6.4. A minor increase in colour also occurs during other dips, though these changes are within the error bars. A likely cause is enhanced Hα emission, which becomes more prominent as the continuum fades. The $r'-i'$ colour becomes bluer during the same dip, likely for the same reason. In contrast, the $g'-i'$ colour, less affected by Hα, shows a reddening trend during the decline around day 100–115, before turning blue near the light curve minimum at day 110.

6.4 Spectroscopy

6.4.1 Observations

The optical and IR spectra of the object were obtained using the telescopes and instruments listed in Table 6.1. All optical spectra were flux calibrated using the nearest available broadband magnitudes in g', r', and i' bands, made possible by the dense photometric coverage from GIT. For the Keck/LRIS spectrum, the interpolated z' magnitude using a least-squares fit was also used in the calibration. The line-of-sight velocities derived from the FWHM of the emission lines were corrected for instrumental broadening before being reported.

Date of Obs (UT)	Tel/Inst	R	Exp (s)	Airmass
2023-10-05 07:46	P200/DBSP	1000	3784	1.01
2023-10-18 19:33	HCT/HFOSC	600	3600	1.10
2023-10-22 08:19	Keck I/LRIS	750	300	1.09
2023-10-26 13:48	HCT/HFOSC	600	3600	1.31
2023-10-26 14:54	HCT/HFOSC	600	3100	1.13
2023-10-29 06:46	Keck II/NIRES	1000	300	1.17
2023-11-19 13:24	HCT/HFOSC	600	3600	1.12

TABLE 6.1: Log of spectroscopic observations of AT 2023tkw

6.4.2 Spectral Evolution

The sequence of spectra presented in Figure 6.5 was obtained at various stages of the light curve, including during dips, primary and secondary maxima, and decline phases, using multiple instruments. Prominent H Balmer emission lines are detected across all optical epochs. In the earliest spectrum, obtained during the rise phase (top panel of Figure 6.5), the continuum appears blue and the Balmer lines are strong, with relatively narrow line widths of $\sim$350 km s^{-1}, indicative of a slowly expanding ejecta. At the light curve maximum, the optical continuum dominates, while the emission lines become weaker and broaden to widths exceeding 600 km s^{-1}. This broadening may be slightly overestimated due to limitations in the HFOSC spectral resolution. During the subsequent decline into the first dip, the Keck/LRIS spectrum shows reduced H line widths (FWHM $\sim$ 400–500 km s^{-1}), and most emission lines exhibit associated P Cygni absorption components blue-shifted by $\sim$700 km s^{-1} (see Figure 6.6). The line strengths and widths then increase again, reaching $\sim$1000 km s^{-1} in the HFOSC and NIRES spectra (fourth and fifth panels of Figure 6.5). Simultaneously, the peak of the SED shifts toward shorter wavelengths, resulting in flatter optical and IR continua

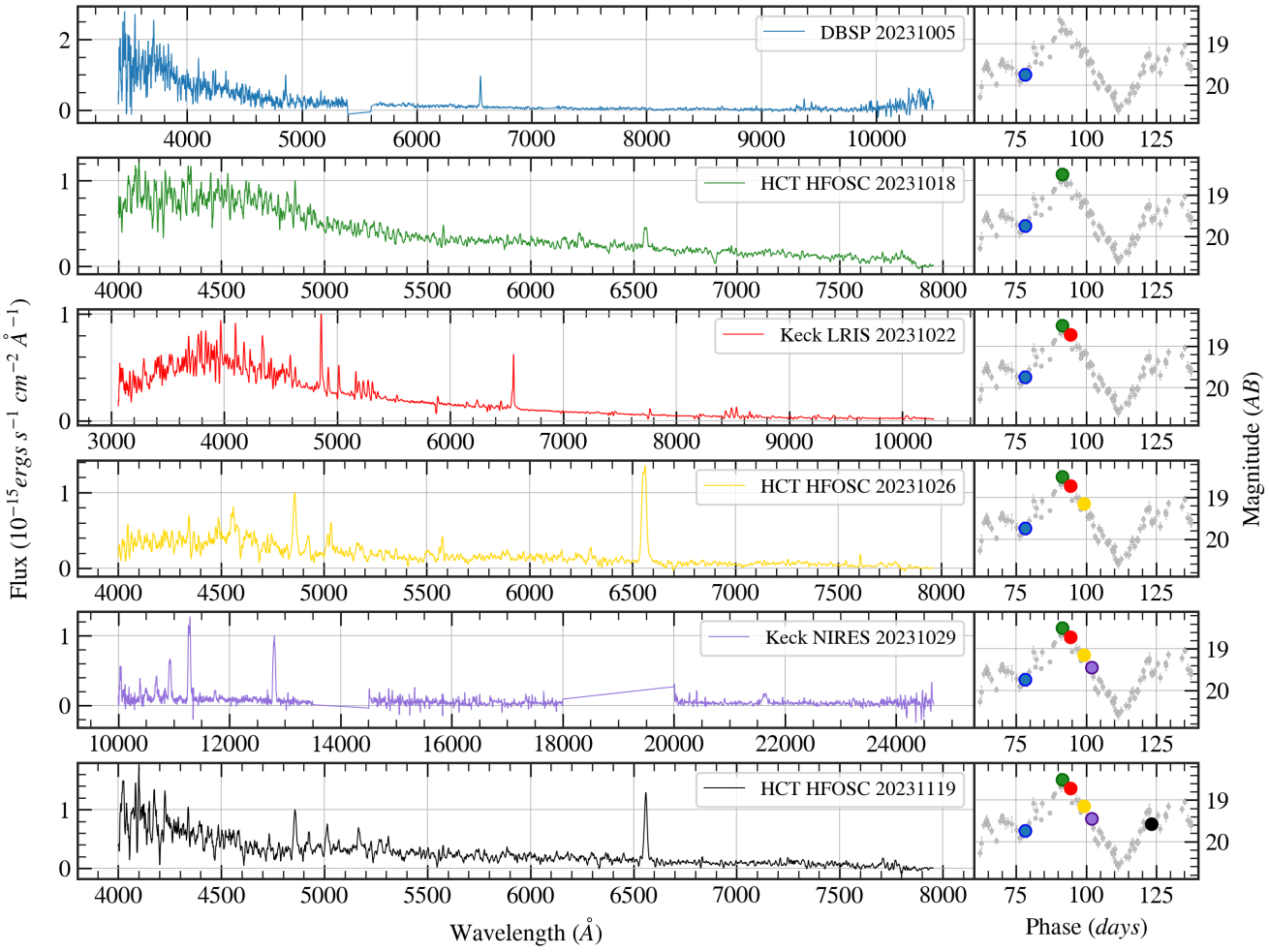

FIGURE 6.5: Evolution of the optical spectra of AT 2023tkw, with the timing of each spectroscopic observation highlighted on the light curve in the right-hand panel.

beyond ∼5000 Å. Typical Fe II lines from multiplets 42, 48, and 49 are observed in the principal spectrum. The second optical maximum shows a similar spectroscopic character to the first, featuring a dominant blue continuum, weakened line intensities, and narrower emission lines (∼500 km s^{-1}). Overall, the observed spectroscopic evolution is consistent with novae exhibiting multiple peaks.

The LRIS spectrum reveals a rich set of spectral features, including H Balmer and Paschen lines, Fe II multiplets, and lines from Ca, O I, N I, and C I, as annotated in Figure 6.6. P Cygni absorption seen in Balmer, Fe II, and O I lines suggests the presence of a dense, outward-moving shell with expansion velocities

of 600–800 km s^{-1}. The NIR spectra show strong Paschen and Brackett series lines, as well as C I and O I features (see Figure 6.6). Line identifications were based on comparisons with line lists from Williams (2012) and Banerjee & Ashok (2012) for the optical and IR regimes, respectively.

Enhanced emission in the O I λ11287 Å and λ8446 Å lines is attributed to fluorescence via Lyman-β pumping, a common mechanism observed in nova spectra (Kastner & Bhatia 1995).

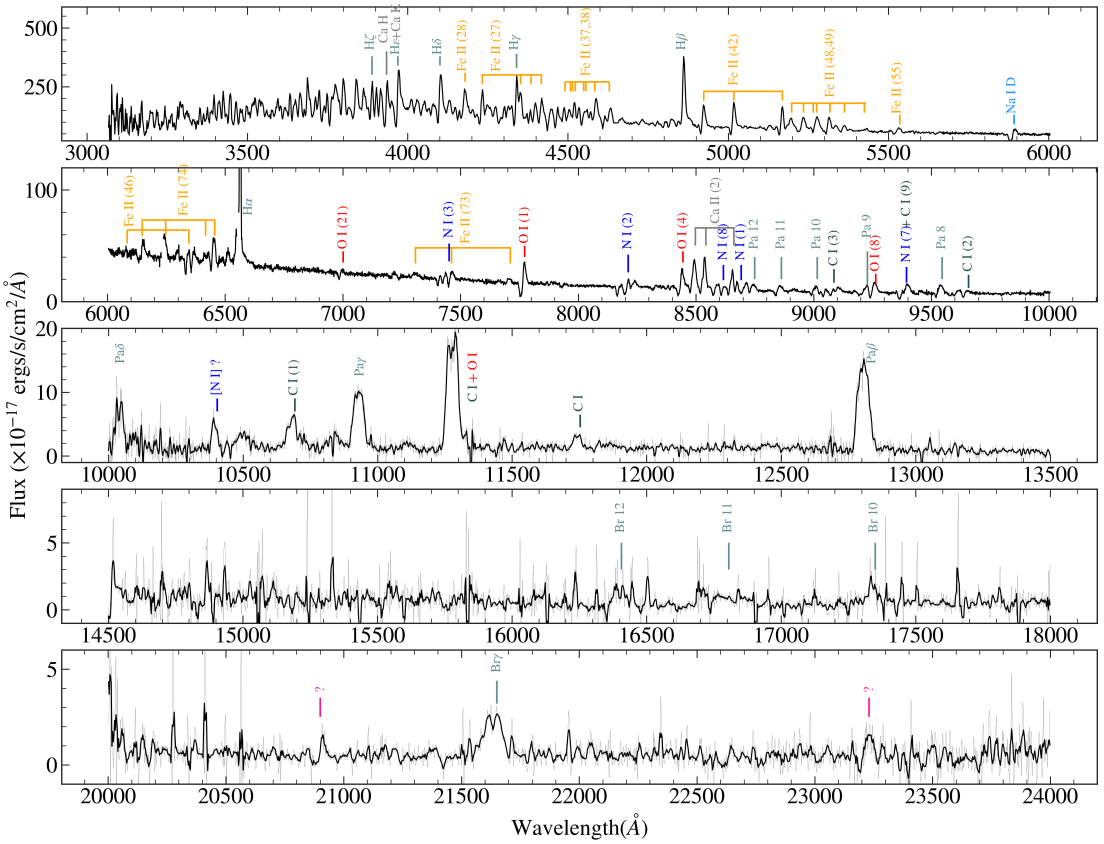

FIGURE 6.6: Identification of lines in the Keck LRIS and NIRES spectra.

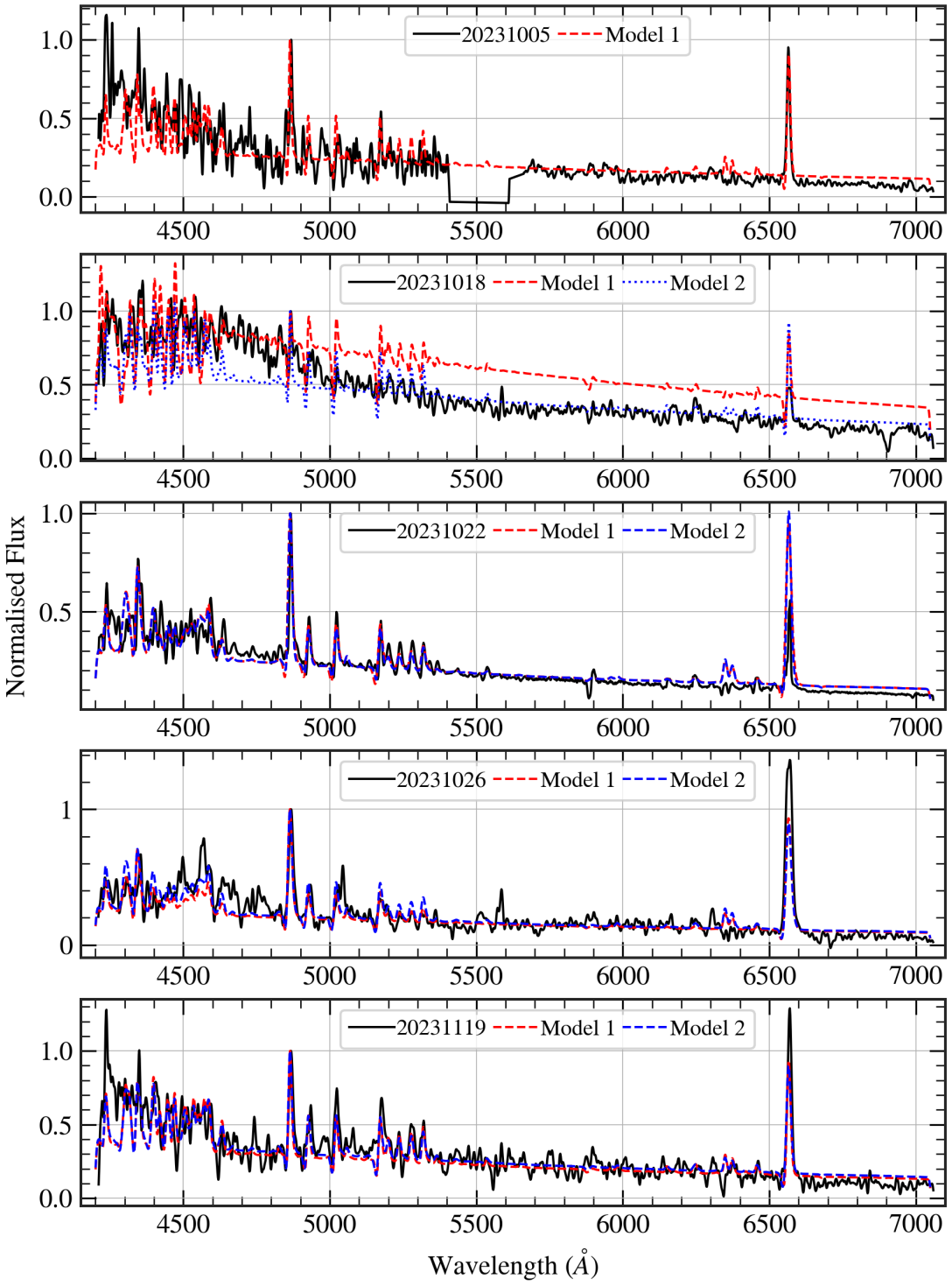

FIGURE 6.7: `PHOENIX` models overplotted on the observed optical spectra.

TABLE 6.2: `PHOENIX` model parameters of optical spectra.

Date (UT)	Phase	T (10^3 K)	v_0 (km s^{-1})	Metallicity
2023-10-05	Pre-maxima	14.0	1000	0.0
2023-10-18	Peak	9.5-12.0	1000-1500	0.0
2023-10-22	Decline	15.0-15.5	1000-1500	0.0
2023-10-26	Decline	15.5	1500	0.0-0.2
2023-11-19	Peak	13.5-14.5	1000-1500	0.0-0.2

6.4.3 Modelling of the Spectra

6.4.3.1 Optically thick phase

To model the dense ejecta near the optical maximum using `PHOENIX`, we generated a grid of models by varying the temperature (T), base velocity (v_0), and metallicity (z). The temperature range explored was 6000–30000 K, velocity between 1000 and 1500 km s^{-1}, and metallicity from 0 to 0.4. The chosen velocity range was constrained by the observed widths of the emission lines in the spectra.

Figure 6.7 shows model spectra that best match the observed optically thick phases during the rise, initial decline, and the secondary maximum. The corresponding model parameters are listed in Table 6.2. These models successfully reproduce both the continuum and emission features for all optical spectra, except the one obtained near the primary peak around day 90 from discovery. The characteristic P Cygni profiles are also well captured by the models.

The relatively low temperatures derived at the time of optical peak suggest that the photosphere was at its largest extent, consistent with theoretical expectations.

As the nova evolves, the ejecta becomes optically thinner, and the shrinking photosphere exposes deeper, hotter layers reflected in the temperature increase shown in the bottom panel of Figure 6.4. While comparing the models with the Keck/LRIS spectrum, the Hα line was excluded due to saturation. Notably, in the spectrum taken on October 26 (about 8 days post-maximum), the observed Hα line appears significantly stronger than predicted, although other features match well. This excess Hα emission may originate from a part of the ejecta that has decoupled from the photosphere and become optically thin, or from ionised circumbinary material.

We also attempted to model the near-IR spectrum using `PHOENIX`, but were unable to match the continuum. In particular, the O I λ11287 Å fluorescence line was underestimated across the entire model grid.

The spectrum taken near the secondary maximum was again well reproduced by `PHOENIX`, both in terms of continuum shape and emission line strengths. The enhanced Hα emission seen at this stage could be due to ionised material left over from an earlier mass-ejection episode. The lower model temperature at this time further supports the interpretation of an extended photosphere during the second peak.

6.4.3.2 Optically thin phase

Motivated by the strengthening hydrogen emission lines and the expanding ejecta observed during the decline phase, we modelled the NIRES spectrum obtained 11 days after the peak using the photoionisation code `Cloudy` (`v22.0`; Ferland et al. 2017a; Chatzikos et al. 2023).

We constructed a 1D model consisting of a single spherically symmetric, expanding

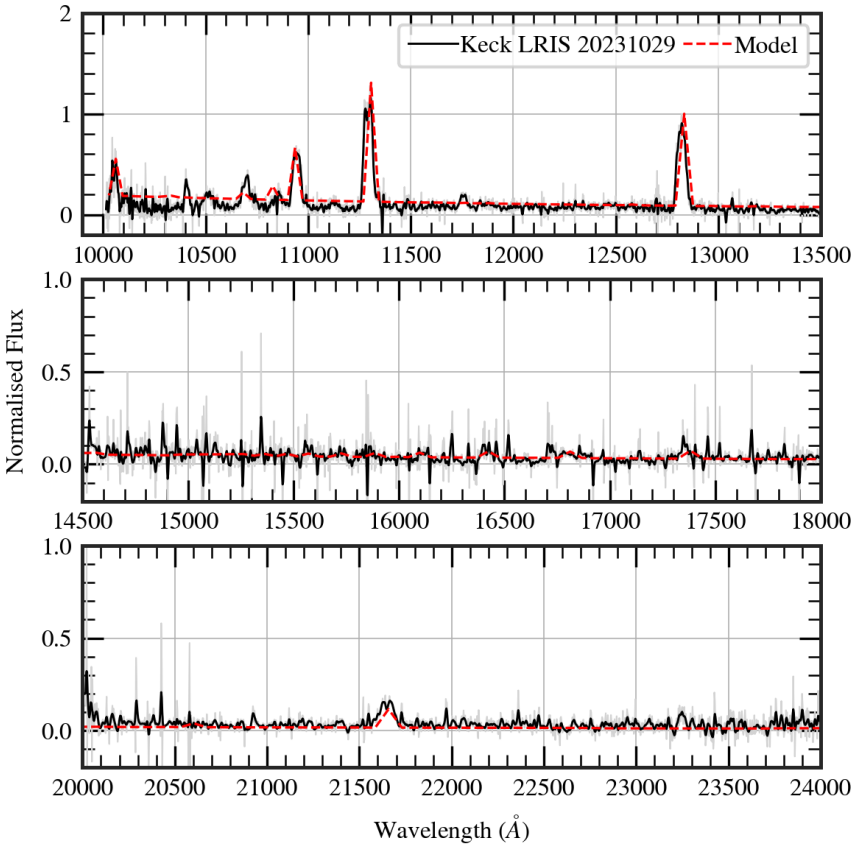

FIGURE 6.8: `Cloudy` model overplotted on the observed IR spectrum.

shell of gas. The model's free parameters included the blackbody temperature of the ionising source, the hydrogen density, and the chemical composition of the ejecta. The best-fitting model corresponds to a blackbody temperature of 21,380 K and a luminosity of 10^{38} erg s^{-1}. To represent a freely expanding (ballistic) shell, we adopted a density profile with a power-law index of $N = -3$, consistent with that used in `PHOENIX`. The inner and outer radii of the ejecta shell were determined from the observed emission line velocities, assuming the time of first detection as the eruption date.

Model parameters were chosen based on the approach outlined in Pavana et al. 2019 and references therein, and are listed in Table 6.3. With a hydrogen density of $\sim 8 \times 10^8$ cm^{-3}, the model successfully reproduces the Paschen and Brackett series lines in the NIR spectrum, as shown in Figure 6.8. To fit the observed

TABLE 6.3: `Cloudy` model parameters of the IR spectrum observed on 2023-10-29.

Parameter	Value
Ionising Source	Blackbody
T_{BB}	21380 K
Luminosity	10^{38} ergs s^{-1}
Hydrogen density	7.94×10^{8} cm^{-3}
Density Parameter N	-3
Inner radius	5.25×10^{14} cm
Outer Radius	10.96×10^{14} cm
Filling factor	0.1
$C/C_{\odot}$ [a]	37.17
Ejected Mass	8.92×10^{-5} $M_{\odot}$

[a] The solar abundance of C relative H was taken to be 2.69×10^{-4} from Grevesse et al. (2010).

carbon lines, an enhanced carbon abundance of $C/C_{\odot} = 37$ was required. Such carbon overabundance, along with enhancements in other elements, is commonly seen in nova ejecta and is attributed to surface material being dredged up from the WD during the TNR phase (Gehrz et al. 1998a).

The total ejecta mass inferred from the model is of the order of 10^{-4} $M_{\odot}$. The temperature of the ionising source inferred from the model supports the scenario of a hot, central remnant surrounded by ejecta that has become optically thin but remains geometrically extended.

6.5 Discussion

6.5.1 The quiescent nova binary system

We investigated the early-phase (days 0–60) ZTF light curve for any signs of periodic variability. However, the periodogram analysis did not yield any statistically significant signals, and no reliable periodicity could be identified.

The extinction-corrected absolute magnitudes of the likely progenitor system detected in the HST/ACS images are 0.66 ± 0.13 in the F475W filter and -1.35 ± 0.08 in the F814W filter (see §6.2). These values are consistent with those expected for evolved stars, while main-sequence stars would be at least 2.5 magnitudes fainter. Using standard filter transformations (Sirianni et al. 2005; Harris 2018), we converted the observed magnitudes to B and I bands and estimated a $B - I$ colour of 3.07. This colour is characteristic of cool, evolved K-type stars, such as K0 III ($B - I \sim 2.3$), K2 III (~ 2.6), and K5 III (~ 3.6). It should be noted that the F475W band could contain contributions from an accretion disk, implying that the true secondary star might be even cooler.

The ejecta mass estimated from `Cloudy` modelling of the NIRES spectrum is approximately 9×10^{-5} $M_\odot$. While this lies on the higher end of typical nova ejecta masses, it remains within the expected range for classical novae, especially those involving slow novae on low-mass CO WDs (e.g., V723 Cas; Evans et al. 2003).

By comparing the observed ejecta mass ($\sim 10^{-4}$ $M_\odot$) and expansion velocity (~ 700 km s^{-1}) to the theoretical nova models of Yaron et al. (2005), we find that the best-matching WD parameters are: $M_{WD} \approx 0.65$ $M_\odot$, $\dot{M} \approx 5 \times 10^{-13}$ $M_\odot$ yr^{-1}, and $T_{WD} \approx 30$ MK. Such systems are expected to evolve slowly, with recurrence timescales on the order of several hundred million years.

While low accretion rates and long evolutionary timescales may seem atypical for systems comprising evolved secondaries, several classical novae with such companions have been documented. Examples include V841 Oph, CP Cru, GK Per, and V723 Cas (Warner 2008). Notably, V723 Cas also exhibited a slow rise and a decline with multiple peaks (Kiyota et al. 2004), resembling the light curve of AT 2023tkw. Additional examples of similar systems are discussed in Mróz et al. 2015 (e.g., V2674 Oph, V5589 Sgr) and Schaefer 2021 (e.g., FM Cir, V392 Per, V1534 Sco, V5583 Sgr). More recently, HV Cet (Beardmore et al. 2012b), V1708 Sco (Sokolovsky et al. 2020), and V3732 Oph (Mroz & Udalski 2021) have been identified as classical novae with evolved secondary stars. Mróz et al. (2015) also noted a bimodal distribution in orbital periods among classical novae, corresponding to systems with main-sequence and evolved secondaries.

6.5.2 Origin of Multiple Peaks in the Light Curve

The light curve of AT 2023tkw exhibits complex structure, notably two distinct brightenings during the rise phase, followed by the main peak, which is followed by a broader secondary maximum 30–45 days after the primary peak (Figure 6.4). Similar rebrightenings have been observed in several novae, including V723 Cas (Kiyota et al. 2004), V2540 Oph (Ak et al. 2005), V1548 Aql, V4745 Sgr (Csák et al. 2005), V1186 Sco (Schwarz et al. 2007), V458 Vul (Poggiani 2008a), V5558 Sgr (Poggiani 2008b), and others such as V1405 Cas, V606 Vul, and FM Cir (Aydi et al. 2024).

Large surveys of M31 by Cao et al. (2012) and Clark et al. (2024) have reported numerous classical novae with pre- and post-peak rebrightenings. These are often associated with slowly evolving light curves. The distribution of smooth and jittery novae in the MMRD plane for M31 (Clark et al. 2024) also resembles that in

the Milky Way (Özdönmez et al. 2018). Below, we explore potential physical mechanisms behind the multi-peaked behaviour of AT 2023tkw.

6.5.2.1 A case of dust dip?

The dip observed in the light curve around day 110 might superficially resemble a classical "dust dip" (see Figure 6.4). However, such dips typically occur 50–100 days after the optical maximum, corresponding to the t_3 decline timescale (Strope et al. 2010a). In contrast, the dip in AT 2023tkw appears just ∼10 days after the peak, well before the t_2 time. Moreover, dust dips are generally characterised by substantial dimming, sometimes exceeding 10 magnitudes (as seen in D-class novae). Strope et al. (2010a) also noted that in some cases with relatively shallow dips, such as OS And, V476 Cyg, and NQ Vul, dust formation may not be the cause. In AT 2023tkw, the dip is modest, amounting to only ∼2.5 mag.

IR observations of M31 novae by Shafter et al. (2011a) with *Spitzer* indicated that the dust condensation timescale correlates with the nova's speed class. This is supported by theoretical models of dust formation in nova ejecta from Williams et al. (2013), which predict that slow novae are less likely to exhibit early dust formation. For AT 2023tkw, a slow nova, the timing and characteristics of the dip do not match those of typical dust dips. Moreover, "classic" dust dips generally appear as sharp deviations from a smooth decline, while here the decline remains continuous. There is also no evidence of significant reddening in the colour evolution (Figure 6.4) or from the spectroscopic sequence (Figure 6.5), which further argues against dust formation. Additionally, a second shallow dip is observed around day 150, reinforcing that these features are unlikely to be dust-related. We therefore rule out dust formation as the origin of the observed dips.

6.5.2.2 Transition from quasi-static to optically thick wind state?

An alternative explanation involves structural changes in the expanding envelope during the nova outburst. According to simulations by Kato & Hachisu (2009), nova eruptions can evolve via two distinct pathways: a steady, quasi-static expansion or a dynamical, optically thick wind phase. Massive WDs tend to follow the wind-driven evolution, producing sharp declining light curve peaks. Intermediate-mass WDs (0.6–0.7 $M_{\odot}$), however, may exhibit either behaviour depending on the ignition mass. A quasi-static evolution leads to a broader, flatter peak, while a transition from this state to the optically thick wind phase can produce erratic or jittery features in the light curve due to structural changes in the envelope.

In a follow-up work, Kato & Hachisu (2011) proposed that such transitions could be triggered by the presence of a close secondary star. In this scenario, the companion is deeply embedded within the nova envelope and can disturb the equilibrium, forcing a shift from a quasi-static to a wind-driven mass-loss phase. Observational evidence for this behaviour has been noted in V723 Cas, a known close binary system. However, this mechanism is unlikely to apply in the case of AT 2023tkw. As discussed in §6.5.1, the secondary in this system is likely an evolved star, suggesting a wide binary separation. This makes it improbable that the companion could significantly affect the envelope structure during the eruption, thereby making this mechanism an unlikely explanation for the multiple peaks seen in the light curve.

6.5.2.3 Photospheric oscillations?

Tanaka et al. (2011b) observed that in V5558 Sgr, the presence of P Cygni profiles corresponded with the light curve maxima, while their disappearance coincided with the minima. This was interpreted as evidence for photospheric expansion

during peaks and contraction during dips. The P Cygni absorption velocities were also found to be lower during the rebrightenings and higher during the declines. Aydi et al. (2024) attributed the low-velocity P Cyg profiles during rebrightenings to a dense and slow-moving outflow, while the higher velocity features away from the peaks were likely formed by intermediate-speed material, resulting from interactions between earlier slow and later fast outflows. Steinberg & Metzger (2020) supported this idea using 1D hydrodynamical models, showing that alternating slow and fast flows from beneath the photosphere can create internal shocks. These shocks briefly increase the system's luminosity, producing peaks in the light curve. As each shock front propagates outward and reaches the photosphere, it causes temporary expansion and cooling, followed by contraction and reheating. Repeated shocks of this nature can induce pulsations in the photosphere, causing variations in both brightness and temperature.

A similar scenario was proposed for V612 Sct (ASASSN-17hx), which exhibited light curve modulations resembling those seen in AT 2023tkw (Pavana 2020). Mason et al. (2020) suggested that these fluctuations may also be caused by oscillations of the photosphere. However, V612 Sct was classified as a nova imposter due to its unusually massive ejecta (~ 7–9×10^{-4} $M_{\odot}$), far exceeding typical nova values. This raised the possibility that the transient originated from a very low-mass WD or represented a different type of eruptive event.

6.5.2.4 Multiple ejections and shocks?

Another plausible explanation for the multiple peaks is episodic mass ejection during the nova outburst. Aydi et al. (2024) proposed that repeated mass ejections could naturally produce multiple brightening phases. Csák et al. (2005) noted that hydrogen burning on the WD surface is inherently unstable, and episodes of expanding photospheres can trigger successive ejections. If dense shells are

expelled at different times, their collisions can generate shocks, which heat the gas to very high temperatures and accelerate particles to relativistic speeds. This process can lead to both thermal and non-thermal radiation.

Such shock-related emission is supported by observations of GeV γ-rays in over 20 novae[‡‡] (see Chomiuk et al. 2021a and references therein). Many of these novae, including V1369 Cen and V5668 Sag (Cheung et al. 2016), V357 Mus (Gordon et al. 2021), V549 Vel (Li et al. 2020), V1405 Cas (Buson et al. 2021), and V1723 Sco (Cheung 2024; Cheung & Jean 2024), exhibit light curves with multiple peaks. Notably, V5856 Sgr (ASASSN-16ma) showed a direct correlation between optical rebrightening and γ-ray peaks (Li et al. 2017), suggesting that much of the optical emission may be reprocessed radiation from shock-heated plasma. This connection was further confirmed in V906 Car (ASASSN-18fv), where Aydi et al. (2020a) detected γ-ray emission approximately 5.3 hours before the optical peak. Their spectra revealed signs of multiple interacting flows and ongoing shocks in the nova ejecta.

However, there are exceptions. For instance, in the case of V549 Vel (Li et al. 2020), no clear correlation was found between the optical and γ-ray light curves. This implies that optical rebrightenings are not always a direct result of shock reprocessing and that other physical mechanisms may also play a role.

6.5.2.5 Increasing time gap between multiple peaks of the lightcurve

As outlined in earlier sections, AT 2023tkw exhibits pronounced modulations in its light curve from the time of detection until the final observation. The most prominent of these are four distinct peaks, as shown in Figure 6.4. A periodogram

[‡‡] https://asd.gsfc.nasa.gov/Koji.Mukai/novae/novae.html

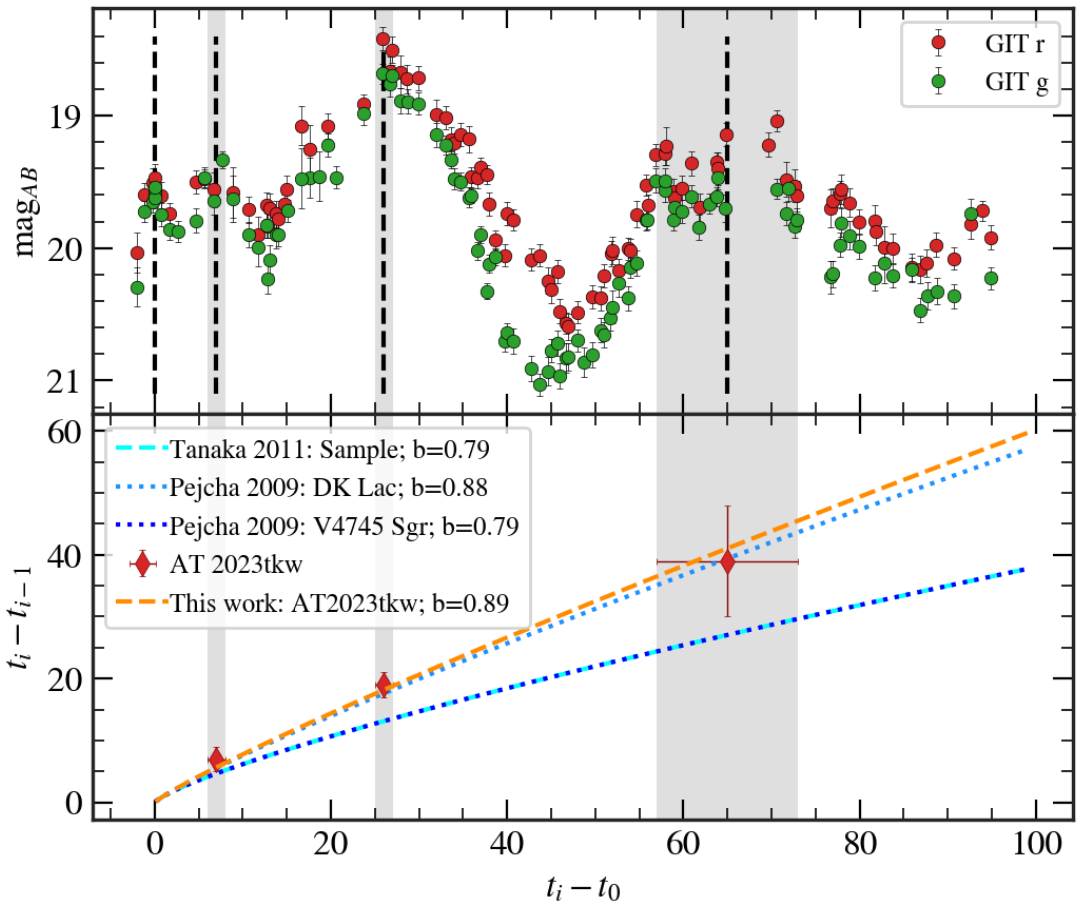

FIGURE 6.9: *Top:* Light curve of AT 2023tkw with the epochs of rebrightenings indicated by vertical dashed lines; shaded regions represent the uncertainties. *Bottom:* Time intervals between consecutive maxima plotted against time since the first peak. The best-fit log–log relation is overplotted, alongside similar results from the literature. The proportionality constant b from the fit is provided in the legend.

analysis of these peaks revealed no strong signal, suggesting that the modulations are not driven by orbital motion or other periodic physical processes.

Pejcha (2009) proposed that such rebrightenings may stem from instabilities in hydrogen burning and suggested a potential connection to the decline rate. In contrast, Strope et al. (2010a) argued that these peaks could occur randomly, questioning a definite cause.

The existence of long-term rebrightening cycles was first noted by Bianchini et al.

(1992), who proposed that they could result from an interplay between gas and radiation pressure when the system operates below the Eddington limit. Both Csák et al. (2005) and Ak et al. (2005) observed that the time intervals between successive peaks increase linearly for novae like V4745 Sgr and V2540 Oph. Tanaka et al. (2011a) further examined this behaviour across a sample of novae, identifying an approximately linear trend between $(t_i - t_{i-1})$ and $(t_i - t_0)$ as described by the following equation:

$$\log\left(t_i - t_{i-1}\right) = b \log\left(t_i - t_0\right); \quad i \in \mathbb{N} \tag{6.4}$$

where t_i is the time of the i^{th} maximum from the first maxima t_0.

Upon looking at the time intervals between successive peaks for AT 2023tkw, we found a correlation between each interval and the elapsed time since the initial maximum (Figure 6.9). The best-fit slope was found to be $b = 0.89 \pm 0.12$ using least-squares minimisation, in agreement with estimates for other novae by Pejcha (2009) and Tanaka et al. (2011a).

An alternative explanation was offered by Ak et al. (2005), who proposed an intermediate polar (IP) model for V2540 Oph. Similarly, V4745 Sgr was suspected to be an IP by Dobrotka et al. (2006). The idea that IP systems exhibit rebrightenings is not new. Retter (2002a,b) noted that the instability of lighter accretion disks in IPs post-eruption can lead to disk oscillations. As the disk gradually reforms and stabilises, the rebrightenings become weaker and less frequent. However, this explanation is applicable to rebrightenings that follow the primary brightest peak. In contrast, AT 2023tkw shows two modest peaks before reaching its main maximum (see Figure 6.9), making the IP model less likely in this case.

Steinberg & Metzger (2020) explored how introducing delayed mass ejections at

different times could trigger shocks between successive ejecta layers. These alternating fast and slow flows can create multiple shocks, potentially producing correlated peaks in both γ-ray and optical emission. The non-uniform spacing of the peaks reflects the timing of individual ejection events within the expanding envelope.

6.5.3 Implication of shocks and/or free-free emission on the peak spectrum

As discussed in §6.4.3.1, the observed spectra of AT 2023tkw generally show good agreement with the `PHOENIX` model spectra. However, the optical spectrum at the primary maximum (second panel of Figure 6.7) displays a noticeable deviation from the `PHOENIX` atmosphere models. This discrepancy leads us to ask if the emission at peak brightness arises solely from an expanding photosphere. It suggests the involvement of additional physical processes during the maxima.

As mentioned in earlier sections, emissions produced by shocks in the UV and X-ray regimes can be reprocessed and emerge in the optical band, potentially contributing significantly to the observed optical spectrum (Chomiuk et al. 2021a). Although γ-ray data are unavailable for AT 2023tkw, the possibility of reprocessed shock emission influencing the optical peak remains plausible. Given recent discoveries of correlated γ-ray and optical emission in novae, it is likely that such processes are common. Forthcoming observations capable of capturing both optical and GeV emission simultaneously will provide clearer insight into this scenario.

Another explanation for the mismatch between observations and the `PHOENIX` models is the contribution of free-free emission from the ejected material. Fast novae are known to exhibit spectra dominated by free-free emission, rather than by the photospheric radiation of an optically thick envelope (Hachisu & Kato 2006). In

contrast, slow novae tend to show a more substantial contribution from the photosphere (see Figure 3 in Hachisu & Kato 2015). In such cases, the optical emission comprises both blackbody radiation and optically thick free-free emission. As the ejecta continues to expand, the photospheric component becomes more dominant near the peak. As it declines, the photosphere shrinks and eventually, as recombination sets in and the ejecta becomes optically thin, photoionised, reprocessed radiation takes over.

6.6 Summary

In this work, we have conducted a comprehensive study of the extragalactic slow nova AT 2023tkw, discovered in M31 through the GIT transient detection pipeline. The nova exhibits a complex optical light curve with multiple peaks and shallow dips, and was followed up extensively with optical imaging and spectroscopy. Our analysis suggests that the multiple peaks in the light curve are likely the result of internal shocks that heat the ejecta. Each successive rebrightening occurring after increasingly longer intervals indicates the presence of shock episodes originating within or near the photosphere. Spectroscopic observations near the primary maximum show signatures of an additional emission component beyond the expanding photosphere, possibly arising from shock-heated ionised gas. Through detailed spectral modelling using stellar atmosphere codes, we find evidence for the expansion and subsequent contraction of the photosphere across the light curve, leading to lower temperatures near peak brightness and higher temperatures during the decline. These variations in the photospheric radius and hence the temperature are plausibly driven by internal shocks. At later stages, once the ejecta becomes optically thin, photoionisation processes begin to dominate. Modelling the NIR spectrum during this phase yields an ejecta mass estimate of $\geq 10^{-4}$ $M_{\odot}$. Finally, comparing our observational results with theoretical models, we infer the system

has a low-mass WD (0.65 $M_\odot$) accreting slowly at a rate of 5×10^{-13} $M_\odot$ yr^{-1} from a cool K-type evolved companion. These properties are consistent with a slowly evolving nova system.

Chapter 7

Summary and Future Work

"If I have seen further, it is by standing on the shoulders of Giants."

— Isaac Newton

7.1 Summary of the thesis work

This thesis presents a multi-wavelength investigation of nova systems through four different studies, advancing our understanding of classical and recurrent novae and their role as astrophysical laboratories.

7.1.1 Key Scientific Contributions

AstroSat UVIT archival data analysis produced the first comprehensive UV catalogue of M31 novae. 42 novae were identified in the archives at different phases of

evolution: outburst and quiescence. Robust detection algorithms and photometric techniques provide frameworks for future extragalactic nova surveys.

M31N 2008-12a, with its 1-year recurrence period, provided insights through 2017-2024 eruption observations. Discovery of jet-like bipolar structures sheds light on nova explosion geometry, suggesting complex 3D ejecta morphologies. Anti-correlated UV–X-ray emission hints at activities of a nascent disk, confirming its presence soon after the outburst. Accretion is resumed early in this system with a massive WD, which could be a type Ia supernova progenitor.

Simultaneous UV and X-ray observations of the 2024 eruption of LMCN 1968-12a show that accretion disks can survive nova eruptions in rapidly recurring systems. The double-peaked X-ray emission with systematic dips potentially from nova super-remnants suggests large structures in the circumstellar environments in recurring systems.

The discovery of multiple optical light curve peaks in CN AT 2023tkw was attributed to internal shock mechanisms, challenging traditional models and demonstrating the importance of shock-induced heating, advancing understanding of nova explosions.

7.1.2 Connecting the Dots: The Multi-wavelength Trump Card

The work presented in this thesis provides a comprehensive view of (extragalactic) novae across different classes and evolutionary phases of outburst.

Comparison between classical (AT 2023tkw) and rapidly recurring (M31N 2008-12a, LMCN 1968-12a) systems demonstrates excellent diversity of quiescent counterparts and outburst properties, observable at different wavelength regimes. (Nearly) Simultaneous optical, UV, and X-ray data provide complementary information about different physical processes occurring at different emission regions of these binary systems.

This thesis demonstrates that novae are complex astrophysical laboratories providing unique insights into binary evolution, shock mechanisms, accretion physics, galactic chemical enrichment, and explosive phenomena physics. The multi-faceted approach combining discovery, characterisation, and population studies provides a comprehensive foundation for advancing our understanding of these cataclysmic systems.

7.2 Future Prospects

7.2.1 Nova super-remnants in the vicinity of recurrent novae

New discoveries of nova super-remnants around the circumbinary material (CBM) of recurrent novae have sparked vigour among scientists as they provide direct evidence for the long-term impact of repeated eruptions on the circumbinary environment. These extended structures, formed by the accumulation of ejected material over thousands of years, offer unique insights into the evolutionary history of RN systems and their interaction with the ISM.

7.2.1.1 Optical Hα Observations of Nova Super-remnants

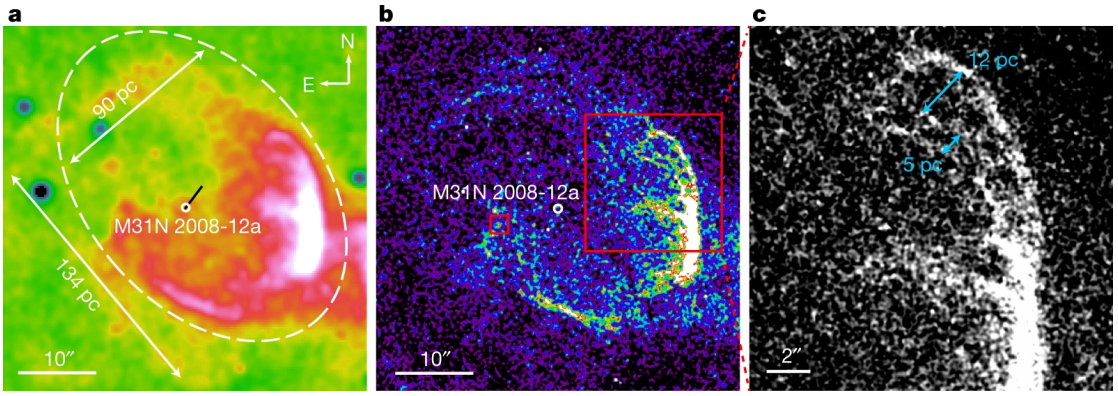

FIGURE 7.1: *(a)*: Narrow-band Hα + [N II] continuum-subtracted image from the Liverpool Telescope revealed a closed, elliptical nebulosity encircling M31N 2008-12a. The position of M31N 2008-12a is indicated; note the offset from the geometric center of the observed nebula. *(b)*: Higher spatial resolution HST Hα + [N II] continuum-subtracted imaging of the identical region shows that the nebulosity is not uniform, but rather exhibits a clumpy and filamentary nature. *(c)* A zoomed-in section shows the presence of filaments. Image adapted from Darnley et al. (2019c).

Optical narrow-band Hα imaging is the primary technique for detecting nova super-remnants. The first detection was around M31N 2008-12a, revealing an elliptical shell structure of 130 pc × 90 pc (Darnley et al. 2015c, 2019c) as shown in Figure 7.1. The formation mechanism involves repeated ejection of material during each eruption at velocities exceeding 1000 km s^{-1}. It sweeps up interstellar medium over millions of years, creating cavities and accumulating in shell-like structures.

Subsequent discoveries of super-remnants include KT Eri (50 pc diameter, Shara et al. 2024a), RS Oph (70 pc diameter, Shara et al. 2025), and T CrB (30 pc diameter, Shara et al. 2024b).

Extremely low surface brightness (21-23 mag arcsec^{-2}) makes the observations of these structures challenging, requiring deep exposures, wide FoVs, and continuum subtraction. Hydrodynamical simulations predict that such structures should

be common around all RNe, though only those with massive WDs and shortest recurrence periods have observable super-remnants (Healy-Kalesh et al. 2023).

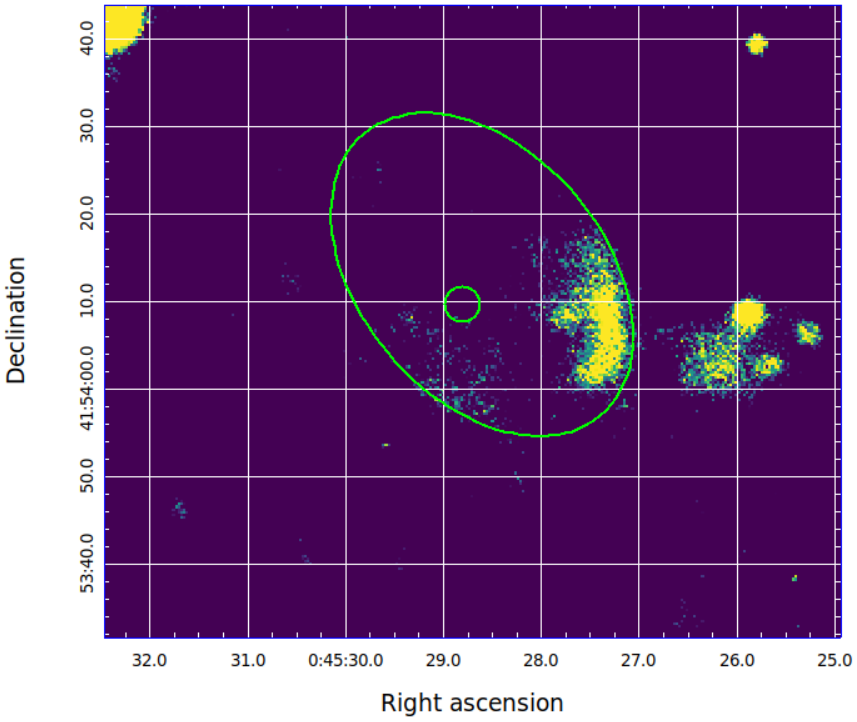

FIGURE 7.2: HCT Hα image of the surroundings of M31N 2008-12a revealing a part of the super-remnant. The green ellipse is reproduced from Darnley et al. (2019c). The green circle locates the nova.

Systematic surveys of M31 recurrent novae have been limited by observation depth. Healy-Kalesh et al. (2024b) searched 20 M31 and 4 LMC systems but found only the known M31N 2008-12a remnant, likely due to the 20 mag survey limit. Super-remnant size and brightness provide clues to WD mass, accretion rate, and recurrence period. M31 hosts 11 RRN, compared to only 2 in our galaxy (Darnley & Henze 2020). This presents us with a golden opportunity to investigate such structures in M31. We have initiated a survey of M31 RRNe fields in Hα and r' bands using HCT/HFOSC to push toward 23 mag arcsec^{-2} sensitivity, which is expected to significantly increase detection rates. Analysis of the M31N 2008-12a field revealed the known super-remnant as shown in Figure 7.2. This encourages us to look for more of them in deeper images of other RRNe in M31.

7.2.1.2 FUV Detection Capabilities

FUV observations represent a complementary technique for detecting nova super-remnants, offering unique advantages for studying hot, shocked gas components. The UV emission arises from collisional excitation in shock-heated gas and continuum emission from hot stellar populations.

Deep observations by UVIT have provided hints of super-remnant structure in the FUV images around M31N 2008-12a, revealing extended emission features tracing portions of the Balmer Hα-detected remnant. FUV data have reduced stellar contamination and enhanced sensitivity towards detecting shock-heated gas.

The combination of optical Hα and FUV observations provides a comprehensive approach to super-remnant characterisation. Multi-wavelength studies can distinguish emission mechanisms, map temperature and density structure, and provide information about the energetics of the remnant structure. As observational capabilities improve, these studies will provide detailed insights into recurrent nova lifecycles and their role in galactic chemical evolution.

7.2.2 Short-term UV variability in M31N 2008-12a?

Repeated FUV observations of M31N 2008-12a with UVIT during its outburst offer a rich dataset to investigate short-term variability in the FUV band. Each UVIT visit consists of multiple 'orbit-wise images', i.e., individual exposures lasting 500–1500 s, captured during AstroSat's each orbit around Earth. Analysing these orbit-wise images can provide insights into the nature of FUV emission on sub-day timescales. It would help to probe photospheric activity following the outburst and disk activity within the subsequent two weeks of the outburst. Higher

time-resolution light curves can also be extracted using `curvit` (Joseph et al. 2021), though this comes at the cost of reduced SNR. We aim to optimise this approach to determine an appropriate temporal resolution for studying short-term variability in the FUV emission from M31N 2008-12a.

7.2.3 Ground-Based and Space-Based Survey Synergies

The multi-wavelength nova studies presented in this thesis motivate coordinated systematic survey programs combining ground-based optical and radio observations with space-based UV observations. It represents a promising pathway for advancing extragalactic nova population studies.

7.2.3.1 GIT Optical Surveys

The GIT has established capabilities for systematic nova monitoring in nearby galaxies through its M31 monitoring program. The current survey monitors the entire M31 galaxy in g' and r' bands (see Figure 7.3) with a daily cadence using an automated transient detection pipeline. It has successfully detected and followed up more than a dozen M31 novae since the start of the survey in July 2022 (Kumar et al. 2023, 2022a). Future enhancements include making the pipeline efficient for more discoveries, implementing machine learning algorithms for improved detection sensitivity and expanding monitoring to other Local Group galaxies such as M33. A complete population study of all the M31 novae detected with the GIT is planned for the future. The main goal of this project would be to estimate the M31 nova rate, addressing its large spread reported in the literature (see Table 7.1).

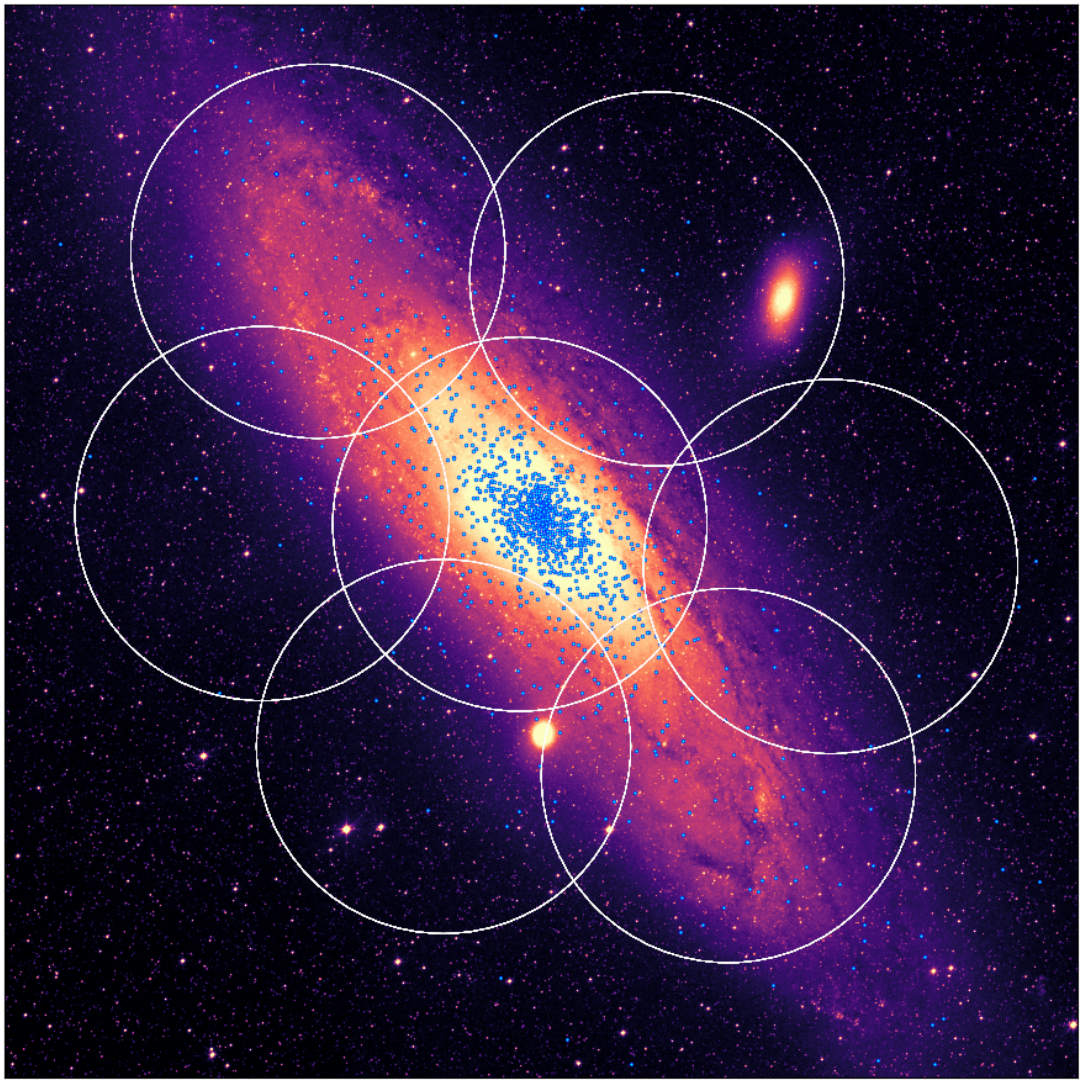

FIGURE 7.3: M31 tiling by GIT with the 7 Andor pointings. Overplotted as blue dots are all the novae detected in M31.

7.2.3.2 UVIT Coordinated Monitoring

AstroSat's UVIT provides unique capabilities in FUV for studying nova physics through coordinated monitoring of M31's central region as shown in Figure 7.4. Combining UVIT FUV observations with simultaneous GIT optical monitoring can trace complete spectral evolution and provide accurate nova rate measurements for M31. Searching for the theoretically predicted pre-maximum UV flash (Kato et al. 2015; Chomiuk et al. 2021a), is a key goal of this project. UV survey is

TABLE 7.1: M31 Nova Rate Estimates in literature

Authors	Years	Filter	Novae	Rate
Hubble (1929)	1909 – 1927	B	85	~ 30
Arp (1956)	1953 – 1954	B	30	26 ± 4
Capaccioli et al. (1989)†	1955 – 1986	U, B	142	29 ± 4
Shafter & Irby (2001)	1990 – 1997	$H\alpha$	72	37^{+12}_{-8}
Darnley et al. (2004, 2006)	1999 – 2003	r', i', g'	20	65^{+16}_{-15}
Soraisam et al. (2016)	...	...	...	~ 106
Chen et al. (2016)	...	...	...	~ 97
Rector et al. (2022) ($\theta = 1$)	1995 – 2016	$H\alpha$	253	48^{+5}_{-4}
Rector et al. (2022) ($\theta = 0.56$)	1995 – 2016	$H\alpha$	253	40^{+5}_{-4}

† Based on observations from Rosino (1964, 1973); Rosino et al. (1989)

also more useful for detecting nova systems with massive WDs, which are brighter in UV. Specialized image subtraction techniques have successfully recovered four novae in quiescence from archival UVIT data, demonstrating potential for discovering previously unknown systems. Success in detecting AT 2023yoa (M31N 2023-11f, Basu et al. 2024a) during the pilot survey, confirmed as the second eruption of M31N 2013-10c (Shafter et al. 2024a), demonstrates the effectiveness of the UV survey.

7.2.3.3 Radio Observations of M31 novae

We have also recently proposed to initiate systematic investigations of radio emission from M31 novae at different frequency bands with the upgraded Giant Metrewave Radio Telescope (uGMRT) and the Very Large Array (VLA). These will complement ongoing optical surveys of M31 novae and observations in FUV/NUV, contributing to a comprehensive multi-wavelength study. The primary goal is

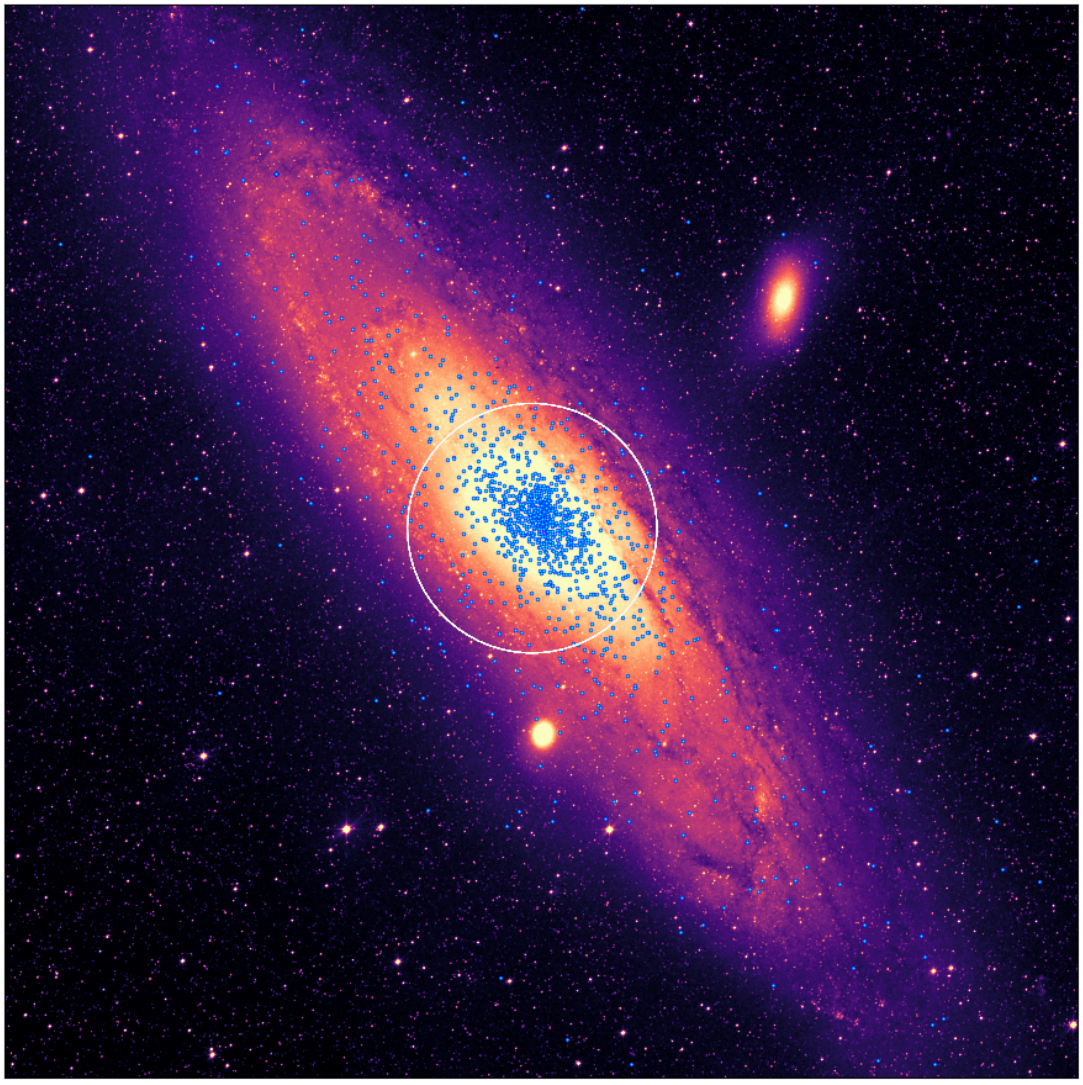

FIGURE 7.4: M31 survey region by UVIT with the central field marked. Overplotted as blue dots are all the novae detected in M31.

to detect radio emission from recently observed novae. Specifically, these observations will seek to address the ejecta mass discrepancy, where radio-derived masses are significantly larger than theoretical predictions, possibly due to clumping (Roy et al. 2012). The nature of complex, multi-component ejection, driven by internal shocks formed by a fast wind colliding with a slower outflow, has emerged as a strong model to explain nova light curves and spectra (Chomiuk et al. 2021a). These shocks are not minor features but contribute significantly to a nova's total bolometric luminosity. Radio observations will help identify the

presence of thermal Bremsstrahlung (from optically thin ionised ejecta) and/or non-thermal synchrotron (from shocked medium) emission mechanisms from these sources (Chomiuk et al. 2021b). Even in the case of non-detections, the observations will provide valuable constraints on radio emission from M31 novae.

7.2.4 Novae in upcoming surveys

7.2.4.1 Vera Rubin Observatory

The advent of new observational facilities promises to revolutionise nova studies. The Vera Rubin Observatory (Ivezić et al. 2019) will dramatically increase the rate of nova discoveries by going deeper and at a higher cadence. Rubin's all-sky coverage, consistent long-term monitoring, and well-suited cadence are ideal for tracking their evolution, enabling the discovery of fainter novae (up to ∼25 mags) at greater distances than previously possible. The survey will provide an unprecedented quantity of well-sampled light curves, leading to improved estimates of nova rates and types across the Milky Way. Crucially, for some nearby systems, Rubin may detect the quiescent system days before the actual outburst, providing new information about the eruption process. Furthermore, the survey is expected to explore the "luminosity gap" between the brightest novae and sub-luminous supernovae, potentially revealing new types of explosive transients (LSST Science Collaboration et al. 2009).

7.2.4.2 Daksha

The Daksha mission (Bhalerao et al. 2024a) will be a valuable tool for studying novae through its Earth occultation technique. It facilitates, using its twin satellites, daily flux measurements of bright hard X-ray sources and slow transients like some novae, which evolve on timescales of days. While soft X-ray emissions from novae are commonly observed, hard X-ray detections remain few, and their emission mechanisms are poorly understood (Gordon et al. 2021). Some novae, such as the 2006 eruption of RS Oph (Bode et al. 2006) and the 2015 eruption of GK Per (Tuerler et al. 2015; Zemko et al. 2015), have indeed exhibited bright hard X-ray emissions. Daksha's sensitivity in the 20–200 keV energy band indicates that it could have detected the 2021 RS Oph outburst from day 3 to 6 (Bhalerao et al. 2024b). Furthermore, Daksha is expected to detect other X-ray novae similar in brightness to MAXI J1535-571, GRS 1739-278, and MAXI J1828-249 (Bhalerao et al. 2024b).

7.2.4.3 Other Telescopes

The James Webb Space Telescope (Gardner 2023) will provide unprecedented IR capabilities for studying dust formation in the aftermath of nova eruptions. It can also track the late-time evolution with its sensitivity and unmatched resolution.

Upcoming UV missions such as *INSIST* (Subramaniam 2022), *CASTOR* (Côte et al. 2012), *UVEX* (Kulkarni et al. 2021), and *ULTRASAT* (Shvartzvald et al. 2024) hold promise for capturing novae across various stages of their UV evolution. These observations will enable detailed investigations of accretion dynamics, disk reformation, and the physical conditions of WDs during outburst and quiescence. Nova models (Kato et al. 2015) predict a UV flash, which has eluded astronomers

to date. UV surveys provide the best possibility to detect these short-lived flashes and would help constrain these models (Chomiuk et al. 2021a).

The synergy between UV monitoring and multi-wavelength surveys such as *ZTF* (Bellm et al. 2019) and *Rubin* in the optical, *XRISM* (XRISM Science Team 2020) and *Daksha* (Bhalerao et al. 2024b) in the X-rays, and the upcoming *Roman Space Telescope* in the IR (Akeson et al. 2019) is expected to play a crucial role in addressing long-standing questions related to nova eruptions and their aftermath.

7.3 Concluding Remarks

Novae serve as unique laboratories for testing fundamental physical processes under extreme conditions. Despite decades of study, many fundamental questions about nova physics remain unanswered. The three-dimensional structure of nova explosions, the role of magnetic fields, and the details of the shock physics are still being actively investigated. The relationship between novae and Type Ia supernovae remains uncertain, which is essential for our understanding of these important cosmological distance indicators.

The future of nova astronomy is promising, driven by advancing observational capabilities, sophisticated theoretical models, and modern data analysis techniques equipped with artificial intelligence.

The multi-wavelength approach will become more powerful with next-generation facilities, enabling unprecedented simultaneous observations across the electromagnetic spectrum. Large surveys will put better constraints on nova populations, while detailed studies will reveal the complex physics of these explosive systems.

Bibliography

Ak, T., Retter, A., & Liu, A. 2005, *Publications of the Astronomical Society of Australia*, 22, 298, doi: 10.1071/AS05017

Akeson, R., Armus, L., Bachelet, E., et al. 2019, arXiv e-prints, arXiv:1902.05569, doi: 10.48550/arXiv.1902.05569

Anupama, G. C., & Pavana, M. 2020, Journal of Astrophysics and Astronomy, 41, 43, doi: 10.1007/s12036-020-09661-8

Anupama, G. C., Kamath, U. S., Ramaprakash, A. N., et al. 2013a, *Astron. Astrophys.*, 559, A121, doi: 10.1051/0004-6361/201321262

—. 2013b, *Astron. Astrophys.*, 559, A121, doi: 10.1051/0004-6361/201321262

Arnaud, K. A. 1996, in Astronomical Society of the Pacific Conference Series, Vol. 101, Astronomical Data Analysis Software and Systems V, ed. G. H. Jacoby & J. Barnes, 17

Arp, H. C. 1956, *Astron. J.*, 61, 15, doi: 10.1086/107284

Ashok, N. M., & Banerjee, D. P. K. 2003, *Astron. Astrophys.*, 409, 1007, doi: 10.1051/0004-6361:20031160

Aydi, E., Page, K. L., Kuin, N. P. M., et al. 2018, *Mon. Not. Roy. Astron. Soc.*, 474, 2679, doi: 10.1093/mnras/stx2678

Aydi, E., Sokolovsky, K. V., Chomiuk, L., et al. 2020a, Nature Astronomy, 4, 776, doi: 10.1038/s41550-020-1070-y

Aydi, E., Chomiuk, L., Izzo, L., et al. 2020b, *Astrophys. J.*, 905, 62, doi: 10.3847/1538-4357/abc3bb

Aydi, E., Chomiuk, L., Mikołajewska, J., et al. 2023, *Mon. Not. Roy. Astron. Soc.*, 524, 1946, doi: 10.1093/mnras/stad1914

Aydi, E., Chomiuk, L., Strader, J., et al. 2024, *Mon. Not. Roy. Astron. Soc.*, 527, 9303, doi: 10.1093/mnras/stad3342

Balcon, C. 2020, Transient Name Server Classification Report, 2020-3397, 1

—. 2023, Transient Name Server Classification Report, 2023-3145, 1

Banerjee, D. P. K., & Ashok, N. M. 2012, Bulletin of the Astronomical Society of India, 40, 243, doi: 10.48550/arXiv.1306.0343

Barbary, K. 2021, extinction: Dust extinction laws, Astrophysics Source Code Library, record ascl:2102.026

Barsukova, E., Fabrika, S., Hornoch, K., et al. 2011, The Astronomer's Telegram, 3725, 1

Basu, J., Anupama, G. C., Ness, J.-U., et al. 2025a, *Astrophys. J.*, 994, 229, doi: 10.3847/1538-4357/ae13e1

Basu, J., Barway, S., Anupama, G. C., Chamoli, S., & Kumar, S. P. 2023a, The Astronomer's Telegram, 16367, 1

Basu, J., Chamoli, S., Barway, S., & Anupama, G. 2024a, The Astronomer's Telegram, 16526, 1

Basu, J., Chamoli, S., Barway, S., Anupama, G. C., & Surya. 2024b, The Astronomer's Telegram, 16945, 1

Basu, J., Krishnendu, S., Barway, S., Chamoli, S., & Anupama, G. C. 2024c, *Astrophys. J.*, 971, 8, doi: 10.3847/1538-4357/ad596b

Basu, J., Kumar, R., Anupama, G. C., et al. 2023b, The Astronomer's Telegram, 16311, 1

Basu, J., Pavana, M., Anupama, G. C., et al. 2024d, *Astrophys. J.*, 966, 44, doi: 10.3847/1538-4357/ad2c8e

—. 2024e, *Astrophys. J.*, 966, 44, doi: 10.3847/1538-4357/ad2c8e

Basu, J., Kumar, R., Anupama, G. C., et al. 2025b, *Astrophys. J.*, 980, 129, doi: 10.3847/1538-4357/ada5fe

Beardmore, A. P., Osborne, J. P., Page, K. L., et al. 2012a, *Astron. Astrophys.*, 545, A116, doi: 10.1051/0004-6361/201219681

—. 2012b, *Astron. Astrophys.*, 545, A116, doi: 10.1051/0004-6361/201219681

Belligoli, R. 2020, Transient Name Server Discovery Report, 2020-3354, 1

Bellm, E. C., Kulkarni, S. R., Graham, M. J., et al. 2019, *Pub. Astron. Soc. Pac.*, 131, 018002, doi: 10.1088/1538-3873/aaecbe

Bertin, E. 2006, in Astronomical Society of the Pacific Conference Series, Vol. 351, Astronomical Data Analysis Software and Systems XV, ed. C. Gabriel, C. Arviset, D. Ponz, & S. Enrique, 112

Bertin, E. 2010, SWarp: Resampling and Co-adding FITS Images Together, Astrophysics Source Code Library, record ascl:1010.068

Bertin, E. 2011, in Astronomical Society of the Pacific Conference Series, Vol. 442, Astronomical Data Analysis Software and Systems XX, ed. I. N. Evans, A. Accomazzi, D. J. Mink, & A. H. Rots, 435

Bertin, E., & Arnouts, S. 1996a, *Astron. Astrophys. Suppl.*, 117, 393, doi: 10.1051/aas:1996164

—. 1996b, *Astron. Astrophys. Suppl.*, 117, 393, doi: 10.1051/aas:1996164

Bertin, E., Mellier, Y., Radovich, M., et al. 2002, in Astronomical Society of the Pacific Conference Series, Vol. 281, Astronomical Data Analysis Software and Systems XI, ed. D. A. Bohlender, D. Durand, & T. H. Handley, 228

Bhalerao, V., Vadawale, S., Tendulkar, S., et al. 2024a, Experimental Astronomy, 57, 24, doi: 10.1007/s10686-024-09926-y

Bhalerao, V., Sawant, D., Pai, A., et al. 2024b, Experimental Astronomy, 57, 23, doi: 10.1007/s10686-024-09923-1

Bhattacharyya, S., Singh, K. P., Stewart, G., et al. 2021, Journal of Astrophysics and Astronomy, 42, 17, doi: 10.1007/s12036-020-09678-z

Bianchini, A., Friedjung, M., & Brinkmann, W. 1992, *Astron. Astrophys.*, 257, 599

Bode, M. F., Harman, D. J., O'Brien, T. J., et al. 2007, *Astrophys. J. Lett.*, 665, L63, doi: 10.1086/520929

Bode, M. F., & Kahn, F. D. 1985a, *Mon. Not. Roy. Astron. Soc.*, 217, 205, doi: 10.1093/mnras/217.1.205

—. 1985b, *Mon. Not. Roy. Astron. Soc.*, 217, 205, doi: 10.1093/mnras/217.1.205

Bode, M. F., O'Brien, T. J., Osborne, J. P., et al. 2006, *Astrophys. J.*, 652, 629, doi: 10.1086/507980

Bode, M. F., Darnley, M. J., Beardmore, A. P., et al. 2016, *Astrophys. J.*, 818, 145, doi: 10.3847/0004-637X/818/2/145

Borczyk, W., Schwarzenberg-Czerny, A., & Szkody, P. 2003, *Astron. Astrophys.*, 405, 663, doi: 10.1051/0004-6361:20030390

Boyd, D., Hornoch, K., Henze, M., et al. 2017, The Astronomer's Telegram, 11116, 1

Bradley, L., Sipőcz, B., Robitaille, T., et al. 2023, astropy/photutils: 1.8.0, 1.8.0, Zenodo, doi: 10.5281/zenodo.7946442

Breeveld, A. A., Landsman, W., Holland, S. T., et al. 2011, in American Institute of Physics Conference Series, Vol. 1358, Gamma Ray Bursts 2010, ed. J. E. McEnery, J. L. Racusin, & N. Gehrels, 373–376, doi: 10.1063/1.3621807

Burrows, D. N., Hill, J. E., Nousek, J. A., et al. 2005, *Space Sci. Rev.*, 120, 165, doi: 10.1007/s11214-005-5097-2

Buson, S., Cheung, C. C., & Jean, P. 2021, The Astronomer's Telegram, 14658, 1

Campaner, P. 2019, Transient Name Server Discovery Report, 2019-2301, 1

Cao, Y., Kasliwal, M. M., Neill, J. D., et al. 2012, *Astrophys. J.*, 752, 133, doi: 10.1088/0004-637X/752/2/133

Capaccioli, M., Della Valle, M., D'Onofrio, M., & Rosino, L. 1989, *Astron. J.*, 97, 1622, doi: 10.1086/115104

Cardelli, J. A., Clayton, G. C., & Mathis, J. S. 1989, *Astrophys. J.*, 345, 245, doi: 10.1086/167900

Carey, G. 2019, Transient Name Server Discovery Report, 2019-1970, 1

Chambers, K. C., Magnier, E. A., Metcalfe, N., et al. 2016, arXiv e-prints, arXiv:1612.05560, doi: 10.48550/arXiv.1612.05560

Chamoli, S., Basu, J., Barway, S., et al. 2025, Challenging Classical Paradigms: Recurrent Nova M31N 2017-01e, a BeWD system in M31? https://arxiv.org/abs/2508.02227

Chatzikos, M., Bianchi, S., Camilloni, F., et al. 2023, *Revista Mexicana de Astronomía y Astrofísica*, 59, 327, doi: 10.22201/ia.01851101p.2023.59.02.12

Chen, H.-L., Woods, T. E., Yungelson, L. R., Gilfanov, M., & Han, Z. 2016, *Mon. Not. Roy. Astron. Soc.*, 458, 2916, doi: 10.1093/mnras/stw458

Cheung, C. C. 2024, The Astronomer's Telegram, 16439, 1

Cheung, C. C., & Jean, P. 2024, The Astronomer's Telegram, 16441, 1

Cheung, C. C., Jean, P., Shore, S. N., et al. 2016, *Astrophys. J.*, 826, 142, doi: 10.3847/0004-637X/826/2/142

Chomiuk, L., Metzger, B. D., & Shen, K. J. 2021a, *Ann. Rev. Astron. Astrophys.*, 59, 391, doi: 10.1146/annurev-astro-112420-114502

Chomiuk, L., Linford, J. D., Aydi, E., et al. 2021b, *Astrophys. J. Suppl.*, 257, 49, doi: 10.3847/1538-4365/ac24ab

Ciardullo, R., Ford, H. C., Neill, J. D., Jacoby, G. H., & Shafter, A. W. 1987, *Astrophys. J.*, 318, 520, doi: 10.1086/165388

Clark, J. G., Hornoch, K., Shafter, A. W., et al. 2024, *Astrophys. J. Suppl.*, 272, 28, doi: 10.3847/1538-4365/ad3c39

Conseil, E. 2018, Transient Name Server Discovery Report, 2018-597, 1

—. 2019, Transient Name Server Discovery Report, 2019-1718, 1

Côte, P., Scott, A., Balogh, M., et al. 2012, in Society of Photo-Optical Instrumentation Engineers (SPIE) Conference Series, Vol. 8442, Space Telescopes and Instrumentation 2012: Optical, Infrared, and Millimeter Wave, ed. M. C. Clampin, G. G. Fazio, H. A. MacEwen, & J. Oschmann, Jacobus M., 844215, doi: 10.1117/12.926198

Csák, B., Kiss, L. L., Retter, A., Jacob, A., & Kaspi, S. 2005, *Astron. Astrophys.*, 429, 599, doi: 10.1051/0004-6361:20035751

Cushing, M. C., Vacca, W. D., & Rayner, J. T. 2004, *Pub. Astron. Soc. Pac.*, 116, 362, doi: 10.1086/382907

Dahiwale, A., & Fremling, C. 2020, Transient Name Server Classification Report, 2020-2139, 1

Dalcanton, J. J., Fouesneau, M., Hogg, D. W., et al. 2015, *Astrophys. J.*, 814, 3, doi: 10.1088/0004-637X/814/1/3

Darnley, M. J. 2020, The Astronomer's Telegram, 14138, 1

Darnley, M. J. 2021, in The Golden Age of Cataclysmic Variables and Related Objects V, Vol. 2-7, 44, doi: 10.22323/1.368.0044

Darnley, M. J., & Healy, M. W. 2022, The Astronomer's Telegram, 15788, 1

Darnley, M. J., Healy, M. W., Henze, M., & Williams, S. C. 2017a, The Astronomer's Telegram, 11117, 1

Darnley, M. J., Healy, M. W., & Williams, S. C. 2018a, The Astronomer's Telegram, 11983, 1

Darnley, M. J., & Henze, M. 2020, Advances in Space Research, 66, 1147, doi: 10.1016/j.asr.2019.09.044

Darnley, M. J., Henze, M., Hachisu, I., et al. 2019a, The Astronomer's Telegram, 13274, 1

—. 2019b, The Astronomer's Telegram, 13290, 1

Darnley, M. J., Henze, M., Shafter, A. W., et al. 2018b, The Astronomer's Telegram, 12177

—. 2018c, The Astronomer's Telegram, 12179, 1

Darnley, M. J., Henze, M., Shafter, A. W., & Kato, M. 2015a, The Astronomer's Telegram, 7964, 1

—. 2015b, The Astronomer's Telegram, 7965, 1

Darnley, M. J., Kuin, N. P. M., & Page, K. L. 2024, The Astronomer's Telegram, 16752, 1

Darnley, M. J., & Pag, K. L. 2021a, The Astronomer's Telegram, 15040, 1

—. 2021b, The Astronomer's Telegram, 15050, 1

Darnley, M. J., & Page, K. L. 2020, The Astronomer's Telegram, 14142, 1

Darnley, M. J., Page, K. L., & Healy, M. W. 2022, The Astronomer's Telegram, 15798, 1

Darnley, M. J., Page, K. L., & Henz, M. 2020a, The Astronomer's Telegram, 14152, 1

Darnley, M. J., Ribeiro, V. A. R. M., Bode, M. F., Hounsell, R. A., & Williams, R. P. 2012, *Astrophys. J.*, 746, 61, doi: 10.1088/0004-637X/746/1/61

Darnley, M. J., Shafter, A. W., Kafka, S., Williams, S., & Henze, M. 2020b, The Astronomer's Telegram, 14130, 1

Darnley, M. J., & Williams, S. C. 2016a, The Astronomer's Telegram, 8710, 1

—. 2016b, The Astronomer's Telegram, 9143, 1

Darnley, M. J., Williams, S. C., Bode, M. F., et al. 2014, *Astron. Astrophys.*, 563, L9, doi: 10.1051/0004-6361/201423411

Darnley, M. J., Bode, M. F., Kerins, E., et al. 2004, *Mon. Not. Roy. Astron. Soc.*, 353, 571, doi: 10.1111/j.1365-2966.2004.08087.x

—. 2006, *Mon. Not. Roy. Astron. Soc.*, 369, 257, doi: 10.1111/j.1365-2966.2006.10297.x

Darnley, M. J., Henze, M., Steele, I. A., et al. 2015c, *Astron. Astrophys.*, 580, A45, doi: 10.1051/0004-6361/201526027

Darnley, M. J., Henze, M., Bode, M. F., et al. 2016, *Astrophys. J.*, 833, 149, doi: 10.3847/1538-4357/833/2/149

Darnley, M. J., Hounsell, R., Godon, P., et al. 2017b, *Astrophys. J.*, 849, 96, doi: 10.3847/1538-4357/aa9062

—. 2017c, *Astrophys. J.*, 847, 35, doi: 10.3847/1538-4357/aa8867

Darnley, M. J., Hounsell, R., O'Brien, T. J., et al. 2019c, *Nature*, 565, 460, doi: 10.1038/s41586-018-0825-4

—. 2019d, *Nature*, 565, 460, doi: 10.1038/s41586-018-0825-4

Darnley, M. J., Oksanen, A., Henze, M., et al. 2019e, The Astronomer's Telegram, 13273, 1

Dekany, R., Smith, R. M., Riddle, R., et al. 2020, Publications of the Astronomical Society of the Pacific, 132, 038001, doi: 10.1088/1538-3873/ab4ca2

Delvaux, C., Greiner, J., & Pietsch, W. 2015, The Astronomer's Telegram, 7104, 1

Dobrotka, A., Retter, A., & Liu, A. 2006, *Mon. Not. Roy. Astron. Soc.*, 371, 459, doi: 10.1111/j.1365-2966.2006.10683.x

Doherty, C. L., Gil-Pons, P., Siess, L., Lattanzio, J. C., & Lau, H. H. B. 2015, *Mon. Not. Roy. Astron. Soc.*, 446, 2599, doi: 10.1093/mnras/stu2180

Dolphin, A. 2016, DOLPHOT: Stellar photometry, Astrophysics Source Code Library, record ascl:1608.013

Dolphin, A. E. 2000, *Pub. Astron. Soc. Pac.*, 112, 1383, doi: 10.1086/316630

Draine, B. T., Aniano, G., Krause, O., et al. 2014, *Astrophys. J.*, 780, 172, doi: 10.1088/0004-637X/780/2/172

Evans, A., Banerjee, D. P. K., Geballe, T. R., et al. 2025, *Mon. Not. Roy. Astron. Soc.*, 536, 1710, doi: 10.1093/mnras/stae2711

Evans, A., Banerjee, D. P. K., Woodward, C. E., et al. 2023, *Mon. Not. Roy. Astron. Soc.*, 522, 4841, doi: 10.1093/mnras/stad1209

Evans, A., Gehrz, R. D., Geballe, T. R., et al. 2003, *Astron. J.*, 126, 1981, doi: 10.1086/377618

Evans, P. A., Page, K. L., Osborne, J. P., et al. 2020, The Astrophysical Journal Supplement Series, 247, 54, doi: 10.3847/1538-4365/ab7db9

Fabrika, S., Barsukova, E. A., Valeev, A. F., et al. 2015, The Astronomer's Telegram, 7158, 1

Fabrika, S., Sholukhova, O., Sarkisyan, A., et al. 2020, The Astronomer's Telegram, 14217, 1

Fabrika, S., Sholukhova, O., Solovyeva, Y., et al. 2019, The Astronomer's Telegram, 13230, 1

Fabrika, S., Sholukhova, O., Valeev, A. F., et al. 2016a, The Astronomer's Telegram, 9557, 1

—. 2016b, The Astronomer's Telegram, 9563, 1

—. 2016c, The Astronomer's Telegram, 9443, 1

Ferland, G. J., & Shields, G. A. 1978, *Astrophys. J.*, 226, 172, doi: 10.1086/156597

Ferland, G. J., Chatzikos, M., Guzmán, F., et al. 2017a, *Revista Mexicana de Astronomía y Astrofísica*, 53, 385, doi: 10.48550/arXiv.1705.10877

—. 2017b, *Revista Mexicana de Astronomía y Astrofísica*, 53, 385, doi: 10.48550/arXiv.1705.10877

Figueira, J., José, J., Cabezón, R., & García-Senz, D. 2025, *Astron. Astrophys.*, 693, A209, doi: 10.1051/0004-6361/202449972

Frank, J., King, A., & Raine, D. 1992, Accretion power in astrophysics., Vol. 21

Fremling, C. 2020, Transient Name Server Discovery Report, 2020-3674, 1

Fryxell, B., Olson, K., Ricker, P., et al. 2000, *Astrophys. J. Suppl.*, 131, 273, doi: 10.1086/317361

Fukue, J. 2002, in 8th Asian-Pacific Regional Meeting, Volume II, ed. S. Ikeuchi, J. Hearnshaw, & T. Hanawa, 325–326

Galloway, D. K., Ackley, K., Wiersema, K., et al. 2020, The Astronomer's Telegram, 14141, 1

Gardner, J. 2023, in APS Meeting Abstracts, Vol. 2023, APS April Meeting Abstracts, A01.001

Gehrels, N., Chincarini, G., Giommi, P., et al. 2004, *Astrophys. J.*, 611, 1005, doi: 10.1086/422091

Gehrz, R. D., Truran, J. W., Williams, R. E., & Starrfield, S. 1998a, *Pub. Astron. Soc. Pac.*, 110, 3, doi: 10.1086/316107

—. 1998b, *Pub. Astron. Soc. Pac.*, 110, 3, doi: 10.1086/316107

Ginsburg, A., Sipőcz, B. M., Brasseur, C. E., et al. 2019, *Astron. J.*, 157, 98, doi: 10.3847/1538-3881/aafc33

Gordon, A. C., Aydi, E., Page, K. L., et al. 2021, *Astrophys. J.*, 910, 134, doi: 10.3847/1538-4357/abe547

Graham, M. J., Kulkarni, S. R., Bellm, E. C., et al. 2019, Publications of the Astronomical Society of the Pacific, 131, 078001, doi: 10.1088/1538-3873/ab006c

Grevesse, N., Asplund, M., Sauval, A. J., & Scott, P. 2010, *Astrophys. Space Sci.*, 328, 179, doi: 10.1007/s10509-010-0288-z

Hachisu, I., & Kato, M. 2006, *Astrophys. J. Suppl.*, 167, 59, doi: 10.1086/508063

—. 2015, *Astrophys. J.*, 798, 76, doi: 10.1088/0004-637X/798/2/76

Hachisu, I., Kato, M., Kato, T., & Matsumoto, K. 2000, *Astrophys. J. Lett.*, 528, L97, doi: 10.1086/312428

Hachisu, I., Kato, M., & Nomoto, K. 1996, *Astrophys. J. Lett.*, 470, L97, doi: 10.1086/310303

Harris, C. R., Millman, K. J., van der Walt, S. J., et al. 2020, *Nature*, 585, 357, doi: 10.1038/s41586-020-2649-2

Harris, W. E. 2018, *Astron. J.*, 156, 296, doi: 10.3847/1538-3881/aaedb8

Hathi, N. P. 2024, in ACS Data Handbook v. 13.0, Vol. 13, 13

Hauschildt, P. H. 2008, in Classical Novae, ed. M. F. Bode & A. Evans, Vol. 43, 102–120, doi: 10.1017/CBO9780511536168.007

Hauschildt, P. H., & Baron, E. 1995, *Journal of Quantitative Spectroscopy and Radiative Transfer*, 54, 987, doi: 10.1016/0022-4073(95)00118-5

Hauschildt, P. H., Shore, S. N., Schwarz, G. J., et al. 1997, *Astrophys. J.*, 490, 803, doi: 10.1086/304904

Healy-Kalesh, M. W., Darnley, M. J., Harvey, É. J., et al. 2023, *Mon. Not. Roy. Astron. Soc.*, 521, 3004, doi: 10.1093/mnras/stad617

Healy-Kalesh, M. W., Darnley, M. J., Harvey, É. J., & Newsam, A. M. 2024a, *Mon. Not. Roy. Astron. Soc.*, 529, L175, doi: 10.1093/mnrasl/slae016

Healy-Kalesh, M. W., Darnley, M. J., Shara, M. M., et al. 2024b, *Mon. Not. Roy. Astron. Soc.*, 529, 236, doi: 10.1093/mnras/stad3190

Healy-Kalesh, M. W., Sasaki, M., Points, S. D., et al. 2025, *Astron. Astrophys.*, 702, L9, doi: 10.1051/0004-6361/202556670

Henze, M., Darnley, M. J., Kabashima, F., et al. 2015a, *Astron. Astrophys.*, 582, L8, doi: 10.1051/0004-6361/201527168

Henze, M., Darnley, M. J., Shafter, A. W., et al. 2016a, The Astronomer's Telegram, 9853, 1

—. 2016b, The Astronomer's Telegram, 9872, 1

—. 2018a, The Astronomer's Telegram, 12182, 1

—. 2018b, The Astronomer's Telegram, 11121, 1

—. 2018c, The Astronomer's Telegram, 11130, 1

—. 2018d, The Astronomer's Telegram, 12207, 1

Henze, M., Ness, J. U., Darnley, M. J., et al. 2014a, *Astron. Astrophys.*, 563, L8, doi: 10.1051/0004-6361/201423410

Henze, M., Pietsch, W., Haberl, F., et al. 2010, *Astron. Astrophys.*, 523, A89, doi: 10.1051/0004-6361/201014710

—. 2011, *Astron. Astrophys.*, 533, A52, doi: 10.1051/0004-6361/201015887

—. 2014b, *Astron. Astrophys.*, 563, A2, doi: 10.1051/0004-6361/201322426

Henze, M., Ness, J.-U., Darnley, M. J., et al. 2015b, *Astron. Astrophys.*, 580, A46, doi: 10.1051/0004-6361/201526028

Henze, M., Darnley, M. J., Shafter, A. W., et al. 2015c, The Astronomer's Telegram, 7984, 1

Henze, M., Darnley, M. J., Williams, S. C., et al. 2018e, *Astrophys. J.*, 857, 68, doi: 10.3847/1538-4357/aab6a6

—. 2018f, *Astrophys. J.*, 857, 68, doi: 10.3847/1538-4357/aab6a6

Hernanz, M., & Jose, J. 1998, in Astronomical Society of the Pacific Conference Series, Vol. 137, Wild Stars in the Old West, ed. S. Howell, E. Kuulkers, & C. Woodward, 368

Hillman, Y., Prialnik, D., Kovetz, A., & Shara, M. M. 2016a, *Astrophys. J.*, 819, 168, doi: 10.3847/0004-637X/819/2/168

—. 2016b, *Astrophys. J.*, 819, 168, doi: 10.3847/0004-637X/819/2/168

Hillman, Y., Shara, M., Prialnik, D., & Kovetz, A. 2020, Advances in Space Research, 66, 1072, doi: 10.1016/j.asr.2019.08.029

Hornoch, K., & Honkova, K. 2015, The Astronomer's Telegram, 7492, 1

Hornoch, K., & Kucakova, H. 2016a, The Astronomer's Telegram, 9373, 1

—. 2016b, The Astronomer's Telegram, 9431, 1

—. 2016c, The Astronomer's Telegram, 9552, 1

—. 2016d, The Astronomer's Telegram, 8785, 1

—. 2016e, The Astronomer's Telegram, 9098, 1

—. 2018, The Astronomer's Telegram, 12262, 1

—. 2019a, The Astronomer's Telegram, 12925, 1

—. 2019b, The Astronomer's Telegram, 13109, 1

—. 2019c, The Astronomer's Telegram, 13207, 1

—. 2020a, The Astronomer's Telegram, 14055, 1

—. 2020b, The Astronomer's Telegram, 14155, 1

—. 2020c, The Astronomer's Telegram, 14068, 1

Hornoch, K., Kucakova, H., & Wolf, M. 2016a, The Astronomer's Telegram, 8787, 1

—. 2019, The Astronomer's Telegram, 13355, 1

Hornoch, K., & Kusnirak, P. 2019, The Astronomer's Telegram, 12895, 1

Hornoch, K., Kusnirak, P., Wolf, M., & Zasche, P. 2010, Central Bureau Electronic Telegrams, 2212, 3

Hornoch, K., Manilla-Robles, A., Tudor, V., Vaduvescu, O., & Ramsay, G. 2013, The Astronomer's Telegram, 5503, 1

Hornoch, K., Vrastil, J., Honkova, K., & Kucakova, H. 2016b, The Astronomer's Telegram, 8877, 1

Hornoch, K., Wolf, M., & Kucakova, H. 2016c, The Astronomer's Telegram, 9545, 1

Hubble, E. P. 1929, *Astrophys. J.*, 69, 103, doi: 10.1086/143167

Hunter, J. D. 2007, Computing in Science & Engineering, 9, 90, doi: 10.1109/MCSE.2007.55

Husser, T. O., Wende-von Berg, S., Dreizler, S., et al. 2013, *Astron. Astrophys.*, 553, A6, doi: 10.1051/0004-6361/201219058

Iijima, T., & Esenoglu, H. H. 2003, *Astron. Astrophys.*, 404, 997, doi: 10.1051/0004-6361:20030528

Itagaki, K., Gao, X., Darnley, M. J., et al. 2016, The Astronomer's Telegram, 9848, 1

Itagaki, K., Vanmunster, T., Watanabe, F., et al. 2021, The Astronomer's Telegram, 15034, 1

Ivezić, Ž., Kahn, S. M., Tyson, J. A., et al. 2019, *Astrophys. J.*, 873, 111, doi: 10.3847/1538-4357/ab042c

Jester, S., Schneider, D. P., Richards, G. T., et al. 2005, *Astron. J.*, 130, 873, doi: 10.1086/432466

Jiang, X., Sun, G., Zhang, M., & Gao, X. 2019, Transient Name Server Discovery Report, 2019-2620, 1

José, J., & Hernanz, M. 1998, *Astrophys. J.*, 494, 680, doi: 10.1086/305244

José, J., Shore, S. N., & Casanova, J. 2020, *Astron. Astrophys.*, 634, A5, doi: 10.1051/0004-6361/201936893

Joseph, P., Stalin, C. S., Tandon, S. N., & Ghosh, S. K. 2021, Journal of Astrophysics and Astronomy, 42, 25, doi: 10.1007/s12036-020-09680-5

Joye, W. A., & Mandel, E. 2003, in Astronomical Society of the Pacific Conference Series, Vol. 295, Astronomical Data Analysis Software and Systems XII, ed. H. E. Payne, R. I. Jedrzejewski, & R. N. Hook, 489

K., I. 2016, J00452885, 4154097

Kasliwal, M., & Cao, Y. 2018a, Transient Name Server Discovery Report, 2018-1344, 1

—. 2018b, Transient Name Server Discovery Report, 2018-1069, 1

Kasliwal, M. M., Cenko, S. B., Kulkarni, S. R., et al. 2011, *Astrophys. J.*, 735, 94, doi: 10.1088/0004-637X/735/2/94

Kastner, S. O., & Bhatia, A. K. 1995, *Astrophys. J.*, 439, 346, doi: 10.1086/175178

Kato, M., & Hachisu, I. 1994, *Astrophys. J.*, 437, 802, doi: 10.1086/175041

—. 2003a, *Astrophys. J. Lett.*, 598, L107, doi: 10.1086/380597

—. 2003b, *Astrophys. J. Lett.*, 587, L39, doi: 10.1086/375043

—. 2009, *Astrophys. J.*, 699, 1293, doi: 10.1088/0004-637X/699/2/1293

—. 2011, *Astrophys. J.*, 743, 157, doi: 10.1088/0004-637X/743/2/157

Kato, M., Saio, H., & Hachisu, I. 2015, *Astrophys. J.*, 808, 52, doi: 10.1088/0004-637X/808/1/52

—. 2022, *Pub. Astron. Soc. Japan*, 74, 1005, doi: 10.1093/pasj/psac051

—. 2024, *Pub. Astron. Soc. Japan*, 76, 666, doi: 10.1093/pasj/psae038

Kato, M., Saio, H., Hachisu, I., & Nomoto, K. 2014a, *Astrophys. J.*, 793, 136, doi: 10.1088/0004-637X/793/2/136

—. 2014b, *Astrophys. J.*, 793, 136, doi: 10.1088/0004-637X/793/2/136

Kato, T., Nakajima, K., Maehara, H., & Kiyota, S. 2009, arXiv e-prints. https://arxiv.org/abs/0904.2228

Kiyota, S., Kato, T., & Yamaoka, H. 2004, *Pub. Astron. Soc. Japan*, 56, S193, doi: 10.1093/pasj/56.sp1.S193

Knigge, C., Toonen, S., & Boekholt, T. C. N. 2022, *Mon. Not. Roy. Astron. Soc.*, 514, 1895, doi: 10.1093/mnras/stac1336

König, O., Wilms, J., Arcodia, R., et al. 2022, *Nature*, 605, 248, doi: 10.1038/s41586-022-04635-y

Korotkiy, S., & Elenin, L. 2011, J00452885, 4154094

Krautter, J. 2008, in Astronomical Society of the Pacific Conference Series, Vol. 401, RS Ophiuchi (2006) and the Recurrent Nova Phenomenon, ed. A. Evans, M. F. Bode, T. J. O'Brien, & M. J. Darnley, 139

Kuin, N. P. M., Page, K. L., Mróz, P., et al. 2020, *Mon. Not. Roy. Astron. Soc.*, 491, 655, doi: 10.1093/mnras/stz2960

Kulkarni, S. R., Harrison, F. A., Grefenstette, B. W., et al. 2021, arXiv e-prints, arXiv:2111.15608, doi: 10.48550/arXiv.2111.15608

Kumar, H., Bhalerao, V., Anupama, G. C., et al. 2022, *Astron. J.*, 164, 90, doi: 10.3847/1538-3881/ac7bea

—. 2022a, *Astron. J.*, 164, 90, doi: 10.3847/1538-3881/ac7bea

Kumar, H., Bhalerao, V., Anupama, G. C., et al. 2022b, Monthly Notices of the Royal Astronomical Society, 516, 4517, doi: 10.1093/mnras/stac2516

Kumar, R., Swain, V., Basu, J., et al. 2023, Transient Name Server AstroNote, 255, 1

Leahy, D., Buick, M., Postma, J., & Morgan, C. 2021, *Astron. J.*, 161, 215, doi: 10.3847/1538-3881/abe9b3

Leahy, D., Craiciu, T., & Postma, J. 2023, *Astrophys. J. Suppl.*, 265, 6, doi: 10.3847/1538-4365/acae90

Leahy, D. A., Postma, J., Chen, Y., & Buick, M. 2020, *Astrophys. J. Suppl.*, 247, 47, doi: 10.3847/1538-4365/ab77a9

Lee, C.-H., Soraisam, M., Narayan, G., Matheson, T., & Saha, A. 2019, The Astronomer's Telegram, 13141, 1

Lee, C. H., Riffeser, A., Seitz, S., et al. 2012, *Astron. Astrophys.*, 537, A43, doi: 10.1051/0004-6361/201117068

Lessing, A. M., Shara, M. M., Hounsell, R., et al. 2023, arXiv e-prints, arXiv:2309.16856, doi: 10.48550/arXiv.2309.16856

Li, K.-L., Hambsch, F.-J., Munari, U., et al. 2020, *Astrophys. J.*, 905, 114, doi: 10.3847/1538-4357/abc3be

Li, K.-L., Metzger, B. D., Chomiuk, L., et al. 2017, Nature Astronomy, 1, 697, doi: 10.1038/s41550-017-0222-1

Liller, W. 1990, *IAU Circ.*, 4961, 2

Lloyd, H. M., O'Brien, T. J., Bode, M. F., et al. 1992, *Nature*, 356, 222, doi: 10.1038/356222a0

LSST Science Collaboration, Abell, P. A., Allison, J., et al. 2009, arXiv e-prints, arXiv:0912.0201, doi: 10.48550/arXiv.0912.0201

Lunt, J. 1926, *Mon. Not. Roy. Astron. Soc.*, 86, 498, doi: 10.1093/mnras/86.7.498

Lyman, J. D. 2021, spalipy: Detection-based astronomical image registration, Astrophysics Source Code Library, record ascl:2103.003

Madrigal-Aguado, A., Alvarez-Hernandez, L., Bayer, J., et al. 2019, The Astronomer's Telegram, 13272, 1

Mandigo-Stoba, M. S., Fremling, C., & Kasliwal, M. 2022, The Journal of Open Source Software, 7, 3612, doi: 10.21105/joss.03612

Martin, P., Dubus, G., Jean, P., Tatischeff, V., & Dosne, C. 2018a, *Astron. Astrophys.*, 612, A38, doi: 10.1051/0004-6361/201731692

Martin, T. B., Drissen, L., & Melchior, A.-L. 2018b, *Mon. Not. Roy. Astron. Soc.*, 473, 4130, doi: 10.1093/mnras/stx2513

Masci, F. J., Laher, R. R., Rusholme, B., et al. 2019, *Pub. Astron. Soc. Pac.*, 131, 018003, doi: 10.1088/1538-3873/aae8ac

Masci, F. J., Laher, R. R., Rusholme, B., et al. 2023, A New Forced Photometry Service for the Zwicky Transient Facility. https://arxiv.org/abs/2305.16279

Maslennikova, N. A., Tatarnikov, A. M., Tatarnikova, A. A., et al. 2024, Astronomy Letters, 49, 501, doi: 10.1134/S1063773723090037

Mason, E., Shore, S. N., Kuin, P., & Bohlsen, T. 2020, *Astron. Astrophys.*, 635, A115, doi: 10.1051/0004-6361/201937025

McLoughlin, D., Blundell, K. M., Lee, S., & McCowage, C. 2021a, *Mon. Not. Roy. Astron. Soc.*, 503, 704, doi: 10.1093/mnras/stab581

—. 2021b, *Mon. Not. Roy. Astron. Soc.*, 505, 2518, doi: 10.1093/mnras/stab1364

Metzger, B. D., Hascoët, R., Vurm, I., et al. 2014, *Mon. Not. Roy. Astron. Soc.*, 442, 713, doi: 10.1093/mnras/stu844

Mikolajewska, J. 2010, arXiv e-prints, arXiv:1011.5657, doi: 10.48550/arXiv.1011.5657

Mondal, A., Das, R., Anupama, G. C., & Mondal, S. 2020, *Mon. Not. Roy. Astron. Soc.*, 492, 2326, doi: 10.1093/mnras/stz3570

Mroz, P., & Udalski, A. 2021, The Astronomer's Telegram, 14410, 1

Mróz, P., Udalski, A., Poleski, R., et al. 2015, *Astrophys. J. Suppl.*, 219, 26, doi: 10.1088/0067-0049/219/2/26

—. 2016, *Astrophys. J. Suppl.*, 222, 9, doi: 10.3847/0067-0049/222/1/9

Mróz, P., Poleski, R., Udalski, A., et al. 2014, Monthly Notices of the Royal Astronomical Society, 443, 784, doi: 10.1093/mnras/stu1181

Mukai, K., Orio, M., & Della Valle, M. 2008, *Astrophys. J.*, 677, 1248, doi: 10.1086/529362

Munari, U. 2025, Contributions of the Astronomical Observatory Skalnate Pleso, 55, 47, doi: 10.31577/caosp.2025.55.3.47

Munari, U., Giroletti, M., Marcote, B., et al. 2022, *Astron. Astrophys.*, 666, L6, doi: 10.1051/0004-6361/202244821

Muraoka, K., Kojiguchi, N., Ito, J., et al. 2024, *Pub. Astron. Soc. Japan*, 76, 293, doi: 10.1093/pasj/psae010

—. 2025, arXiv e-prints, arXiv:2503.20559, doi: 10.48550/arXiv.2503.20559

Naito, H., Watanabe, F., Sano, Y., et al. 2018, The Astronomer's Telegram, 11133, 1

Nasa High Energy Astrophysics Science Archive Research Center (Heasarc). 2014, HEAsoft: Unified Release of FTOOLS and XANADU, Astrophysics Source Code Library, record ascl:1408.004. http://ascl.net/1408.004

Nauenberg, M. 1972, *Astrophys. J.*, 175, 417, doi: 10.1086/151568

Ness, J.-U. 2020, Advances in Space Research, 66, 1202, doi: 10.1016/j.asr.2019.09.002

Ness, J. U., Drake, J. J., Beardmore, A. P., et al. 2009, *Astron. J.*, 137, 4160, doi: 10.1088/0004-6256/137/5/4160

Ness, J. U., Schaefer, B. E., Dobrotka, A., et al. 2012, *Astrophys. J.*, 745, 43, doi: 10.1088/0004-637X/745/1/43

Ness, J. U., Beardmore, A. P., Bezak, P., et al. 2022, *Astron. Astrophys.*, 658, A169, doi: 10.1051/0004-6361/202142037

Ness, J. U., Beardmore, A. P., Bode, M. F., et al. 2023, *Astron. Astrophys.*, 670, A131, doi: 10.1051/0004-6361/202245269

Nishiyama, K., & Kabashima, F. 2008, CBAT IAU, http://www.cbat.eps.harvard.edu/iau/CBAT_M31.html#2008 12a

Nishiyama, K., & Kabashima, F. 2012, J00452884, 4154095

Nomoto, K., Saio, H., Kato, M., & Hachisu, I. 2007, *Astrophys. J.*, 663, 1269, doi: 10.1086/518465

Nordin, J., Brinnel, V., Giomi, M., et al. 2019, Transient Name Server Discovery Report, 2019-2130, 1

O'Brien, T. J., Bode, M. F., Porcas, R. W., et al. 2006, *Nature*, 442, 279, doi: 10.1038/nature04949

Ogilvie, G. I., & Livio, M. 2001, *Astrophys. J.*, 553, 158, doi: 10.1086/320637

Oke, J. B., & Gunn, J. E. 1982, *Pub. Astron. Soc. Pac.*, 94, 586, doi: 10.1086/131027

Oke, J. B., Cohen, J. G., Carr, M., et al. 1995, *Pub. Astron. Soc. Pac.*, 107, 375, doi: 10.1086/133562

Oksanen, A., Darnley, M. J., Shafter, A. W., et al. 2019, The Astronomer's Telegram, 13269, 1

OpenAI. 2025, ChatGPT (July 13 version). https://chat.openai.com

Orio, M., Parmar, A., Benjamin, R., et al. 2001, *Mon. Not. Roy. Astron. Soc.*, 326, L13, doi: 10.1046/j.1365-8711.2001.04448.x

Osborne, J. P., Page, K. L., Beardmore, A. P., et al. 2011, *Astrophys. J.*, 727, 124, doi: 10.1088/0004-637X/727/2/124

Ovcharov, E., Kostov, A., Kurtenkov, A., Valcheva, A., & Nedialkov, P. 2015a, The Astronomer's Telegram, 7065, 1

Ovcharov, E., Kurtenkov, A., Nikolov, G., et al. 2013, The Astronomer's Telegram, 5475, 1

Ovcharov, E., Minev, M., Bozhilov, V., et al. 2015b, The Astronomer's Telegram, 7789, 1

Özdönmez, A., Ege, E., Güver, T., & Ak, T. 2018, *Mon. Not. Roy. Astron. Soc.*, 476, 4162, doi: 10.1093/mnras/sty432

Page, K. L., Beardmore, A. P., & Osborne, J. P. 2020a, Advances in Space Research, 66, 1169, doi: 10.1016/j.asr.2019.08.003

Page, K. L., & Darnley, M. J. 2024, The Astronomer's Telegram, 16957, 1

Page, K. L., Kuin, N. P. M., & Darnley, M. J. 2020b, The Astronomer's Telegram, 13731, 1

Page, K. L., Kuin, N. P. M., & Osborne, J. P. 2022a, Universe, 8, 643, doi: 10.3390/universe8120643

—. 2022b, Universe, 8, 643, doi: 10.3390/universe8120643

Pagnotta, A., & Schaefer, B. E. 2014, *Astrophys. J.*, 788, 164, doi: 10.1088/0004-637X/788/2/164

Pagnotta, A., Schaefer, B. E., Clem, J. L., et al. 2015, *Astrophys. J.*, 811, 32, doi: 10.1088/0004-637X/811/1/32

Patterson, J. 1984, *Astrophys. J. Suppl.*, 54, 443, doi: 10.1086/190940

Pavana, M. 2020, PhD thesis, Pondicherry University, doi: 10.5281/zenodo.8310053

Pavana, M. 2020, PhD thesis, Indian Institute of Astrophysics, Bangalore

Pavana, M., Anche, R. M., Anupama, G. C., Ramaprakash, A. N., & Selvakumar, G. 2019, *Astron. Astrophys.*, 622, A126, doi: 10.1051/0004-6361/201833728

Paxton, B., Bildsten, L., Dotter, A., et al. 2011, *Astrophys. J. Suppl.*, 192, 3, doi: 10.1088/0067-0049/192/1/3

Payne-Gaposchkin, C., & Kiess, C. C. 1958, Physics Today, 11, 29, doi: 10.1063/1.3062371

Pedregosa, F., Varoquaux, G., Gramfort, A., et al. 2011, Journal of Machine Learning Research, 12, 2825

Pejcha, O. 2009, *Astrophys. J. Lett.*, 701, L119, doi: 10.1088/0004-637X/701/2/L119

Perez-Fournon, I., Poidevin, F., Aznar Menargues, G., et al. 2022, The Astronomer's Telegram, 15786, 1

Perez-Fournon, I., Poidevin, F., Reyes-Rodriguez, E., et al. 2023, The Astronomer's Telegram, 16370, 1

Perley, D. A. 2019, *Pub. Astron. Soc. Pac.*, 131, 084503, doi: 10.1088/1538-3873/ab215d

Pietsch, W. 2010, Astronomische Nachrichten, 331, 187, doi: 10.1002/asna.200911324

Pietsch, W., Henze, M., Burwitz, V., et al. 2010a, The Astronomer's Telegram, 3076, 1

Pietsch, W., Lloyd, J., Henze, M., et al. 2010b, The Astronomer's Telegram, 2964, 1

Pietsch, W., Haberl, F., Sala, G., et al. 2007, *Astron. Astrophys.*, 465, 375, doi: 10.1051/0004-6361:20066812

Poggiani, R. 2008a, *Astrophys. Space Sci.*, 315, 79, doi: 10.1007/s10509-008-9796-5

—. 2008b, *New Astronomy*, 13, 557, doi: 10.1016/j.newast.2008.03.001

Pojmanski, G. 2002, *Acta Astronomica*, 52, 397, doi: 10.48550/arXiv.astro-ph/0210283

Poole, T. S., Breeveld, A. A., Page, M. J., et al. 2008, *Mon. Not. Roy. Astron. Soc.*, 383, 627, doi: 10.1111/j.1365-2966.2007.12563.x

Postma, J. E., & Leahy, D. 2017, *Pub. Astron. Soc. Pac.*, 129, 115002, doi: 10.1088/1538-3873/aa8800

—. 2021a, Journal of Astrophysics and Astronomy, 42, 30, doi: 10.1007/s12036-020-09689-w

—. 2021b, Journal of Astrophysics and Astronomy, 42, 30, doi: 10.1007/s12036-020-09689-w

Prialnik, D., & Kovetz, A. 1995, *Astrophys. J.*, 445, 789, doi: 10.1086/175741

Rector, T. A., Jacoby, G. H., Corbett, D. L., Denham, M., & RBSE Nova Search Team. 1999, in American Astronomical Society Meeting Abstracts, Vol. 195, American Astronomical Society Meeting Abstracts, 36.08

Rector, T. A., Shafter, A. W., Burris, W. A., et al. 2022, *Astrophys. J.*, 936, 117, doi: 10.3847/1538-4357/ac87ad

Retter, A. 2002a, in American Institute of Physics Conference Series, Vol. 637, Classical Nova Explosions, ed. M. Hernanz & J. José (AIP), 279–283, doi: 10.1063/1.1518214

Retter, A. 2002b, in Astronomical Society of the Pacific Conference Series, Vol. 261, The Physics of Cataclysmic Variables and Related Objects, ed. B. T. Gänsicke, K. Beuermann, & K. Reinsch, 655, doi: 10.48550/arXiv.astro-ph/0110102

Ribeiro, V. A. R. M., Bode, M. F., Darnley, M. J., et al. 2009, *Astrophys. J.*, 703, 1955, doi: 10.1088/0004-637X/703/2/1955

Roming, P. W. A., Kennedy, T. E., Mason, K. O., et al. 2005, *Space Sci. Rev.*, 120, 95, doi: 10.1007/s11214-005-5095-4

Rosino, L. 1964, Annales d'Astrophysique, 27, 498

—. 1973, *Astron. Astrophys. Suppl.*, 9, 347

Rosino, L., Capaccioli, M., D'Onofrio, M., & della Valle, M. 1989, *Astron. J.*, 97, 83, doi: 10.1086/114959

Roy, N., Chomiuk, L., Sokoloski, J. L., et al. 2012, Bulletin of the Astronomical Society of India, 40, 293, doi: 10.48550/arXiv.1302.4455

Rupen, M. P., Mioduszewski, A. J., & Sokoloski, J. L. 2008, *Astrophys. J.*, 688, 559, doi: 10.1086/525555

Ryon, J. E., & Stark, D. V. 2023, in ACS Instrument Handbook for Cycle 32 v. 23.0, Vol. 23, 23

Schaefer, B. E. 2010, VizieR Online Data Catalog, 218

—. 2021, Research Notes of the American Astronomical Society, 5, 150, doi: 10.3847/2515-5172/ac0d5b

—. 2023, *Mon. Not. Roy. Astron. Soc.*, 524, 3146, doi: 10.1093/mnras/stad735

Schwarz, G. J., Hauschildt, P. H., Starrfield, S., et al. 1997, *Mon. Not. Roy. Astron. Soc.*, 284, 669, doi: 10.1093/mnras/284.3.669

—. 1998, *Mon. Not. Roy. Astron. Soc.*, 300, 931, doi: 10.1046/j.1365-8711.1998.01964.x

Schwarz, G. J., Page, K. L., Kuin, P. M., & Darnley, M. J. 2020, Research Notes of the American Astronomical Society, 4, 142, doi: 10.3847/2515-5172/abae72

Schwarz, G. J., Shore, S. N., Starrfield, S., et al. 2001, *Mon. Not. Roy. Astron. Soc.*, 320, 103, doi: 10.1046/j.1365-8711.2001.03960.x

Schwarz, G. J., Woodward, C. E., Bode, M. F., et al. 2007, *Astron. J.*, 134, 516, doi: 10.1086/519240

Selvelli, P., & Gilmozzi, R. 2013, *Astron. Astrophys.*, 560, A49, doi: 10.1051/0004-6361/201220627

—. 2019, *Astron. Astrophys.*, 622, A186, doi: 10.1051/0004-6361/201834238

Shafter, A. W., Bode, M. F., Darnley, M. J., et al. 2011a, *Astrophys. J.*, 727, 50, doi: 10.1088/0004-637X/727/1/50

Shafter, A. W., Curtin, C., Pritchet, C. J., Bode, M. F., & Darnley, M. J. 2014, in Astronomical Society of the Pacific Conference Series, Vol. 490, Stellar Novae: Past and Future Decades, ed. P. A. Woudt & V. A. R. M. Ribeiro, 77, doi: 10.48550/arXiv.1307.2296

Shafter, A. W., Hornoch, K., Ciardullo, J. V. R., Darnley, M. J., & Bode, M. F. 2012, The Astronomer's Telegram, 4503, 1

Shafter, A. W., & Irby, B. K. 2001, *Astrophys. J.*, 563, 749, doi: 10.1086/324044

Shafter, A. W., Rau, A., Quimby, R. M., et al. 2009, *Astrophys. J.*, 690, 1148, doi: 10.1088/0004-637X/690/2/1148

Shafter, A. W., Taguchi, K., Zhao, J., & Hornoch, K. 2022a, Research Notes of the American Astronomical Society, 6, 241, doi: 10.3847/2515-5172/aca2a6

Shafter, A. W., Yousuf, I., Luo, A., et al. 2023a, The Astronomer's Telegram, 16382, 1

Shafter, A. W., Darnley, M. J., Hornoch, K., et al. 2011b, *Astrophys. J.*, 734, 12, doi: 10.1088/0004-637X/734/1/12

Shafter, A. W., Burris, W. A., Horst, J. C., et al. 2022b, The Astronomer's Telegram, 15797, 1

Shafter, A. W., Adurkar, A., Bautista, V., et al. 2023b, The Astronomer's Telegram, 16362, 1

Shafter, A. W., Hornoch, K., Kučáková, H., et al. 2024a, Research Notes of the American Astronomical Society, 8, 5, doi: 10.3847/2515-5172/ad19de

Shafter, A. W., Zhao, J., Hornoch, K., et al. 2024b, Research Notes of the American Astronomical Society, 8, 256, doi: 10.3847/2515-5172/ad84d5

Shappee, B., Prieto, J., Stanek, K. Z., et al. 2014, in American Astronomical Society Meeting Abstracts, Vol. 223, American Astronomical Society Meeting Abstracts #223, 236.03

Shara, M. M., Prialnik, D., Hillman, Y., & Kovetz, A. 2018, *Astrophys. J.*, 860, 110, doi: 10.3847/1538-4357/aabfbd

Shara, M. M., Lessing, A. M., Hounsell, R., et al. 2023, *Astrophys. J. Suppl.*, 269, 42, doi: 10.3847/1538-4365/ad02fd

Shara, M. M., Lanzetta, K. M., Garland, J. T., et al. 2024a, *Mon. Not. Roy. Astron. Soc.*, 529, 224, doi: 10.1093/mnras/stad3612

Shara, M. M., Lanzetta, K. M., Masegian, A., et al. 2024b, *Astrophys. J. Lett.*, 977, L48, doi: 10.3847/2041-8213/ad991e

—. 2025, arXiv e-prints, arXiv:2505.09510, doi: 10.48550/arXiv.2505.09510

Sharov, A. S., & Alksnis, A. 1991, *Astrophys. Space Sci.*, 180, 273, doi: 10.1007/BF00648182

Sharov, A. S., Alksnis, A., Zharova, A. V., & Shokin, Y. A. 2000, Astronomy Letters, 26, 433, doi: 10.1134/1.20416

Shore, S. N. 2008, in Classical Novae, ed. M. F. Bode & A. Evans, Vol. 43, 194–231, doi: 10.1017/CBO9780511536168.011

Shore, S. N., Kenyon, S. J., Starrfield, S., & Sonneborn, G. 1996, *Astrophys. J.*, 456, 717, doi: 10.1086/176692

Shumkov, V., Lipunov, V., Rebolo, R., et al. 2017, The Astronomer's Telegram, 10506, 1

Shvartzvald, Y., Waxman, E., Gal-Yam, A., et al. 2024, *Astrophys. J.*, 964, 74, doi: 10.3847/1538-4357/ad2704

Sievers, J. 1970, Information Bulletin on Variable Stars, 448, 1

Singh, K. P., & Bhattacharya, D. 2017, Current Science, 113, 602, doi: 10.18520/cs/v113/i04/602-609

Singh, K. P., Girish, V., Pavana, M., et al. 2021, *Mon. Not. Roy. Astron. Soc.*, 501, 36, doi: 10.1093/mnras/staa3303

Singh, K. P., Tandon, S. N., Agrawal, P. C., et al. 2014, in Society of Photo-Optical Instrumentation Engineers (SPIE) Conference Series, Vol. 9144, Space Telescopes and Instrumentation 2014: Ultraviolet to Gamma Ray, ed. T. Takahashi, J.-W. A. den Herder, & M. Bautz, 91441S, doi: 10.1117/12.2062667

Singh, K. P., Stewart, G. C., Westergaard, N. J., et al. 2017, Journal of Astrophysics and Astronomy, 38, 29, doi: 10.1007/s12036-017-9448-7

Sirianni, M., Jee, M. J., Benítez, N., et al. 2005, *Pub. Astron. Soc. Pac.*, 117, 1049, doi: 10.1086/444553

Skopal, A. 2015, *New Astronomy*, 36, 139, doi: 10.1016/j.newast.2014.09.007

Sokoloski, J. L., Rupen, M. P., & Mioduszewski, A. J. 2008, *Astrophys. J. Lett.*, 685, L137, doi: 10.1086/592602

Sokolovsky, K., Aydi, E., Chomiuk, L., et al. 2020, The Astronomer's Telegram, 14078, 1

Soraisam, M., Lee, C.-H., Narayan, G., Matheson, T., & Saha, A. 2019a, The Astronomer's Telegram, 13210, 1

Soraisam, M., Lee, C.-H., Nunez, R., et al. 2019b, The Astronomer's Telegram, 13317, 1

Soraisam, M., McKinnon, K., Nunez, R., et al. 2020, The Astronomer's Telegram, 14150, 1

Soraisam, M. D., Gilfanov, M., Wolf, W. M., & Bildsten, L. 2016, *Mon. Not. Roy. Astron. Soc.*, 455, 668, doi: 10.1093/mnras/stv2359

Srivastav, S., Smartt, S. J., McBrien, O., et al. 2020, Transient Name Server Classification Report, 2020-3471, 1

Stanek, K. Z., & Garnavich, P. M. 1998, The Astrophysical Journal, 503, L131, doi: 10.1086/311539

Starrfield, S. 1986, in ESA Special Publication, Vol. 263, New Insights in Astrophysics. Eight Years of UV Astronomy with IUE, ed. E. J. Rolfe & R. Wilson, 239

Starrfield, S. 1999, *Physics Reports*, 311, 371, doi: 10.1016/S0370-1573(98)00116-1

Starrfield, S. 2017, Evolution of Accreting White Dwarfs to the Thermonuclear Runaway, ed. A. W. Alsabti & P. Murdin (Cham: Springer International Publishing), 1211–1236, doi: 10.1007/978-3-319-21846-5_59

Starrfield, S., Bose, M., Iliadis, C., et al. 2020, *Astrophys. J.*, 895, 70, doi: 10.3847/1538-4357/ab8d23

Starrfield, S., Iliadis, C., & Hix, W. R. 2016, *Pub. Astron. Soc. Pac.*, 128, 051001, doi: 10.1088/1538-3873/128/963/051001

Starrfield, S., Truran, J. W., & Sparks, W. M. 2000, *New Astronomy Reviews*, 44, 81, doi: 10.1016/S1387-6473(00)00018-X

Starrfield, S. G., Sparks, W. M., & Truran, J. W. 1975, Memoires of the Societe Royale des Sciences de Liege, 8, 425

Steffen, W., Koning, N., Wenger, S., Morisset, C., & Magnor, M. 2011, IEEE Transactions on Visualization and Computer Graphics, 17, 454, doi: 10.1109/TVCG.2010.62

Steinberg, E., & Metzger, B. D. 2020, *Mon. Not. Roy. Astron. Soc.*, 491, 4232, doi: 10.1093/mnras/stz3300

Strope, R. J., Schaefer, B. E., & Henden, A. A. 2010a, *Astron. J.*, 140, 34, doi: 10.1088/0004-6256/140/1/34

—. 2010b, *Astron. J.*, 140, 34, doi: 10.1088/0004-6256/140/1/34

Subramaniam, A. 2022, Journal of Astrophysics and Astronomy, 43, 80, doi: 10.1007/s12036-022-09870-3

Subramaniam, A., Tandon, S. N., Hutchings, J., et al. 2016, in Society of Photo-Optical Instrumentation Engineers (SPIE) Conference Series, Vol. 9905, Space Telescopes and Instrumentation 2016: Ultraviolet to Gamma Ray, ed. J.-W. A. den Herder, T. Takahashi, & M. Bautz, 99051F, doi: 10.1117/12.2235271

Sun, G., Xu, J., Zhang, M., et al. 2023, The Astronomer's Telegram, 16361, 1

Tan, H., & Gao, X. 2018, The Astronomer's Telegram, 12200

Tan, H., Zhang, M., Zhao, J., et al. 2021, The Astronomer's Telegram, 15037, 1

Tanaka, J., Nogami, D., Fujii, M., Ayani, K., & Kato, T. 2011a, *Pub. Astron. Soc. Japan*, 63, 159, doi: 10.1093/pasj/63.1.159

Tanaka, J., Nogami, D., Fujii, M., et al. 2011b, *Pub. Astron. Soc. Japan*, 63, 911, doi: 10.1093/pasj/63.4.911

Tandon, S. N., Hutchings, J. B., Ghosh, S. K., et al. 2017a, Journal of Astrophysics and Astronomy, 38, 28, doi: 10.1007/s12036-017-9445-x

—. 2017b, Journal of Astrophysics and Astronomy, 38, 28, doi: 10.1007/s12036-017-9445-x

Tandon, S. N., Subramaniam, A., Girish, V., et al. 2017c, *Astron. J.*, 154, 128, doi: 10.3847/1538-3881/aa8451

Tandon, S. N., Postma, J., Joseph, P., et al. 2020, *Astron. J.*, 159, 158, doi: 10.3847/1538-3881/ab72a3

Tang, S., Cao, Y., & Kasliwal, M. M. 2013, The Astronomer's Telegram, 5607, 1

Tang, S., Bildsten, L., Wolf, W. M., et al. 2014, *Astrophys. J.*, 786, 61, doi: 10.1088/0004-637X/786/1/61

Tody, D. 1993, in Astronomical Society of the Pacific Conference Series, Vol. 52, Astronomical Data Analysis Software and Systems II, ed. R. J. Hanisch, R. J. V. Brissenden, & J. Barnes, 173

Tomaney, A. B., & Crotts, A. P. S. 1996, *Astron. J.*, 112, 2872, doi: 10.1086/118228

Tomaney, A. B., & Shafter, A. W. 1992, *Astrophys. J. Suppl.*, 81, 683, doi: 10.1086/191702

Tonry, J. L., Denneau, L., Heinze, A. N., et al. 2018, *Pub. Astron. Soc. Pac.*, 130, 064505, doi: 10.1088/1538-3873/aabadf

Townsley, D. M., & Bildsten, L. 2004, *Astrophys. J.*, 600, 390, doi: 10.1086/379647

Tuerler, M., Ferrigno, C., Eckert, D., Watanabe, K., & Kuulkers, E. 2015, The Astronomer's Telegram, 7244, 1

Vacca, W. D., Cushing, M. C., & Rayner, J. T. 2003, *Pub. Astron. Soc. Pac.*, 115, 389, doi: 10.1086/346193

Valcheva, A., Kostov, A., Minev, M., Ovcharov, E., & Nedialkov, P. 2018, The Astronomer's Telegram, 12261, 1

Valcheva, A., Kurtenkov, A., Ovcharov, E., et al. 2016, The Astronomer's Telegram, 9559, 1

Valcheva, A., Minev, M., Ovcharov, E., & Nedialkov, P. 2020, The Astronomer's Telegram, 14212, 1

Van Rossum, G., & Drake, F. L. 2009, Python 3 Reference Manual (Scotts Valley, CA: CreateSpace)

Virtanen, P., Gommers, R., Oliphant, T. E., et al. 2020, Nature Methods, 17, 261, doi: 10.1038/s41592-019-0686-2

Wagner, R. M., Woodward, C. E., Starrfield, S., Rothberg, B., & Kuhn, O. 2021, The Astronomer's Telegram, 15036, 1

Wang, B. 2018a, Research in Astronomy and Astrophysics, 18, 049, doi: 10.1088/1674-4527/18/5/49

—. 2018b, Research in Astronomy and Astrophysics, 18, 049, doi: 10.1088/1674-4527/18/5/49

Warner, B. 1995, *Astrophys. Space Sci.*, 232, 89, doi: 10.1007/BF00627546

—. 2003, Cataclysmic Variable Stars, doi: 10.1017/CBO9780511586491

—. 2008, in Classical Novae, ed. M. F. Bode & A. Evans, Vol. 43, 16–33, doi: 10.1017/CBO9780511536168.004

Wes McKinney. 2010, in Proceedings of the 9th Python in Science Conference, ed. Stéfan van der Walt & Jarrod Millman, 56 – 61, doi: 10.25080/Majora-92bf1922-00a

White, N. E., Giommi, P., Heise, J., Angelini, L., & Fantasia, S. 1995, *Astrophys. J. Lett.*, 445, L125, doi: 10.1086/187905

Williams, B. F., Garcia, M. R., Kong, A. K. H., et al. 2004, *Astrophys. J.*, 609, 735, doi: 10.1086/421315

Williams, R. 2012, *Astron. J.*, 144, 98, doi: 10.1088/0004-6256/144/4/98

Williams, R. E. 1992, *Astron. J.*, 104, 725, doi: 10.1086/116268

Williams, R. E., Ney, E. P., Sparks, W. M., et al. 1985, *Mon. Not. Roy. Astron. Soc.*, 212, 753, doi: 10.1093/mnras/212.4.753

Williams, S. C., Bode, M. F., Darnley, M. J., et al. 2013, *Astrophys. J. Lett.*, 777, L32, doi: 10.1088/2041-8205/777/2/L32

Williams, S. C., & Darnley, M. J. 2015a, The Astronomer's Telegram, 8218, 1

—. 2015b, The Astronomer's Telegram, 8281, 1

Williams, S. C., Darnley, M. J., Bode, M. F., Keen, A., & Shafter, A. W. 2014, *Astrophys. J. Suppl.*, 213, 10, doi: 10.1088/0067-0049/213/1/10

Williams, S. C., Darnley, M. J., Bode, M. F., & Shafter, A. W. 2016, *Astrophys. J.*, 817, 143, doi: 10.3847/0004-637X/817/2/143

Williams, S. C., Darnley, M. J., & Healy, M. W. 2019a, The Astronomer's Telegram, 12349, 1

Williams, S. C., Darnley, M. J., Healy, M. W., Murphy-Glaysher, F. J., & Ransome, C. L. 2019b, The Astronomer's Telegram, 13078, 1

—. 2019c, The Astronomer's Telegram, 13228, 1

—. 2020a, The Astronomer's Telegram, 14053, 1

—. 2020b, The Astronomer's Telegram, 13384, 1

Williams, S. C., Darnley, M. J., Healy, M. W., et al. 2020c, The Astronomer's Telegram, 14121, 1

Wilms, J., Allen, A., & McCray, R. 2000, *Astrophys. J.*, 542, 914, doi: 10.1086/317016

Wilson, J. C., Henderson, C. P., Herter, T. L., et al. 2004, in Society of Photo-Optical Instrumentation Engineers (SPIE) Conference Series, Vol. 5492, Ground-based Instrumentation for Astronomy, ed. A. F. M. Moorwood & M. Iye, 1295–1305, doi: 10.1117/12.550925

Wolf, W. M., Bildsten, L., Brooks, J., & Paxton, B. 2013, *Astrophys. J.*, 777, 136, doi: 10.1088/0004-637X/777/2/136

XRISM Science Team. 2020, arXiv e-prints, arXiv:2003.04962, doi: 10.48550/arXiv.2003.04962

Yaron, O., Prialnik, D., Shara, M. M., & Kovetz, A. 2005, *Astrophys. J.*, 623, 398, doi: 10.1086/428435

Zackay, B., Ofek, E. O., & Gal-Yam, A. 2016, *Astrophys. J.*, 830, 27, doi: 10.3847/0004-637X/830/1/27

Zamanov, R. K., Marchev, V., Marti, J., & Latev, G. Y. 2023, arXiv e-prints, arXiv:2308.04104, doi: 10.48550/arXiv.2308.04104

Zemko, P., Orio, M., & Evans, P. A. 2015, The Astronomer's Telegram, 7404, 1

Zhang, M., & Gao, X. 2018a, Transient Name Server Discovery Report, 2018-2050, 1

—. 2018b, Transient Name Server Discovery Report, 2018-2069, 1

—. 2019a, Transient Name Server Discovery Report, 2019-1827, 1

—. 2019b, Transient Name Server Discovery Report, 2019-2512, 1

—. 2020a, Transient Name Server Discovery Report, 2020-2924, 1

—. 2020b, Transient Name Server Discovery Report, 2020-3315, 1

—. 2020c, Transient Name Server Discovery Report, 2020-3322, 1

—. 2020d, Transient Name Server Discovery Report, 2020-3028, 1

—. 2020e, Transient Name Server Discovery Report, 2020-3130, 1

Zhao, J., & Ren, Y. 2024, The Astronomer's Telegram, 16946, 1

Zhao, J., Shafter, A. W., Horst, J. C., et al. 2024, The Astronomer's Telegram, 16942, 1